



國立中央大學天文研究所  
鹿林天文台年報

**2018**

**No.16**

國立中央大學天文研究所 編

# 目錄

## 研究論文

Star-disk Interaction in Multi-band Photometric Monitoring of the Classical T Tauri Star GI Tau, Guo, Z., Herczeg, G. J., Jose, J., et al., <i>Astroph. J.</i> , 852, 56 (2018) .....	4
Photometric survey and taxonomic identifications of 92 near-Earth asteroids, Lin, C.-H., Ip, W.-H., Lin, Z.-Y., et al., <i>Planetary and Space Science</i> , 152, 116-135., 2018 .....	19
Confirmation of Large Super-fast Rotator (144977) 2005 EC127, Pittori, C., Lucarelli, F., Verrecchia, F., et al., <i>Astroph. J.</i> , 856, 99, 2018 .....	39
The sdB pulsating star V391 Peg and its putative giant planet revisited after 13 years of time-series photometric data, Silvotti, R.; Schuh, S.; Kim, S.-L., et al., <i>Astronomy &amp; Astrophysics</i> , 611, A85, 2018 .....	48
SN 2017ens: The Metamorphosis of a Luminous Broadlined Type Ic Supernova into an SN IIn, Chen, T.-W.; Inserra, C.; Fraser, M.; et al., <i>Astroph. J.</i> , 867, L31, 2018 .....	61

## 工作報告

鹿林天文台觀測時數統計(2003-2018).....	70
鹿林天文台LOT 觀測研究計畫統計 (2018).....	72
鹿林天文台工作報告2018, 林宏欽.....	77
鹿林天文台團體參觀及觀測教學2018.....	83
Analysis of Lunar Impact Flashes Recorded during the Geminids meteor shower in 2017, Zong-Yi Lin ,Chih-Cheng Liu , Bo-Hao Wang , Yan-Syun Jhang , Bingsyun Wu , Jim Lee , Zhong-Yi Lin , Hung-Chin Lin , Hsin-Chang Chi.....	85
Meteor investigations using the TMDS, Bo-Hao Wang , Zong-Yi Lin , Chih-Cheng Liu , Yan-Syun Jhang , Bingsyun Wu , Jim Lee , Zhong-Yi Lin , Hsin-Chang Chi .....	89
Lulin Widefield Telescope (LWT): a Robotic Telescope for the Near-Earth Objects Follow-up Observation, Jian-Fong Huang, Chow-Choong Ngeow , Ting-Jhang Yang , Hung-Chin Lin.....	93

## 新聞報導

新聞報導.....	95
-----------	----

# 研究論文



# Star–Disk Interactions in Multiband Photometric Monitoring of the Classical T Tauri Star GI Tau

Zhen Guo<sup>1,2</sup>, Gregory J. Herczeg<sup>1</sup>, Jessy Jose<sup>1</sup>, Jianning Fu<sup>3</sup>, Po-Shih Chiang<sup>4</sup>, Konstantin Grankin<sup>5</sup>, Raúl Michel<sup>6</sup>, Ram Kesh Yadav<sup>7</sup>, Jinzhong Liu<sup>8</sup>, Wen-ping Chen<sup>4</sup>, Gang Li<sup>3</sup>, Huifang Xue<sup>3</sup>, Hubiao Niu<sup>3,8</sup>, Annapurni Subramaniam<sup>9</sup>, Saurabh Sharma<sup>10</sup>, Nikom Prasert<sup>7</sup>, Nahiel Flores-Fajardo<sup>1,11</sup>, Angel Castro<sup>6,12</sup>, and Liliana Altamirano<sup>6,12</sup>

<sup>1</sup> Kavli Institute for Astronomy and Astrophysics, Peking University, Yi He Yuan Lu 5, Haidian District, Beijing 100871, People's Republic of China; [guozhen9057@hotmail.com](mailto:guozhen9057@hotmail.com)

<sup>2</sup> Department of Astronomy, School of Physics, Peking University, Yi He Yuan Lu 5, Haidian District, Beijing 100871, People's Republic of China

<sup>3</sup> Department of Astronomy, Beijing Normal University, Beijing 100875, People's Republic of China

<sup>4</sup> Graduate Institute of Astronomy, National Central University, No. 300, Zhongda Rd., Zhongli Dist., Taoyuan City 32001, Taiwan

<sup>5</sup> Crimean Astrophysical Observatory, pos. Nauchnyi, Crimea, 298409 Russia

<sup>6</sup> Instituto de Astronomía, Universidad Nacional Autónoma de México, Apartado Postal 877, C.P. 22800, Ensenada, B.C., México

<sup>7</sup> National Astronomical Research Institute of Thailand, Chiang Mai, 50200, Thailand

<sup>8</sup> Xinjiang Astronomical Observatory, Urumqi, Xinjiang 830011, People's Republic of China

<sup>9</sup> Indian Institute of Astrophysics, Koramangala, Bangalore 560 034, India

<sup>10</sup> Aryabhata Research Institute of Observational Sciences, Manora Peak, Nainital 263 002, India

<sup>11</sup> Instituto de Ciencias Nucleares, Universidad Nacional Autónoma de México. Cd. Universitaria, 04510 Ciudad de México, México

<sup>12</sup> Universidad Autónoma de Ciudad Juárez, Instituto de Ingeniería y Tecnología. 1210 Plutarco Elías Calles, 32310 Cd. Juárez, CH, México

Received 2017 September 7; revised 2017 November 11; accepted 2017 November 20; published 2018 January 5

## Abstract

The variability of young stellar objects is mostly driven by star–disk interactions. In long-term photometric monitoring of the accreting T Tauri star GI Tau, we detect extinction events with typical depths of  $\Delta V \sim 2.5$  mag that last for days to months and often appear to occur stochastically. In 2014–2015, extinctions that repeated with a quasi-period of 21 days over several months are the first empirical evidence of slow warps predicted by magnetohydrodynamic simulations to form at a few stellar radii away from the central star. The reddening is consistent with  $R_V = 3.85 \pm 0.5$  and, along with an absence of diffuse interstellar bands, indicates that some dust processing has occurred in the disk. The 2015–2016 multiband light curve includes variations in spot coverage, extinction, and accretion, each of which results in different traces in color–magnitude diagrams. This light curve is initially dominated by a month-long extinction event and a return to the unocculted brightness. The subsequent light curve then features spot modulation with a 7.03 day period, punctuated by brief, randomly spaced extinction events. The accretion rate measured from *U*-band photometry ranges from  $1.3 \times 10^{-8}$  to  $1.1 \times 10^{-10} M_{\odot} \text{ yr}^{-1}$  (excluding the highest and lowest 5% of high- and low- accretion rate outliers), with an average of  $4.7 \times 10^{-9} M_{\odot} \text{ yr}^{-1}$ . A total of 50% of the mass is accreted during bursts of  $>12.8 \times 10^{-9} M_{\odot} \text{ yr}^{-1}$ , which indicates limitations on analyses of disk evolution using single-epoch accretion rates.

**Key words:** stars: pre-main sequence – stars: variables: T Tauri, Herbig Ae/Be

**Supporting material:** data behind figures

## 1. Introduction

Classical T Tauri stars (CTTSs) are low-mass young stars surrounded by an accretion disk. The stellar magnetic field truncates the disk at a few stellar radii and channels gas from the disk onto the star (e.g., Camenzind 1990; Koenigl 1991; Shu et al. 1994). The measured strengths and geometries of magnetic fields and the profiles of emission and absorption lines are consistent with expectations of the magnetospheric accretion model (e.g., Johns-Krull 2007; Donati & Landstreet 2009; Hartmann et al. 2016). Magnetohydrodynamic (MHD) simulations of the magnetospheric accretion suggest that the accretion flow may be either stable or unstable, depending on the accretion rate, the magnetic field strength and morphology, and the inclination angle between the stellar spin and magnetic dipole (e.g., Romanova et al. 2013; Blinova et al. 2016).

The photometric variability of T Tauri stars has been studied for decades (Wenzel 1969; Grinin 1988; Herbst et al. 1994; Bouvier et al. 2013; Cody et al. 2017). When star–disk interactions are steady, an accretion column and the associated inner disk warp rotate around the star, periodically occulting the central star (e.g., Bouvier et al. 2007; McGinnis et al. 2015). In non-steady accretion, these extinction events may appear more stochastically and last for days, months, or even years. The obscure dust is located in a persistent puffed-up disk and inner rim (Dullemond et al. 2003; Ke et al. 2012), a warp induced by binarity (Hamilton et al. 2001), a disk instability at larger distances (Zhang et al. 2015), or perhaps even a non-axisymmetric bridge that links an inner disk with an outer disk (Loomis et al. 2017). The changes in the height of the inner disk have also been seen in anticorrelated variability of near- and mid-IR disk emission (Espaillat et al. 2011), with a possible relationship to accretion rate (Ingleby et al. 2015). The disk interpretation is challenged in one case (J1604–2130) by the measurement of a face-on inclination of an outer disk (Ansdell et al. 2016a). In a second case (RW Aur), the occultation source is uncertain and may be a dusty wind



Original content from this work may be used under the terms of the [Creative Commons Attribution 3.0 licence](https://creativecommons.org/licenses/by/3.0/). Any further distribution of this work must maintain attribution to the author(s) and the title of the work, journal citation and DOI.

(Petrov et al. 2015; Schneider et al. 2015b), a tidal encounter of the secondary star (Dai et al. 2015), the combination of occultation and time-variable accretion (Takami et al. 2016), or partial occultation of the inner disk (Facchini et al. 2016).

In this paper, we focus on short- and long-term extinction events detected in one CTTS, GI Tau. Stars with short-duration (1–5 days) extinction events, called dippers, are obscured by dust structures at or near the disk truncation radius (e.g., Alencar et al. 2010; Cody et al. 2014; Scaringi et al. 2016). AA Tau is the historical prototype for dippers (e.g., Bouvier et al. 1999, 2003). Periodic and quasi-periodic dippers have a periodicity distribution consistent with the distributions of stellar rotations (Cody et al. 2014). Long-term extinction events, called faders, occur when the star is occulted by disk components for weeks to years (e.g., Bouvier et al. 2013; Findeisen et al. 2013; Rodriguez et al. 2015, 2016b; Loomis et al. 2017); KH 15D is the prototype for faders (Hamilton et al. 2001). Some stars, including AA Tau, have exhibited both types of extinction events. Deep extinction events have also been called Type III variables or UXors (Herbst et al. 1994), especially when the occulted object is a Herbig AeBe star (e.g., Grinin et al. 1994; Natta et al. 1997).

In the midst of this extinction variability, emission is also always changing because of unstable accretion and spot rotation. Accretion variability is common in young stellar objects, as 10% of CTTSs have similar bursty light curves (Findeisen et al. 2013; Cody et al. 2014, 2017; Stauffer et al. 2014). The variable accretion process appears as changes in excess continuum and line emission above the photosphere (e.g., Alencar et al. 2012; Fang et al. 2013; Costigan et al. 2014), and the corresponding changes in photometry (Venuti et al. 2014; Sousa et al. 2016; Stauffer et al. 2016; Tofflemire et al. 2017a) are driven by either unsteady star-disk connections (e.g., Romanova et al. 2013) or changes in the disk density at the inner rim (Robinson et al. 2017). Spot modulation is also commonly seen among young stars with typical variations of  $\Delta V \lesssim 0.5$  mag (e.g., Herbst et al. 1994; Grankin et al. 2007), although spots in light curves of some CTTSs can be difficult to distinguish from extinction and accretion variations. Extinction, accretion, and spot variability each have particular patterns in high time-resolution photometry (Alencar et al. 2010, 2012; Morales-Calderón et al. 2011; Cody et al. 2017), multiband photometry (Herbst et al. 1994; Grankin et al. 2007; Venuti et al. 2015), and spectroscopic monitoring (Bouvier et al. 2007).

In this paper, we describe and analyze the multiband optical monitoring of the CTTS GI Tau obtained over two years. Our work provides a method to identify the variation mechanisms using the color information and to probe the star-disk interaction at the inner edge of the circumstellar disk. The paper is organized as follows. In Section 2, we describe our observation and data reduction. The photometric results and periodicity analysis are described in Section 3. In Section 4, we analyze this photometric variability in terms of the warp size and changes in accretion.

## 2. Observations

### 2.1. Properties of GI Tau

GI Tau is a Classical T Tauri star associated with the B18 cloud in the Taurus star-forming region (Myers 1982; Kenyon et al. 2008) and is separated by 13 arcsec from a wide

companion, GK Tau (Figure 1; see also, e.g., Kraus & Hillenbrand 2009). GI Tau has a circumstellar disk (e.g., Kenyon & Hartmann 1995; Luhman et al. 2010; Rebull et al. 2010) and ongoing accretion (e.g., Valenti et al. 1993; Gullbring et al. 1998). The average VLBI parallax distance of 140 pc to the Taurus star-forming region (Loinard et al. 2007; Torres et al. 2009, 2012) is adopted as the distance to GI Tau.

Companion searches with high-resolution near-IR imaging (e.g., Daemgen et al. 2015) and high-resolution spectroscopy (Nguyen et al. 2012) have yielded non-detections, indicating that GI Tau is likely a single star. A  $\sim 7$  day period has been detected in some epochs (Vrba et al. 1986; Herbst et al. 1994) but is absent in other epochs (e.g., Grankin et al. 2007; Rodriguez et al. 2017a), perhaps because spot changes may be masked by complications in the light curve from extinction and accretion variability.

The estimated spectral type of GI Tau ranges from K5–M0.5 (Rydgren et al. 1976; Herbig 1977; Cohen & Kuhl 1979; Hartigan et al. 1994; Taguchi et al. 2009; Herczeg & Hillenbrand 2014), with differences caused by methodology and a non-uniform temperature distribution on the stellar surface (see, e.g., Gully-Santiago et al. 2017). Extinction events have been previously detected from photometry (Herbst et al. 1994; Grankin et al. 2007; Rodriguez et al. 2016a). In three optical spectra, Herczeg & Hillenbrand (2014) found that fixing the spectral type to a single value required an extinction that varied from  $A_V = 1.05$  to 2.55 mag. Our analysis in Section 4.3 indicates a minimum  $A_V = 0.75$ –1.0 mag, which is likely interstellar; any additional extinction is likely caused by the disk.

Adopting a spectral type of M0.4 ( $T_{\text{eff}} = 3828$  K) and  $\log(L/L_{\odot}) = -0.25$  (Herczeg & Hillenbrand 2014; see also Grankin 2016), the mass and age are  $0.53 M_{\odot}$  and 1.4 Myr as inferred from the pre-main-sequence evolutionary tracks of Baraffe et al. (2015), and  $0.92 M_{\odot}$  and 4 Myr from the magnetic tracks of Feiden (2016). These parameters are sensitive to the unknown spot properties of the star (Gully-Santiago et al. 2017). However, dynamical masses measured from disk rotation around stars of similar spectral types lead to masses of  $0.60$ – $0.95 M_{\odot}$  (Simon et al. 2017).

The disk inclination has not been measured. Given a radius  $R = 1.7 R_{\odot}$ , rotational period  $P_{\text{rot}} = 7.03 \pm 0.02$  day (see Section 3.1), and stellar rotational velocity  $v \sin i = 12.7 \pm 1.9$  km s $^{-1}$  (Nguyen et al. 2009), the stellar inclination is  $>60^{\circ}$  (see also Johns-Krull & Valenti 2001). Broad redshifted absorption in He I  $\lambda 10830$  has a similar profile as that seen in AA Tau (Fischer et al. 2008) and supports this high inclination.

### 2.2. SNIFS Photometry and Spectroscopy

We obtained spectra and photometry of GI Tau with the Super-Nova Integral Field Spectrograph (SNIFS; Aldering et al. 2002; Lantz et al. 2004) from 2014 November 26 to December 15. SNIFS is an Integral Field Spectrograph on the UH 88 inch telescope on Maunakea that produces  $R \sim 1000$  spectra from 3200 to 10,000 Å over a  $6'' \times 6''$  field of view (FOV). Short acquisition images were obtained with a  $9/6 \times 9/6$  FOV imager with a V-band filter and are used here for photometry.

The full set of our SNIFS observations include spectroscopic monitoring of  $\sim 30$  CTTSs. GI Tau was initially selected as a target based on past identification of extinction events (see,

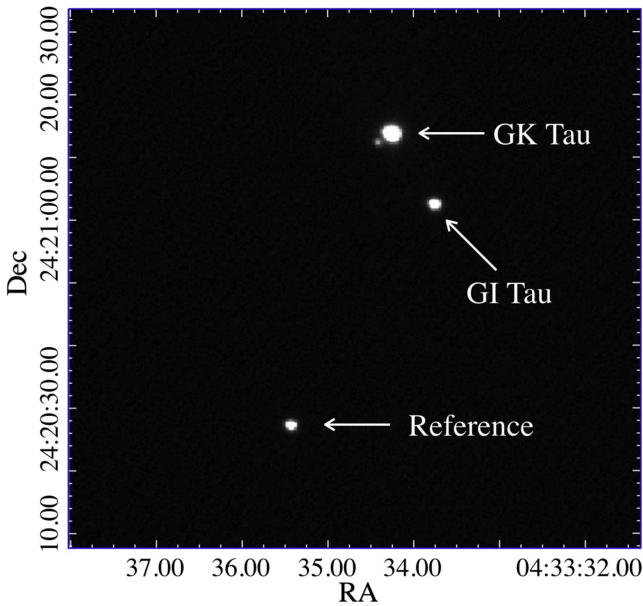


**Figure 1.** V-band image of GI Tau and GK Tau obtained using SNIFS at the UH88 telescope. GI Tau, GK Tau and its close visual companion, and one of the reference stars are marked in the image.

e.g., Grankin et al. 2007; Herczeg & Hillenbrand 2014). We detected a deep extinction event at the beginning of our SNIFS campaign and decided to intensively monitor GI Tau for the remainder of our campaign. Two spectra from this spectroscopic monitoring campaign are analyzed in this paper (see Section 2.5).

### 2.3. Subsequent Photometric Campaigns (2014–2016)

Following our SNIFS photometry, we monitored GI Tau from 2014 to 2016 with 11 other telescopes. The details of the telescopes, instruments, and observations are described in Table 1. The complete set of photometry is listed in an online table.

From 2014 December 16 (MJD 57007) until 2015 March 25 (MJD 57108), photometry was obtained in the V-band filter with a cadence of one to two visits per night. From 2015 October–2016 February, multiband photometry was obtained in the B, V, R, and I bands, and in U when available. Different observational strategies were set based on the time allowance of each telescope. SLT, the 1 m Thailand Southern Telescope, and the 1.3 m JCBT observed the selected field one to three times on each clear night. The 0.5 m telescope at TNO and 2 m HCT also contributed weeks-long observations. The NOWT (Liu et al. 2014) and NBT monitored GI Tau for 4–6 hr for seven and three consecutive nights, respectively, to measure variations on short timescales.

### 2.4. Data Reduction of Photometry

The data were reduced with custom-written routines in IDL. The images were corrected for detector bias, flat-field, and cosmic rays. The stellar brightnesses of GI Tau, GK Tau, and many field stars in the frame are measured with aperture photometry. For field stars, the sky background is measured in an annulus with an 8 arcsec inner radius and 10 arcsec outer radius around the star. Since the distance between GI Tau and GK Tau is only 13.2 arcsec, the background levels are adopted

directly from the sky background of the nearby reference star. The counts for each star are then extracted using a radius equal to two times the seeing (in FWHM), with an upper limit on the radius of  $6''.5$  arcsec. Photometry with fixed apertures of  $1''$ ,  $3''$ , and  $6''$  and PSF fitting yield results that are generally consistent with our approach, but with larger standard deviations in the photometry.

Four bright stars are identified as non-variables (Figure 2) and are selected as reference stars to calibrate the BVR photometry of GI Tau. The measured standard deviations of all reference stars are 0.017 mag in I, 0.028 mag in V, and 0.042 mag in the B band, after excluding the images obtained during the full moon. The measurements are less reliable ( $\Delta I > 0.05$  mag) in observations with seeing larger than  $4''$ . The number of reference stars used for each telescope depends on the FOV and is listed in Table 1.

In U-band observations, only one field star, with  $m_U = 13.50$  mag,<sup>13</sup> located within the  $10' \times 10'$  FOV is bright enough to be used as a calibrator. Unsaturated images in the B, V and I bands indicate that this calibrator is not variable. The accuracy of our U-band observations is typically limited to  $\sim 0.05$  mag by the signal-to-noise ratio of GI Tau. The differential effects of telluric absorption versus airmass are not corrected.

A reflection nebulosity around GI Tau and GK Tau (Arce & Sargent 2006) is detected in stacked images, with a surface brightness of  $I = 22.8$  mag arcsec $^{-2}$  and  $B = 25.5$  mag arcsec $^{-2}$ . The flux contribution from the nebulosity within a  $6''.5$  radius aperture is 17.5 mag in the I band and 20.2 mag in the B band, or  $\sim 4$  mag fainter than the faintest measurements of GI Tau. Compared with the photometric accuracy and variability of GI Tau, the differential flux contribution from the nebulosity introduced by using different aperture sizes is negligible.

For absolute photometric calibration, we observed the GI Tau field and the region PG 02331 from Landolt (1992) at a range of airmasses with the 2 m HCT on 2015 December 1. The atmospheric extinction and instrument coefficients are measured from PG 02331 and applied to bright stars in the GI Tau field. The standard magnitudes of these reference stars are then used to apply the zero-point shifts to each observation obtained by all other telescopes in this study.

The absolute photometric calibration accuracy should be  $\sim 0.02$  mag in the V and I bands and 0.05 mag in the B band, following the uncertainties in the Landolt star calibrations. However, an absolute offset of 0.09 mag in V-band calibration is identified when comparing our photometry to the historical photometry of Grankin et al. (2007; see Figure 5) and to the synthetic photometry obtained from our flux-calibrated SNIFS spectra. The source of this problem could not be identified. Our relative photometric calibration should be unaffected. The synthetic  $\Delta V$  between our SNIFS spectra is within 0.01 mag of the directly measured  $\Delta V$  obtained in our acquisition images.

### 2.5. Data Reduction of Spectroscopy

The SNIFS spectra of GI Tau and the spectrophotometric standard G191B2B (Oke 1990) were reduced with custom-written routines in IDL. The emission is split at  $\sim 5200$  Å by a dichroic into separate red and blue channels. The raw images consist of 225 separate spectra, each from a given spaxel in the

<sup>13</sup> This U-band measurement was measured by Audard et al. (2007) with the XMM-Newton Optical and UV Monitor ( $U_{OM}$ ). With a spectral type of B8, the offset between the  $U_{OM}$  and Johnson U system of  $U - U_{OM} \sim -0.02$  is small and is ignored in our analysis.

**Table 1**  
Summary of Observations

Telescope	Location	Diameter (m)	Pix Size (")	Field of View	No. Ref	Filter	Nights of Obs.	No. Visits/Night
2014–2015								
UH88	Maunakea, Hawaii	2.2	0.27	9'3 × 9'3	2	V	18	1–6
YNAO	YNAO, China	1	0.41	7'3 × 7'3	2	V	4	4
AZT-11	CrAO, Russia	1.25	0.62	10'6 × 10'7	3	V	6	1
OAN-SPM (0.84)	SPM, Mexico	0.84	0.44	7'6 × 7'6	4	VR	4	2 hr <sup>a</sup>
HCT	Hanle, India	2	0.30	10'2 × 10'2	4	V	23	1
2015–2016								
OAN-SPM (1.5)	SPM, Mexico	1.5	0.32	5'4 × 5'4	1	VI	34	2 hr <sup>a</sup>
HCT	Hanle, India	2	0.30	10'2 × 10'2	4	UVI	23	1–3
SLT	Lulin, Taiwan	0.40	0.78	26'8 × 26'8	4	UBVI	74	1–3
NOWT	XAO, China	1	1.13	1'3 × 1'3	4	BVRI	5	>5 hr <sup>a</sup>
JCBT	VBO, India	1.3	0.24	16'5 × 8'6	4	BVI	20	1
TST	CTIO, Chile	0.6	0.63	22' × 22'	4	BVRI	45	1
NBT	Xinglong, China	0.85	0.91	30' × 30'	4	UBVRI	10	>5 hr <sup>a</sup>
TNO	TNO, Thailand	0.5	0.63	21'5 × 21'5	4	BVI	21	1–2

**Note.** UH88: University of Hawaii 2.2 m telescope. YNAO: 1 m RCC telescope at Yunnan Astronomical Observatory, Kunming, China. AZT-11: 1.25 m telescope at Crimean Astronomical Observatory, Russia. OAN-SPM: 0.84 m and 1.5 m telescopes at Observatorio Astronomico Nacional, Sierra San Pedro Mártir, Mexico. HCT: 2 m Himalayan Chandra Telescope at Indian Astronomical Observatory, Hanle (Ladakh), India. SLT: 40 cm telescope at Lulin Observatory, Taiwan. NOWT: Nanshan One meter Wide-field Telescope at Xinjiang Astronomical Observatory, Urumqi, China. JCBT: 1.3 m J.C. Bhattacharya Telescope at Vainu Bappu Observatory, Kavalur, India. TST: 0.6 m Thai Southern Hemisphere Telescope (PROMPT-8), operated by the Skynet Robotic Telescope Network, at the Cerro Tololo Inter-American Observatory, Chile. NBT: 85 cm reflection telescope at Xinglong Station of the National Astronomical Observatories of China. TNO: 0.5 m telescope at Thai National Observatory, National Astronomical Research Institute of Thailand (NARIT).

<sup>a</sup> Represents consecutive observation for X hours.

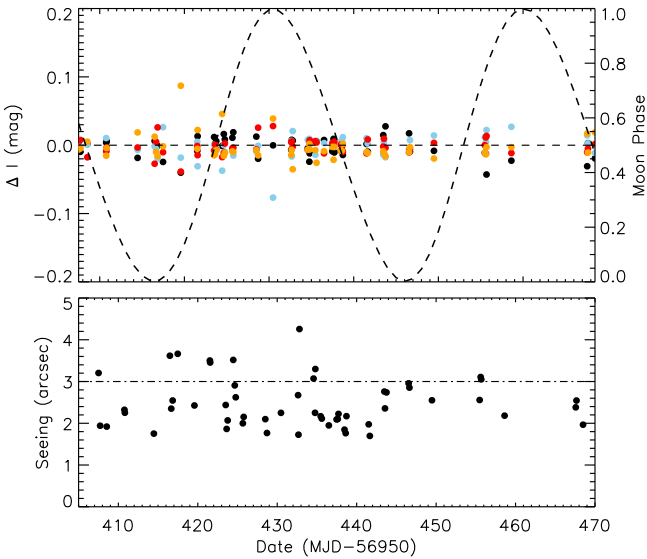


**Figure 2.** Top: accuracy of the *I*-band photometric calibration of the four reference stars (separated by different colors) taken by SLT, plotted as the difference between each observation and the median magnitude,  $\Delta I$ . The standard deviations of each reference stars are 0.016, 0.018, 0.013, and 0.018 mag. The lunar phase is shown by a dashed black curve. Bottom: the seeing during each observation, with the horizontal dotted–dashed line indicating 3".

15 × 15 integral field unit. The counts in each spectrum are extracted by fitting a cross-spectrum profile, measured from flats, to each wavelength pixel. The spectra in each spaxel was then wavelength-calibrated to  $\sim 10 \text{ km s}^{-1}$  using arc lamps, flat-corrected in each spaxel, and then regridded onto the same wavelength scale.

The final spectra are extracted from the data cube by fitting a 2D profile and sky background at each wavelength bin. The

spectra of GI Tau were then flux-calibrated using G191B2B spectra obtained within 1 hr of GI Tau. The average airmass correction was calculated using spectra of G191B2B over the 20 night run and was then applied to each epoch. Two spectra were selected for use in this paper because they were obtained in photometric conditions, near in time to the photometric calibrators, and at the local minimum and maximum of the light curve.

### 3. Results and Analysis

In the 2014–2015 light curve of GI Tau, the most prominent features are several extinction events with depths of  $\Delta m_V > 2.5$  mag and durations of three to five days (see Figure 3). The 2015–2016 light curve of GI Tau began with a dim epoch that lasted  $\sim 50$  days, followed by a period with smaller periodic brightness variations (Figure 4).

These photometric variations are summarized by the color–color and color–magnitude diagrams in Figure 5. The *V*-band brightness varied by 2 mag, the *V* – *I* color by 0.8 mag, and the *B* – *V* color by 0.5 mag. The locus of points on the color–magnitude diagram is similar to that seen in the long-term monitoring of GI Tau by Grankin et al. (2007), except for the offset in the *V* band discussed in Section 2.4.

In faint epochs, a “blue turnaround” is seen, in which the color variation is achromatic with further dimming of *V*. This blue turnaround, also seen in AA Tau (Bouvier et al. 1999) and other CTTSs (Grankin et al. 2007), is likely caused by an increased importance of the scattered light, since stars with edge-on disks typically appear blue at optical wavelengths (e.g., Padgett et al. 1999; Herczeg & Hillenbrand 2014). These epochs are ignored when calculating accretion rates. However, if the bluer colors are caused by higher accretion rates during these faint epochs, then this choice would bias our results.



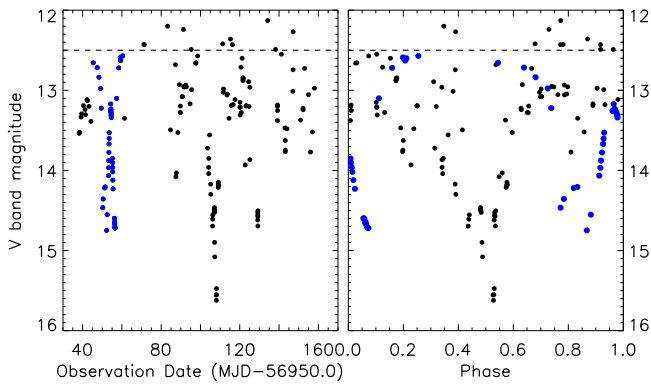


**Figure 3.** *V*-band light curve of GI Tau during 2014–2015 vs. time (left) and phase-folded for the  $\sim 21$  day period (right) and binned to 30 minute intervals where relevant. A “double dip” feature from days 45 to 61 is shown by the blue dots. The horizontal dashed line is the approximate baseline of GI Tau used here to calculate the occultation depth. The data used to create this figure are available.

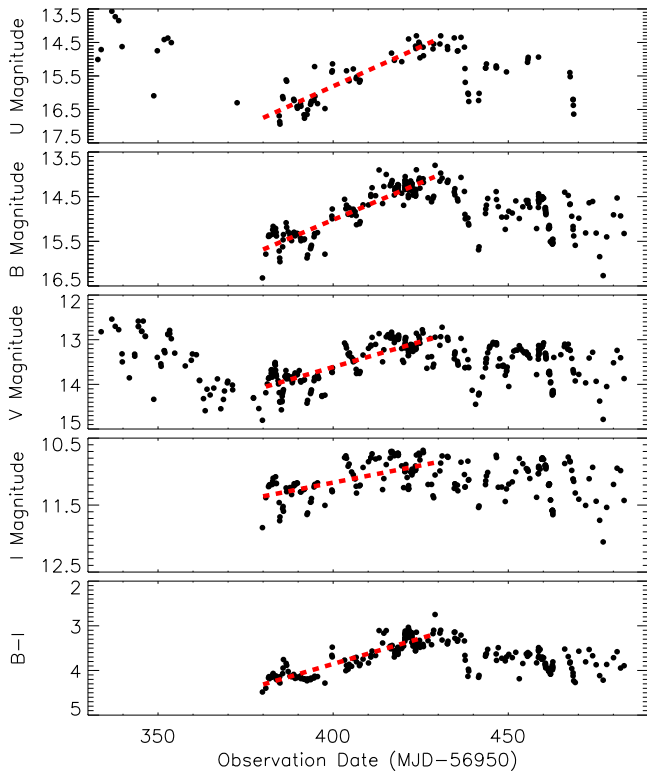


**Figure 4.** From top to bottom, the *U*, *B*, *V*, and *I* bands and *B* – *I* light curves of GI Tau during the 2015–2016 campaign. The general brightening that occurred from day 380 is fit with the red dashed lines. The data used to create this figure are available.

In this section, we describe how the light curves are combined with the color–color and color–magnitude diagrams are used to identify variability caused by stellar spots, circumstellar extinction events, and accretion bursts.

### 3.1. Spot Modulation in 2015–2016

Periodicity in the 2015–2016 light curve is most prominent in the *I* band. The Generalized Lomb–Scargle (GLS) periodogram (Zechmeister & Kürster 2009) of the *I*-band light curve

yields a best-fit period of  $7.03 \pm 0.02$  days, with the error bar adopted from the FWHM of the periodogram profile (Figure 6). Prior to the fit, the long-term trends were approximated as a third-order polynomial and were removed from the data (Zajtseva 2010). Fitting parameters to the *B*-, *V*-, and *I*-band light curves are shown in Table 2.

The sinusoidal morphology of the phase-folded light curves indicates the presence of a single large spot, similar to some other young stars with similar spectral types (e.g., Alencar et al. 2010; Rebull et al. 2016; Gully-Santiago et al. 2017). The standard deviation of the residual of 0.11 mag is likely caused by extinction and accretion events (discussed in Sections 3.2–3.4). The power of the periodogram,  $\zeta = p_{\max}/\sigma_p$ , is highest in the *I* band, since the other bands are more sensitive to accretion and extinction variations. The variations in the colors are synchronous (Figure 7).

False-alarm probabilities<sup>14</sup> for the period are computed using a Fisher randomization test with input periods between 2 and 100 days (e.g., Linnell Nemec & Nemec 1985). The 7.03 day period exceeds the 99% confidence level. This period is consistent with past measurements of the photometric period. In other epochs, including our monitoring in 2014–2015 and the 2008–2014 light curves described by Rodriguez et al. (2017b), any modulation from spots is masked by the much stronger variability caused by extinction.

### 3.2. Extinction Events in 2014–2015

Several photometric dips are shown in the *V*-band light curve of the 2014–2015 campaign, with depths of 1.5–3.1 mag relative to the out-of-extinction brightness of  $\sim 12.5$  mag and durations of 3–5 days (see list of extinction dips in Table 3).

The light curve of GI Tau reveals a wide range of durations and frequencies of extinction events. Our initial SNIFS monitoring included a double-dip extinction event, during which the *V*-band emission from the star faded, brightened, and then quickly faded again. The separation of the two minima is 5 days, and the total combined duration is 11 days, longer than one stellar rotation period. The  $R_V$  measurement based on spectra will be discussed in Section 4.2.

Subsequent follow-up photometry over the next months led to the detection of four dips with  $A_V > 1.5$  mag (see Table 3). These dips have a centroid time that repeats with a  $\sim 21$  day period. However, the preceding double-dip is inconsistent with this quasi-period. The extinctions that occur in the following year, described below, are also inconsistent with any periodicity.

### 3.3. Extinction Events in 2015–2016

The light curve during our 2015–2016 campaign is initially dominated by a gradual fade that reaches  $\Delta V = 1.5$  mag and then returns to the bright state, in total covering a period of  $\sim 80$  days (Figure 4). In addition to this months-long fading event, several small and large photometric dips are detected with

<sup>14</sup> False-alarm probabilities are the fraction of permutations (i.e., shuffled time series) that include a peak higher than that of the periodogram of the unrandomized data set at any frequency. This therefore represents the probability that, given the frequency search parameters, no periodic component is present in the data with this period. To ensure reliable significance values, the number of permutations was set to 1000. If the false alarm probabilities lie between 0.00 and 0.01, then the quoted period is a correct one with 95% confidence. The periodogram is computed at 5000 frequencies between 0 and  $0.5 \text{ day}^{-1}$ .

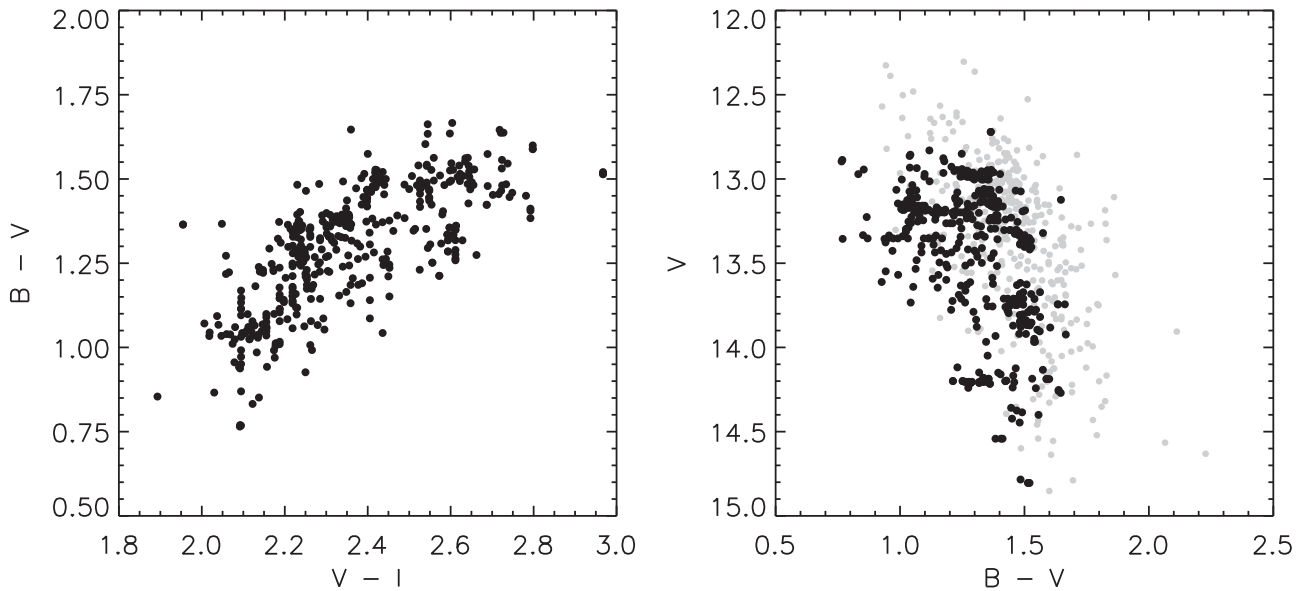


**Figure 5.** Color-color and color-magnitude diagrams of GI Tau during the 2015–2016 observation campaign, with data in our work shown by the black dots and archival data from Grankin et al. (2007) shown by the gray dots.

durations of 3–8 days, after correcting for spot-induced periodicity (see Figures 4 and 8 and Table 3).

Figure 4 shows a brief ( $\sim 3$  day) dip in the spot-corrected light curve at day 397, with a depth of  $\Delta I = 0.39$  mag,  $\Delta V = 0.45$  mag, and  $\Delta B = 0.56$  mag. A deeper and longer dip occurred around day 440, lasting for  $\sim 8$  days (Figure 8). Gaussian fits to the dips, as measured after accounting for spot rotation, yield  $A_I = 0.60$  mag,  $A_V = 1.22$  mag, and  $A_B = 1.56$  mag, and FWHMs of 3.73, 3.52, and 3.76 days, respectively. In those fits, the depths are measured relative to the post-dip light curve, which is well fit by a sine curve. There is no obvious periodicity of this extinction event.

### 3.4. Short Timescale Bursts

Photometry in the  $U$  and  $B$  bands is more sensitive to accretion than photometry with longer wavelength filters. At short wavelengths, the photospheric emission of GI Tau is faint relative to the continuum emission produced by the accretion shock (see the review by Hartmann et al. 2016). In our monitoring, the  $U$  and  $B$  bands exhibit stronger variations than the  $V$  and  $I$  bands.

Our campaign included five nights with constant monitoring of GI Tau on NOWT, during which several short bursts occurred (see Table 4 and Figure 9). The largest burst in  $B$ , detected during the first night, reached a peak of  $\Delta B \sim 0.3$  mag and lasted  $\sim 3.5$  hr. Four other shorter, smaller bursts are detected in the last two days. The average duration of these five bursts detected by NOWT is  $\sim 1.7$  hr, and the maximum amplitude in the  $B$  band is 0.31 mag. The changes in the brightness caused by these accretion bursts are an order of magnitude smaller than those caused by the deep extinctions. The corresponding increases of accretion rate during these bursts are calculated in Section 4.3. In one case, the  $B$ -band brightness is consistent with a non-detection, so the minimum and maximum accretion rates before and during the burst are not reported. These short bursts are attributed here to accretion but could alternatively be attributed to stellar flares (e.g., Kowalski et al. 2016; Tofflemire et al. 2017a, 2017b).

### 3.5. Color Analysis

Variable extinction, accretion, and spot coverage are all identified from the optical light curve of GI Tau. The traces of different phenomena in the color-magnitude diagrams can be used to distinguish the variation mechanisms. In this section, we describe the different signatures that changes in each of these properties imprint on the color-color and color-magnitude diagrams (Figure 10).

The short extinctions dips in the 2015–2016 campaign exhibit similar changes in the color-magnitude diagram with  $\Delta V = 2.10 \pm 0.08 \Delta(V - I)$  and  $\Delta I = 0.7 \pm 0.1 \Delta(B - I)$ . The long-term variation seen in the first half of the 2015–2016 campaign appears similar to the dips and is also attributed to extinction. These empirical relationships are consistent with expectations for dust reddening. The accretion bursts appear as horizontal changes in  $B - I$  versus  $I$ , indicating that the accretion only has a minor effect on the  $I$ -band brightness and that the  $B - I$  color is a good tracer of accretion. In this case, accretion is much flatter than extinction in the  $I$  versus  $B - I$  diagram (Figure 10 and Table 5). Venuti et al. (2015) obtained similar results in two weeks of monitoring young stars in NGC 2264 with CFHT in the  $u'$  and  $r$  bands.

As the spot rotates, the  $V - I$  colors change by 0.06 mag while the  $B - V$  colors change by 0.08 mag. These small color changes during spot modulation are consistent with those of the weak-line T Tauri star LkCa 4 during three decades of photometry (Grankin et al. 2008; Gully-Santiago et al. 2017). The locus that spot modulation traces on the color-magnitude diagrams has a slope between that of accretion and extinction. However, since the spot modulation has a unique periodicity, the spot information is readily extracted from a frequency analysis.

Pre-main-sequence stellar evolution tracks from Baraffe et al. (2015) are also presented in the color-magnitude diagrams, with colors adopted from Allard (2014). In distant clusters, properties of low-mass stars are often inferred from photometry (e.g., Reggiani et al. 2011; Jose et al. 2016; Beccari et al. 2017). Extinction events, accretion bursts, and spots each influence the inferred mass and age of member stars. Extinction

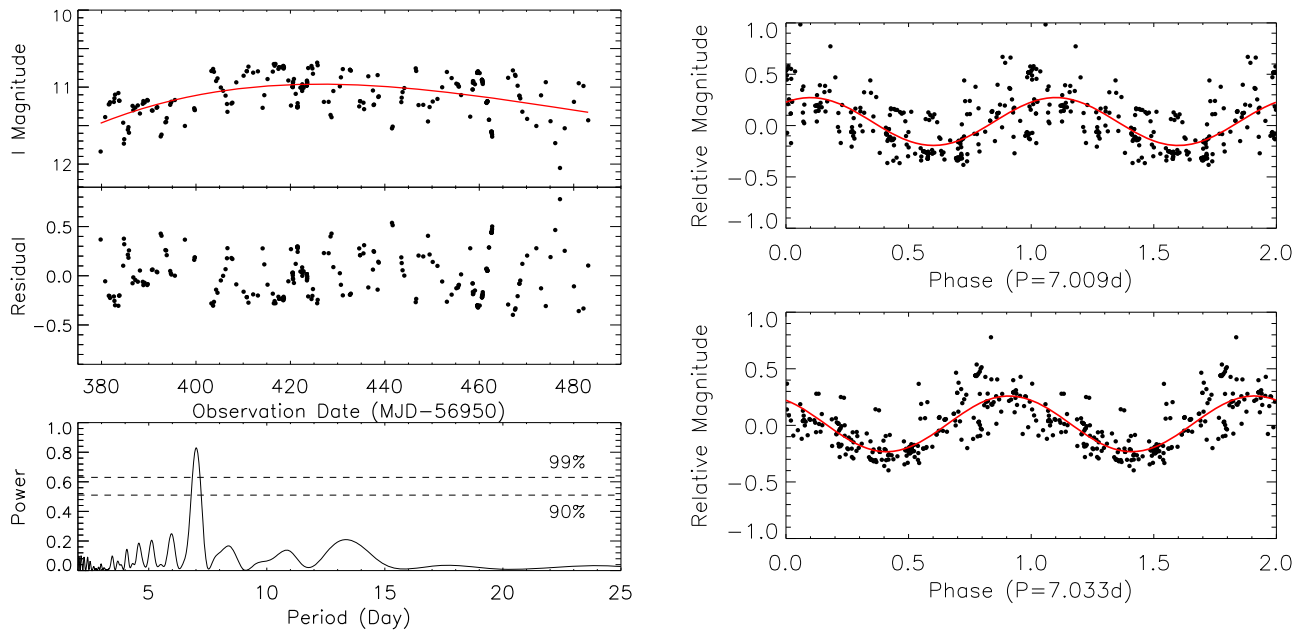


**Figure 6.** Top left: the  $I$ -band light curve of GI Tau, with a red line showing a third order polynomial fit to long-term variations. Middle left: the residual of the fit from the upper panel. Bottom left: the periodogram calculated from the light curve in the middle panel, showing a peak at 7.03 days. Top right: phase-folded  $I$ -band light curve in campaign 2015–2016 using the raw data from the top-left panel. Bottom right: phase-folded  $I$ -band light curve by the residuals from the left-middle panel.

curves are parallel to the color isochrone of cool stars in the  $V - I$  versus  $V$  diagram, which indicate that the age determination from  $V$ - and  $I$ -band photometry is robust to extinction changes (see also discussion in Sicilia-Aguilar et al. 2005). The age of GI Tau inferred from the Baraffe et al. (2015) models is consistently between 1 and 2 Myr (see also the age estimation in Section 2.1). However, the  $V - I$  color range introduces uncertainty in the mass or  $T_{\text{eff}}$  estimates when analysis is restricted to photometry, with larger uncertainties when using non-simultaneous photometry.

#### 4. Discussion

Photometric dips, accretion bursts, and a 7.03 day periodicity all shape the light curve of GI Tau during our monitoring over two years. The properties of the inner edge of the circumstellar disk and the star–disk interactions can be determined from the morphology and color changes during the variation events. The existence of quasi-periodic extinctions in the first year and the non-detection during our second campaign, and the change in morphology and frequency of events within each campaign, indicate an evolution of the inner disk structure over at most a few orbital timescales. In this section, we discuss the 2014–2015 quasi-periodicity in terms of a warp model, the extinction curve, and the distribution of accretion rates.

##### 4.1. The Slow Warp Model for the Quasi-periodic Dips of 2014–2015

Emission from young stars is periodically occulted by the inner edge of the circumstellar disk, when the disk is viewed close to edge-on. The presence of asymmetric disk warps or puffed-up inner rims will extinct the stellar brightness (see, e.g., the radiative transfer simulations of Kesseli et al. 2016). Figure 11 presents the periods and amplitudes of extinction events seen in young stars. For most dippers, these occultations are thought to occur once per stellar period, last  $\sim 1$  day, and are caused by inner disk warps related to accretion funnel flows

(e.g., Bouvier et al. 2007; Romanova et al. 2013). For faders, the occultations are prolonged and may last months or even years. The GI Tau light curve exhibits some characteristics of both dippers and faders.

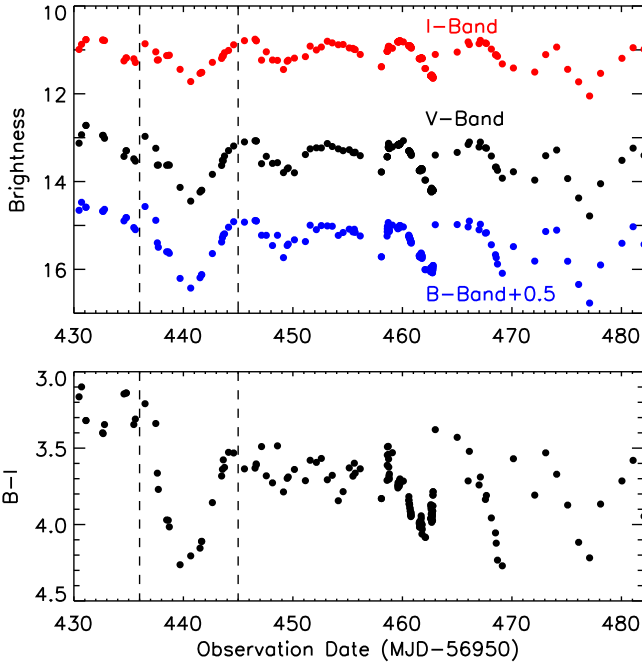
In the 2014–2015 monitoring, the (quasi)-periodic dips of 1.5–2.5 mag in  $V$  occurred every  $\sim 21$  days. In contrast, all previous periodic dippers have periodicity on much shorter timescales that are consistent with the stellar rotation period (Bouvier et al. 2007; Grankin et al. 2007; Alencar et al. 2010; McGinnis et al. 2015) and have depths of  $A_V = 0.1 - 1$  mag. The deep obscuration depth of GI Tau in this campaign is comparable to UXors, which are usually early-type PMSs undergoing variable extinctions with depths  $A_V > 1$  mag (Grinin et al. 1991, 1994; Herbst et al. 1994; Natta et al. 1997; Dullemond et al. 2003). However, no clear periodicity has been reported in UXors.

The deep events of GI Tau recur near every  $\sim 3$  stellar rotation periods and may be evidence of the slow warp in the MHD simulations of magnetospheric accretion by Romanova et al. (2013). In these simulations, two warps form in the circumstellar disk: a thin warp located at the co-rotation radius ( $R_{\text{cor}}$ ) and a thick warp outside of the co-rotation radius. Material can be trapped by the thick warp because of coupling between the stellar rotation and global oscillations in the disk. The thick warp is expected to rotate several times more slowly than the star, since it is located at a larger radii in the disk and also cause dips that are more optically thick than those in thin warps at the inner disk edge. The thick warp has a high scale height, so that it periodically intercepts our line of sight and causes extinction. Although this slow warp was quasi-periodic over  $\sim 60$  days, the feature was short-lived: it formed soon after our initial 20 night monitoring and had evolved or dissipated by the next year.

The  $\sim 80$  day long fade and return at the end of 2015 is much shorter than equivalent events in other stars, such as the years-long fading on AA Tau and V409 Tau (Bouvier et al. 2013; Rodriguez et al. 2015). The obscuration source may be an

**Table 2**  
Sine Fit Results

Parameters	<i>I</i> +poly	<i>I</i>	<i>V</i>	<i>B</i>
Period (days)	$7.03 \pm 0.02$	$7.01 \pm 0.03$	$7.09 \pm 0.08$	$7.20 \pm 0.09$
Frequency (1/day)	$0.1422 \pm 0.0004$	$0.1426 \pm 0.0006$	$0.140 \pm 0.002$	$0.139 \pm 0.002$
Maximum Power: $p_{\max}$	0.829	0.417	0.645	0.567
Standard deviation: $\sigma_p$	0.037	0.022	0.078	0.110
Index: $p_{\max} / \sigma_p$	21.82	18.77	8.26	5.15
Amplitude (mag)	$0.24 \pm 0.01$	$0.23 \pm 0.02$	$0.32 \pm 0.09$	$0.41 \pm 0.03$
rms of Residual (mag)	0.145	0.202	0.167	0.488

**Figure 7.** Top: *B*- (offset by 0.5 mag), *V*-, and *I*-band light curves of GI Tau between days 430–485, showing a combination of spots and occultations. Bottom: the *B* – *I* color, with large dips that indicate occultations.**Table 3**  
Extinction Events on GI Tau

Time (MJD-56950)	$V_{\min}$ (mag)	$\Delta V$ (mag)	Duration (days)
50.2	14.34	1.84	5
56.5	14.72	2.22	4
87.5	14.07	1.57	>3
108.1	15.62	3.12	5
129.2	14.70	2.20	...
380.0	14.34	1.54	80
396.8	14.27	0.48	3
440.6	14.45	1.15	8
477.1	14.78	0.96	4

azimuthally symmetric warp located close to the inner edge of the disk (e.g., Dullemond et al. 2003), distant disk structures (e.g., Zhang et al. 2015), or a bridge between an outer and inner disk (Loomis et al. 2017).

As the obscuration source of the extinction dips is located not far from the inner edge of the circumstellar disk or the co-rotation and truncation radius, we calculate the co-rotation radius of GI Tau based on the stellar parameters and spin

period obtained from this work:

$$R_{\text{cor}} = (G M_* P_*^2)^{1/3} (2\pi)^{-2/3} = 7.35 R_* = 0.06 \text{ au}, \quad (1)$$

where  $M_* = 0.53 M_{\odot}$ ,  $R_* = 1.7 R_{\odot}$ , and  $P_* = 7.03$  days.

The morphology of the dips is related to the disk inclination, orientation of the magnetic field dipole, and warp opacity. The short durations of the dips detected in GI Tau indicates a moderate inclination viewing angle (Bodman et al. 2017). The shape of the dips depends on the ingress timescale, i.e., the timescale for the structure to move in front of the star. The orbital velocity is calculated by the duration of the ingress time following the equation

$$V_{\text{orbit}} \times \sin \theta = L/t_{\text{ingress}}, \quad (2)$$

where the definition of  $L$  is half of the angular size of the warp (Bouvier et al. 1999), and the  $t_{\text{ingress}}$  should be around half of the total obscuration time. As shown in Figure 8, the typical  $t_{\text{ingress}}$  is 4 days while the occultation lasts for 8 days. A disk warp located at  $\sim 1.5 R_{\text{cor}}$  has a local disk rotation velocity  $v_{\text{rot}} = 43.5 \text{ km s}^{-1}$ . A Gaussian shape warp modeled by Romanova et al. (2013) with  $v_{\text{warp}} = 0.25 v_{\text{rot}}$  should have a width  $L = 6.9 R_*$  in horizontal size for an 8 day duration.

The maximum observed duration of the dips in the 2014–2015 campaign is 5 days, or 25% of the occultation period ( $P \sim 20$  days). If we assume that the warp system is located at 1.2–1.5 co-rotation radius, as indicated by the Romanova et al. (2013) simulations, the angular width of the warp  $L$  is as large as  $2.35 R_{\text{cor}}$  or  $\sim 18.6 R_*$ . A hydrogen gas column density is derived by Bohlin et al. (1978):  $N_{\text{H}}/E(B - V) = 5.8 \times 10^{21} \text{ cm}^{-2} \text{ mag}^{-1}$ , assuming an  $R_V = 3.85$  extinction (see Section 4.2). We also assume an ISM gas-to-dust ratio of 100: 1, although this may not be valid for inner disks. The gas mass within the warp is then roughly estimated by

$$M_{\text{warp,gas}} = 1.5 \times 10^{21} \times A_V \times m_{\text{H}} \times S_{\text{warp}}, \quad (3)$$

where  $m_{\text{H}}$  is the atomic mass of hydrogen and  $S_{\text{warp}}$  represents the cross-section area of the warp. We infer from the light curve that the warps have a Gaussian shape with a central height  $H = 2 R_*$ . The estimated gas mass is  $1.6 \times 10^{20} \text{ g}$  for warps with an average extinction of  $A_V = 1 \text{ mag}$ . The short-duration extinction events in 2015–2016 are less deep and would therefore either have less mass or a lower scale height.

#### 4.2. The Extinction Curve of the Dips of GI Tau

Extinction events in single-band photometry have degenerate explanations: the star may be entirely occulted by dust described by some column density and extinction law, or a fraction of the star may be entirely occulted by a large column

**Table 4**  
Hours-long Timescale Bursts

Time (MJD-56950)	$\Delta B$ (mag)	$\Delta V$ (mag)	$\Delta I$ (mag)	Duration (hr) <sup>a</sup>	$\dot{M}_{\text{acc,min}}$ <sup>b</sup>	$\dot{M}_{\text{acc,max}}$ <sup>b</sup>
458.7	>0.31	0.32	0.12	2.4	2.27	7.31
461.7	0.04	0.03	0.005	1.0	<sup>c</sup>	<sup>c</sup>
462.6	0.10	0.07	0.02	2.2	8.77	11.1
462.7	0.06	0.02	...	1.7	11.5	14.4
462.8	0.17	0.10	0.10	>1.44	11.6	15.4

**Notes.**

<sup>a</sup> Full duration of bursts measured by  $\Delta B$  in Figure 9.

<sup>b</sup> The mass accretion rates are in units of  $1 \times 10^{-9} M_{\odot} \text{ yr}^{-1}$ .

<sup>c</sup> The  $B$ -band photometry is below the detection limit set in Section 4.3.

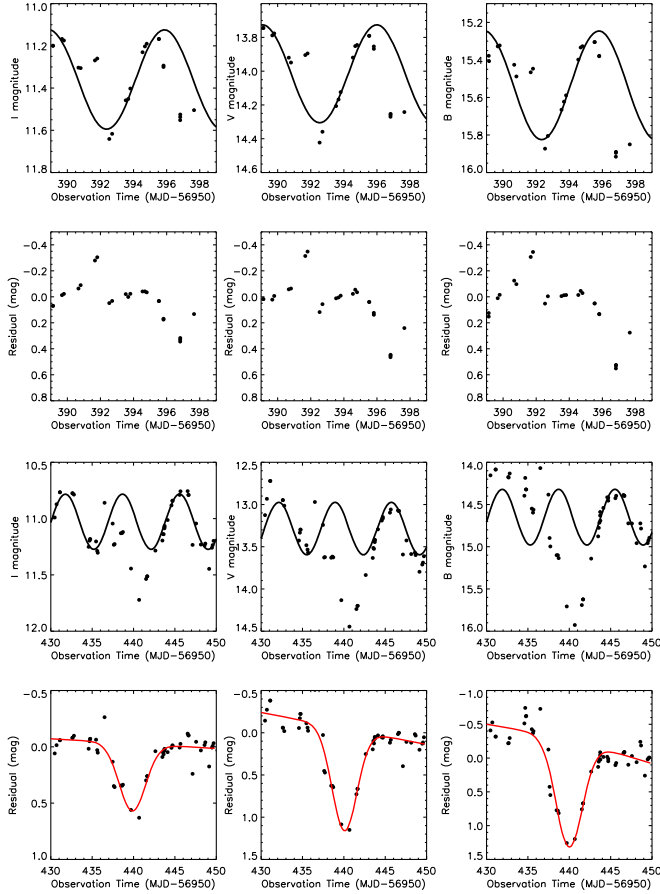


**Figure 8.** Top two panels:  $I$ -,  $V$ -, and  $B$ -band light curves of GI Tau from days 391–399, with sinusoidal fits with the 7.02 day period and residuals from the fit. Curves in the upper panels show the sine fit as spot modulation. Bottom two panels: same as the top set of panels, for days 430–450 and showing a Gaussian profile fit to extinction events in red.

of dust (see discussion in, e.g., Bodman et al. 2017). If the star is entirely occulted by dust, then the wavelength dependence of the extinction will lead to an estimate of grain growth, as long as reflected light is not significant. If only a fraction of the star is covered by opaque dust, then the star will get fainter but the color will not change.

Figure 12 shows the flux-calibrated spectra of GI Tau obtained at minimum brightness during an extinction event and maximum brightness obtained at the end of that event. The ratio of the two spectra demonstrates that GI Tau is much redder during occultation than out of occultation. The TiO band

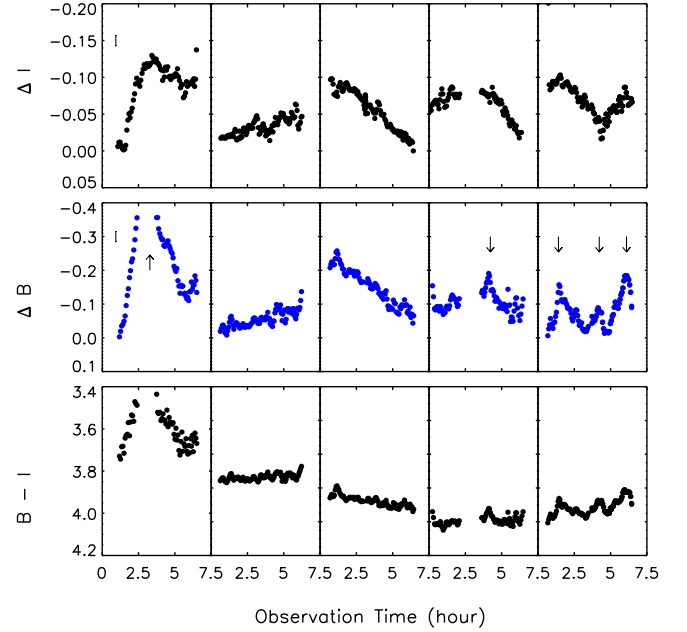


**Figure 9.**  $B$ -,  $I$ -, and  $B - I$  light curves of GI Tau from five consecutive half-nights using NOWT. The  $B$ - and  $I$ -band light curves are normalized to the minimum brightness within each day to compare their morphologies. Strong accretion bursts are marked by arrows. Error bars for the  $B$  and  $I$  bands are shown at the upper-left corner.

ratios and Balmer jumps are similar, indicating that the changes are caused by extinction rather than any change in spot coverage or accretion. The redder spectrum in this epoch is consistent with our other spectra obtained during the same run, the few spectra analyzed by Herczeg & Hillenbrand (2014), and our photometric results.

The flux ratio between 4000 and 8500 Å is fit with an extinction curve from Cardelli et al. (1989), with free parameters  $A_V$  and a total-to-selective extinction  $R_V$  between 2.1 and 5.8. The best-fit  $R_V = 3.85 \pm 0.5$  indicates possible grain growth relative to the ISM. This fit is constrained primarily by flux at  $<5000$  Å. The flux ratio<sup>15</sup> of the spectrum deviates from the fit above 8000 Å for all  $R_V$ . This analysis ignores any contribution from dust scattering, which is likely important at bluer wavelengths (see, e.g., the analysis of AA Tau by Schneider et al. 2015a). The  $V$ -band magnitude of the fainter spectrum is in the range where the “blue turnaround” makes the spectrum appear bluer than one would expect from extinction alone. If considered, scattering

<sup>15</sup> The flux ratio does not include any jump at 8200 Å that could be caused by Paschen absorption in the gas in our line of sight.

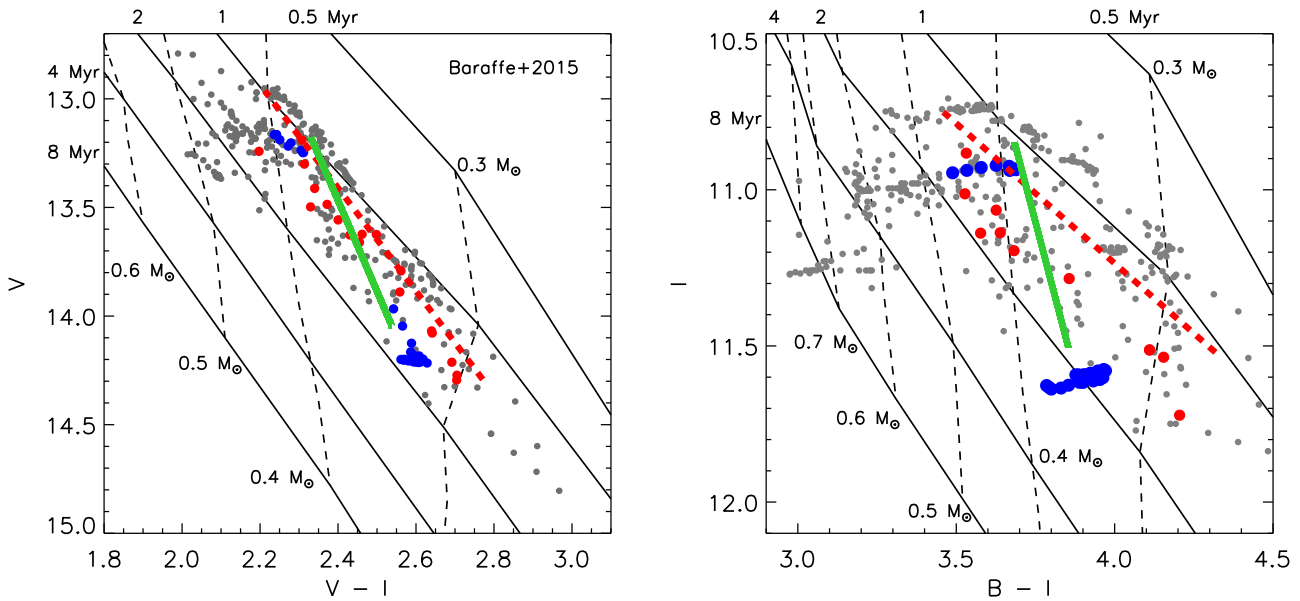


**Figure 10.** Left: the  $V - I$  vs.  $V$  color–magnitude diagram from our multiband monitoring of GI Tau, with observed data from 2015–2016 in gray. Pre-main-sequence evolutionary models by Baraffe et al. (2015) are presented to show the isochrones and mass tracks shifted to a 140 pc distance. The red dots show the extinction event around day 440. The red dashed line shows the fit to the long-time fading event shown in Figure 4. The blue dots are two short accretion bursts detected by NOWT. Spot modulation is shown by the green line. Right: the  $V - I$  vs.  $I - I$  color–magnitude diagram, with the same points as on the left.

**Table 5**  
Trace on the Color–Magnitude Diagram

Mechanism	$\Delta B$	$\Delta V$	$\Delta R$	$\Delta I$	$\Delta I / \Delta(B - I)$
Spot	0.38	0.32	0.25	0.24	1.71
Accretion	0.20	0.07	0.04	0.02	0.11
Extinction dip <sup>a</sup>	1.56	1.22	...	0.60	0.63
Long term	1.80	1.50	...	0.80	0.80

**Note.**

<sup>a</sup> The extinction dip represents the extinction event centered at day 440.

**Table 6**  
Photometric Period of GI Tau

Year	Period (day)	Amp. $V$ (mag)	Number of Obs.	References
1984	$7.18 \pm 0.05$	0.22	68	a
1987	$7.13 \pm 0.06$	0.34	38	b
1988	$7.01 \pm 0.17$	0.33	45	b
1989	$7.00 \pm 0.06$	0.20	66	b
1990	$7.06 \pm 0.05$	0.35	57	b
1991	$7.28 \pm 0.18$	0.40	31	b
1992	$7.33 \pm 0.14$	0.47	24	b
1993	...	1.64	35	b
2003	...	0.60	9	c
2014	(21)	2.20	174	d
2015	$7.03 \pm 0.02$	0.26	324	d

**Note.** The periods listed in this table are photometric periods of GI Tau. In this work, we claim that the  $\sim 7$  day periods are close to the stellar spin and the 21 day period is an obscuration period contributed by the “slow warp” located outside the inner edge of circumstellar disk. The Amp.  $V$  here is the amplitude of the sinusoidal fit from the Generalized Lomb–Scargle (GLS) periodogram and does not represent the obscuration depth. In the years 1993 and 2003, there is no period detected from the periodicity analysis.

**References:** (a) Vrba et al. (1986), (b) Herbst et al. (1994), (c) Grankin et al. (2007), (d) this work.

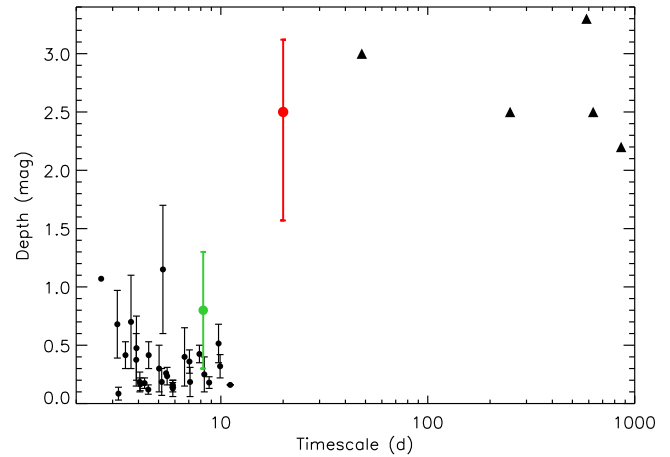


**Figure 11.** Depth and timescale for extinction events of classical T Tauri stars, with the 2014–2015 quasi-periodicity and the months-long extinction from late 2015 shown in red. Periodic or quasi-periodic targets from McGinnis et al. (2015), Stauffer et al. (2015), and Ansdell et al. (2016b) are shown as circles and cluster at periods consistent with stellar rotation and extinctions of 0.1–1 mag. Periodic variation of AA Tau is marked in green. Long-term extinction events of the faders KH 15D, RW Aur, V409 Tau, and DM Ori from Kearns & Herbst (1998) and Rodríguez et al. (2015, 2016b) are shown by triangles and plotted with “timescale” indicating the duration of the event. These extinction events are usually deeper, though this may be an observational bias.

would lead to a lower  $R_V$  and may also explain the deviation at red wavelengths. If some fraction of the star is covered by a much higher dust extinction, then  $R_V$  would need to be much lower for the visible fraction of the star.

Diffuse interstellar bands (see the review by Herbig 1995) are not detected in any spectrum, but would be expected to be strong if the dust composition were similar to the ISM (Friedman et al. 2011). These bands are strong in lines of sight through molecular clouds (e.g., Vos et al. 2011), and when seen in the spectra of some young stars (e.g., Oudmaijer et al. 1997;

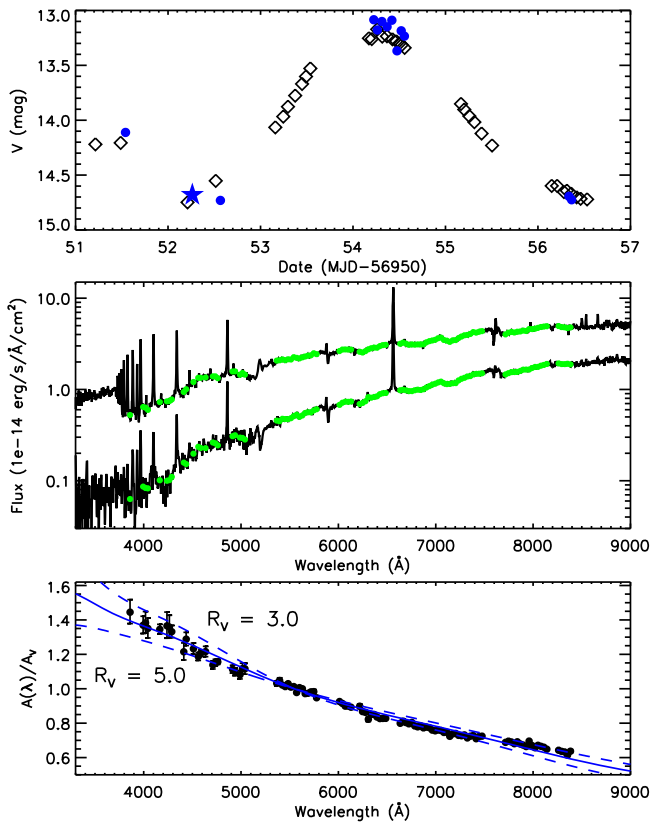


**Figure 12.** Top: Bessell  $V$ -band light curve of GI Tau during the SNIFS survey. The photometry by acquisition images are shown by the black diamonds, while the blue dots and stars are the synthetic photometry obtained from our flux-calibrated spectra. Middle: two SNIFS spectra of GI Tau, with one obtained during a bright epoch on day 54 and one obtained during a faint epoch on day 52 (both marked as stars above). The green dots mark the locations of the spectra used to measure the extinction law. Bottom: extinction law (flux ratio) of the spectra shown in the middle panel, normalized by  $A(\lambda)$  at  $5500 \text{ \AA}$ . The blue lines show the reddening curves of Cardelli et al. (1989) for  $R_V = 3.85$  (solid) and 3.0 and 5.0 (dotted).

Rodgers et al. 2002) are likely caused by the interstellar medium rather than the disk. Dust heating and processing within the disk of GI Tau must have destroyed the complex molecules that cause these bands. This difference could provide a method to distinguish disk extinction from interstellar extinction.

The flux in the  $[\text{O I}] 6300 \text{ \AA}$  emission does not change between epochs, despite the change in extinction. High-resolution spectra of GI Tau include broad and narrow components (e.g., Simon et al. 2016). The bulk of this emission must originate above the star, where the outflow would not be occulted by an inner disk warp.

The wavelength-dependent ratio of the two spectra is consistent with that of the other spectra obtained during the rise from days 52–54. The Balmer jump and therefore the accretion changes between days 54–56, so the later spectra are not immediately useful for  $R_V$  calculations. On the other hand, when calculated from our photometry of extinction events (see Table 5), we obtained  $R_V = A_V / (A_B - A_V) \sim 5$  for the long-term extinction (fader), and the dip in day 440 (dipper) yields  $R_V = 3.6$ . The fits to the long-term fade may be less reliable because they include different points for each band and cover accretion bursts and spot rotation.

The  $R_V$  measurement indicates a low opacity of the obscuration source, in contrast to previous interpretations that

the periodic dips of AA Tau are optically thick (Bouvier et al. 2003). Any optically thin dust in the accretion flow or at the inner disk edge should be quickly destroyed by strong stellar irradiation. In MHD simulations, the accretion stream drags dust grains from the optically thick disk (Romanova et al. 2003), which may replenish the dust in our line of sight. However, the occultation timescales of the dips (e.g., 5 days) are relatively long compared with the crossing timescale of an inner disk warp at the co-rotation radius. Alternative explanations, such as the dust being located in disk winds at larger radii, rather than in the disk itself, could explain the long survival time of the dust (Bans & Königl 2012; Petrov et al. 2015, 2017).

### 4.3. Accretion on Different Timescales

Mass accretion rates ( $\dot{M}_{\text{acc}}$ ) are measured here by calculating the excess continuum and line emission produced by the accretion flow. Our  $B$ -band and limited  $U$ -band monitoring of 2015–2016 are shown in Figure 4, with variations caused by changes in accretion, extinction, and spot coverage. Because scattered light during deep extinction events strongly affects the colors (the “blue turnaround”), accretion rates are calculated only for epochs when  $V < 14.0$  mag.

To measure the excess  $U$ -band luminosity, we first remove the spot modulation effects by a 7.03 day sinusoidal light curve. We then extract the extinction-corrected photospheric emission from the flux-calibrated optical spectra of Herczeg & Hillenbrand (2014). The combined fit of a photospheric template and accretion continuum to the spectrum yields photospheric luminosities of  $U_{\text{photosphere}} = 14.54 \pm 0.1$  mag,  $B_{\text{photosphere}} = 13.44 \pm 0.05$  mag, and  $I_{\text{photosphere}} = 10.43 \pm 0.05$  mag, when corrected to  $A_V = 0$  mag. Any extinction-corrected  $U$ -band emission above this brightness is attributed to accretion. The color of accretion is calculated as  $U - I \sim 0.15$  mag, using assumptions for the accretion continuum from Herczeg & Hillenbrand (2014), as estimated from veiling measurements of Fischer et al. (2011). The color variations are then calculated for a variable extinction, following the  $R_V = 3.85$  curve from Cardelli et al. (1989) with  $A_U = 1.47 A_V$ ,  $A_B = 1.25 A_V$ , and  $A_I = 0.56 A_V$ . Figure 13 shows how extinction and accretion affect the  $U - B$  and  $I$ -band magnitude of GI Tau.

The optical spectral energy distributions of the spot- and extinction-removed examples are presented in Figure 14. The accretion excess usually contributes  $\sim 60\%$  of the emission in the  $U$ -band filter but only  $\sim 15\%$  of the emission in the  $B$ -band filter on the median mass accretion rate  $\dot{M}_{\text{acc}} = 1 \sim 4 \times 10^{-9} M_{\odot} \text{ yr}^{-1}$ , consistent with expectations from accretion models (e.g., Calvet & Gullbring 1998). A similar relationship is seen by comparing the left and right panels of Figure 13 where the data points are more scattered in  $U$ .

Following the empirical relationship from Gullbring et al. (1998),  $\log(L_{\text{acc}}/L_{\odot}) = 1.09^{+0.04}_{-0.18} \log(L_U^{\text{ex}}/L_{\odot}) + 0.98^{+0.02}_{-0.07}$ , the accretion luminosity of GI Tau is calculated using the  $U$ -band accretion luminosity,  $L_{\text{acc}}$ , from

$$L_U^{\text{acc}} = 4\pi d^2 F_{\text{zeropoint}} \times (10^{-0.4U_{\text{unred}}} - 10^{-0.4U_{\text{photosphere}}}), \quad (4)$$

where  $F_{\text{zeropoint}}$  is the zero point of the generic  $U$  band, the distance  $d = 140$  pc, and  $U_{\text{unred}}$  is the spot modulation and extinction reddening removed  $U$  magnitude. The accretion luminosity ranges from  $\sim 0$  to  $41 \times 10^{-2} L_{\odot}$ . The accretion

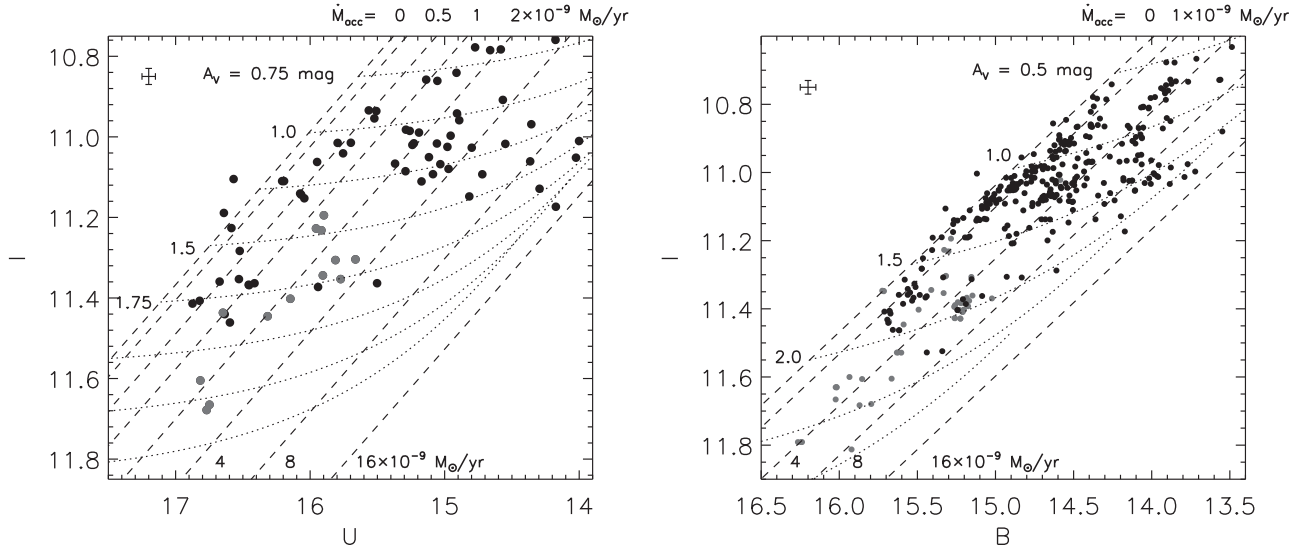


**Figure 13.** Spot-corrected  $U$  vs.  $I$  (left) and  $B$  vs.  $I$  (right) during our 2015–2016 monitoring of GI Tau. The spots are removed as sinusoidal light curves with parameters in Table 2. This grid is calculated based on two assumptions: (a)  $I = U - 0.15$  as the accretion and (b) extinction amplitudes in each band follow the  $R_V = 3.85$  curve from Cardelli et al. (1989). The estimated extinction ranges from  $A_V = 0.5$  to 2.5 mag assuming out of extinction brightness  $I = 10.43$  mag (Herczeg & Hillenbrand 2014).

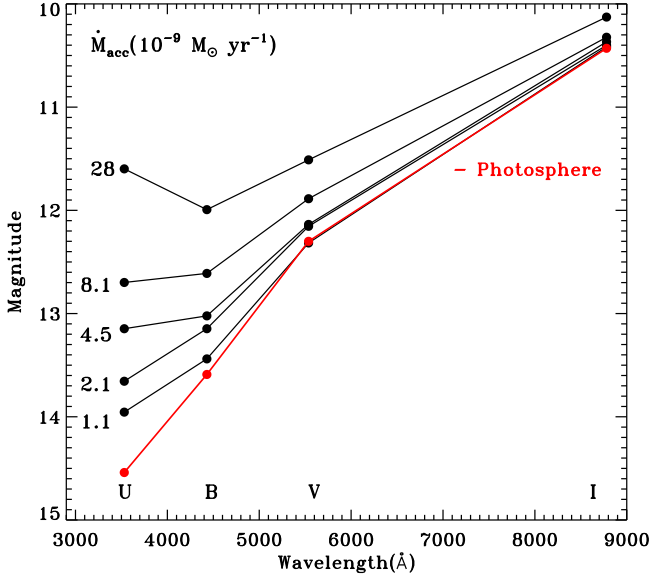


**Figure 14.** Optical spectral energy distributions of GI Tau obtained at five different accretion rates, alongside a photospheric template (red). The photometry has been corrected for extinction. The photospheric template is  $U_{\text{photosphere}} = 14.54$  mag,  $B_{\text{photosphere}} = 13.59$  mag,  $V_{\text{photosphere}} = 12.29$  mag, and  $I_{\text{photosphere}} = 10.43$  mag.

rate  $\dot{M}_{\text{acc}}$  is then derived from the accretion luminosity,

$$\dot{M}_{\text{acc}} \sim 1.25 L_{\text{acc}} R_* / GM_*, \quad (5)$$

where  $R_*$  and  $M_*$  are the radius and mass of GI Tau. The calculated mass accretion rate of GI Tau ranges from  $\sim(0\text{--}52) \times 10^{-9} M_{\odot} \text{yr}^{-1}$  for stellar parameters  $R_* = 1.7 R_{\odot}$  and  $M_* = 0.53 M_{\odot}$ .

We also develop a method to estimate the accretion rate from  $B$ -band photometry, because our time coverage in  $B$  is more extensive than that in  $U$ . After removing the sinusoidal spot modulation, the extinction and accretion for each  $B$  and  $I$  data point are estimated from the grid shown in Figure 13. The excess  $B$ -band emission produced by accretion is

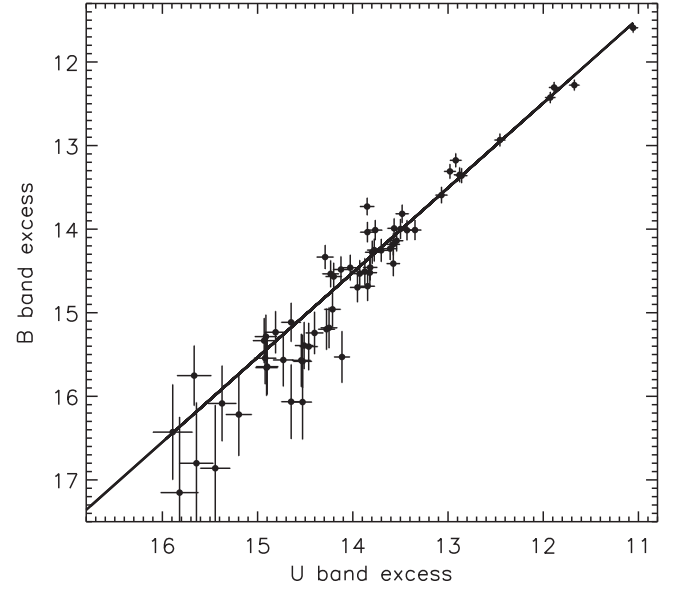


**Figure 15.** Correlation of the  $U$ - and  $B$ -band excess of GI Tau, both generated by accretion. The photometry has been corrected for spots, de-reddened, with an excess then measured against an estimated photospheric magnitude of  $U_{\text{photosphere}} = 14.54$  mag,  $B_{\text{photosphere}} = 13.44$  mag. The best linear fitting result is  $U_{\text{ex}} = 0.93B_{\text{ex}} + 0.52$ .

calculated from

$$B_{\text{ex}} = -2.5 \log(10^{-0.4B_{\text{unred}}} - 10^{-0.4B_{\text{photosphere}}}), \quad (6)$$

where  $B_{\text{unred}}$  is the de-reddened magnitude in the  $B$  band using the extinction curve of  $R_V = 3.85$ . Figure 15 shows a linear relationship between nearly simultaneous  $U_{\text{ex}}$  and  $B_{\text{ex}}$ , with a best-fit

$$U_{\text{ex}} = 0.93B_{\text{ex}} + 0.52. \quad (7)$$

The bolometric correction of the  $B$ -band excess is then combined with Equation (7) and the empirical relationship



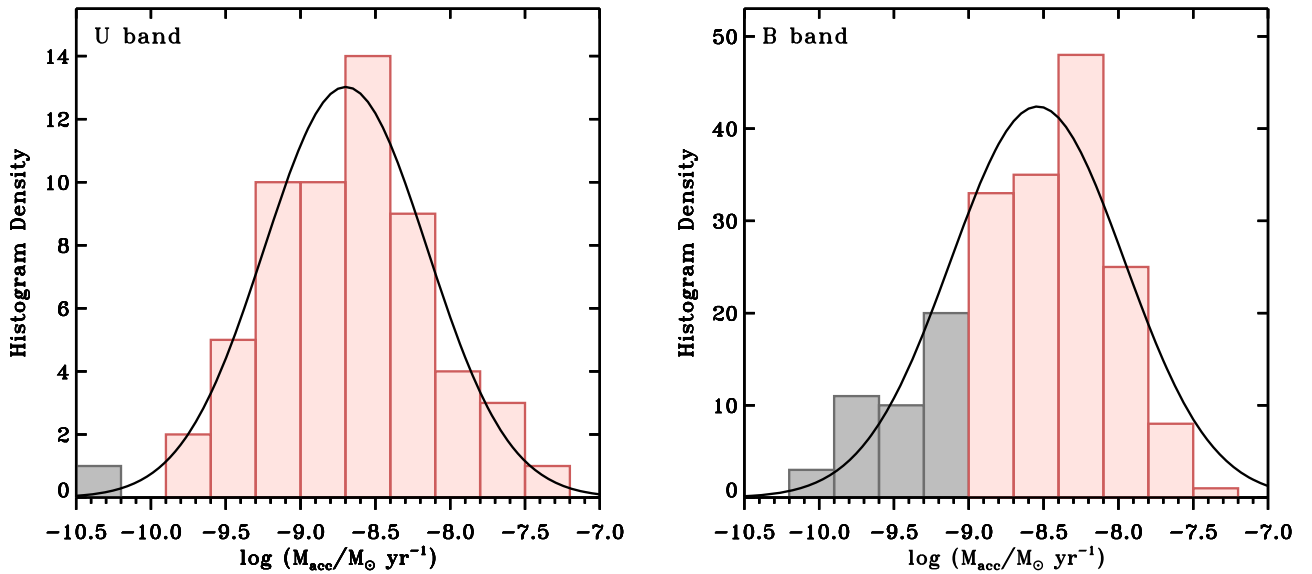


**Figure 16.** Histograms of accretion rates calculated using the  $U$ - (left) and  $B$ -band (right) excess throughout the entire 2015–2016 campaign. The data points taken within 2 hr are binned as one. The mass accretion rates higher and lower than the detection limit are shown in pink and gray, respectively. Gaussian fits of the histograms are shown by thick lines.

given by Gullbring et al. (1998) as

$$\log(L_{\text{acc}}/L_{\odot}) = 1.22_{-0.19}^{+0.05} \log(L_B^{\text{ex}}/L_{\odot}) + 1.46_{-0.10}^{+0.06}. \quad (8)$$

Based on the accuracy of our photometry and the correction for spots, estimated as  $\sim 0.1$  mag in both  $B$  and  $U$  bands, our detection limits of the accretion rate measurement are set as  $\log(M_{\text{acc}}/M_{\odot} \text{ yr}^{-1}) > -9.0$  for the  $B$  band and  $> -10.0$  for the  $U$  band. The correlation between the near-simultaneous  $B$ -band and  $U$ -band accretion rates is tight at rates higher than  $\log(M_{\text{acc}}/M_{\odot} \text{ yr}^{-1}) > -8.2$  but unreliable at lower accretion rates.

The mass accretion rates of GI Tau calculated from  $U$ - and  $B$ -band excesses are summarized in Figure 16. As measured from the  $U$ -band excess, the 5th to 95th percentile range of  $\log(M_{\text{acc}}/M_{\odot} \text{ yr}^{-1})$  is  $-7.89$  to  $-9.77$ , with a center at  $-8.70$  and sigma of 0.53 dex in the Gaussian fit. These results are consistent with results from the more extensive  $B$ -band photometry, which yielded an average  $\log M_{\text{acc}}/M_{\odot} \text{ yr}^{-1} = -8.55$  with 0.6 dex scatter. These estimates are obtained by creating mock sets of accretion rates over a range of values for the average and standard deviations and assuming a Gaussian distribution and upper limits. The adopted values are then obtained from maximizing the probability from a Kolmogorov–Smirnov test between the observed distribution and each mock data set. The distribution of  $B$ -band accretion rates includes the NOWT data sampled at a time resolution of one hour. The best-fit  $B$ -band data overpredict the number of data points at high accretion rates, as seen in Figure 16. Differences in results between the  $B$ -band and  $U$ -band accretion rates are likely attributable to the large scatter in the  $B$  band at average and weaker accretion rates.

This distribution of accretion rates is consistent with the distribution of accretion rates measured for stars of similar mass (e.g., Fang et al. 2013; Venuti et al. 2014; Manara et al. 2017). However, the distribution demonstrates the importance of accretion bursts in models of disk evolution. The average mass accretion rate of GI Tau is  $4.7 \times 10^{-9} M_{\odot} \text{ yr}^{-1}$ , two times faster than the average inferred from  $\log(M_{\text{acc}}/M_{\odot} \text{ yr}^{-1})$ . Moreover, a total of 50% of the mass is accreted during

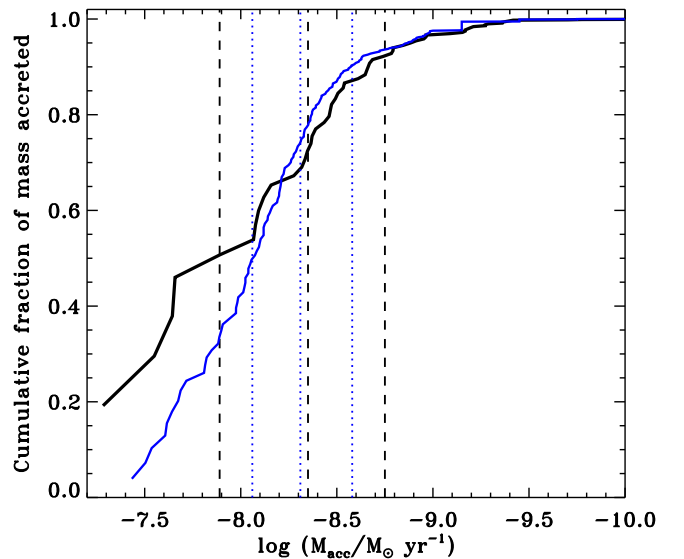


**Figure 17.** Distribution of the mass accretion rate measured using  $U$ - (black) and  $B$ -band (blue) photometry. Vertical dashed/dotted lines from left to right indicate the accretion rate above which half the mass is accreted, the average accretion rate, and the average mass accretion rate in log space.

accretion bursts when the accretion rate is higher than  $12.8 \times 10^{-9} M_{\odot} \text{ yr}^{-1}$  (Figure 17). Such bursts are seen in our high-cadence NOWT monitoring, where, for example, the accretion rate increased from  $\sim 2.3 \times 10^{-9} M_{\odot} \text{ yr}^{-1}$  to  $7.3 \times 10^{-9} M_{\odot} \text{ yr}^{-1}$  over several hours on day 458.

The periods of high accretion deplete most of the disk; the periods of low accretion are irrelevant. However, models of disk evolution (e.g., Rosotti et al. 2016; Lodato et al. 2017; Mulders et al. 2017; Rafikov 2017) assume that the accretion rates are static. Although these distributions cannot be fully explained by variability (Costigan et al. 2014; Venuti et al. 2015) and surely include some stars that are strong accretors and others that are weak, bursts should be expected to play a significant role in the mass accretion. The distribution of high accretion rates could also be in excess over a Gaussian

distribution. Future analyses should incorporate time-averaged accretion rates (e.g., Venuti et al. 2015) over many epochs and perhaps even many years.

## 5. Conclusions

Our two-year multiband photometric monitoring of the classical T Tauri star GI Tau revealed variability caused by extinction, accretion, and spots, each with unique signatures in color–magnitude diagrams. The deep extinction events of  $\Delta V = 2\text{--}3$  mag were seemingly stochastic in their timing and duration, with some occultations lasting 3–5 days and one 80 day-long dimming. During three months in 2014–2015, the short dips recurred with a quasi-period of  $\sim 21$  days, as might be expected from the sub-Keplerian slow warp seen in the simulations of Romanova et al. (2013). The stellar rotation period of  $7.03 \pm 0.02$  days is recovered from the second half of the 2015–2016 light curve but is not apparent in our earlier light curve, consistent with previous period estimates from some epochs (see Table 6) and with an inability to recover that period in other epochs.









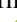
A wavelength-dependent extinction curve is fitted by spectral ratios, with best-fit  $R_V = 3.85 \pm 0.5$ . Diffuse interstellar bands are not detected from the spectra. The average mass accretion rate of GI Tau of  $\sim 4.7 \times 10^{-9} M_\odot \text{yr}^{-1}$  is calculated from excess *U*- and *B*-band light curves, after accounting for extinction and spots. The distribution of accretion rates demonstrates that most of the accretion occurs during bursts, so the quiescent accretion rates may provide a misleading evaluation of accretion as a diagnostic of disk physics.

We thank the anonymous referee for helpful comments and suggestions that improved the clarity and robustness of the results. Z.G. thanks Prof. Douglas N. C. Lin for helpful discussions. We also thank Hiro Takami, Stefano Facchini, and Carlo Manara for discussions on RW Aur, and Petr Petrov for discussions on extinction in disk winds. We also thank all of the observers and staff who contributed to this project, including those at the HCT (operated by the Indian Institute of Astrophysics), YNAO, VBO, TNO, HCT, and Lulin observatories.

We thank Guojie Feng, Chunhai Bai, Shuguo Ma, Guangxin Pu, Abudusaimaitijiang Yisikandeer, and Xuan Zhang from Xingjiang Astronomical Observatory for organizing and running the NOWT observations that are partially supported by the CAS “Light of West China” program (2015-XBQN-A-02).

Z.G., G.J.H., and J.J. are supported by general grant 11473005 awarded by the National Science Foundation of China. J.N.F. acknowledges the support from the National Natural Science Foundation of China (NSFC) through grant 11673003 and the National Basic Research Program of China (973 Program 2014CB845700 and 2013CB834900).

## ORCID iDs

Zhen Guo  <https://orcid.org/0000-0003-0292-4832>  
 Gregory J. Herczeg  <https://orcid.org/0000-0002-7154-6065>  
 Jianning Fu  <https://orcid.org/0000-0001-8241-1740>  
 Po-Shih Chiang  <https://orcid.org/0000-0003-3167-2523>  
 Raúl Michel  <https://orcid.org/0000-0003-1263-808X>  
 Ram Kesh Yadav  <https://orcid.org/0000-0002-6740-7425>  
 Wen-ping Chen  <https://orcid.org/0000-0003-0262-272X>  
 Saurabh Sharma  <https://orcid.org/0000-0001-5731-3057>  
 Angel Castro  <https://orcid.org/0000-0002-7832-5337>

## References

- Aldering, G., Adam, G., Antilogus, P., et al. 2002, *Proc. SPIE*, 4836, 61  
 Alencar, S. H. P., Bouvier, J., Walter, F. M., et al. 2012, *A&A*, 541, A116  
 Alencar, S. H. P., Teixeira, P. S., Guimarães, M. M., et al. 2010, *A&A*, 519, A88  
 Allard, F. 2014, in IAU Symp. vol 299, Exploring the Formation and Evolution of Planetary Systems, ed. M. Booth, B. C. Matthews, & J. R. Graham (Cambridge: Cambridge Univ. Press), 271  
 Ansdell, M., Gaidos, E., Rappaport, S. A., et al. 2016b, *ApJ*, 816, 69  
 Ansdell, M., Gaidos, E., Williams, J. P., et al. 2016a, *MNRAS*, 462, L101  
 Arce, H. G., & Sargent, A. I. 2006, *ApJ*, 646, 1070  
 Audard, M., Briggs, K. R., Grosso, N., et al. 2007, *A&A*, 468, 379  
 Bans, A., & Königl, A. 2012, *ApJ*, 758, 100  
 Baraffe, I., Homeier, D., Allard, F., & Chabrier, G. 2015, *A&A*, 577, A42  
 Beccari, G., Bellazzini, M., Magrini, L., et al. 2017, *MNRAS*, 465, 2189  
 Blinova, A. A., Romanova, M. M., & Lovelace, R. V. E. 2016, *MNRAS*, 459, 2354  
 Bodman, E. H. L., Quillen, A. C., Ansdell, M., et al. 2017, *MNRAS*, 470, 202  
 Bohlin, R. C., Savage, B. D., & Drake, J. F. 1978, *ApJ*, 224, 132  
 Bouvier, J., Alencar, S. H. P., Boutelier, T., et al. 2007, *A&A*, 463, 1017  
 Bouvier, J., Chelli, A., Allain, S., et al. 1999, *A&A*, 349, 619  
 Bouvier, J., Grankin, K., Ellerbroek, L. E., Bouy, H., & Barrado, D. 2013, *A&A*, 557, A77  
 Bouvier, J., Grankin, K. N., Alencar, S. H. P., et al. 2003, *A&A*, 409, 169  
 Calvet, N., & Gullbring, E. 1998, *ApJ*, 509, 802  
 Camenzind, M. 1990, *RvMA*, 3, 234  
 Cardelli, J. A., Clayton, G. C., & Mathis, J. S. 1989, *ApJ*, 345, 245  
 Cody, A. M., Hillenbrand, L. A., David, T. J., et al. 2017, *ApJ*, 836, 41  
 Cody, A. M., Stauffer, J., Baglin, A., et al. 2014, *AJ*, 147, 82  
 Cohen, M., & Kuhl, L. V. 1979, *ApJS*, 41, 743  
 Costigan, G., Vink, J. S., Scholz, A., Ray, T., & Testi, L. 2014, *MNRAS*, 440, 3444  
 Daemgen, S., Bonavita, M., Jayawardhana, R., Lafrenière, D., & Janson, M. 2015, *ApJ*, 799, 155  
 Dai, F., Facchini, S., Clarke, C. J., & Haworth, T. J. 2015, *MNRAS*, 449, 1996  
 Donati, J.-F., & Landstreet, J. D. 2009, *ARA&A*, 47, 333  
 Dullemond, C. P., van den Ancker, M. E., Acke, B., & van Boekel, R. 2003, *ApJL*, 594, L47  
 Espaillat, C., Furlan, E., D’Alessio, P., et al. 2011, *ApJ*, 728, 49  
 Facchini, S., Manara, C. F., Schneider, P. C., et al. 2016, *A&A*, 596, A38  
 Fang, M., Kim, J. S., van Boekel, R., et al. 2013, *ApJS*, 207, 5  
 Feiden, G. A. 2016, arXiv:1604.08036  
 Findeisen, K., Hillenbrand, L., Ofek, E., et al. 2013, *ApJ*, 768, 93  
 Fischer, W., Edwards, S., Hillenbrand, L., & Kwan, J. 2011, *ApJ*, 730, 73  
 Fischer, W., Kwan, J., Edwards, S., & Hillenbrand, L. 2008, *ApJ*, 687, 1117  
 Friedman, S. D., York, D. G., McCall, B. J., et al. 2011, *ApJ*, 727, 33  
 Grankin, K. N. 2016, *AstL*, 42, 314  
 Grankin, K. N., Bouvier, J., Herbst, W., & Melnikov, S. Y. 2008, *A&A*, 479, 827  
 Grankin, K. N., Melnikov, S. Y., Bouvier, J., Herbst, W., & Shevchenko, V. S. 2007, *A&A*, 461, 183  
 Grinin, V. P. 1988, *SvAL*, 14, 27  
 Grinin, V. P., Kiselev, N. N., Chernova, G. P., Minikulov, N. K., & Voshchinnikov, N. V. 1991, *Ap&SS*, 186, 283  
 Grinin, V. P., The, P. S., de Winter, D., et al. 1994, *A&A*, 292, 165  
 Gullbring, E., Hartmann, L., Briceño, C., & Calvet, N. 1998, *ApJ*, 492, 323  
 Gully-Santiago, M. A., Herczeg, G. J., Czekala, I., et al. 2017, *ApJ*, 836, 200  
 Hamilton, C. M., Herbst, W., Shih, C., & Ferro, A. J. 2001, *ApJL*, 554, L201  
 Hartigan, P., Strom, K. M., & Strom, S. E. 1994, *ApJ*, 427, 961  
 Hartmann, L., Herczeg, G., & Calvet, N. 2016, *ARA&A*, 54, 135  
 Herbig, G. H. 1977, *ApJ*, 214, 747  
 Herbig, G. H. 1995, *ARA&A*, 33, 19  
 Herbst, W., Herbst, D. K., Grossman, E. J., & Weinstein, D. 1994, *AJ*, 108, 1906  
 Herczeg, G. J., & Hillenbrand, L. A. 2014, *ApJ*, 786, 97  
 Ingleby, L., Espaillat, C., Calvet, N., et al. 2015, *ApJ*, 805, 149  
 Johns-Krull, C. M. 2007, *ApJ*, 664, 975  
 Johns-Krull, C. M., & Valenti, J. A. 2001, *ApJ*, 561, 1060  
 Jose, J., Kim, J. S., Herczeg, G. J., et al. 2016, *ApJ*, 822, 49  
 Ke, T. T., Huang, H., & Lin, D. N. C. 2012, *ApJ*, 745, 60  
 Kearns, K. E., & Herbst, W. 1998, *AJ*, 116, 261  
 Kenyon, S. J., Gómez, M., & Whitney, B. A. 2008, in Handbook of Star Forming Regions, Vol. I: The Northern Sky, ed. B. Reipurth (San Francisco, CA: ASP), 405

- Kenyon, S. J., & Hartmann, L. 1995, *ApJS*, **101**, 117
- Kesseli, A. Y., Petkova, M. A., Wood, K., et al. 2016, arXiv:1607.00385
- Koenigl, A. 1991, *ApJL*, **370**, L39
- Kowalski, A. F., Mathioudakis, M., Hawley, S. L., et al. 2016, *ApJ*, **820**, 95
- Kraus, A. L., & Hillenbrand, L. A. 2009, *ApJ*, **704**, 531
- Landolt, A. U. 1992, *AJ*, **104**, 340
- Lantz, B., Aldering, G., Antilogus, P., et al. 2004, *Proc. SPIE*, **5249**, 146
- Linnell Nemeč, A. F., & Nemeč, J. M. 1985, *AJ*, **90**, 2317
- Liu, J., Zhang, Y., Feng, G., & Bai, C. 2014, in IAU Symp. 298, Setting the scene for Gaia and LAMOST, ed. S. Feltzing et al. (Cambridge: Cambridge Univ. Press), 427
- Lodato, G., Scardoni, C. E., Manara, C. F., & Testi, L. 2017, arXiv:1708.09467
- Loinard, L., Torres, R. M., Mioduszewski, A. J., et al. 2007, *ApJ*, **671**, 546
- Loomis, R. A., Öberg, K. I., Andrews, S. M., & MacGregor, M. A. 2017, *ApJ*, **840**, 23
- Luhman, K. L., Allen, P. R., Espaillat, C., Hartmann, L., & Calvet, N. 2010, *ApJS*, **186**, 111
- Manara, C. F., Testi, L., Herczeg, G. J., et al. 2017, arXiv:1704.02842
- McGinnis, P. T., Alencar, S. H. P., Guimarães, M. M., et al. 2015, *A&A*, **577**, A11
- Morales-Calderón, M., Stauffer, J. R., Hillenbrand, L. A., et al. 2011, *ApJ*, **733**, 50
- Mulders, G. D., Pascucci, I., Manara, C. F., et al. 2017, arXiv:1708.09464
- Myers, P. C. 1982, *ApJ*, **257**, 620
- Natta, A., Grinin, V. P., Mannings, V., & Ungerechts, H. 1997, *ApJ*, **491**, 885
- Nguyen, D. C., Brandeker, A., van Kerkwijk, M. H., & Jayawardhana, R. 2012, *ApJ*, **745**, 119
- Nguyen, D. C., Scholz, A., van Kerkwijk, M. H., Jayawardhana, R., & Brandeker, A. 2009, *ApJL*, **694**, L153
- Oke, J. B. 1990, *AJ*, **99**, 1621
- Oudmajer, R. D., Busfield, G., & Drew, J. E. 1997, *MNRAS*, **291**, 797
- Padgett, D. L., Brandner, W., Stapelfeldt, K. R., et al. 1999, *AJ*, **117**, 1490
- Petrov, P. P., Babina, E. V., & Artemenko, S. A. 2017, in ASP Conf. Ser. 510, Stars: From Collapse to Collapse, ed. Y. Y. Balega et al. (San Francisco, CA: ASP), 94
- Petrov, P. P., Gahm, G. F., Djupvik, A. A., et al. 2015, *A&A*, **577**, A73
- Rafikov, R. R. 2017, *ApJ*, **837**, 163
- Rebull, L. M., Padgett, D. L., McCabe, C.-E., et al. 2010, *ApJS*, **186**, 259
- Rebull, L. M., Stauffer, J. R., Bouvier, J., et al. 2016, *AJ*, **152**, 113
- Reggiani, M., Robberto, M., Da Rio, N., et al. 2011, *A&A*, **534**, A83
- Robinson, C. E., Owen, J. E., Espaillat, C. C., & Adams, F. C. 2017, *ApJ*, **838**, 100
- Rodgers, B., Wooden, D. H., Grinin, V., Shakhovskiy, D., & Natta, A. 2002, *ApJ*, **564**, 405
- Rodríguez, J. E., Ansdell, M., Oelkers, R. J., et al. 2017a, *ApJ*, **848**, 97
- Rodríguez, J. E., Pepper, J., Stassun, K. G., et al. 2015, *AJ*, **150**, 32
- Rodríguez, J. E., Pepper, J., & Stassun, K. G. 2016a, in IAU Symp. 314, Young Stars Planets Near the Sun, ed. J. H. Kastner, B. Stelzer, & S. A. Metchev (Cambridge: Cambridge Univ. Press), 167
- Rodríguez, J. E., Reed, P. A., Siverd, R. J., et al. 2016b, *AJ*, **151**, 29
- Rodríguez, J. E., Zhou, G., Cargile, P. A., et al. 2017b, *ApJ*, **836**, 209
- Romanova, M. M., Ustyugova, G. V., Koldoba, A. V., & Lovelace, R. V. E. 2013, *MNRAS*, **430**, 699
- Romanova, M. M., Ustyugova, G. V., Koldoba, A. V., Wick, J. V., & Lovelace, R. V. E. 2003, *ApJ*, **595**, 1009
- Rosotti, G. P., Juhasz, A., Booth, R. A., & Clarke, C. J. 2016, *MNRAS*, **459**, 2790
- Rydgren, A. E., Strom, S. E., & Strom, K. M. 1976, *ApJS*, **30**, 307
- Scaringi, S., Manara, C. F., Barenfeld, S. A., et al. 2016, *MNRAS*, **463**, 2265
- Schneider, P. C., France, K., Günther, H. M., et al. 2015a, *A&A*, **584**, A51
- Schneider, P. C., Günther, H. M., Robrade, J., et al. 2015b, *A&A*, **584**, L9
- Shu, F., Najita, J., Ostriker, E., et al. 1994, *ApJ*, **429**, 781
- Sicilia-Aguilar, A., Hartmann, L. W., Hernández, J., Briceño, C., & Calvet, N. 2005, *AJ*, **130**, 188
- Simon, M., Guilloteau, S., Di Folco, E., et al. 2017, *ApJ*, **844**, 158
- Simon, M. N., Pascucci, I., Edwards, S., et al. 2016, *ApJ*, **831**, 169
- Sousa, A. P., Alencar, S. H. P., Bouvier, J., et al. 2016, *A&A*, **586**, A47
- Stauffer, J., Cody, A. M., Baglin, A., et al. 2014, *AJ*, **147**, 83
- Stauffer, J., Cody, A. M., McGinnis, P., et al. 2015, *AJ*, **149**, 130
- Stauffer, J., Cody, A. M., Rebull, L., et al. 2016, *AJ*, **151**, 60
- Taguchi, Y., Itoh, Y., & Mukai, T. 2009, *PASJ*, **61**, 251
- Takami, M., Wei, Y.-J., Chou, M.-Y., et al. 2016, *ApJ*, **820**, 139
- Tofflemire, B. M., Mathieu, R. D., Ardila, D. R., et al. 2017a, *ApJ*, **835**, 8
- Tofflemire, B. M., Mathieu, R. D., Herczeg, G. J., Akeson, R. L., & Ciardi, D. R. 2017b, *ApJL*, **842**, L12
- Torres, R. M., Loinard, L., Mioduszewski, A. J., et al. 2012, *ApJ*, **747**, 18
- Torres, R. M., Loinard, L., Mioduszewski, A. J., & Rodríguez, L. F. 2009, *ApJ*, **698**, 242
- Valenti, J. A., Basri, G., & Johns, C. M. 1993, *AJ*, **106**, 2024
- Venuti, L., Bouvier, J., Flaccomio, E., et al. 2014, *A&A*, **570**, A82
- Venuti, L., Bouvier, J., Irwin, J., et al. 2015, *A&A*, **581**, A66
- Vos, D. A. I., Cox, N. L. J., Kaper, L., Spaans, M., & Ehrenfreund, P. 2011, *A&A*, **533**, A129
- Vrba, F. J., Rydgren, A. E., Chugainov, P. F., Shakovskaia, N. I., & Zak, D. S. 1986, *ApJ*, **306**, 199
- Wenzel, W. 1969, *MitVS*, **5**, 75
- Zajtseva, G. V. 2010, *Ap*, **53**, 212
- Zechmeister, M., & Kürster, M. 2009, *A&A*, **496**, 577
- Zhang, K., Blake, G. A., & Bergin, E. A. 2015, *ApJL*, **806**, L7



# Photometric survey and taxonomic identifications of 92 near-Earth asteroids

Chien-Hsien Lin<sup>a,c</sup>, Wing-Huen Ip<sup>a,b,\*</sup>, Zhong-Yi Lin<sup>b</sup>, Yu-Chi Cheng<sup>b</sup>, Hsing-Wen Lin<sup>b</sup>,  
Chan-Kao Chang<sup>b</sup>

<sup>a</sup> Space Science Institute, Macau University of Science and Technology, Macau S.A.R., China

<sup>b</sup> Institute of Astronomy, National Central University, Taoyuan, Taiwan

<sup>c</sup> Key Laboratory for the Structure and Evolution of Celestial Objects, Chinese Academy of Science, Kunming, Yunnan, China

## ARTICLE INFO

### Keywords:

Near-Earth asteroids  
Photometry  
Taxonomy

## ABSTRACT

A photometric survey of near-Earth asteroids (NEAs) was conducted from 2012 through 2014 at Lulin Observatory, Taiwan. The measurements of the color indices, B-V, V-R, and V-I allow the classification of 92 NEAs into seven taxonomic types. Of these samples, 39 of them are new classifications. The fractional abundances of these taxonomic complexes are: A ~3%, C~6.5%, D~8%, Q~26%, S~37%, V~6.5%, and X~13%. This result is similar to that of Thomas et al. (2011) even though the populations of the D- and X-complex with low albedos are under-represented. The ratio of the C-cluster to the total population of S + C clusters are  $0.22 \pm 0.06$  for  $H \leq 17.0$  and  $0.31 \pm 0.06$  for  $H > 17.0$ , indicating a slightly higher fraction of dark-object population with sizes smaller than 1 km.

## 1. Introduction

The asteroidal population is characterized by different chemical compositions and taxonomic types at different heliocentric distances. The S-type asteroids can be found most often in the inner asteroid belt while the C-type asteroids dominate the outer belt population (Tholen, 1984; Bus and Binzel, 2002; DeMeo et al., 2009; DeMeo and Carry, 2013). The Near-Earth Asteroids (NEAs) with orbits near or crossing the Earth's orbit are products of collisional fragmentation of main belt parent bodies. How these small pieces of km to sub-km size range can be transported from the main belt to the Mars and Earth crossing orbits via the 3:1 mean motion resonance,  $\nu_6$  secular resonance, or the Yarkovsky effect has been investigated in detail by a number of authors (Bottke et al., 2002; Morbidelli and Vokrouhlicky, 2003; Greenstreet et al., 2012; Granvik et al., 2016). The taxonomic mapping of NEAs can therefore provide important information on their source regions and evolutionary histories (DeMeo and Carry, 2014; Carry et al., 2016).

On the basis of the Bus-system (Bus, 1999), several observational studies have shown that the S, Q, X and C-complexes in total account for about 90% of the NEA population while the rest is comprised of the A, D and V types (Dandy et al., 2003; Binzel et al., 2004; de Leo'n et al., 2010; Ye, 2011; Thomas et al., 2011).

The C-type and D-type NEAs are of special interest because of their volatile contents (Nichols, 1993; Reddy et al., 2012a). The C-type NEAs

are likely originated from the outer main belt which is known to be the reservoir of asteroids of carbonaceous composition (Bus and Binzel, 2002; DeMeo and Carry, 2014) and the so-called main belt comets with active outgassing phenomenon (Hsieh and Jewitt, 2006; Bertini, 2011). At the same time, the D-type and P-type NEAs could be of cometary origin (Jones et al., 1990; Rivkin, 2006; Volquardsen, 2007). The D-type objects are rather rare in the NEA population (Perna et al., 2016). Search for these volatile-rich NEAs as potential targets for future space missions is one of the scientific goals of the Lulin photometric survey.

Some S-type and Q-type are likely the same as ordinary chondritic composition (Tholen, 1984; Vernazza et al., 2008). That the S-type asteroids are redder and darker than the Q-type asteroids implies with the higher level of space weathering effect (Brunetto et al., 2006, 2015; Clark et al., 2002; Ishiguro et al., 2007). This also means that the Q-type asteroids should have younger (fresher) surfaces. The direct evidence of space weathering on surface particles has been derived from asteroid Itokawa from Hayabusa mission (Nakamura et al., 2011; Brunetto et al., 2015). Comparisons of the Q/S ratios in the main belt and the NEA population (Bus and Binzel, 2002; Lazzaro et al., 2004; Binzel et al., 2004; Dandy et al., 2003; Lin et al., 2015) have led to the interpretation that some physical mechanism must be at work to rejuvenate the surfaces of the Q-type objects once being injected into the orbital region of the terrestrial planets. Seismic shaking or removal of the surface materials by tidal effect during close encounters with the Earth and Venus has been

\* Corresponding author. Space Science Institute, Macau University of Science and Technology, Macau S.A.R., China.  
E-mail address: [wingip@astro.ncu.edu.tw](mailto:wingip@astro.ncu.edu.tw) (W.-H. Ip).

<https://doi.org/10.1016/j.pss.2017.12.019>

Received 17 May 2017; Received in revised form 18 December 2017; Accepted 31 December 2017

Available online 4 January 2018

0032-0633/© 2018 Elsevier Ltd. All rights reserved.

proposed and apparently supported by numerical studies showing that the Q-type NEAs tended to have more close encounters with the Earth and Venus than the S-type NEAs (Binzel et al., 2010; Nesvorný et al., 2010; Carry et al., 2016). DeMeo et al. (2014) even added that Mars could also be important for such surface rejuvenation process, yet Carry et al. (2016) did not find the significant difference in orbital properties of Q- and S-types in their encounters with Mars.

Another mechanism of potential importance has to do with the YORP effect of asteroidal rotation (Rubincam, 2000). The increase of the rotational rate because of the YORP effect to a certain critical value upon which the surface materials would be either spun off (Jacobson and Scheeres, 2011; Polishook et al., 2014) or turned over (Walsh et al., 2012; Scheeres, 2015) could play a role in keeping a higher Q/S ratio (Graves et al., 2016).

Of the 14,000 NEAs discovered up to now, only 800 have been classified by spectroscopic observations (Binzel et al., 2002: Data Base of Physical and Dynamical Properties of NEAs on E.A.R.N.) and 300 by photometric measurements in terms of color indices from SDSS (Carry et al., 2016) and the Bessel system photometry (Rabinowitz, 1998; Binzel et al., 2002 (NEA database); Dandy et al., 2003; Ye, 2011). Therefore there is a need to acquire more taxonomic data so that a number of major issues in NEAs as discussed above can be addressed.

## 2. Previous studies on the boulder shape and destruction mechanisms

### 2.1. Procedure

The 2012–2014 observations were carried out monthly at the Lulin Observatory in the middle of Taiwan (latitude = 23° 28' 07" N, longitude = 120° 52' 25" E and altitude = 2862 m) using either the Lulin One-meter Telescope (LOT) or the Super Light Telescope (SLT) with a primary mirror of 41 cm. The CCD camera installed on LOT was PI-1300 which has a field of view (FOV) of 11'×11' and an effective pixel scale of 0.516"/pxl; the one on SLT was U42 with FOV of 27'×27' and a pixel scale of 0.78"/pxl. The filters for both telescopes were Bessel broad-band BVRI filters with central wavelengths at 442, 540, 647 and 786 nm, respectively. Our observational strategy was to select NEAs with visible magnitude brighter than 19.0 in each month irrespective of whether their taxonomical classifications were known or not. All data sets considered had been obtained with air mass below 2.0. About 30% of the observations – 21 out of 92 our NEAs - were conducted with the color sequence as RBRVRIR especially for those brighter targets whose exposure time was able to be acquired in shorter time duration, while others were obtained simply with the sequence as BVRI for most of long exposures. The observational log can be found in Appendix A.

### 2.2. Data reduction

The observations in each night had their own set of Landolt standard stars used for flux calibration (Landolt, 1992). The routine procedure of fitting for air mass extinction and imaging photometry was performed by using the IRAF package (Image Reduction and Analysis Facility supplied by National Optical Astronomy Observatories); the WCS information on the images was applied with the code from [astrometry.net](http://astrometry.net) (Lang et al., 2010). Some observational data in specific dates were excluded from observation log (Appendix A) because of bad extinction value for color calibration, background star eclipse by the target NEAs, or photometric error with magnitude  $\Delta m > 0.15$ . Each target has at least once full BVRI exposures. There are some targets with multiple serial exposures as requested.

### 2.3. Color indices

The absolute magnitudes (H) of our NEA targets ranged from 9.45 to

21.8. This means that some of the observations were done during the close approaches of the NEAs to the Earth. The apparent brightness of each band was derived from aperture photometry. The color indices were then computed for B-V, V-R and V-I. For multiple sets of BVRI exposures, the average values are used. The results are summarized in Table 1. Note that five NEAs in the table have one missing color index because of stellar eclipse during individual observations. Overall, the Bessel color indices for 64 of the NEAs are derived for the first time from this work.

## 3. Taxonomic classifications

### 3.1. Integrated classes

The definition of asteroidal spectral types we used here is the Bus-DeMeo system (DeMeo et al., 2009). However, the broad-band photometry employed cannot give high resolution data as spectroscopic observations do, and our measurements were also limited in the optical wavelength range, without near-infrared coverage. We therefore made use of the classification scheme given by Binzel et al. (2004) and Stuart and Binzel (2004) with some modification. As shown in Table 2, we have seven main taxonomic complexes, namely, A, C, D, Q, S, V, X, whose subdivisions are listed. The main points are that, we combined the R-type into the V-type because they have similar spectral slopes in visible. By the same token, the O-type and the Q-type were merged into the Q-complex. The resultant SEDs of the seven taxonomical groups are illustrated in Fig. 1 which is a composite plot of different types of reflectance spectra to show the range of spectral variations. The actual dispersion should be more than depicted here because the Bus-DeMeo taxonomic classification is based on 371 spectra out of a population of about one million objects. In principle, these curves capture most of the main spectral signatures, namely, the absorption feature near 1  $\mu\text{m}$  for the Q- and V-types, the flatter slopes of X- and C-types, and the reddish color of the A- and D-types. Table 2 also gives the color indices specific to different taxonomic groups.

### 3.2. Classification

The distribution of the color indices of different taxonomic types is shown in the V-R/B-V color-color diagram in Fig. 2. This figure was constructed by collecting the known color indices of 150 NEAs from the Database of Physical Properties of NEAs by E.A.R.N. (Binzel et al., 2002) and several photometric surveys (Rabinowitz, 1998; Dandy et al., 2003; Ye, 2011). The color indices from the Lulin observations are superimposed over the reference data points. Some of the Lulin data points have relatively large error bars, but most of them fall into the domain of the reference groups aligned by the A-V-S-Q axis and the D-X-C axis.

In order to examine the taxonomic types of the observed NEAs by three color indices, representing different slopes of their SEDs, we adopted the method of principal component analysis (cf. Ivezić et al., 2001) to identify the uncorrelated indices in the B-V and V-R phase space. According to the line of linear regression to the mean indices of the seven taxonomic complexes, we can rotate the B-V and V-R axes by an angle ( $\theta$ ) of  $37.43^\circ$  (with a deviation of  $+2.714^\circ/-2.937^\circ$  from the fitting slope of  $0.765 \pm 0.078$ ) from which we can derive a principal component index (PCI) according to Equation (1).

$$\text{PCI} = (B - V)\cos\theta + (V - R)\sin\theta \quad (1)$$

The main method to classify the NEAs is analogous to that of DeMeo and Carry (2013) while using PCI and the R-I index in the present study. Fig. 3.a shows the PCI vs. R-I index of the known taxonomic types. It helps us to identify the boundaries of different complexes according to the Bus-DeMeo system, which described the ranges from the average spectra of the specific classes. Furthermore, we also considered the distributions of previous classifications referred in Fig. 3.a. Fig. 3.b shows the positions of our data points in such a map.



Table 1 (continued)

NEA	B	$\Delta B$	V	$\Delta V$	R	$\Delta R$	I	$\Delta I$	B-V	$\Delta B-V$	V-R	$\Delta V-R$	V-I	$\Delta V-I$	R-I	$\Delta R-I$	$PCII$	$\Delta PCII$
(230111) 2001 BE10	18.391	0.109	17.581	0.052	17.196	0.054	16.980	0.060	0.810	0.145	0.385	0.056	0.601	0.067	0.216	0.087	0.880	0.150
(249595) 1997 GH28	18.226	0.020	17.483	0.013	17.031	0.014	16.590	0.016	0.743	0.025	0.452	0.015	0.893	0.018	0.441	0.023	0.866	0.029
(249886) 2001 RY11	18.959	0.051	18.312	0.032	17.885	0.034	17.518	0.041	0.647	0.065	0.427	0.036	0.794	0.048	0.324	0.064	0.774	0.074
(262623) 2006 WY2	18.194	0.024	17.373	0.015			16.477	0.017	0.821	0.031			0.896	0.019				
(276397) 2002 XA40	17.449	0.011	16.628	0.008	16.160	0.010	15.832	0.010	0.821	0.014	0.468	0.011	0.796	0.012	0.333	0.016	0.938	0.018
(276786) 2004 KD1	19.226	0.057	18.519	0.037	18.203	0.040	17.978	0.054	0.707	0.072	0.316	0.043	0.541	0.066	0.225	0.079	0.756	0.083
(277127) 2005 GW119	18.948	0.066	18.099	0.038	17.627	0.040	17.310	0.048	0.849	0.086	0.472	0.042	0.789	0.057	0.310	0.071	0.963	0.094
(285263) 1998 QE2	11.860	0.007	11.127	0.003	10.804	0.005	10.425	0.005	0.733	0.009	0.323	0.007	0.702	0.006	0.380	0.009	0.781	0.011
(294739) 2008 CM	17.538	0.019	16.791	0.011	16.321	0.012	15.962	0.014	0.747	0.025	0.470	0.012	0.829	0.016	0.359	0.020	0.880	0.027
(297274) 1996 SK	17.042	0.013	16.275	0.013	15.793	0.013	15.474	0.013	0.767	0.013	0.482	0.013	0.801	0.013	0.320	0.013	0.903	0.018
(326732) 2003 HB6	17.554	0.094	16.878	0.046	16.490	0.047	16.092	0.050	0.676	0.124	0.388	0.048	0.786	0.054	0.398	0.073	0.774	0.128
(329338) 2001 JW2	17.319	0.029	16.521	0.016	16.025	0.018	15.637	0.023	0.798	0.037	0.496	0.019	0.884	0.028	0.383	0.034	0.936	0.041
(330825) 2008 XE3	16.704	0.014	15.870	0.008	15.400	0.009	15.020	0.011	0.834	0.018	0.470	0.009	0.850	0.013	0.380	0.016	0.950	0.020
(333358) 2001 WN1	17.378	0.030	16.668	0.018	16.230	0.020	15.873	0.024	0.710	0.039	0.438	0.021	0.795	0.029	0.357	0.036	0.831	0.044
(334412) 2002 EZ2	19.390	0.078	18.590	0.051	18.025	0.060	17.718	0.068	0.800	0.098	0.565	0.068	0.872	0.081	0.308	0.106	0.979	0.119
(339492) 2005 GQ21	17.387	0.011	16.587	0.007	16.125	0.009	15.746	0.010	0.800	0.014	0.462	0.010	0.841	0.012	0.379	0.016	0.918	0.017
(339714) 2005 ST1	18.177	0.053	17.323	0.028	16.847	0.032	16.438	0.039	0.854	0.070	0.476	0.036	0.885	0.048	0.409	0.060	0.970	0.078
(340666) 2006 RO36	19.223	0.032	18.539	0.022	18.135	0.024	17.789	0.029	0.684	0.040	0.404	0.026	0.750	0.034	0.346	0.043	0.790	0.048
(341816) 2007 YK	19.036	0.112	18.262	0.051	17.833	0.057	17.561	0.046	0.774	0.150	0.429	0.062	0.701	0.040	0.272	0.073	0.877	0.157
(343098) 2009 DV42	17.391	0.042	16.565	0.022	16.027	0.026	15.584	0.026	0.826	0.055	0.538	0.029	0.981	0.030	0.445	0.043	0.984	0.061
(345722) 2007 BG29	19.428	0.082	18.438	0.040	17.787	0.043	17.339	0.043	0.990	0.109	0.651	0.046	1.099	0.045	0.448	0.064	1.183	0.115
(349068) 2006 YT13	16.761	0.034	15.969	0.018	15.503	0.021	15.127	0.021	0.792	0.044	0.466	0.023	0.842	0.024	0.365	0.035	0.914	0.049
(355256) 2007 KN4	19.557	0.089	18.666	0.054	18.228	0.059	17.814	0.069	0.891	0.113	0.438	0.064	0.852	0.082	0.414	0.105	0.977	0.129
(356394) 2010 QD2	18.965	0.033	18.080	0.017	17.626	0.019	17.272	0.020	0.885	0.043	0.454	0.020	0.808	0.022	0.354	0.030	0.981	0.046
(361071) 2006 AO4	17.218	0.032	16.415	0.018	16.038	0.025			0.803	0.041	0.377	0.030					0.870	0.051
(363790) 2005 JE46	18.442	0.090	17.690	0.051	17.284	0.062	16.974	0.061	0.752	0.117	0.406	0.071	0.716	0.069	0.310	0.100	0.846	0.136
(378610) 2008 FT6	19.004	0.015	18.092	0.008	17.594	0.009	17.204	0.011	0.912	0.019	0.498	0.010	0.888	0.014	0.390	0.017	1.029	0.021
(389694) 2011 QD48	19.610	0.049	18.755	0.034	18.249	0.038	17.937	0.045	0.855	0.061	0.506	0.041	0.818	0.053	0.312	0.067	0.988	0.073
(411280) 2010 SL13	18.171	0.014	17.485	0.009	17.046	0.010	16.627	0.012	0.686	0.018	0.439	0.011	0.858	0.015	0.419	0.019	0.813	0.021
(441825) 2009 SK1	19.231	0.066	18.558	0.044	18.084	0.048	17.777	0.059	0.673	0.083	0.474	0.051	0.781	0.071	0.308	0.087	0.823	0.097
2002 TY68	18.445	0.023	17.673	0.016	17.240	0.018	16.835	0.019	0.772	0.029	0.433	0.020	0.838	0.022	0.417	0.031	0.878	0.035
2005 RQ6	18.674	0.054	17.943	0.028	17.484	0.032	17.162	0.054	0.731	0.071	0.459	0.036	0.781	0.071	0.317	0.059	0.861	0.078
2010 TN54	18.053	0.061	17.239	0.035	16.804	0.052	16.492	0.053	0.814	0.079	0.435	0.064	0.747	0.066	0.313	0.016	0.913	0.102
2010 XZ67	16.346	0.004	15.555	0.002			14.791	0.003	0.791	0.006			0.764	0.004				
2011 WV134	16.217	0.011	15.431	0.006	14.990	0.007	14.597	0.008	0.786	0.014	0.441	0.008	0.834	0.009	0.394	0.012	0.894	0.016
2012 ER14	18.030	0.012	17.424	0.007	17.044	0.008	16.647	0.010	0.606	0.015	0.380	0.009	0.777	0.013	0.397	0.016	0.713	0.017
2013 SO19	19.968	0.071	19.228	0.050			18.311	0.064	0.740	0.087			0.917	0.075				
2013 UH9	18.520	0.092	17.814	0.052	17.299	0.055	16.865	0.057	0.706	0.119	0.515	0.057	0.949	0.062	0.434	0.084	0.874	0.130

<sup>a</sup> It indicates that this NEA was derived for its Bessel-system color indices from the photometry for the first time.

**Table 2**

A list of the seven merged complexes and their subgroups together with the individual color indices.

Taxonomic complex	Subgroups	B-V	V-R	V-I
A	A, Sa	0.926	0.556	0.900
C	C, Cb, Cg, Cgh, Ch, B	0.694	0.365	0.696
D	D, T	0.744	0.444	0.868
Q	Q, Sq, O	0.792	0.444	0.747
S	K, L, Ld, S, Sr, Sv, Sk, Sl	0.818	0.484	0.871
V	V, R	0.861	0.519	0.825
X	X, Xc, Xe, Xk	0.716	0.410	0.785

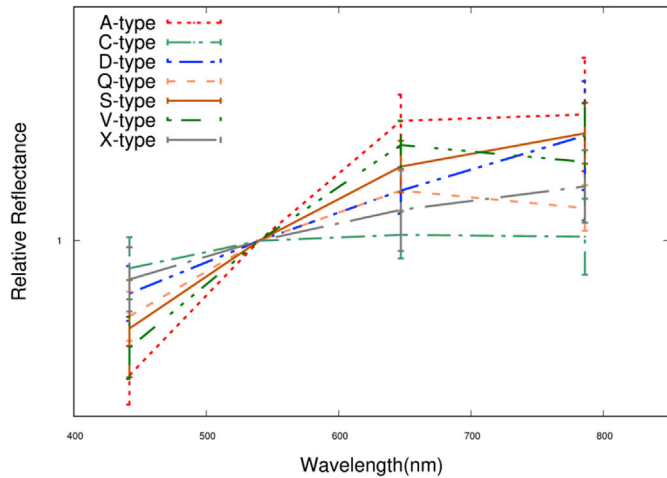


**Fig. 1.** The relative reflectance spectra of the seven taxonomic complexes. The four conjunct points of 442, 540, 647, and 786 nm correspond to the median wavelengths of the band widths from our BVRI filters. The reflective irradiance is normalized according to the V-band. The error bars are derived from the dispersions of the mean spectra (DeMeo et al., 2009).

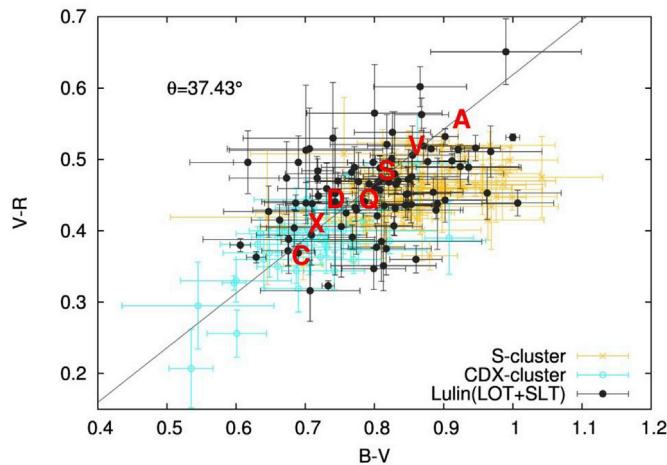


**Fig. 2.** The color-color diagrams for the spectral indices of the two taxonomic clusters, S- (yellow) and CDX-clusters (blue) (will also be described in Section 5) from the literature and the Lulin observations (black dots). The centers of the mean colors of different spectral complexes are identified with the corresponding red bold letters.

It can be noticed that some of the taxonomic domains overlap with others and that a few of the data points from the Lulin photometric survey fall outside the outer limit of the taxonomic boundaries. The flow chart in

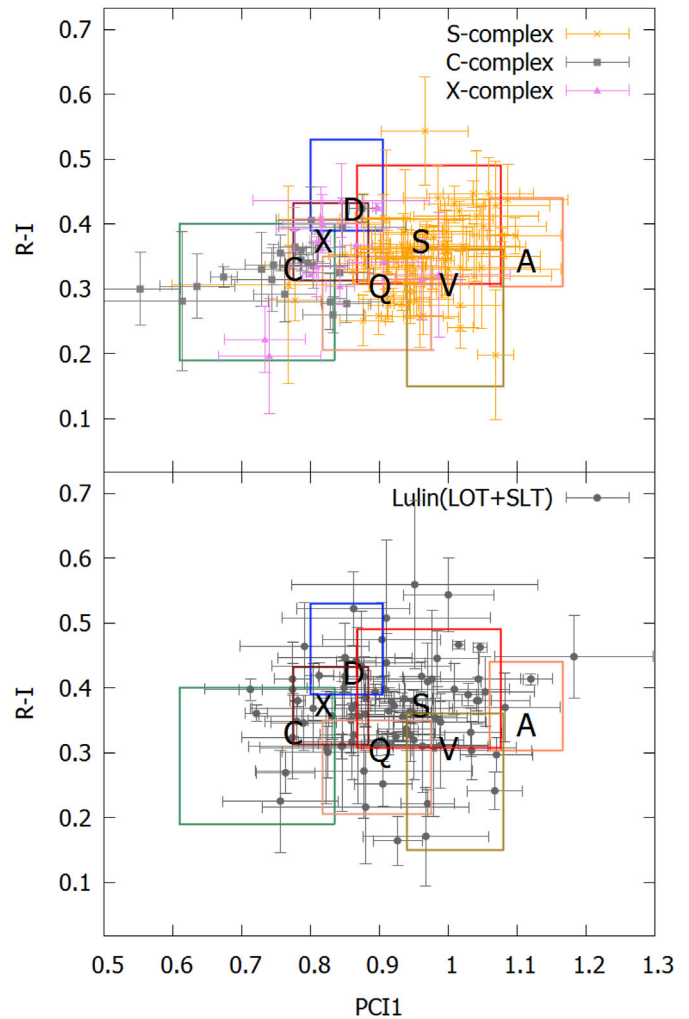


**Fig. 3.** An illustration of the correlation between the principle-component index (PCI) and the color index, R-I. The black bold letters specify the mean colors of the seven taxonomic complexes, A, C, D, Q, S, V and X. Each has its own domain boundary which is plotted in different colors. (a) Top: The global pattern of the seven domains and the distributions of the three large complexes: C-, S- and X-complexes in the PCI vs. R-I plot. (b) Bottom: Distribution of the 87 NEAs in the same plot.

Fig. 4 illustrates the steps taken to prioritize their identification. Basically, we classified our NEAs according to the boundaries of taxonomic complexes in Fig. 3. Inevitably some photometric classifications would fall into two or more taxonomical regions. If it is really close to the mean indices of one taxonomic complex with the distance of (PCI, R-I) smaller than 0.01, we would classify it to be that one. Otherwise, we have perform priority check as displayed in Fig. 4. The reason is that the Q-complex has some such feature like that, we would consider it as having some Q-type surfaces on it. The majority of the NEA taxonomic classes are inside silicate complexes with a larger amount of V-type than A-type. As for the group of C, D, X-complexes, the X-complex has a higher fraction of overlapping with the regions of C and D complexes and also a larger distinguished population within the CDX-cluster. Therefore, classification of the X-complex has priority.

Five NEAs of the program have only two color indices because of the observational condition. They are classified by visual inspection and comparison of the segmental slopes with the SED templates of the seven



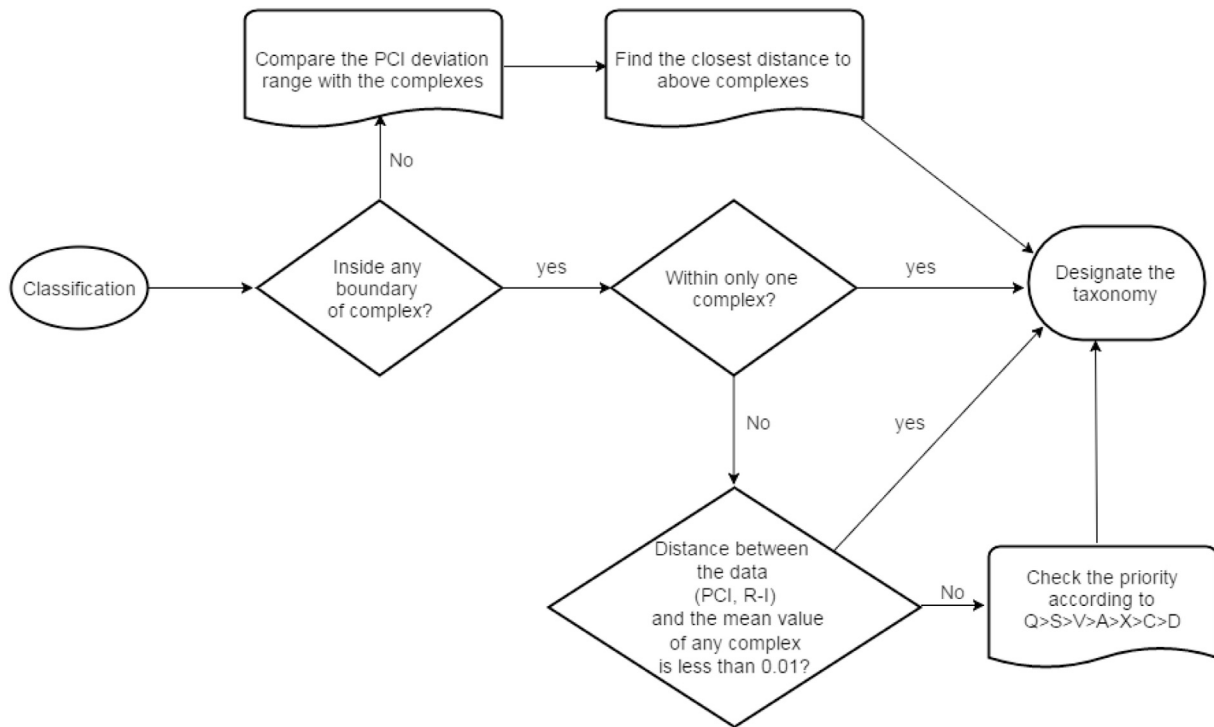


Fig. 4. The flow chart for the classification scheme of NEA taxonomy according to the relative positions of NEAs in Fig. 3.

taxonomic types. The results are listed in Table 3 and Table 4. Note that the sizes of NEAs without albedo measurements have been estimated by using the mean albedos of individual spectral types given in Thomas et al. (2011). Finally, Fig. 5 shows the composite SEDs of the 87 NEAs with full sets of BVRI measurements according to their assigned complexes. The spectra and the descriptions of individual entries can be found in the Appendices.

#### 4. Spectral trends

According to the spectral classifications as described above, it can be seen that there are A = 3%, C = 6.5%, D = 8%, Q = 26%, S = 37%, V = 6.5%, and X = 13% in our Lulin sample (see Fig. 6). In general, such distribution is compatible to the results of Thomas et al. (2011) covering 118 NEAs, with C = 4%, D = 2%, Q = 34%, S = 39%, V = 6%, and X = 15%, but lacking the A-type. The A-complex has similar reddish trend as the S-complex. If we combine A and S together in the Lulin survey, the resultant S-complex will be 40% which is close to the value of Thomas et al. (2011).

It is interesting to see in Fig. 5 that while the spectral classification has been divided into 7 complexes, they could also be grouped into two main clusters, namely, the S-cluster consisting of the S, Q, V and A complexes, and the C-cluster consisting of the C, D and X complexes. The ratio of simply lumped clusters of S and C classes would be more comparable with other results as well as reducing some disadvantage of lower spectral resolution from the photometry. In general, our photometric measurements allow spectral typing according to the Bus-DeMeo system. In our Lulin sample, the S-cluster accounts for nearly 73% of the total number of NEAs and the C-cluster 27%. The corresponding S-cluster to C-cluster (or S/C) ratio is therefore about 2.7. Note that the bias-corrected estimate by Stuart and Binzel (2004) gives a S/C (i.e., bright to dark) ratio of 1.6. Carry et al. (2016) shows the S/C ratio of objects with diameter between 3 and 5 km to be about 2.0 according to SDSS

photometric measurements. A larger S/C ratio of 3.3 was reported by Gietzen (2009) based on infrared and other observations.

Furthermore, the overall ratio of C- to C- plus S-cluster of the Lulin samples is 25 over 25 + 67 or  $0.27 \pm 0.05$ . The error of the fraction is derived by variance of the beta distribution and will be applied thereafter. The ratio of C-like/S-like is 25/67 or 0.37. This value is larger than the results of previous photometric NEA surveys from Dandy et al. (2003) for 0.21 and Ye (2011) for 0.14. However, it is close to the spectroscopic measurements of 36 NEAs from Lazzarin et al. (2005) for 0.27.

Rabinowitz (1998) suggested that NEAs with  $H > 17.0$  and  $H < 17.0$ , respectively, do not share the same color distributions. Fig. 7 shows the taxonomic distribution divided into two groups of sizes in our Lulin observations. The smaller NEAs with  $H > 17.0$  appear to have significantly more C- and D-complex objects. As for the S- and Q-complex objects, the differences are not as obvious. In the Lulin samples, the C-cluster/(C-cluster + S-cluster) ratio of large NEAs with  $H \leq 17.0$  is  $0.22 \pm 0.06$ , and the smaller ones (with  $17.0 < H \leq 22.0$ ) is  $0.31 \pm 0.06$ . This means that the fraction of C-cluster is larger within the smaller NEAs, which have diameters smaller than 1 km using an average albedo of 0.28 (Thomas et al., 2011). Our results show a similar trend as the photometric measurements by Ye (2011) in which the C-like/S-like ratio for H between 18 and 22 is about twice as high as that for  $H < 18$ , namely, 0.33 vs. 0.17, respectively.

Previous studies by Dandy et al. (2003) and Ye (2011) both supported the hypothesis that smaller NEAs generally have less space weathered surfaces simply because of the lack of regolith. Specifically, the ratio of Q-complex/SQ-group (Q/SQ, hereafter) may be larger for the smaller NEAs. We integrated our Lulin classifications with the previous results for S- and Q-complexes (Binzel et al., 2002: Data Base of Physical and Dynamical Properties of NEAs on E.A.R.N.) and divided the population close to 600 NEAs into two groups according to H, relevant to their sizes. The ratio of Q/SQ for  $H > 17.0$  is  $0.45 \pm 0.03$ , as to that for  $H \leq 17.0$  is

**Table 3**  
Physical properties of the NEAs in the Lulin sample which have been taxonomically identified before.

NEA	a(AU)	e	i(°)	q(AU)	H	albedo	D(km)	T <sub>J</sub> <sup>a</sup>	Pre. tax. by spectroscopy	Pre. tax. by photometry	Taxonomy in this work
(1036) Ganymed	2.663	0.534	26.692	1.241	9.45	0.228	36.49	3.03	S	S	S
(1627) Ivar	1.863	0.396	8.451	1.124	13.2	0.134	8.37	3.88	S	S	Q
(1685) Toro	1.367	0.436	9.381	0.771	14.23	0.26	3.75	4.72	S	S	S
(1943) Anteros	1.430	0.256	8.706	1.064	15.75	0.17	2.48	4.64	S; L;Sw		S
(2100) Ra-Shalom	0.832	0.437	15.758	0.469	16.05	0.14	2.24	6.95	K; Sr; C		Q
(3554) Amun	0.974	0.280	23.362	0.701	15.82	0.142	3.34	6.11	X; M;D		X
(4055) Magellan	1.820	0.327	23.257	1.226	14.6	0.33	2.781	3.89	V		V
(4179) Toutatis	2.534	0.629	0.447	0.939	15.3	0.13	4.3	3.14	S; Sk		S
(4450) Pan	1.442	0.586	5.520	0.596	17.1		0.9–1.1 <sup>b</sup>	4.46	S/Sr	S	Q
(4954) Eric	2.002	0.449	17.446	1.104	12.6	mh	9.5	3.66	S	S	A
(6047) 1991 TB1	1.454	0.352	23.473	0.942	17.8	0.8	1.2	4.49	S		Q
(7350) 1993 VA	1.356	0.391	7.262	0.826	17	0.05	2.363	4.77	C; X		X
(7753) 1988 XB	1.468	0.482	3.123	0.760	18.6	d	1	4.47	B		C
(8013)	2.199	0.432	7.571	1.249	16.9	m	1.2	3.53	Sr		S
Gordonmoore											
(10115) 1992 SK	1.248	0.325	15.322	0.843	17	0.28	1	5.06	S; Sq		S
(11284) Belenus	1.740	0.337	1.993	1.153	18.1		0.58–0.67 <sup>b</sup>	4.08		S	S
(11405) 1999 CV3	1.460	0.394	22.863	0.885	15.2	m	3.4	4.46	Sq		A
(12923) Zephyr	1.962	0.492	5.304	0.997	15.8	0.176	2.06	3.72	S		D/S
(21088) Chelyabinsk	1.707	0.239	38.461	1.299	14.2	0.179	4.23	3.92	Sl; Q	S	S/S
(22753) 1998 WT	1.219	0.570	3.207	0.524	17.7	0.27	0.9	5.06	Q; Sq		Q
(24761) Ahau	1.335	0.306	21.921	0.927	17.3		2.3–4.6 <sup>b</sup>	4.79	CX	S	D
(25916) 2001 CP44	2.560	0.498	15.749	1.284	13.6	0.262	5.683	3.20	Q,Sq		S
(40267) 1999 GJ4	1.339	0.808	34.529	0.257	15.4	0.249	1.62	4.38	Sq		S
(52762) 1998 MT24	2.418	0.651	33.894	0.843	14.8	0.052	6.71	3.01		X	X
(53435) 1999 VM40	2.309	0.485	15.388	1.188	14.7	mh	3.8	3.38	S; Srw		S
(55532) 2001 WG2	1.795	0.696	38.500	0.546	16.1	0.14	1.96	3.56	Sk		V
(68216) 2001 CV26	1.319	0.326	17.997	0.889	16.4	0.29	1.4	4.85	Sq	R	S
(85990) 1999 JV6	1.007	0.311	5.326	0.694	20.1	0.095	0.451	6.00	Xk		D
(89355) 2001 VS78	1.787	0.308	22.666	1.236	15.6	0.18	2.3	3.94	S; Sr		S
(99942) Apophis	0.922	0.191	3.331	0.746	19.2	0.3	0.375	6.47	Sq,Scom		S
(137062) 1998 WM	1.225	0.315	22.516	0.838	16.6	0.284	1.265	5.10	Q; Sq		Q
(137199) 1999 KX4	1.457	0.293	16.570	1.031	16.9		1.0–1.2 <sup>b</sup>	4.54	Sq		Q
(137805) 1999 YK5	0.829	0.558	16.742	0.366	16.6	0.027	3.879	6.91	X	RQ	X
(141052) 2001 XR1	1.246	0.550	17.659	0.560	17.3	0.22	1	4.96	Sq		Q
(141484) 2002 DB4	0.858	0.370	16.603	0.541	16.4		1.2–1.5 <sup>b</sup>	6.79	S; S-		Q
(152756) 1999 JV3	1.451	0.415	15.223	0.848	18.9	mh	0.5	4.51	Sa; S		V
(154347) 2002 XK4	1.850	0.692	17.806	0.570	16		1.5–1.75 <sup>b</sup>	3.63	S-		S
(162566) 2000 RJ34	2.635	0.574	13.861	1.121	15.7	0.07	4.41	3.11		X	C
(163249) 2002 GT	1.344	0.335	6.967	0.894	18.4		0.37–0.5 <sup>b</sup>	4.82	Sq		V
(163364) 2002	1.366	0.369	4.188	0.862	18.8		0.4–0.5 <sup>b</sup>	4.76	Sq		Q
OD20											
(214869) 2007 PA8	2.824	0.662	1.984	0.955	16.3	0.29	1.9	2.95	Q; S	Xc	Q
(215188) 2000 NM	2.690	0.663	22.357	0.907	15.4	m	2.6	2.93	Sr	R	S/A
(219071) 1997 US9	1.053	0.282	20.017	0.756	17.1	0.35	1.2	5.75	Q; S		S
(230111) 2001 BE10	0.823	0.369	17.510	0.519	19.1	0.253	0.4	7.03	Scomp	R	Q
(277127) 2005	1.641	0.233	2.882	1.258	18.7		0.43–0.52 <sup>b</sup>	4.26	Sq		Q
GW119											
(285263) 1998 QE2	2.423	0.572	12.857	1.038	17.3	0.06	2.75	3.24	Ch	Ch	C
(297274) 1996 SK	2.434	0.795	1.964	0.500	16.7		1.09–1.3 <sup>b</sup>	2.97		S	Q
(330825) 2008 XE3	2.607	0.550	7.476	1.172	16.3		1.33–1.52 <sup>b</sup>	3.17		S	S
(333358) 2001 WN1	1.502	0.303	14.070	1.047	19.5		0.19–1.18 <sup>b</sup>	4.46		C	X
(349068) 2006 YT13	1.323	0.426	38.243	0.760	18.3		0.53–0.61 <sup>b</sup>	4.65		AR	S
(363790) 2005 JE46	1.903	0.553	8.264	0.851	17.7		0.69–0.82 <sup>b</sup>	3.73	C/X/T		Q
2005 RQ6	2.504	0.551	12.484	1.124	18.9		0.40–0.47 <sup>b</sup>	3.21	S/Sr		Q
2011 WV134	2.784	0.679	6.047	0.893	17.2		0.88–1.01 <sup>b</sup>	2.94		S	S

<sup>a</sup> The Jovian Tisserand parameters.

<sup>b</sup> Note that the sizes are estimated by using the mean albedos of different spectral types of the NEAs according to [Thomas et al. \(2011\)](#).

0.34 ± 0.03, greater than the former one. It indicates that the proportion of Q-complex, namely, those with relatively younger surface occupies more within the smaller NEAs. It is consistent with the surveys as mentioned above.

## 5. Discussion and summary

Photometric observations of NEAs carried out at the Lulin observatory between 2012 and 2014 have produced BVRI color indices of 92 NEAs. These NEA samples cover the largest NEA, 1036 Ganymed, with a diameter of 35 km to sub-kilometer sized objects with diameter as small

as 200 m. The main results are as follows.

- (1) The spectral types of the 92 NEAs can be classified into seven merged spectral groups: A, C, D, Q, S, V and X complexes.
- (2) Sixty four of the NEAs observed in the present survey are provided with newly identified colors representing 40% increase of the present database of the Bessel-system color indices, as to thirty nine of them present 5% increase to the number of NEAs with classified taxonomic types.
- (3) The fractional abundances of seven spectral complexes in this work can be summarized as: A = 3%, C = 6.5%, D = 8%, Q = 26%,

**Table 4**  
Physical properties of the NEAs in the Lulin sample which have new taxonomic identifications.

NEA	a(AU)	e	i	q(AU)	H	albedo	D(km)	$T_J^a$	Taxonomy in this work
(3360) Syrinx	2.468	0.746	21.153	0.628	15.9	0.07	1.8	2.96	D
(4487) Pochahontas	1.730	0.296	16.403	1.217	17.4		0.8–0.92 <sup>b</sup>	4.06	S
(5731) Zeus	2.263	0.654	11.428	0.784	15.7	0.031	5.231	3.28	X
(17188) 1999 WC2	2.216	0.637	29.444	0.805	16.5	0.147	1.819	3.22	S
(68031) 2000 YK29	1.376	0.129	15.173	1.199	18.1		0.58–0.67 <sup>b</sup>	4.77	S
(88263) 2001 KQ1	2.097	0.432	38.819	1.191	15.4	0.048	5.31	3.37	X
(90075) 2002 VU94	2.133	0.576	8.916	0.905	15.2	0.197	2.857	3.47	S
(136900) 1998 HL49	1.747	0.636	11.000	0.635	17.3		0.84–0.96 <sup>b</sup>	3.86	S
(152889) 2000 CF59	1.679	0.640	41.590	0.604	16.5	0.388	1.022	3.75	Q
(162004) 1991 VE	0.891	0.665	7.221	0.299	18.2		0.35–2.15 <sup>b</sup>	6.46	X
(168378) 1997 ET30	2.138	0.449	6.812	1.179	16.8		1.04–1.24 <sup>b</sup>	3.57	Q
(249595) 1997 GH28	2.004	0.371	7.014	1.260	17.7		1.92–3.83 <sup>b</sup>	3.74	D
(249886) 2001 RY11	1.483	0.283	22.846	1.063	17.4		1.01–1.56 <sup>b</sup>	4.45	C
(262623) 2006 WY2	0.983	0.333	27.554	0.656	18.6	0.122	0.761	6.02	S
(276397) 2002 XA40	2.263	0.482	4.453	1.172	17.1		0.91–1.08 <sup>b</sup>	3.45	Q
(276786) 2004 KD1	1.720	0.330	10.124	1.152	17.7		0.88–1.36 <sup>b</sup>	4.09	C
(294739) 2008 CM	1.567	0.408	35.998	0.927	17.3		0.84–0.96 <sup>b</sup>	4.13	S
(326732) 2003 HB6	2.718	0.572	6.594	1.164	17.6		0.46–2.84 <sup>b</sup>	3.09	X
(329338) 2001 JW2	1.698	0.489	9.586	0.868	19.1		0.36–0.42 <sup>b</sup>	4.05	S
(334412) 2002 EZ2	1.249	0.046	13.025	1.192	20.1	0.4	0.21	5.12	V
(339492) 2005 GQ21	1.426	0.215	47.024	1.119	18.2		0.56–0.64 <sup>b</sup>	4.35	S
(339714) 2005 ST1	1.451	0.371	20.234	0.913	20.4		0.20–0.23 <sup>b</sup>	4.51	S
(340666) 2006 R036	0.906	0.231	23.857	0.697	17.8		0.42–2.59 <sup>b</sup>	6.49	X
(341816) 2007 YK	1.870	0.321	31.838	1.269	17.5		0.76–0.90 <sup>b</sup>	3.75	Q
(343098) 2009 DV42	1.615	0.275	19.926	1.170	18.7		0.44–0.50 <sup>b</sup>	4.23	S
(345722) 2007 BG29	0.833	0.335	18.511	0.554	18	0.258	0.653	6.97	A
(355256) 2007 KN4	3.342	0.630	12.538	1.235	16.8		1.06–1.21 <sup>b</sup>	2.77	S/D
(356394) 2010 QD2	2.010	0.785	10.639	0.431	17.4		0.80–0.92 <sup>b</sup>	3.35	S
(361071) 2006 AO4	2.629	0.584	24.392	1.095	15.4		1.98–2.39 <sup>b</sup>	3.03	Q
(378610) 2008 FT6	2.138	0.426	13.585	1.228	17.4		0.80–0.92 <sup>b</sup>	3.56	S
(389694) 2011 QD48	1.545	0.492	19.067	0.785	18.2		0.41–0.55 <sup>b</sup>	4.26	V
(411280) 2010 SL13	2.005	0.415	3.041	1.173	19.3		0.21–1.30 <sup>b</sup>	3.72	X
(441825) 2009 SK1	1.611	0.223	30.818	1.252	18.3		0.52–0.62 <sup>b</sup>	4.16	Q
2002 TY68	2.217	0.514	20.800	1.077	18.7		1.21–2.42 <sup>b</sup>	3.39	D
2010 TN54	2.110	0.445	4.721	1.172	19.2		0.35–0.41 <sup>b</sup>	3.60	Q
2010 XZ67	2.061	0.494	11.841	1.042	19.7		0.27–0.33 <sup>b</sup>	3.60	Q/V
2012 ER14	1.637	0.363	6.863	1.042	20.5		0.24–0.37 <sup>b</sup>	4.22	C
2013 SO19	2.228	0.498	12.936	1.118	21.8		0.07–0.41 <sup>b</sup>	3.44	X/D
2013 UH9	2.580	0.597	13.075	1.039	18.6		1.27–2.53 <sup>b</sup>	3.12	D

<sup>a</sup> The Jovian Tisserand parameters.

<sup>b</sup> Note that the sizes are estimated by using the mean albedos of different spectral types of the NEAs according to Thomas et al. (2011).

S = 37%, V = 6.5%, and X = 13%. This distribution is in agreement with the results of Thomas et al. (2011).

- (4) The ratios of C- cluster to itself plus S- cluster are  $0.22 \pm 0.06$  for  $H \leq 17.0$  and  $0.31 \pm 0.06$  for  $H > 17.0$ , respectively, indicating a slightly higher fraction of dark-object population in sub-kilometer size range.
- (5) There is also an interesting S-complex target, (355256) 2007 KN4 with Tisserand parameter ( $T_J$ ) = 2.77 that needs to be investigated further to see if it is a candidate object of cometary origin.
- (6) The sizes of the observed NEAs are estimated using either published albedo values or the mean albedos specific to individual taxonomic types.

There are still some anomalous SED curves among our NEAs. For example, the NEA 12923, 24761, 85990, 136900, 441825 etc. have unusual slopes in their reflectance spectra (see Appendix B). It is possibly due to the effect of rotation since the surface spectra of NEAs might have large variations (Lin et al., 2014) and many of them have fast spin rates. As mentioned in Section 2, there were only 31 targets applied with the exposure sequence of RBRVRIR. And we additionally conducted interpolation method to avoid the color deviation from the rotation for this small group within our targets. We also compared the colors both with and without interpolation and found that there are differences of color indices merely less than 2% for these 31 NEAs. However, it is possible

that these targets were observed in short exposure time (total time of single sequence < 10 min). If the NEAs were observed over long durations of exposure time (total time of single sequence > 10 min) and only had simple filter sequence of BVRI, it might cause larger deviations of the color measurements. Thus, it would lead to the deformed spectra and subsequently misguide our classifications.

While most of the results of Thomas et al. (2011) and our present work are in very good agreement, the D- and Q-complexes somehow show noticeable differences (Fig. 6). The D-complex difference could be a matter of small number statistics in the Lulin sample. The Q-complex difference is significant and needs to be checked by collecting a large photometric data set in future.

Compared with the previous classifications of the individual NEAs (Appendix C), we assume that there are 3 mis-distinguished targets of each taxonomic complex in average. Hence we can generally added an uncertainty to each fractional abundance of our spectral complexes: A =  $3 \pm 3\%$ , C =  $6.5 \pm 3\%$ , D =  $8 \pm 3\%$ , Q =  $26 \pm 3\%$ , S =  $37 \pm 3\%$ , V =  $6.5 \pm 3\%$ , and X =  $13 \pm 3\%$ .

In order to find the difference of bias between our and others' taxonomic distribution during the same observing years, we collected many results of taxonomic detection from late 2011 to the end of 2014 as possible. The results were derived from both spectrometric and photometric observations (Polishook et al., 2014; Lim et al., 2012; Godunova et al., 2013; Ieva et al., 2014; Popescu et al., 2014; Kuroda et al., 2014;

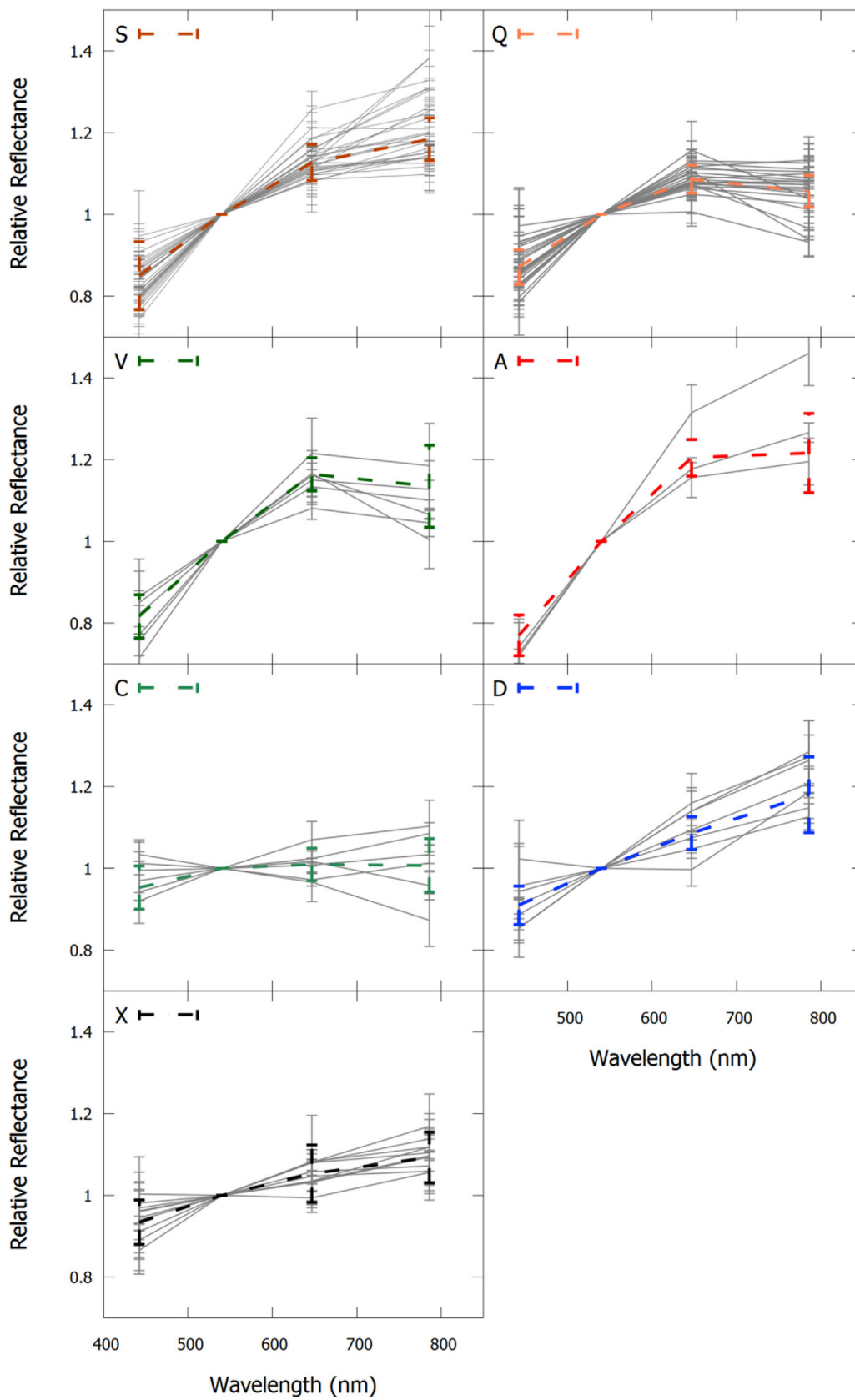
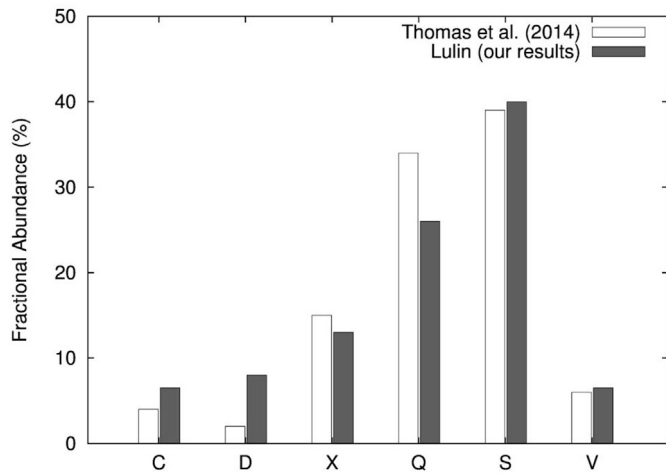
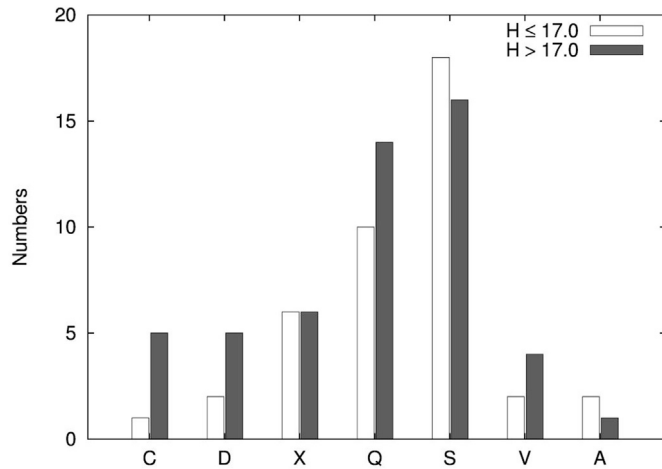


Fig. 5. The composite diagrams of the classified NEA spectra in the 7 taxonomic complexes with the templates of the relative reflectance spectra used in this work.



**Fig. 6.** The fractional abundances of the taxonomic complexes classified within the Lulin samples of 92 NEAs as well as the comparable results of Thomas et al. (2014). The three largest groups in order are S (37%), Q (26%) and X (13%).



**Fig. 7.** The numbers of NEAs in different spectral complexes according to their sizes in terms of magnitudes  $H \leq 17.0$  and  $H > 17.0$ , respectively.

Tubiana et al., 2015; Perna et al., 2016; Hicks' Atel. in 2011–2014 (Hicks

## Appendix A. Supplementary data

Supplementary data related to this article can be found at <https://doi.org/10.1016/j.pss.2017.12.019>.

## Appendices.

- The observation log
- The figure panels of relative reflectance spectra of 87 NEAs
- The elaborations of observation results for individual NEAs in this paper

and Dombroski, 2012; Hicks et al., 2011, 2012a, 2012b, 2012c, 2012d, 2012e, 2012f, 2012g, 2012h, 2013a, 2013b, 2013c, 2013d, 2013e, 2014a, 2014b; Hicks and Ebelhar, 2013a, 2013b, 2014a, 2014b); Rayner et al., 2003: The MIT-UH-IRTF Joint Campaign for NEO Spectral Reconnaissance). There are total 80 NEAs of targets and some of them are overlapping with ours. Their spectral classifications are also issued into the seven complexes we described above. Thus, the fractional abundances of these external results are of S = 35%, Q = 35%, A = 1%, V = 5%, C = 15%, D = 1%, X = 8%. The ratio of lumped S-/C-cluster is about 3.2, kind of higher than ours (2.7). The distribution of Q, C, D and X complexes are also distinct from our fractions. Certainly there are biases existing in both our and these results since the estimated S/C ratio of debias distribution of NEAs from Stuart and Binzel (2004) is lower (1.6). Note that our spectral distribution is not debiased and the bias might be coming from the target selection, detecting limit of the various instruments and undetected dark population etc. In addition, we integrated our results with the above ones, and then the total fractional abundances would become S = 36%, Q = 30%, A = 2%, V = 6%, C = 10.5%, D = 5%, X = 10.5%. These fractions might be a little more reliable because of larger sample numbers.

Our present study together with the previous work by Ye (2011) showed that photometric measurements at Lulin Observatory can provide very useful taxonomic classifications of NEAs. Even though the color ratios for the relative reflectance spectra are not able to classify the spectral types of the asteroids more specifically and some mis-classification may occur, the simpler taxonomic complexes described in this paper are still generally distinguishable. In future work, we will organize more efficient scheme for observations and data analysis. A topic we will investigate is the correlation of the orbital parameters with the shapes and rotation periods of NEAs in different spectral types. Some interesting insight on their origin and dynamical evolution might be revealed by such statistical study.

## Acknowledgments

This work was mainly supported by the Project 017/2014/A1 of Macau Science and Technology Development Fund: MSAR No. 0426 as well as the Lulin Observatory which is operated by Institute of Astronomy, National Central University, Taiwan, under MOST grant: MOST 104-2119-M-008-024. We specially acknowledge that the Lulin staff, Hung-Chin Lin, Chi-Sheng Lin and Hsiang-Yao Hsiao have provided assistance in observations; also the partial support from the open project (No. OP201306) of Key Laboratory for the Structure and Evolution of Celestial Objects, Chinese Academy of Sciences.

## A. Observation log

Here displays the observation log of this work. Some targets were observed more than one night. If there are two exposure times (Exp. Time) in a row, the first quantity is for B-filter and the second is for V, R, I.

Designation	$\Delta$ (A.U.) <sup>i</sup>	$r$ (A.U.) <sup>ii</sup>	El. ( $^{\circ}$ ) <sup>iii</sup>	Ph. ( $^{\circ}$ ) <sup>iv</sup>	Observed Date	Vobs	Exp. Time	BVRI sets <sup>v</sup>	Telescope
(1036) Ganymed	3.817	4.062	97.3	13.9	2014 Jan. 9	16.1	180s, 150s	1	LOT
(1627) Ivar	0.378	1.181	107.1	55.1	2013 May 31	13.0	30s	2	SLT
	0.322	1.123	101.0	62.7	2013 Jul. 7	12.4	60s	3	SLT
(1685) Toro	0.991	1.496	98.4	40.6	2013 Jan. 27	16.3	90s	1	LOT
	0.982	1.508	100.1	40.0	2013 Jan. 29	16.4	60s	1	LOT
(1943) Anteros	0.515	1.434	144.5	23.4	2014 Jan. 9	16.2	180s, 150s	1	LOT
(2100) Ra-Shalom	0.348	1.129	101.7	60.8	2013 Sep. 14	16.4	90s, 60s	1	LOT
(3360) Syrinx	0.540	1.510	161.1	12.3	2012 Nov. 13	16.4	30s	1	LOT
(3554) Amun	0.743	1.235	90.1	52.9	2013 Jan. 29	17.6	180s	1	LOT
(4055) Magellan	1.388	2.280	147.5	13.4	2014 Jan. 9	18.0	270s, 240s	1	LOT
(4179) Toutatis	0.298	1.271	162.0	13.9	2013 Jan. 18	14.4	60s	3	SLT
(4450) Pan	0.364	1.304	139.3	30.2	2013 Sep. 14	17.2	90s, 60s	1	LOT
(4487) Pocahontas	0.354	1.221	121.5	44.2	2012 Oct. 9	17.5	60s	2	LOT
	0.358	1.219	120.6	44.8	2012 Oct. 12	17.6	60s	6	LOT
	0.360	1.219	120.2	45.0	2012 Oct. 13	17.6	60s	6	LOT
	0.469	1.233	110.2	48.8	2012 Nov. 13	18.3	60s	2	LOT
(4954) Eric	1.546	1.926	96.6	30.5	2014 Jan. 11	16.7	180s, 150s	1	LOT
(5731) Zeus	0.706	1.346	102.9	46.3	2012 Oct. 9	17.7	45s	3	LOT
	0.416	1.009	80.6	75.4	2012 Nov. 13	17.4	30s	3	LOT
(6047) 1991 TB1	0.476	1.405	142.1	25.9	2012 Oct. 9	18.0	60s	2	LOT
(7350) 1993 VA	0.322	1.054	90.9	71.4	2012 Oct. 9	17.3	45s	2	LOT
(7753) 1988 XB	0.272	1.284	173.3	5.2	2013 May 31	16.1	240s	3	SLT
(8013) Gordonmoore	1.091	2.006	147.1	15.7	2013 Oct. 5	19.6	300s, 240s	1	LOT
	1.125	2.022	144.2	16.8	2013 Oct. 8	19.9	360s, 300s	2	LOT
(10115) 1992 SK	0.419	1.154	103.0	56.3	2013 Jan. 29	17.7	180s	3	LOT
(11284) Belenus	0.248	1.163	131.3	39.5	2013 Jan. 28	17.0	60s	1	LOT
(11405) 1999 CV3	0.661	1.556	141.2	23.4	2013 Jan. 29	16.6	60s	2	LOT
(12923) Zephyr	1.266	1.684	95.2	36.3	2013 Oct. 3	18.9	300s, 240s	1	LOT
	1.192	1.797	110.1	31.4	2013 Oct. 20	18.8	300s, 240s	1	LOT
(17188) 1999 WC2	0.324	1.299	146.6	25.6	2013 Jul. 7	15.6	180s	3	SLT
(21088) Chelyabinsk	1.145	1.309	74.3	48.3	2013 May 31	17.2	300s	1	SLT
(22753) 1998 WT	0.547	1.529	172.4	4.9	2013 Jan. 30	17.8	180s	3	LOT
(24761) Ahau	0.401	1.046	87.3	70.2	2013 Jan. 30	18.5	180s	2	LOT
(25916) 2001 CP44	2.207	2.023	66.3	26.4	2014 Jan. 12	18.1	270s, 240s	1	LOT
(40267) 1999 GJ4	0.981	1.537	103.0	38.6	2014 Jan. 11	18.6	270s, 240s	1	LOT
(52762) 1998 MT24	1.251	2.172	147.7	14.4	2013 Sep. 1	17.6	300s	2	SLT
(53435) 1999 VM40	0.660	1.219	91.7	55.5	2013 Sep. 14	16.5	90s, 60s	1	LOT
	0.638	1.528	139.8	24.6	2014 Jan. 9	15.8	180s, 150s	1	LOT
(55532) 2001 WG2	0.710	1.499	123.7	33.1	2014 Jan. 11	17.8	180s, 150s	1	LOT
(68031) 2000 YK29	0.363	1.221	123.2	42.4	2014 Jan. 9	18.0	270s, 240s	1	LOT
(68216) 2001 CV26	0.353	1.066	93.5	67.2	2013 Jan. 27	16.9	60s	1	LOT
	0.351	1.076	95.3	65.7	2013 Jan. 29	16.9	60s	1	LOT
(85990) 1999 JV6	0.150	1.057	115.8	56.9	2014 Jan. 9	19.0	270s, 240s	1	LOT
(88263) 2001 KQ1	0.838	1.425	101.4	43.4	2012 Oct. 9	17.7	60s	1	LOT
(89355) 2001 VS78	0.893	1.284	86.2	49.8	2014 Jan. 12	18.4	270s, 240s	1	LOT
(90075) 2002 VU94	1.193	1.619	95.7	37.2	2014 Jan. 9	18.1	270s, 240s	1	LOT
	1.162	1.603	96.4	37.6	2014 Jan. 11	18.6	270s, 240s	1	LOT
(99942) Apophis	0.100	1.062	139.9	36.7	2013 Jan. 18	15.8	180s	3	SLT
	0.113	1.079	144.8	31.7	2013 Jan. 29	15.7	60s	3	LOT
	0.115	1.081	144.6	31.9	2013 Jan. 30	15.4	60s	2	LOT
(136900) 1998 HL49	0.688	1.109	80.1	62.2	2013 Oct. 20	19.0	300s, 240s	1	LOT
(137062) 1998 WM	0.446	1.197	107.6	51.5	2014 Jan. 12	17.2	180s, 150s	1	LOT
(137199) 1999 KX4	0.224	1.145	131.6	40.0	2013 Jan. 18	15.9	120s	3	SLT
	0.285	1.226	133.1	37.2	2013 May 31	15.9	240s	1	SLT
(137805) 1999 YK5	0.333	1.134	108.3	55.5	2013 Jan. 18	16.5	240s	4	SLT
(141052) 2001 XR1	0.646	1.509	131.5	29.8	2013 Oct. 2	18.6	210s, 180s	1	LOT
	0.680	1.559	135.7	26.6	2013 Oct. 10	18.6	300s, 240s	1	LOT
(141484) 2002 DB4	0.372	0.934	71.4	86.4	2014 Jan. 11	17.1	180s, 150s	2	LOT
(152756) 1999 JV3	0.146	1.109	127.5	46.6	2013 May 31	16.6	300s	1	SLT
(152889) 2000 CF59	0.487	1.317	123.2	38.8	2013 Jan. 30	17.0	180s	2	LOT
(154347) 2002 XK4	0.523	1.460	149.7	19.9	2013 Jan. 18	16.4	240s	3	SLT
	0.644	1.573	149.3	18.7	2013 Jan. 29	17.1	120s	1	LOT
(162004) 1991 VE	0.223	1.191	152.0	22.9	2012 Nov. 13	16.5	30s	2	LOT
(162566) 2000 RJ34	0.435	1.153	101.6	56.7	2014 Jan. 11	16.6	180s, 150s	1	LOT
(163249) 2002 GT	0.179	1.158	140.7	33.7	2013 May 31	16.5	240s	3	SLT
(163364) 2002 OD20	0.062	1.068	150.0	28.3	2013 May 31	14.2	30s	5	SLT
(168378) 1997 ET30	0.655	1.646	168.9	6.7	2013 Oct. 9	17.8	240s, 180s	1	LOT

(continued on next page)

(continued)

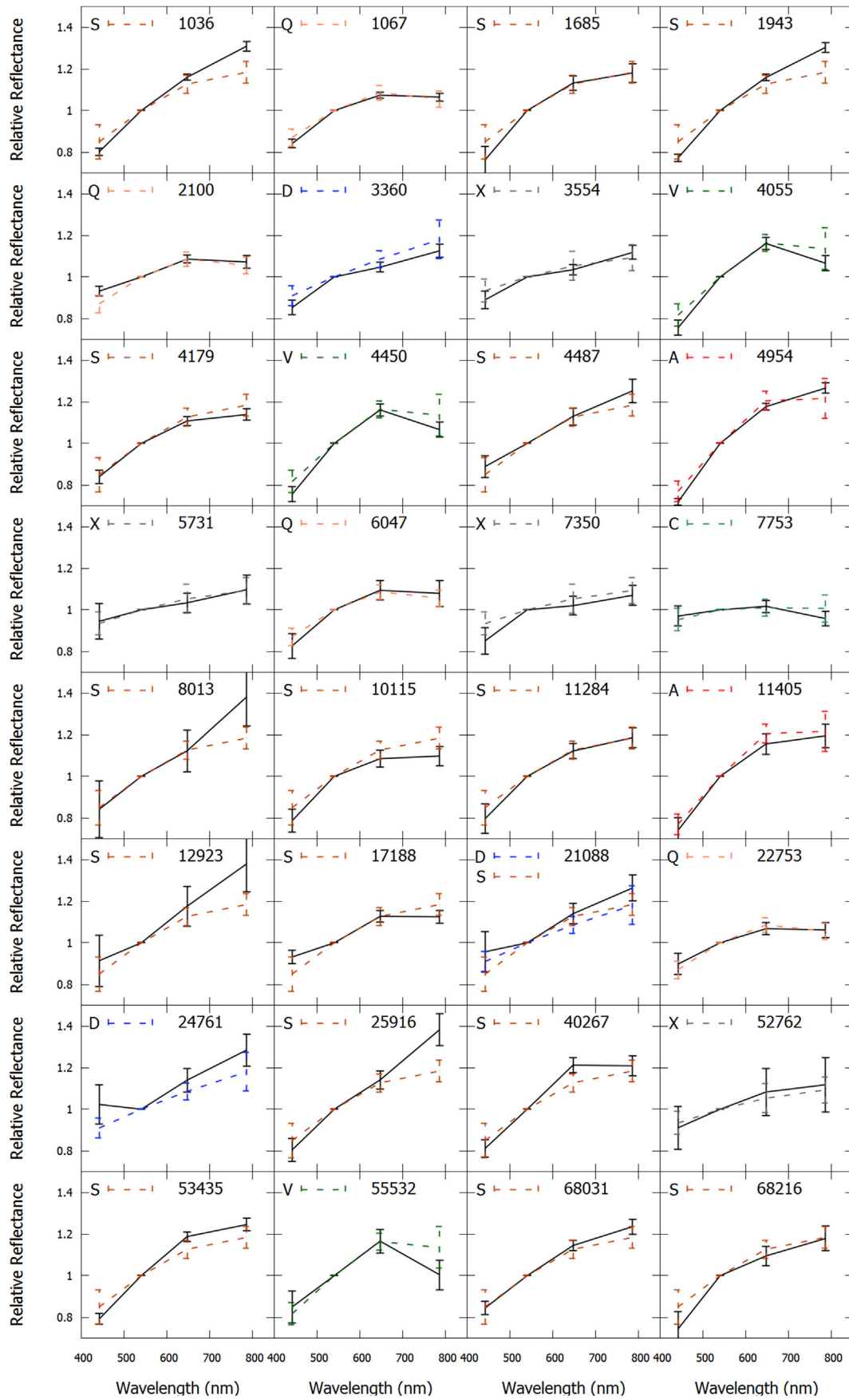
Designation	$\Delta$ (A.U.) <sup>i</sup>	$r$ (A.U.) <sup>ii</sup>	El. (°) <sup>iii</sup>	Ph. (°) <sup>iv</sup>	Observed Date	Vobs	Exp. Time	BVRI sets <sup>v</sup>	Telescope
	0.663	1.652	167.7	7.4	2013 Oct. 10	17.6	240s, 180s	1	LOT
(214869) 2007 PA8	0.185	1.181	169.3	9.0	2012 Oct. 9	13.7	30s	7	LOT
	0.362	1.187	115.8	48.3	2013 Jan. 18	16.4	240s	2	SLT
	0.393	1.268	128.6	37.4	2013 Jan. 28	16.4	90s	2	LOT
(215188) 2000 NM	1.019	1.274	79.0	49.3	2014 Jan. 11	17.6	270s, 240s	1	LOT
(219071) 1997 US9	0.665	1.168	86.6	58.8	2013 Oct. 2	19.0	210s, 180s	1	LOT
(230111) 2001 BE10	0.193	1.111	126.6	45.4	2013 Jan. 28	17.6	180s	1	LOT
(249595) 1997 GH28	0.363	1.277	138.3	30.8	2014 Jan. 9	17.8	180s, 150s	2	LOT
	0.360	1.280	139.9	29.7	2014 Jan. 11	17.4	180s, 150s	1	LOT
	0.359	1.282	140.7	29.1	2014 Jan. 12	16.9	180s, 150s	1	LOT
(249886) 2001 RY11	0.640	1.612	165.1	9.0	2013 Jan. 30	18.3	180s	3	LOT
(262623) 2006 WY2	0.279	1.247	158.3	16.9	2014 Jan. 9	17.4	180s, 150s	1	LOT
(276397) 2002 XA40	0.293	1.173	120.2	47.3	2012 Oct. 12	16.6	60s	5	LOT
	0.294	1.173	120.2	47.3	2012 Oct. 13	16.6	60s	4	LOT
(276786) 2004 KD1	0.575	1.532	151.9	17.9	2013 Oct. 2	18.5	210s, 180s	1	LOT
	0.610	1.569	153.6	16.4	2013 Oct. 10	18.5	300s, 240s	1	LOT
(277127) 2005 GW119	0.287	1.258	156.5	18.3	2012 Nov. 13	18.1	45s	4	LOT
(285263) 1998 QE2	0.039	1.049	153.3	25.7	2013 May 31	11.6	20s	6	SLT
	0.039	1.051	158.7	20.5	2013 Jun. 1	11.4	10s	13	SLT
(294739) 2008 CM	0.222	1.026	94.8	72.8	2014 Jan. 11	16.8	180s, 150s	1	LOT
(297274) 1996 SK	0.443	1.454	173.9	4.2	2012 May 22	16.2	60s	6	LOT
	0.456	1.467	172.8	5.0	2012 May 23	16.5	60s	1	LOT
(326732) 2003 HB6	0.272	1.211	130.6	39.6	2012 July 5	16.9	60s	3	LOT
(329338) 2001 JW2	0.165	1.139	153.0	23.2	2012 Nov. 13	16.5	30s	5	LOT
(330825) 2008 XE3	0.292	1.221	134.8	35.4	2012 Oct. 12	15.6	60s	3	LOT
	0.294	1.225	135.4	34.9	2012 Oct. 13	15.7	60s	2	LOT
	0.404	1.364	154.0	18.5	2012 Nov. 13	16.0	30s	5	LOT
(333358) 2001 WN1	0.131	1.109	154.1	23.0	2012 Nov. 13	16.7	30s	6	LOT
(334412) 2002 EZ2	0.211	1.193	154.9	20.8	2012 Oct. 12	18.1	60s	2	LOT
	0.214	1.193	153.5	21.9	2012 Oct. 13	18.2	60s	2	LOT
(339492) 2005 GQ21	0.198	1.165	144.5	29.8	2012 Oct. 12	16.6	60s	5	LOT
	0.198	1.167	145.6	28.9	2012 Oct. 13	16.6	60s	5	LOT
(339714) 2005 ST1	0.137	1.123	153.8	23.1	2012 Oct. 9	17.3	30s	5	LOT
(340666) 2006 RO36	0.456	1.108	91.1	64.6	2013 Oct. 2	18.5	210s, 180s	1	LOT
(341816) 2007 YK	0.554	1.456	140.4	25.5	2013 Jan. 29	18.3	300s	2	LOT
(343098) 2009 DV42	0.199	1.180	170.3	8.1	2013 Jan. 18	16.3	180s	3	SLT
	0.231	1.195	152.9	22.1	2013 Jan. 29	17.0	120s	2	LOT
(345722) 2007 BG29	0.341	1.108	102.2	60.3	2013 Jan. 29	18.4	300s	1	LOT
(349068) 2006 YT13	0.214	1.195	170.2	8.0	2013 Jan. 18	16.0	180s	3	SLT
(355256) 2007 KN4	0.889	1.843	155.0	13.3	2013 Oct. 6	18.5	210s, 180s	1	LOT
	0.930	1.874	152.6	14.2	2013 Oct. 10	18.8	300s, 240s	1	LOT
(356394) 2010 QD2	0.521	1.453	147.9	21.1	2013 Jan. 30	18.1	180s	1	LOT
(361071) 2006 AO4	0.535	1.381	122.7	38.3	2013 Jul. 10	16.4	300s	3	SLT
(363790) 2005 JE46	0.215	1.020	84.7	83.2	2013 Jul. 7	17.7	300s	2	SLT
(378610) 2008 FT6	0.487	1.278	116.7	43.4	2014 Jan. 9	18.1	270s, 240s	1	LOT
(389694) 2011 QD48	0.505	1.362	126.6	36.1	2013 Oct. 9	18.8	300s	1	LOT
(411280) 2010 SL13	0.215	1.178	151.8	23.2	2014 Jan. 9	17.5	180s, 150s	1	LOT
(441825) 2009 SK1	0.508	1.498	164.9	10.0	2013 Oct. 2	18.4	210s, 180s	1	LOT
	0.544	1.522	160.6	12.6	2013 Oct. 10	18.7	300s, 240s	1	LOT
2002 TY68	0.273	1.230	144.3	28.3	2012 Oct. 12	17.7	60s	4	LOT
2005 RQ6	0.262	1.151	119.0	49.5	2013 Oct. 3	18.1	210s, 180s	1	LOT
	0.241	1.125	116.8	52.2	2013 Oct. 20	17.8	210s, 180s	1	LOT
2010 TN54	0.204	1.198	155.3	20.6	2013 Sep. 1	17.2	300s	2	SLT
2010 XZ67	0.086	1.063	156.6	21.6	2014 Jan. 9	15.6	180s, 150s	1	LOT
2011 WV134	0.196	1.153	132.1	40.7	2012 May 23	15.4	30s	8	LOT
2012 ER14	0.101	1.076	138.2	38.2	2013 Oct. 10	17.4	300s, 240s	1	LOT
2013 SO19	0.175	1.166	160.8	16.4	2013 Oct. 6	19.2	300s, 240s	1	LOT
2013 UH9	0.190	1.040	100.4	69.3	2013 Nov. 17	17.8	150s, 120s	1	LOT

i. Geocentric distance; ii. Heliocentric distance; iii. Solar elongation; iv. Phase angles; v. one set comprises of every single exposure of B, V, R, I bands.

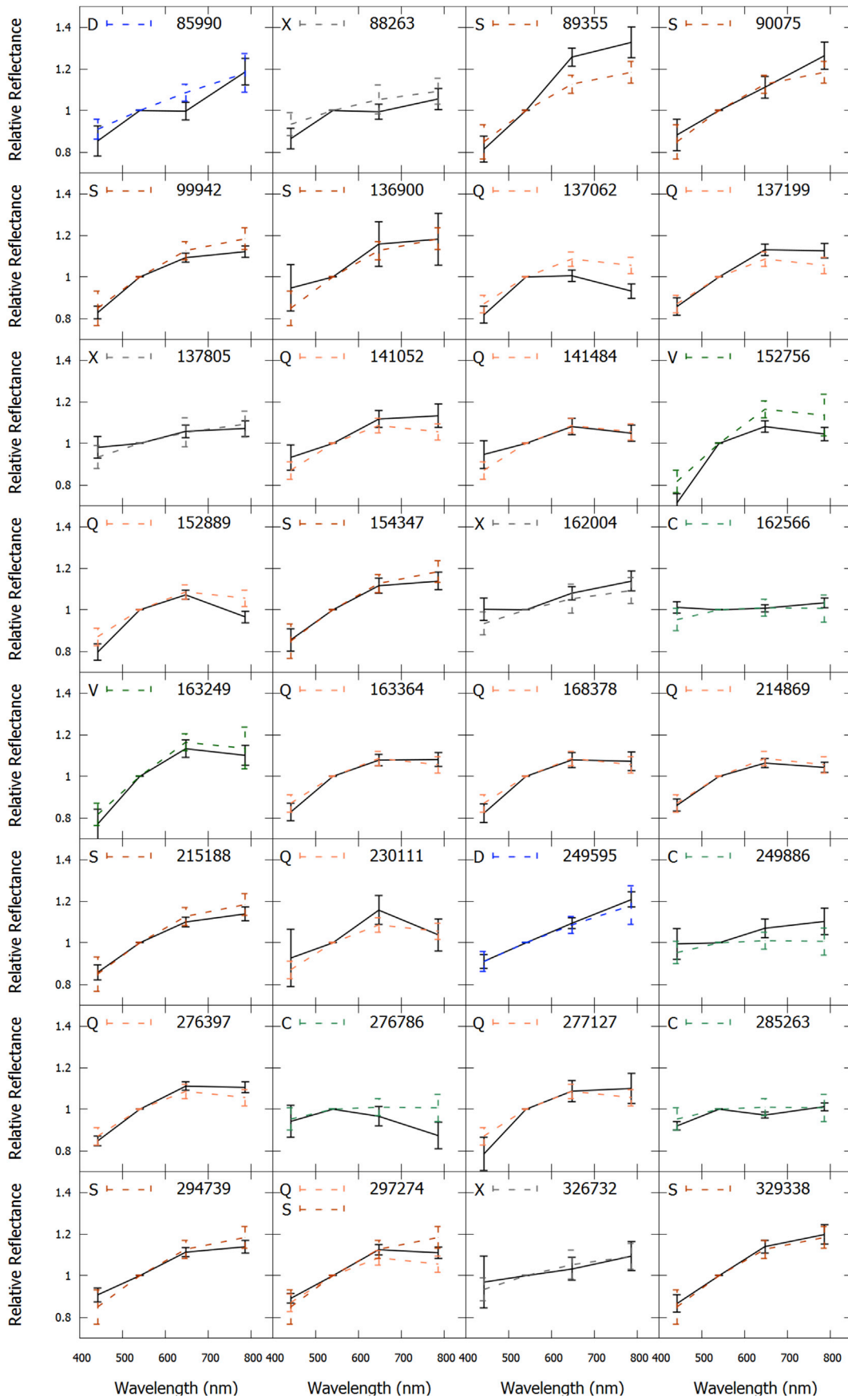
The values of i to iv are based exactly at 16:00 UT on each observation date.

### B. The figure panels of relative reflectance spectra of 87 NEAs

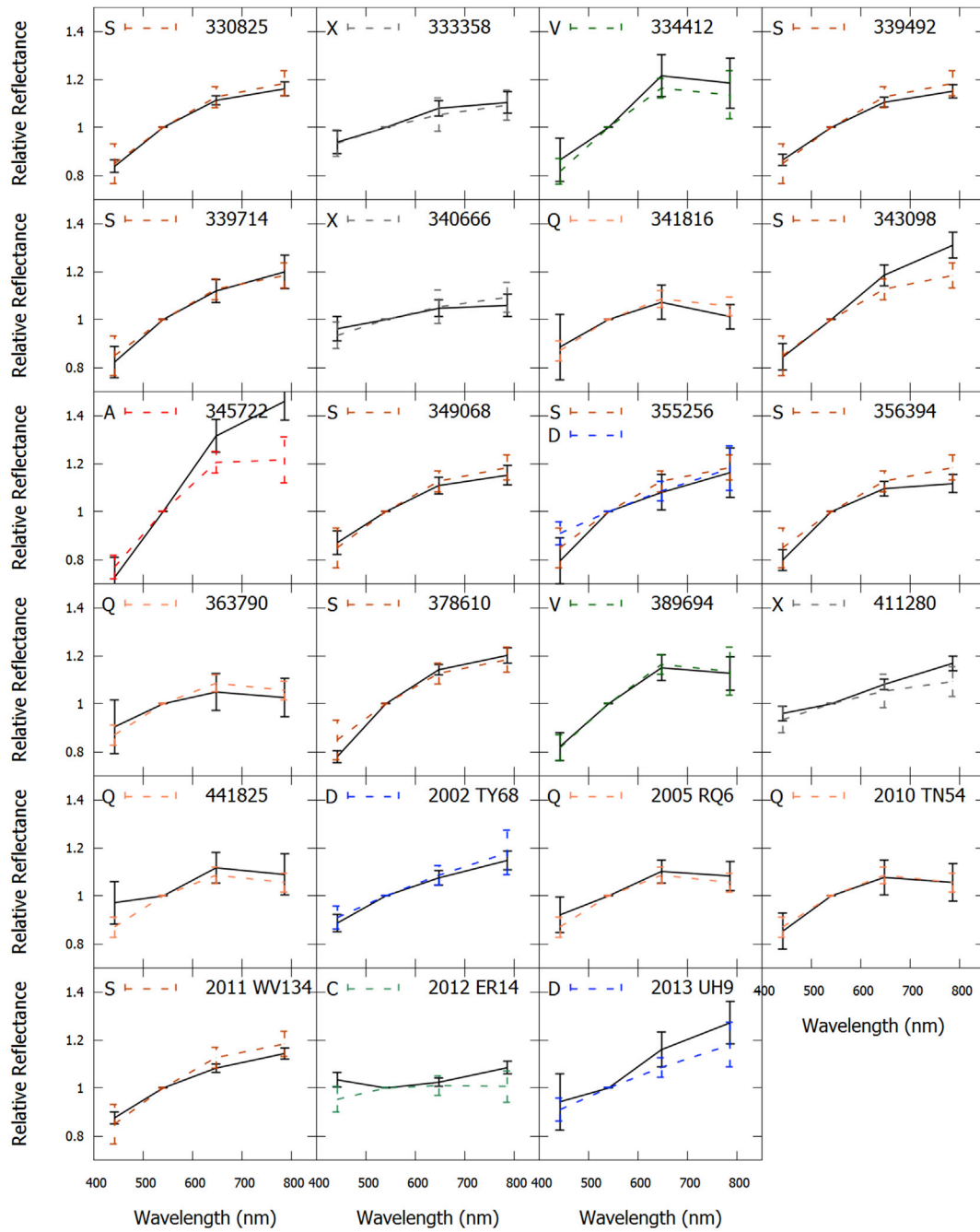
The panels display the individual relative-reflectance spectra of 87 NEAs as well as their classified taxonomic types in comparison to the corresponding template spectra with dashed lines. The panels are listed by the order of asteroid numbers and the 7 taxonomic templates are also labeled with the different colors respectively.







(continued).



(continued).

C. The elaborations of observation results for individual NEAs in this paper

Here are the elaborations of our results and some comparisons with the previous reports.

The C-D-X cluster

The C-D-X cluster shown in Fig. 3.a consists of non-silicate NEAs without evident spectral features of absorption bands. Our classifications in this cluster are described below as C-, D-, and X-complexes respectively.

The C-complex

There are six members in this group.

(7753) 1988 XB: It was classified as B-type in previous spectroscopic survey (Xu et al., 1995; Bus and Binzel, 2002; Binzel et al., 2004). Since the C-complex we defined here includes the B-type subgroup as well, our classification is consistent with the previous result.

(162566) 2000 RJ34: With  $B-V = 0.755 \pm 0.136$ ,  $V-R = 0.400 \pm 0.032$ , and  $R-I = 0.436 \pm 0.057$ , Ye (2011) classified this object to be X-type. We classified it to be C-type instead on the basis of the slope of the SED. It has a low albedo (0.07) according to the NEOWISE observations (Mainzer et al., 2011).

(249886) 2001 RY11: This is a new measurement. By assuming the average albedo ( $0.13 \pm 0.05$ ) of the C-complex (Thomas et al., 2011), the diameter can be estimated to be 1.01–1.56 km.

(276786) 2004 KD1: This is a new measurement. With the average albedo of the C-complex, its size is estimated to be 0.88–1.36 km.

(285263) 1998 QE2: It was recognized as a binary asteroid by radar imaging observation with an albedo of 0.06 (Springmann et al., 2014). Its color indices from Hicks et al. (2013a) are  $B-V = 0.706 \pm 0.013$ ,  $V-R = 0.353 \pm 0.008$ , and  $R-I = 0.374 \pm 0.006$ . These values are close to our results. Hicks et al. (2013b) identified this object to be of Ch-type.

2012 ER14: This is a new measurement. The slopes of this NEA are between those of the C- and X-complex. It is classified to be C-complex according to the decision tree (Fig. 4). Its size is 0.24–0.37 km from using an average albedo of  $0.13 \pm 0.5$ .

#### The X-complex

There are 12 NEAs in this group from our observations. It is noted that the X-type objects include those classified to be E-, M- and P-type by Tholen (1984). They have rather different albedo values, namely, E-type has the highest value  $\geq 0.3$ , M-type  $\sim 0.1$ –0.2 and P-type  $\leq 0.1$ .

(3554) Amun: It was classified to be M-type (Gradie and Tedesco, 1987), X-type (Somers et al. (2010)), and P-type (Thomas et al., 2014), respectively, in previous studies. It is basically in the CDX-cluster domain from our Lulin measurement. Mainzer et al., 2014 reported an albedo value of  $0.142 \pm 0.065$  from the NEOWISE observations. The D-type designation requiring very low albedo ( $\sim 0.07$ ) can be excluded. This object could therefore be classified as M-type.

(5731) Zeus: This is a new measurement. The albedo from the NEOWISE measurements is 0.031 (Mainzer et al., 2011). This object may belong to P-type, which has the lowest albedo by the Tholen classification scheme within the X-complex.

(7350) 1993 VA: Our taxonomic classification is consistent with the C- or X-type designation from the spectroscopic observations by Thomas et al. (2014). The albedo derived by NEOWISE is 0.05 (Mainzer et al., 2011). This means that 1993 VA is likely a P-type object.

(52762) 1998 MT24: Our photometric results are in agreement with the previous classification of X-type (Whiteley, 2001; Hicks et al., 2013c). The earlier photometry,  $B-V = 0.713 \pm 0.038$ ,  $V-R = 0.41 \pm 0.03$ , and  $R-I = 0.401 \pm 0.016$  (Hicks et al., 2013c) are also very close to ours. 1998 MT24 has a low albedo reported to be 0.052 (Pravec et al., 2012) from WISE thermal observations. It can be classified as P-type.

(88263) 2001 KQ1: This is a new measurement. The color indices from the Lulin observations have large error bars. On the basis of its spectral slopes and the decision tree, we classified it to be closer to the X-type than the C-type. This object has a low albedo of 0.048 from NEOWISE (Mainzer et al., 2011) and hence is likely to be a P-type.

(137805) 1999 YK5: It was previously classified to be X-type by SMASS II (Bus and Binzel, 2002) and RQ-type by photometry with color indices of  $B-V = 0.908 \pm 0.035$ ,  $V-R = 0.390 \pm 0.051$ , and  $R-I = 0.314 \pm 0.062$  (Ye, 2011). However, our results are very different from the latter work. The albedo of 0.027 from NEOWISE (Mainzer et al., 2011) is extremely low compared to the R/Q-type asteroids in the S-cluster. Therefore, 1999 YK5 could be likely of P-type in the X-complex.

(162004) 1991 VE: This is a new measurement. The situation is similar to (88263) 2001 KQ1 in that the spectral slope is between the X- and D-type. We assigned it to be the X-type on the basis of our selection criterion. Without an albedo measurement, it could vary between 0.02 and 0.75 as suggested for the X-complex (Thomas et al., 2011). This means that its size is between 0.46 and 2.83 km.

(326732) 2003 HB6: This is a new measurement. It has no albedo measurements. As a consequence, its size could be between 0.46 and 2.83 km because of the large variation in the albedo values of the X-type objects.

(333358) 2001 WN1: It was reported to be C-type with photometric colors,  $B-V = 0.703 \pm 0.044$ ,  $V-R = 0.402 \pm 0.023$ , and  $R-I = 0.336 \pm 0.012$  (Hicks and Dombroski, 2012). Although we classified 2001 WN1 to be X-complex, the spectral slope obtained by Hicks and Dombroski (2012) indicated that it could be Xc-type also. There is no albedo measurement, and its size is estimated to be 0.19–1.18 km as described above.

(340666) 2006 RO36: This is a new measurement. Its size is estimated to be 0.42–2.59 km as constrained by the albedo range of the X-type objects.

(411280) 2010 SL13: This is a new measurement. Its size is estimated to be 0.21–1.30 km as constrained by the albedo range of the X-type objects.

2013 SO10: Due to the lack of the V-R index, we can only use the other two color indices for its taxonomic classification. Its B-V index falls into the region of the C/D/X-cluster and it has a slightly higher slope at the red end. It is more likely to belong to the X-complex and the D-complex according to the priority setting scheme. In the absence of published albedo value, its size is estimated to be 0.07–0.41 km for an X-type object.

#### The D-complex

There are seven NEAs in this group.

(3360) Syrinx: This is a new measurement. The published albedo of 0.07 (Veeder et al., 1989) is consistent with our D-type classification.

(21088) Chelyabinsk: Previously spectroscopic observations indicated that it is SI-type (de Leon et al., 2010), A-type (Thomas et al., 2014). Photometric measurements by Ye (2011) assigned it to be S-type. The Lulin data showed that it could be a D-type NEA. It is noted that the B-V index is different that of the measurements of Ye (2011), perhaps because of our larger error bar in the B-band. The definite taxonomic classification would require future observations.

(24761) Ahau: It was previously classified to be S-type by photometric observations with  $B-V = 0.835 \pm 0.023$ ,  $V-R = 0.469 \pm 0.008$ , and  $R-I = 0.403 \pm 0.008$  (Ye, 2011), and also C/X-complex by NIR spectroscopic observations (Thomas et al., 2014). Our Lulin results agree with the second one since they belong to the same group of C/D/X-cluster. There is no albedo measurement. An average albedo value of  $0.02 \pm 0.01$  for the D-type objects (Thomas et al., 2011) would lead to a size of 2.30–4.61 km.

(85990) 1999 JV6: Bus and Binzel (2002) classified this object to be Xk-type according to the SMASS II database. Our designation of D-type is consistent with this previous result since they belong to the same C/D/X-cluster. The low albedo of 0.095 (Mainzer et al., 2011) is in agreement with the D-type classification also.

(249595) 1997 GH28: This is a new measurement. In lieu of published albedo values, its size is estimated to be 1.92–3.83 km.

2002 TY68: This is a new measurement. There is no albedo measurement either. By assuming the D-type mean albedo from Thomas et al. (2011), we estimated the diameter of this object to be 1.21–2.42 km.

2013 UH9: This is a new measurement. There is no published albedo value either. We estimated its size to be 1.27–2.53 km following the same procedure as before.

### The S-Cluster

The S-cluster shown in Fig. 3.a consists of the silicate NEAs with obvious absorption features, especially in the section of SED (I-band) approaching to 1  $\mu\text{m}$ . The S-complex and Q-complex objects, which are of similar compositions but differ in the level of space weathering effect together account for a majority of the NEA population. Hence we combined them as a larger group, namely, S/Q-group hereafter. We will have more analysis about S/Q-group in section 5. Our classifications are described below as S-, Q-, A-, V-complexes respectively.

### The S-complex

There are 34 NEAs in this group.

(1036) Ganymed: This large NEA of 30-km size was previously classified to be S-type by both photometric measurements (Velichko and Magnusson, 2012) and spectroscopic observations (Whiteley, 2001; Bus and Binzel, 2002; Binzel et al., 2004; Hicks et al., 2011; Fieber-Beyer et al., 2011). The color indices and taxonomic type are in excellent agreement with the Lulin results.

(1685) Toro: It was classified to be an S-type NEA by SMASS observations (Binzel et al., 2004) and photometric measurements by Rabinowitz (1998); Sq-type by DeMeo et al. (2014). The Lulin results are compatible with these earlier works.

(1943) Anteros: It was before classified to be L-type (Binzel et al., 2004), S-type (Thomas et al., 2011) and Sw-type (Thomas et al., 2014). Since our definition of the S-complex contains the Sw- and L-type (see Table 3), The Lulin results are compatible with these earlier works.

(4179) Toutatis: This NEA has many observational results, both by photometry and spectroscopy. It was classified to be S-type (Howell et al., 1994; Xu et al., 1995; Lupishko et al., 1995; Davies et al., 2007; Reddy et al., 2012b) and Sk-type (Binzel et al., 2004). These taxonomic classifications and the color indices reported by Rabinowitz (1998) are in accordance with our result.

(4487) Pocahontas: This is a new measurement. There is no albedo measurement. Taking the mean value of S-type albedo as  $0.26 \pm 0.03$  (Thomas et al., 2011), its size can be estimated to be about 0.80–0.92 km.

(8013) Gordonmoore: It was classified to be Sr-type by Lazzarin et al. (2010) which is in agreement with the Lulin results even though our data have large error bars. It has high spectral slope in the range of R-I bands. Nevertheless, the other two spectral slopes from B to R band are closer to those of the S-complex.

(10115) 1992 SK: It was classified to be a member of the S-complex (Binzel et al., 2004; DeMeo et al., 2014) and Sq-type (Thomas et al., 2014). Our Lulin results are compatible with these previous results.

(11284) Belenus: Hicks et al. (2013d) classified this object to be S-type with color indices:  $B0V = 0.897 \pm 0.165$ ;  $V-R = 0.47 \pm 0.052$  and  $R-I = 0.33 \pm 0.014$ . The R-I index of Hicks et al. (2013d) has a small difference from the Lulin value, but the taxonomic type is in general agreement with each other. With a nominal S-type albedo, its size can be estimated to be 0.58–0.67 km.

(12923) Zephyr: It was previously classified to be S-type (Binzel et al., 2004; Thomas et al., 2014). Although our measurements of its color indices have large error bars, we can still classify it as S-complex following our decision tree.

(17188) 1999 WC2: This is a new measurement.

(25916) 2001 CP44: It was classified to be Sq/Q-type by NIR spectroscopy before (Thomas et al., 2014). Our results showed slightly different classification, but they basically belong to the same S/Q-group.

(40267) 1999 GJ4: It was previously reported to be Sq-type (Binzel et al., 2004) which is not too different from our S-complex classification and still in the same S/Q-group.

(53435) 1999 VM40: It was classified to be S-type (Binzel et al., 2004) and Srw-type (Thomas et al., 2014), which are all parts of the S-complex in agreement with our classification.

(68031) 2000 YK29: This is a new measurement. With a nominal S-type albedo, its size can be estimated to be 0.58–0.67 km.

(68216) 2001 CV26: It has the near-infrared spectroscopic observation (Reddy, 2010). It was previously classified to be R-type by Ye (2011), Sq-type by Thomas et al. (2014) and S-complex by DeMeo et al. (2014). The previous two are different from our S-complex designation here, yet they are all parts of the S-cluster.

(89355) 2001 VS78: It was previously classified to be S-type (Binzel et al., 2004) and Sr-type (Thomas et al., 2014). They are both compatible with our S-complex designation.

(90075) 2002 VU94: This is a new measurement. The spectral slopes from the Lulin observations are intermediate between the D- and S-type. The S-complex classification is supported by the albedo value of 0.197 determined by NEOWISE (Nugent et al., 2015).

(99942) Apophis: This famous PHA was detected to be Sq-type by Binzel et al. (2009). It is generally in agreement with our results. The detected albedo is about 0.3 (Mu"ller et al., 2014).

(136900) 1998 HL49: This is a new measurement. With a nominal S-type albedo, its size can be estimated to be 0.84–0.96 km.

(154347) 2002 XK4: This object was previously observed by NIR spectroscopy and classified to be S-complex (Lazzarin et al., 2010). With a nominal S-type albedo, its size can be estimated to be 1.5–1.8 km.

(215188) 2000 NM: It was previously classified to be Sr-type by spectroscopy (Binzel et al., 2004) and R-type by photometry (Dandy et al., 2003).

(219071) 1997 US9: We only have two color indices of B-V and V-I for this NEA. Its hyper-reddish end of the I band probably indicates a spectral signature of the A-type asteroids, but the B-V slope is more like that of the S-complex. Our S-complex classification is in line with the S-type designation by Whiteley (2001) and Q-type (Binzel et al., 2004; Thomas et al., 2014; DeMeo et al., 2014).

(262623) 2006 WY2: This is a new measurement. We only measured two color indices, namely, B-V and V-I, of this NEA. Without the V-R slope we could still approximately classify it to be of S-complex because of the trends of the other two slopes.

(294739) 2008 CM: This is a new measurement. With a nominal S-type albedo, its size can be estimated to be 0.84–0.96 km.

(329338) 2001 JW2: This is a new measurement. With a nominal S-type albedo, its size can be estimated to be 0.36–0.42 km.

(330825) 2008 XE3: This potentially binary NEA was classified to be S-type by photometric observations (Hicks et al., 2012a). The reported color indices are similar to our Lulin results and the classifications are identical. With a nominal S-type albedo, its size can be estimated to be 1.33–1.52 km.

(339492) 2005 GQ21: This is a new measurement. With a nominal S-type albedo, its size can be estimated to be 0.56–0.64 km.

(339714) 2005 ST1: This is a new measurement. With a nominal S-type albedo, its size can be estimated to be 0.20–0.23 km.

(343098) 2009 DV42: The R-I slope is similar to the reddish feature of the A-type objects. However, the overall SED trends fit better with those of the S-complex according to the decision tree (see Fig. 4). Both of the taxonomic type and albedo have not been investigated before. With a nominal S-type albedo, its size can be estimated to be 0.44–0.50 km.

(349068) 2006 YT13: It was classified to be A/R-type by photometry, with  $B-V = 1.042 \pm 0.088$  and  $V-R = 0.475 \pm 0.057$  (Ye, 2011). These color indices are somewhat different from the Lulin results even though they are consistent with our S-cluster classification. With a nominal S-type albedo, its size can be estimated to be 0.53–0.61 km.

(355256) 2007 KN4: This is a new measurement. The corresponding SED has rather large error bars and the B-V slope is higher than that of the D-complex but similar to the S-complex value. We designated two possible taxonomic types with the S-type to be followed by the D-type. It is interesting to note that 2007 KN4 is the only object in our sample with the Jovian Tisserand parameter ( $T_J = 2.77$ ) being less than 3.0. This means that this NEA could be an extinct comet (Carusi et al., 1987). We would need more observations in future to determine whether this object should be classified as D-type instead as appropriate to a cometary nucleus. For the present moment, with a nominal S-type albedo, its size can be estimated to be 1.06–1.21 km.

(356394) 2010 QD2: This is a new measurement. With a nominal S-type albedo, its size can be estimated to be 0.80–0.92 km.

(378610) 2008 FT6: This is a new measurement. With a nominal S-type albedo, its size can be estimated to be 0.80–0.92 km.

2011 WV134: Previous photometric observations indicated that it is an S-type (Hicks et al., 2012b) in agreement with our Lulin result. With a nominal S-type albedo, its size can be estimated to be 0.88–1.01 km.

### The Q-complex

There are 24 NEAs in this group.

(1627) Ivar: It was previously classified to be S-type by spectroscopic observations (Bus and Binzel, 2002; Binzel et al., 2004; Davies et al., 2007) and photometry, with  $B-V = 0.80 \pm 0.02$ ,  $V-R = 0.45 \pm 0.01$ , and  $R-I = 0.34 \pm 0.01$  (Hahn et al., 1989; Velichko and Rikhteghar, 2011). These color indices are similar to the Lulin results. However, our classification is slightly different.

(2100) Ra-Shalom: It was classified to be K-type (Shepard et al., 2008), Sr-type (Harris et al., 1998), and C-type (Binzel et al., 2004), which are very different from our present classification. Its SED in the Figure of Appendix B shows that the spectral slope of B-V is flatter and similar to that of the C-/X-complex. On the other hand, the slopes from V to I band are close to those of the Q-complex with absorption feature near 1  $\mu\text{m}$ .

(4450) Pan: It was classified to be S-type by photometric observations with

$B-V = 0.82 \pm 0.02$ ,  $V-R = 0.48 \pm 0.02$  and  $R-I = 0.28 \pm 0.02$  (Carbognani, 2008) and S/Sr-type by spectroscopy (Perna et al., 2016). Our classification is different but in the general S/Q-group. There is no albedo measurement. With a nominal Q-type albedo of  $0.29 \pm 0.03$  (Thomas et al., 2011), its size can be estimated to be 0.9–1.1 km.

(6047) 1991 TB1: This NEA was classified to be S-type before (Binzel et al., 2004; DeMeo et al., 2009; Thomas et al., 2014). In the Lulin measurements, the R-I spectral slope is better fit by the Q-complex value.

(22753) 1998 WT: It was classified to be Q-type (Whiteley, 2001) and Sq-type (Thomas et al., 2014). They are both consistent with our result.

(137062) 1998 WM: It was classified to be Sq-type (Binzel et al., 2004; Thomas et al., 2014) and Q-type (DeMeo et al., 2014). They are both consistent with our result.

(137199) 1999 KX4: It was classified to be Sq-type by spectroscopy (Hicks et al., 2013b). With a nominal Q-type albedo, its size can be estimated to be 1.0–1.2 km.

(141052) 2001 XR1: Our result is consistent with the taxonomic identification of Sq-type by Binzel et al. (2004) and Thomas et al. (2011).

(141484) 2002 DB4: It was classified to be S-type (Michelsen et al., 2006) and S-complex (Lazzarin et al., 2010). There is no albedo measurement. With a nominal Q-type albedo, its size can be estimated to be 1.2–1.5 km.

(152889) 2000 CF59: This is a new measurement.

(163364) 2002 OD20: It was reported to be Sq-type by Hicks et al. (2013b). With a nominal Q-type albedo, its size can be estimated to be 0.4–0.5 km.

(168378) 1997 ET30: This is a new measurement. With a nominal Q-type albedo, its size can be estimated to be 1.04–1.24 km.

(214869) 2007 PA8: It was classified to be Q-type (Kuroda et al., 2014; Fornasier et al., 2015; Sanchez et al., 2015; Perna et al., 2016), S-type (Godunova et al., 2013), and Xc-type by broad-band photometry (Hicks et al., 2012c). The albedo was detected to be  $0.29 \pm 0.14$  (Brozović et al., 2017).

(230111) 2001 BE10: It was classified to be S-complex by spectroscopic observation (DeMeo et al., 2014) and R-type by photometry (Ye, 2011) with color indices:  $B-V = 0.956 \pm 0.087$ ,  $V-R = 0.458 \pm 0.035$  and  $R-I = 0.412 \pm 0.101$ . These identifications together with our Lulin result are basically in the S-cluster.

(276397) 2002 XA40: This is a new measurement. With a nominal Q-type albedo, its size can be estimated to be 0.91–1.08 km.

(277127) 2005 GW119: It was classified to be Sq-type (Ieva et al., 2014) in accordance with our result. With a nominal Q-type albedo, its size can be estimated to be 0.43–0.52 km.

(297274) 1996 SK: It was identified to be S-type with apparent rotational color variability by Lin et al. (2014). Our present Lulin measurement showed that its spectral slope is intermediate between S-type and Q-type thus indicating that this NEA probably has inhomogeneous surface composition as reported before. We classified 1996 SK with the first taxonomic type to be Q-complex and second to be S-complex according to the decision tree (see Fig. 4). With a nominal Q-type albedo, its size can be estimated to be 1.09–1.3 km.

(341816) 2007 YK: This is a new measurement. With a nominal Q-type albedo, its size can be estimated to be 0.76–0.9 km.

(361071) 2006 AO4: This is a new measurement. With a nominal Q-type albedo, its size can be estimated to be 1.98–2.36 km.

(363790) 2005 JE46: It was classified to be C/X/D-complex by spectroscopic observations (Thomas et al., 2014). The spectral slopes between B to R in Figure of Appendix B are indeed similar to those of the X-complex, but the R-I slope is more like that of the Q-complex. With a nominal Q-type albedo, its size can be estimated to be 0.69–0.82 km.

(441825) 2009 SK1: This is a new measurement. With a nominal Q-type albedo, its size can be estimated to be 0.52–0.62 km.

2005 RQ6: It was previously classified to be S/Sr-type (DeMeo et al., 2014) in the same S/Q-group as our identification. With a nominal Q-type albedo, its size can be estimated to be 0.4–0.47 km.

2010 TN54: This is a new measurement. With a nominal Q-type albedo, its size can be estimated to be 0.35–0.41 km.

2010 XZ67: This is a new measurement. The V-R color index is missing. The taxonomic characterization can be done by consideration of the partial SED which is more likely to be Q-complex than the V-complex. With a nominal Q-type albedo, its size can be estimated to be 0.27–0.32 km.

### The A-complex

There are three NEAs in this group.

(4954) Eric: It was classified to be S-type by both photometry (Rabinowitz, 1998) and SMASS observations (Binzel et al., 2004). Yet our Lulin measurements indicated that its spectral slopes with reddening feature close to the A-complex slopes. However, according to Gietzen et al. (2012), the NIR spectra of 4954 Eric exhibits an absorption feature at 2 micron indicating the presence of clinopyroxene. Because A-type does not have the pyroxene absorption band, the classification here might be wrong and this NEA should be classified as S-type.

(11405) 1999 CV3: It was classified to be Sq-type by SMASS database. But the Lulin result showed that it is close to A-complex.

(354722) 2007 EG29: This is a new measurement.

### The V-complex

Some of the V-type NEAs are supposed to be small members of the Vesta family got transported into the orbital region of the terrestrial planets. Their spectral slopes between B to R are similar to those of the S-complex. But there is a significant descending slope between the R and I band because of a deeper absorption feature close to 1  $\mu\text{m}$ . There are six objects in this group from our Lulin observations.

(4055) Magellan: It was classified to be V-type by several spectroscopic observations (Cruikshank et al., 1991; Binzel et al., 2004; Whiteley, 2001; Sanchez et al., 2013; Thomas et al., 2014). We have exactly the same classification. The albedo was detected to be about 0.33 (Delbo et al., 2003) (55532) 2001 WG2: It was classified to be Sk-type by SMASS observations (Binzel et al., 2004). This is different from our identification though in the same S-cluster.

(152756) 1999 JV3: It was classified to be S-type (Binzel et al., 2004) and Sa-type (Hicks et al., 2013b). They are both different from our identification though in the same S-cluster.

(163249) 2002 GT: It was classified to be Sq-type by spectroscopic observation (Hicks et al., 2013b). Its spectral slopes between V to I are intermediate between the S- and Q-type, but that of B-V is more similar to the V-type. With the nominal albedo of  $0.42 \pm 0.11$  (Thomas et al., 2011) for the V-type NEAs, its size can be estimated to be 0.37–0.5 km.

(334412) 2002 EZ2: Our Lulin measurements have relatively large error bars, but the SED is close to that of the V-complex. In addition, the detected albedo of 0.4 by the warm Spitzer survey (Thrilling et al., 2010) is close to the mean albedo of the V-type NEAs (Thomas et al., 2011).

(389694) 2011 QD48: This is a new measurement. With the nominal albedo of the V-type asteroids, its size can be estimated to be 0.41–0.55 km.

## References

- Bertini, I., 2011. Main Belt Comets: a new class of small bodies in the solar system. *Planet. Space Sci.* 59, 365–377.
- Binzel, R.P., et al., 2002. Physical Properties of Near-earth Objects. In: *Asteroids III*. Univ. of Arizona press, p. 255.
- Binzel, R.P., et al., 2004. Observed spectral properties of near-Earth objects: results for population distribution, source regions, and space weathering processes. *Icarus* 170, 259–294.
- Binzel, R.P., et al., 2009. Spectral properties and composition of potentially hazardous Asteroid (99942). *Apophis*. *Icarus* 200, 480–485.
- Binzel, R.P., et al., 2010. Earth encounters as the origin of fresh surfaces on near-Earth asteroids. *Nature* 463, 331–334.
- Bottke, W.F., et al., 2002. Debiased orbital and absolute magnitude distribution of the near-Earth objects. *Icarus* 156, 399–433.
- Brozović, M., et al., 2017. Goldstone radar evidence for short-axis mode non-principal-axis rotation of near-Earth asteroid (214869) 2007 PA8. *Icarus* 286, 314–329.
- Brunetto, R., et al., 2006. Modeling asteroid surfaces from observations and irradiation experiments: the case of 832 Karin. *Icarus* 184, 327–337.
- Brunetto, R., et al., 2015. Asteroid Surface Alteration by Space Weathering Processes. *Asteroid IV*. University of Arizona Press, pp. 597–616.
- Bus, S.J., 1999. Compositional Structure in the Asteroid Belt: results of a Spectroscopic Survey. PhD. Thesis.
- Bus, S.J., Binzel, R.P., 2002. Phase II of the small main-belt asteroid spectroscopic survey. A feature-based taxonomy. *Icarus* 158, 146–177.
- Carbognani, A., 2008. MPB. Light Curve Photometry of NEAs 4450 PAN, (170891) 2004 TY16, 2002 RC118, and 2007 VD12; 2006NM, 35, pp. 109–110.
- Carry, B., et al., 2016. Spectral properties of near-Earth and Mars-crossing asteroids using Sloan photometry. *Icarus* 268, 340–354.
- Carusi, A., et al., 1987. High-order librations of Halley-type comets. *Astron. Astrophys.* 187, 899–905.
- Clark, B.E., et al., 2002. NEAR infrared spectrometer photometry of asteroid 433 Eros. *Icarus* 155, 189–204.
- Cruikshank, D.P., et al., 1991. Three basaltic earth-approaching asteroids and the source of the basaltic meteorites. *Icarus* 89, 1–13.
- Dandy, C.L., Fitzsimmons, A., Collander-Brown, S.J., 2003. Optical colors of 56 near-Earth objects: trends with size and orbit. *Icarus* 163, 363–373.
- Davies, J.K., et al., 2007. Near-infrared spectra of 12 near-Earth objects. *Icarus* 186, 111–125.
- de Leo'n, L., et al., 2010. Observations, compositional, and physical characterization of near-Earth and Mars-crosser asteroids from a spectroscopic survey. *Astron. Astrophys.* 517, A23.
- Delbo, M., et al., 2003. Keck observations of near-Earth asteroids in the thermal infrared. *Icarus* 166, 116–130, 4055 albedo.
- DeMeo, F.E., Carry, B., 2013. The taxonomic distribution of asteroids from multifilter all-sky photometric surveys. *Icarus* 226, 723–741.
- DeMeo, F.E., Carry, B., 2014. Solar System evolution from compositional mapping of the asteroid belt. *Nature* 505, 629–634.
- DeMeo, F.E., et al., 2009. An extension of the Bus asteroid taxonomy into the near infrared. *Icarus* 202, 160–180.
- DeMeo, F.E., Binzel, R.P., Lockhart, M., 2014. Mars encounters cause fresh surfaces on some near-Earth asteroids. *Icarus* 227, 112–122.
- Fieber-Beyer, S.K., Gaffey, M.J., Abell, P.A., 2011. Mineralogical characterization of near-Earth asteroid (1036). *Ganymed*. *Icarus* 212, 149–157.
- Fornasier, S., et al., 2015. The potentially hazardous asteroid (214869) 2007 PA8: an unweathered L chondrite analogue surface. *Icarus* 250, 280–286.
- Gietzen, K.M., 2009. Near Infrared Spectral Data for 27 Asteroids: an Investigation of Meteorite-asteroid Relationships by Using the Modified Gaussian Method. PhD thesis. University of Arkansas.
- Gietzen, K.M., et al., 2012. IRTF observations of S complex and other asteroids: implications for surface compositions, the presence of clinopyroxenes, and their relationship to meteorites. *Meteor. Planet. Sci.* 47, 1789.
- Godunova, V., et al., 2013. Spectrophotometric studies of near-Earth asteroids at the Terskol Observatory. EGU2013-13797-1 (Abstract).
- Gradie, J.C., Tedesco, E.F., 1987. 1986 DA and 1986 EB: iron objects in near-earth orbits. *Lun. Plant. Sci. Con* 18, 349.
- Granvik, M., et al., 2016. Super-catastrophic disruption of asteroids at small perihelion distances. *Nature* 530, 303–306.
- Graves, K., et al., 2016. Size and Perihelion Distribution of S and Q-type Asteroid Spectral Slopes from the Near Earth Region through the Main Belt. DPS Meeting. #48, id. 510.09.
- Greenstreet, et al., 2012. The orbital distribution of Near-Earth Objects inside Earth's orbit. *Icarus* 217, 355–366.
- Hahn, G., et al., 1989. Physical studies of Apollo-Amor asteroids - UBVRI photometry of 1036 Ganymed and 1627 Ivar. *Icarus* 78, 363–381.
- Harris, A.W., et al., 1998. Thermal infrared spectrophotometry of the near-earth asteroids 2100 Ra-Shalom and 1991 EE. *Icarus* 135, 441–450.
- Hicks, M., Dombroski, D., 2012. Physical characterization of (333358) 2001 WN1: a large, possibly water-rich, low delta-V near-Earth asteroid. *The Astron. Tel.* 4623.
- Hicks, M., Ebelhar, S., 2013a. Broadband photometry of the large potentially hazardous asteroid 138095 (2000 DK79). *The Astron. Tel.* 5591.
- Hicks, M., Ebelhar, S., 2013b. Broadband photometry of the potentially hazardous asteroid 2013 RH74. *The Astron. Tel.* 5562.
- Hicks, M., Ebelhar, S., 2014a. Broad-band photometry of the potentially hazardous asteroid 2006 DP14. *The Astron. Tel.* 5928.
- Hicks, M., Ebelhar, S., 2014b. Broadband photometry of the potentially hazardous asteroid 251346 (2007 SJ). *The Astron. Tel.* 5801.
- Hicks, M., et al., 2011. Palomar spectroscopy of near-earth asteroids 2004 SV55, 2000 SP43, 1986 LA, 1036 Ganymed, and 2002 AG29. *The Astron. Tel.* 3678.
- Hicks, M., et al., 2012a. Broadband photometry 330825 (2008 XE3): a potential binary near-earth asteroid. *The Astron. Tel.* 4591.
- Hicks, M., et al., 2012b. Physical characterization of the potentially hazardous asteroid 2011 WV134. *The Astron. Tel.* 4251.

- Hicks, M., et al., 2012c. Broadband photometry of 214869 (2007 PA8): a slowly rotating potentially hazardous asteroid. *The Astron. Tel.* 4625.
- Hicks, M., et al., 2012d. Broadband photometry of the near-earth asteroid 136993 (1998 ST49). *The Astron. Tel.* 4588.
- Hicks, M., et al., 2012e. Broadband photometry of the potentially hazardous asteroid 329614 (2003 KU2). *The Astron. Tel.* 4262.
- Hicks, M., et al., 2012f. Broadband photometry of 2012 LZ1: a large, dark potentially hazardous asteroid. *The Astron. Tel.* 4252.
- Hicks, M., et al., 2012g. Broadband photometry of 2007 LE: a binary near-earth asteroid. *The Astron. Tel.* 4188.
- Hicks, M., et al., 2012h. Optical photometry of 2012 EG5: constraints on taxonomy and spin rate. *The Astron. Tel.* 4016.
- Hicks, M., et al., 2013a. BVRI photometry of the potentially hazardous asteroid 285263 (1998 QE2). *The Astron. Tel.* 5121.
- Hicks, M., et al., 2013b. Palomar spectroscopy of near-earth asteroids 137199 (1999 KX4), 152756 (1999 JV3), 163249 (2002 GT), 163 364 (2002 OD20), and 285263 (1998 QE2). *The Astron. Tel.* 5132.
- Hicks, M., et al., 2013c. Broad-band photometry of 52762 (1998 MT24). *The Astron. Tel.* 5306.
- Hicks, M., et al., 2013d. Broadband photometry of 11284 Belenus: a large low delta-V near-Earth asteroid. *The Astron. Tel.* 4969.
- Hicks, M., et al., 2013e. Broadband photometry of the potentially asteroid 277475 (2005 WK4) and corrected 52762 (1998 MT24) colors. *The Astron. Tel.* 5311.
- Hicks, M., et al., 2014a. Broad-band photometry of the near-earth asteroid 2014 CR. *The Astron. Tel.* 5955.
- Hicks, M., et al., 2014b. Broad-band photometry of NHATS target 387733 (2003 GS). *The Astron. Tel.* 6090.
- Howell, E.S., et al., 1994. Visible and near-infrared spectral observations of 4179 Toutatis. *Icarus* 111, 468–474.
- Hsieh, H.H., Jewit, D., 2006. A population of comets in the Main Asteroid Belt. *Science* 312, 561.
- Ieva, S., et al., 2014. Low Delta-V Near-Earth Asteroids: a survey of suitable targets for space missions. *Astron. Astrophys.* 569, A59.
- Ishiguro, M., et al., 2007. Global mapping of the degree of space weathering on asteroid 25143 Itokawa by Hayabusa/AMICA observations. *Meteoritics Planet. Sci.* 42, 1791–1800.
- Ivezic, Z., et al., 2001. AJ. Solar System Objects Observed in the Sloan Digital Sky Survey Commissioning Data, 122, pp. 2749–2784.
- Jacobson, S.A., Scheeres, D.J., 2011. Dynamics of rotationally fissioned asteroids: source of observed small asteroid systems. *Icarus* 214, 161–178.
- Jones, T.D., et al., 1990. The composition and origin of the C, P, and D asteroids - water as a tracer of thermal evolution in the outer belt. *Icarus* 88, 172–192.
- Kuroda, D., et al., 2014. Visible-wavelength spectroscopy of subkilometer-sized near-Earth asteroids with a low delta-v. *PAJ* 66, 51.
- Landolt, A.U., 1992. UBVR photometry standard stars in the magnitude range  $11.5 < V < 16.0$  around the celestial equator. *Astron. J.* 104, 340–371.
- Lang, D., et al., 2010. Astrometry.net: blind astrometric calibration of arbitrary astronomical images. *Astron. J.* 139, 1782–1800.
- Lazzarin, M., et al., 2005. Spectroscopic investigation of near-earth objects at telescopio nazionale Galileo. *Mon. Not. R. Astron. Soc.* 359, 1575–1582.
- Lazzarin, M., Marchi, S., Magrin, S., 2010. Spectroscopic Investigation of Near-earth Objects. SINEO Database.
- Lazzaro, D., et al., 2004. S3OS2: the visible spectroscopic survey of 820 asteroids. *Icarus* 172, 179–220.
- Lim, L.F., et al., 2012. The near-earth encounter of asteroid 308635 (2005 YU55). In: Thermal IR Observations. AAS 2012 DPS Meeting. #44, id.305.01L.
- Lin, C.-H., et al., 2014. Detection of large color variation of potentially hazardous asteroid (297274) 1996 SK. *Res. Astron. Astrophys.* 14, 311.
- Lin, H.-W., et al., 2015. A search for subkilometer-sized ordinary chondrite like asteroids in the main-belt. *Icarus* 254, 202–212.
- Lupishko, D.F., et al., 1995. UBVR-polarimetry of asteroid 4179 Toutatis. *Icarus* 113, 200–205.
- Mainzer, A., et al., 2011. Preliminary results from NEOWISE: an enhancement to the wide-field infrared survey explorer for solar system science. *Astron. Astrophys. J.* 731, 53M.
- Mainzer, A., et al., 2014. Initial performance of the NEOWISE reactivation mission (prel.diameters & albedos for 61 NEOs. *Astron. Astrophys. J.* 792, 30.
- Michelsen, R., et al., 2006. Spectroscopy of near-Earth asteroids. *Astron. Astrophys.* 451, 331–337.
- Morbidelli, A., Vokrouhlický, D., 2003. The Yarkovsky-driven origin of near-Earth asteroids. *Icarus* 163, 120–134.
- Müller, T.G., et al., 2014. Thermal infrared observations of asteroid (99942) Apophis with herchel. *Astron. Astrophys.* 566, A22.
- Nakamura, T., et al., 2011. Itokawa dust particles: a direct link between S-Type asteroids and ordinary chondrites. *Science* 333, 1113.
- Nesvorný, D., et al., 2010. Do planetary encounters reset surfaces of near Earth asteroids? *Icarus* 209, 510–519.
- Nichols, C.R., 1993. Volatile Products from Carbonaceous Asteroids. In Resources of Near-earth Space, Part III. No. 21. University of Arizona Press.
- Nugent, C.R., et al., 2015. NEOWISE reactivation mission year one: preliminary asteroid diameters and albedos. *Astrophys. J.* 814, 117, 13 pp.
- Perna, D., et al., 2016. Grasping the nature of potentially hazardous asteroids. *Astron. J.* 151, 11, 14pp.
- Polishook, D., et al., 2014. Observations of fresh and weathered surfaces on asteroid pairs and their implications on the rotational-fission mechanism. *Icarus* 233, 9–26.
- Popescu, M., et al., 2014. Spectral properties of the largest asteroids associated with Taurid Complex. *A&A* 572, A106.
- Pravec, P., et al., 2012. Absolute magnitudes of asteroids and a revision of asteroid albedo estimates from WISE thermal observations. *Icarus* 221, 365–387.
- Rabinowitz, D.L., 1998. Size and orbit dependent trends in the reflectance colors of earth-approaching asteroids. *Icarus* 134, 342–346.
- Rayner, J.T., et al., 2003. SpeX: a Medium-resolution 0.8-5.5 Micron Spectrograph and Imager for the NASA Infrared Telescope Facility, vol 115. *PASP*, p. 362.
- Reddy, V., 2010. IRTF Near-earth Asteroid Spectra V1.0, NASA Planetary Data System, EAR-A-10046-5-REDDYSPEC-V1.0.
- Reddy, V., et al., 2012a. Composition of near-Earth Asteroid 2008 EV5: potential target for robotic and human exploration. *Icarus* 221, 678–681.
- Reddy, V., et al., 2012b. Composition of near-earth asteroid (4179) Toutatis. *Icarus* 221, 1177–1179.
- Rivkin, A.S., 2006. An introduction to near-earth objects. *Johns Hopkins APL Technical Digest* 27 (No. 2).
- Rubincam, D.P., 2000. Radiative spin-up and spin-down of small asteroids. *Icarus* 148, 2–11.
- Sanchez, J.A., Michelsen, R., Reddy, V., Nathues, A., 2013. Surface composition and taxonomic classification of a group near-Earth and Mars-crossing asteroids. *Icarus* 225 (Iss. 1), 131–140.
- Sanchez, J.A., Reddy, V., Dykhus, M., Lindsay, S., Le Corre, L., 2015. Composition of potentially hazardous asteroid (214869) 2007 PA8: an H chondrite from outer asteroid belt. *Astrophys. J.* 808, 93.
- Scheeres, D.J., 2015. Landslides and Mass shedding on spinning spheroidal asteroids. *Icarus* 247, 1–17.
- Shepard, M.K., et al., 2008. Multi-wavelength observations of asteroid 2100 Ra-Shalom. *Icarus* 193, 20–38.
- Somers, J.M., et al., 2010. Optical characterization of planetary radar targets, low-delta-V, and potentially hazardous asteroids: results from 2009-2010. *DPS* 42, 1316.
- Springmann, A., et al., 2014. Radar derived shape model of binary near-earth asteroids (285263) 1998 QE2. *Lun. Plant. Sci. Con* 45, 1313.
- Stuart, J.S., Binzel, R.P., 2004. Bias-corrected population, size distribution, and impact hazard for the near-Earth objects. *Icarus* 170, 295–311.
- Tholen, D.J., 1984. Asteroid Taxonomy from Cluster Analysis of Photometry (Ph.D. Thesis).
- Thomas, C.A., et al., 2011. ExploreNEOs. V. Average albedo by taxonomic complex in the near-earth asteroid population. *Astron. J.* 142, 85, 12pp.
- Thomas, C.A., et al., 2014. Physical characterization of Warm Spitzer-observed near-Earth objects. *Icarus* 228, 217–246.
- Thrilling, D.E., et al., 2010. EXPLORENEOs. I. Description and first results from the warm spitzer near-earth object survey. *Astron. J.* 140, 770–784.
- Tubiana, C., et al., 2015. A&A. 2P/Encke, the Taurid Complex NEOs and the Maribo and Sutter's Mill Meteorites, vol 584, p. A97.
- Veeder, G.J., et al., 1989. Radiometry of near-Earth asteroids. *Astron. J.* 97, 1211–1219.
- Velichko, F.P., Magnusson, P., 2012. Photometry and polarimetry of the largest NEA 1036 Ganymed. *Astron. Tsirk.* 1575.
- Velichko, F.P., Rikhteghar, A., 2011. Light curves, colours and magnitude phase dependences of the asteroids 433 Eros and 1627 Ivar. *Astronomy* 47, 41–43.
- Vernazza, P., et al., 2008. Composition differences between meteorites and near-Earth asteroids. *Nature* 454, 858–860.
- Volquardsen, E.L., 2007. Composition of hydrated near-Earth object (100085) 1992 UY4. *Icarus* 187, 464–468.
- Walsh, K.J., Richardson, D.C., Michel, P., 2012. Spin-up of rubble-pile asteroids: disruption, satellite formation, and equilibrium shapes. *Icarus* 220, 514–529.
- Whiteley, R.J., 2001. A Compositional and Dynamical Survey of the Near-earth Asteroids. Ph.D. Thesis. University of Hawaii.
- Xu, S., et al., 1995. Small main-belt asteroid spectroscopic survey: initial results. *Icarus* 115 (no. 1), 1–35.
- Ye, Q.-Z., 2011. BVRI photometry of 53 unusual asteroids. *Astron. J.* 141, 32, 8pp.



# The Bright $\gamma$ -ray Flare of 3C 279 in 2015 June: *AGILE* Detection and Multifrequency Follow-up Observations

C. Pittori<sup>1,2</sup> , F. Lucarelli<sup>1,2</sup> , F. Verrecchia<sup>1,2</sup> , C. M. Raiteri<sup>3</sup> , M. Villata<sup>3</sup>, V. Vittorini<sup>4</sup> , M. Tavani<sup>4,5,6</sup> , S. Puccetti<sup>7</sup> , M. Perri<sup>1,8</sup>, I. Donnarumma<sup>4,7</sup>, S. Vercellone<sup>9</sup> , J. A. Acosta-Pulido<sup>10,11</sup>, R. Bachev<sup>12</sup>, E. Benítez<sup>13</sup>, G. A. Borman<sup>14</sup>, M. I. Carnerero<sup>3</sup>, D. Carosati<sup>15,16</sup>, W. P. Chen<sup>17</sup>, Sh. A. Ehgamberdiev<sup>18</sup>, A. Goded<sup>10,11</sup>, T. S. Grishina<sup>19</sup>, D. Hiriart<sup>20</sup>, H. Y. Hsiao<sup>17</sup>, S. G. Jorstad<sup>21,22</sup>, G. N. Kimeridze<sup>23</sup>, E. N. Kopatskaya<sup>19</sup>, O. M. Kurtanidze<sup>23,24</sup>, S. O. Kurtanidze<sup>23</sup>, V. M. Larionov<sup>19,25</sup>, L. V. Larionova<sup>19</sup>, A. P. Marscher<sup>21</sup>, D. O. Mirzaqulov<sup>18</sup>, D. A. Morozova<sup>19</sup>, K. Nilsson<sup>26</sup>, M. R. Samal<sup>17</sup>, L. A. Sigua<sup>23</sup>, B. Spassov<sup>12</sup>, A. Strigachev<sup>12</sup>, L. O. Takalo<sup>27</sup>, L. A. Antonelli<sup>1</sup>, A. Bulgarelli<sup>28</sup>, P. Cattaneo<sup>29</sup>, S. Colafrancesco<sup>30</sup>, P. Giommi<sup>7</sup>, F. Longo<sup>31</sup>, A. Morselli<sup>32</sup> , and F. Paoletti<sup>4,33</sup>

<sup>1</sup> ASI Space Science Data Center (SSDC), Via del Politecnico snc, I-00133 Roma, Italy; [carlotta.pittori@ssdc.asi.it](mailto:carlotta.pittori@ssdc.asi.it)

<sup>2</sup> INAF, Osservatorio Astronomico di Roma, via Frascati 33, I-00078 Monte Porzio Catone (Roma), Italy

<sup>3</sup> INAF, Osservatorio Astrofisico di Torino, via Osservatorio 20, I-10025 Pino Torinese, Italy

<sup>4</sup> INAF/IAPS–Roma, Via del Fosso del Cavaliere 100, I-00133 Roma, Italy

<sup>5</sup> Univ. “Tor Vergata”, Via della Ricerca Scientifica 1, I-00133 Roma, Italy

<sup>6</sup> Gran Sasso Science Institute, viale Francesco Crispi 7, I-67100 L’Aquila, Italy

<sup>7</sup> Agenzia Spaziale Italiana (ASI), Via del Politecnico snc, I-00133 Roma, Italy

<sup>8</sup> INAF–OAR, via Frascati 33, I-00078 Monte Porzio Catone (Roma), Italy

<sup>9</sup> INAF, Osservatorio Astronomico di Brera, Via E. Bianchi 46, I-23807 Merate (LC), Italy

<sup>10</sup> Instituto de Astrofísica de Canarias (IAC), E-38205 La Laguna, Tenerife, Spain

<sup>11</sup> Departamento de Astrofísica, Universidad de La Laguna, E-38206 La Laguna, Tenerife, Spain

<sup>12</sup> Institute of Astronomy and National Astronomical Observatory, Bulgarian Academy of Sciences,

72 Tsarigradsko shosse Boulevard, 1784 Sofia, Bulgaria

<sup>13</sup> Instituto de Astronomía, Universidad Nacional Autónoma de México, Apdo. Postal 70-264, 04510 Cd. de México, Mexico

<sup>14</sup> Crimean Astrophysical Observatory, P/O Nauchny, 298409, Russia

<sup>15</sup> EPT Observatories, Tjarafe, E-38780 La Palma, Spain

<sup>16</sup> INAF, TNG Fundación Galileo Galilei, E-38712 La Palma, Spain

<sup>17</sup> Graduate Institute of Astronomy, National Central University, Jhongli City, Taoyuan County 32001, Taiwan

<sup>18</sup> Ulugh Beg Astronomical Institute, Maidanak Observatory, 33 Astronomicheskaya str., Tashkent, 100052, Uzbekistan

<sup>19</sup> Astronomical Institute, St. Petersburg State University, 198504 St. Petersburg, Russia

<sup>20</sup> Instituto de Astronomía, Universidad Nacional Autónoma de México, Ensenada, Baja California, Mexico

<sup>21</sup> Institute for Astrophysical Research, Boston University, 725 Commonwealth Avenue, Boston, MA 02215, USA

<sup>22</sup> Astronomical Institute, St. Petersburg State University, Universitetskij Pr. 28, Petrodvorets, 198504 St. Petersburg, Russia

<sup>23</sup> Abastumani Observatory, Mt. Kanobili, 0301 Abastumani, Georgia

<sup>24</sup> Engelhardt Astronomical Observatory, Kazan Federal University, Tatarstan, Russia

<sup>25</sup> Pulkovo Observatory, 196140 St. Petersburg, Russia

<sup>26</sup> Finnish Centre for Astronomy with ESO (FINCA), University of Turku, Väisäläntie 20, FI-21500 Piikkiö, Finland

<sup>27</sup> Tuorla Observatory, Department of Physics and Astronomy, University of Turku, FI-20014 Turku, Finland

<sup>28</sup> INAF-IASF Bologna, via Gobetti 101, I-40129 Bologna, Italy

<sup>29</sup> INFN-Pavia, via Bassi 6, I-27100 Pavia, Italy

<sup>30</sup> School of Physics, University of the Witwatersrand, Johannesburg Wits 2050, South Africa

<sup>31</sup> Dipartimento di Fisica, Univ. di Trieste and INFN, via Valerio 2, I-34127 Trieste, Italy

<sup>32</sup> INFN Roma “Tor Vergata”, via della Ricerca Scientifica 1, I-00133 Roma, Italy

<sup>33</sup> East Windsor RSD, 25a Leshin Lane, Hightstown, NJ 08520, USA

Received 2018 January 17; revised 2018 February 19; accepted 2018 February 20; published 2018 March 28

## Abstract

We report the *AGILE* detection and the results of the multifrequency follow-up observations of a bright  $\gamma$ -ray flare of the blazar 3C 279 in 2015 June. We use *AGILE* and Fermi gamma-ray data, together with Swift X-ray and optical-ultraviolet data, and ground-based GASP-WEBT optical observations, including polarization information, to study the source variability and the overall spectral energy distribution during the  $\gamma$ -ray flare. The  $\gamma$ -ray flaring data, compared with as yet unpublished simultaneous optical data that will allow constraints on the big blue bump rising disk luminosity, show very high Compton dominance values of  $\sim 100$ , with the ratio of  $\gamma$ -ray to optical emission rising by a factor of three in a few hours. The multiwavelength behavior of the source during the flare challenges one-zone leptonic theoretical models. The new observations during the 2015 June flare are also compared with already published data and nonsimultaneous historical 3C 279 archival data.

**Key words:** galaxies: active – gamma rays: galaxies – polarization – quasars: individual (3C 279) – radiation mechanisms: non-thermal – X-rays: general

## 1. Introduction

Blazars are a subclass of radio-loud active galactic nuclei with relativistic jets pointing toward the observer (Urry & Padovani 1995). Their emission extends from the radio band to the  $\gamma$ -ray band above 100 MeV up to TeV  $\gamma$ -rays, and it is

dominated by variable nonthermal processes. They come in two main flavors, with very different optical spectra: Flat Spectrum Radio Quasars (FSRQs) that have strong, broad optical emission lines; and BL Lacertae objects (BL Lacs) with an optical spectrum that can be completely featureless or can



show, at most, weak emission lines and some absorption features (e.g., see Giommi et al. 2012 for a detailed review on blazar classification). The blazar spectral energy distribution (SED) is, in general, characterized by two broad bumps: the low-energy one, spanning from the radio to the X-ray band, is attributed to synchrotron radiation, while the high-energy one, from the X-ray to the  $\gamma$ -ray band, is thought to be due to inverse Compton (IC) emission. In the leptonic scenario, this second component is due to relativistic energetic electrons scattering their own synchrotron photons—Synchrotron self-Compton (SSC)—or photons external to the jet—External Compton (EC). Blazars of both flavors have been found to be highly variable and particularly so in  $\gamma$ -rays.<sup>34</sup> The correlated variability between X-rays and  $\gamma$ -rays is usually well explained in the SSC or EC framework (Ghisellini et al. 1998). In fact, a new class of “orphan”  $\gamma$ -ray flares from FSRQ blazars is now emerging from observations, challenging the current simple one-zone leptonic models. In particular, a number of  $\gamma$ -ray flares from some extensively monitored FSRQs, such as 3C 279, do not correlate with optical and soft X-ray events of comparable power and timescales; see, for example, the results of a previous multiwavelength campaign on 3C 279 during flaring states in 2013–2014 (Hayashida et al. 2015).

Gamma-ray observations of flaring blazars and simultaneous multiwavelength data are thus the key to investigate possible alternative theoretical scenarios, such as a recently proposed model based on a mirror-driven process within a clumpy jet inducing localized and transient enhancements of synchrotron photon density beyond the broad-line region (BLR; Tavani et al. 2015; Vittorini et al. 2017). Other scenarios consider special structures, such as spine-sheath jet layers radiative interplay (Tavecchio & Ghisellini 2008; Sikora et al. 2016) or “rings” of fire, i.e., synchrotron-emitting rings of electrons representing a shocked portion of the jet sheath (MacDonald et al. 2015).

3C 279 is associated with a luminous FSRQ at  $z = 0.536$  (Lynds et al. 1965), with prominent broad emission lines detected in all accessible spectral bands and revealing highly variable emission. It consistently shows strong  $\gamma$ -ray emission, which are already clearly detected by EGRET (Hartman et al. 1992; Kniffen et al. 1993), *AGILE* (Giuliani et al. 2009), *Fermi*-Hayashida et al. 2012, 2015), and also detected above 100 GeV by MAGIC (Albert et al. 2008). The central black hole mass estimates are in the range of  $(3\text{--}8) \times 10^8 M_{\odot}$  (Gu et al. 2001; Woo & Urry 2002; Nilsson et al. 2009). The 3C 279 jet features strings of compact plasmoids, as indicated by radio observations (Hovatta et al. 2009), which may be a by-product of the magnetic reconnection process (Petropoulou et al. 2016), even though it must be taken into account that the superluminal knots observed in Very Long Baseline Interferometry images are probably much larger structures than the reconnection plasmoids formed on kinetic plasma scales, hence this connection is uncertain (Chatterjee et al. 2008).

Here we present the results of a multiband observing campaign on the blazar 3C 279 triggered by the detection of intense  $\gamma$ -ray emission above 100 MeV by the *AGILE* satellite in 2015 June (Lucarelli et al. 2015). The source is one of the  $\gamma$ -ray blazars monitored by the *GLAST-AGILE*<sup>35</sup> Support Program (GASP) of the Whole Earth Blazar Telescope

(WEBT) Collaboration<sup>36</sup> (Bottcher et al. 2007; Larionov et al. 2008; Villata et al. 2008; Abdo et al. 2010).

The *AGILE*-Gamma-ray Imaging Detector (–GRID)  $\gamma$ -ray data of 3C 279 in 2015 June are compared with as yet unpublished (*R*-band) optical GASP-WEBT observations during the flare, including the percentage and angle of polarization, and with *Fermi*-Fermi-Large Area Telescope (–LAT; Paliya et al. 2015; Ackermann et al. 2016) and other multiwavelength data from the *Swift*-Ultraviolet/Optical Telescope (–UVOT) and the *Swift*-X-Ray Telescope (–XRT) Target of Opportunities (ToO). The analysis of the source multiwavelength behavior is crucial in order to study the correlation (if any) of the  $\gamma$ -ray radiation with the optical-ultraviolet (–UV) and X-ray emissions. The 2015 June flaring data are also compared with nonsimultaneous archival data from the NASA/IPAC Extragalactic Database and from the ASI Space Science Data Center (SSDC, previously known as ASDC).

## 2. Observations and Data Analysis

### 2.1. *AGILE* Observations

*AGILE* (Tavani et al. 2009) is a small mission of the Italian Space Agency (ASI) devoted to  $\gamma$ -ray astrophysics, operating in a low Earth orbit since 2007 April 23. The main *AGILE* instrument is GRID, which is sensitive in the energy range 30–50 GeV. *AGILE*-GRID consists of a silicon-tungsten tracker, a cesium iodide mini-calorimeter, and an anticoincidence system (AC) made of segmented plastic scintillators.

The *AGILE* Quick Look (QL) alert system (Pittori 2013; Bulgarelli et al. 2014) detected increased  $\gamma$ -ray emission from 3C 279 starting from 2015 June 13 (MJD = 57186) and lasted up to 2015 June 17 (MJD = 57190).

The *AGILE*-GRID data were analyzed using the *AGILE* Standard Analysis Pipeline (see Vercellone et al. 2008 for a description of the *AGILE* data reduction). Counts, the exposure, and Galactic diffuse background maps for energy  $E \geq 100$  MeV were created, including all events collected up to  $60^\circ$  off-axis. Scientific data acquisition is inhibited during the South Atlantic Anomaly passages, and we rejected all  $\gamma$ -ray events whose reconstructed directions form angles with the satellite–Earth vector  $\leq 80^\circ$  to reduce the  $\gamma$ -ray Earth albedo contamination. We used the latest public *AGILE* software Package (*AGILE* SW 5.0 SourceCode) with calibration files (I0023), and the *AGILE*  $\gamma$ -ray diffuse emission model (Giuliani et al. 2004), which is publicly available at the SSDC site.<sup>37</sup>

### 2.2. GASP-WEBT Observations

Optical observations of 3C 279 were carried out by the GASP-WEBT Collaboration in the Cousins’ *R* band. Data were provided by the following observatories: Abastumani (Georgia), Belogradchik (Bulgaria), Crimean (Russia), Lowell (USA; Perkins telescope), Lulin (Taiwan), Mt. Maidanak (Uzbekistan), Roque de los Muchachos (Spain; KVA), San Pedro Martir (Mexico), Skinakas (Greece), St. Petersburg (Russia), Teide (Spain; IAC80 and STELLA-I), and Tjarafe (Spain). The calibrated source magnitude was obtained by differential photometry with respect to Stars 1, 2, 3, and 5 of the photometric sequence by Raiteri et al. (1998). The optical light curve (see Section 3.1) was visually inspected and checked. No significant offset was noticed between different data sets.

<sup>34</sup> The SED movie of the blazar 3C 279 from 2008.05 to 2016.37 by P. Giommi: <http://www.youtube.com/watch?v=o0JJBakFUXQ>.

<sup>35</sup> GLAST refers to the Fermi Gamma-ray Space Telescope, formerly known as the Gamma-ray Large Area Space Telescope.

<sup>36</sup> <http://www.oato.inaf.it/blazars/webt/>

<sup>37</sup> <http://agile.ssdsc.asi.it/publicsoftware.html>

**Table 1**  
*Swift* Follow-up Observations of 3C 279 Following the *AGILE*  $\gamma$ -ray Flare Alert in 2015 June, and On-source Net Exposures in the Pointing Observing Mode for the XRT (Photon Counting Readout Mode) and UVOT Instruments within Each Observation

OBS Start Time (UTC)	MJD	XRT Exposure (s)	UVOT Exposure (s)	obsID
2015 Jun 15 14:27:58	57188.6028	1987.8	1994.1	00035019176
2015 Jun 16 03:27:59	57189.1444	958.9	961.7	00035019180
2015 Jun 16 16:04:58	57189.6701	934.0	936.1	00035019181
2015 Jun 17 04:40:59	57190.1951	936.5	938.2	00035019185
2015 Jun 17 20:59:58	57190.8750	489.5	488.6	00035019187
2015 Jun 18 04:37:59	57191.1930	1246.1	1249.2	00035019188

Polarimetric information in the  $R$  band was acquired at the Crimean, Lowell, San Pedro Martir, and St. Petersburg observatories.

### 2.3. *Swift* ToO Observations

Following the 3C 279  $\gamma$ -ray flare detected by *AGILE*, a prompt *Swift* target of opportunity observation was performed on 2015 June 15, for a total net exposure time of about 2.0 ks. Another five *Swift*-XRT observations were carried out on 2015 June 16–18. A summary of these observations is given in Table 1, where the net exposures with the XRT and UVOT instruments are also reported.

#### 2.3.1. XRT Observations

The XRT onboard *Swift* (Gehrels et al. 2004) is sensitive to the 0.3–10 keV X-ray energy band (Burrows et al. 2004). The six 2015 June XRT follow-up observations of 3C 279 were all carried out using the most sensitive Photon Counting readout mode for a total net exposure time of about 6.5 ks. The XRT data sets were first processed with the XRTDAS software package (v.3.1.0) developed at SSC and distributed by the High Energy Astrophysics Science Archive Research Center (HEASARC) within the HEASoft package (v. 6.17). Event files were calibrated and cleaned with standard filtering criteria with the *xrtpipeline* task using the calibration files available in the version 20150721 of the *Swift*-XRT calibration database (CALDB). Except for the last two observations, the source count rate was initially high enough to cause some photon pile-up in the inner 3 pixels radius circle centered on the source position, as derived from the comparison of the observed point-spread function (PSF) profile with the analytical model derived in Moretti et al. (2005). We avoided pile-up effects by selecting events within an annular region with an inner radius of 3 pixels and an outer radius of 30 pixels. The background was extracted from a nearby source-free annular region of the 50/90 pixel inner/outer radius. The ancillary response files were generated with the *xrtmkarf* task, applying corrections for the PSF losses and CCD defects using the cumulative exposure map. The response matrices available in the *Swift* CALDB at the time of analysis were used. The source spectra were binned to ensure a minimum of 30 counts per bin.

For all *Swift* ToO observations, fits of the XRT spectra were performed using the XSPEC package. The observed X-ray spectrum (0.3–10 keV) can be fit by an absorbed power-law model with a HI column density that is consistent with the Galactic value in the direction of the source,  $n_{\text{H}} = 2.2 \times 10^{20} \text{ cm}^{-2}$  (Kalberla et al. 2005). The results of photon index

**Table 2**

Results of the X-ray Spectral Analysis of the *Swift*-XRT Follow-up Data

XRT Date Start (UTC)	Photon Index	XRT Flux (0.3–10 keV) ( $\text{erg cm}^{-2} \text{ s}^{-1}$ )
2015 Jun 15 14:32	$1.36 \pm 0.06$	$(5.5 \pm 0.4) \times 10^{-11}$
2015 Jun 16 03:31	$1.32 \pm 0.08$	$(9.4 \pm 0.8) \times 10^{-11}$
2015 Jun 16 16:08	$1.4 \pm 0.1$	$(3.5 \pm 0.5) \times 10^{-11}$
2015 Jun 17 04:44	$1.4 \pm 0.1$	$(2.7 \pm 0.4) \times 10^{-11}$
2015 Jun 17 21:02	$1.3 \pm 0.2$	$(2.0 \pm 0.5) \times 10^{-11}$
2015 Jun 18 04:41	$1.5 \pm 0.1$	$(1.7 \pm 0.2) \times 10^{-11}$

**Note.** The errors are at 90% level of confidence, and fluxes are corrected for the galactic absorption

**Table 3**

Results of the Analysis of the *Swift*-UVOT ToO Follow-up Data

UVOT Date Start (UTC)	Filter (of the day)	UVOT Magnitude
2015 Jun 15 14:33	U	$14.93 \pm 0.03$
2015 Jun 16 03:32	W2	$15.35 \pm 0.04$
2015 Jun 16 16:09	W2	$15.44 \pm 0.04$
2015 Jun 17 04:45	M2	$15.38 \pm 0.04$
2015 Jun 17 21:04	M2	$15.64 \pm 0.05$
2015 Jun 18 04:41	W1	$15.65 \pm 0.04$

**Note.** Observed magnitudes, which are not corrected for galactic extinction, and errors at the  $1\sigma$  confidence level.

and fluxes corrected for the Galactic absorption for each follow-up observation are shown in Table 2.

#### 2.3.2. UVOT Observations

Co-aligned with the XRT, the *Swift*-UVOT instrument (Roming et al. 2005) provides simultaneous UV and optical coverage (170–650 nm). UVOT ToO observations were performed with the optical/UV filter of the day, namely U, W2, and M2, as described in Table 3. We performed aperture photometry using the standard UVOT software distributed within the HEASoft package (v. 6.17), and the calibration included in the latest release of the CALDB. The values of the UVOT observed magnitudes of the source are given in Table 3. Source counts were extracted from an aperture of the 5 arcsec radius for all filters, while the background ones were extracted from an annular region of the inner aperture 26 arcsec and size 9 arcsec, then the source counts were converted to fluxes using the standard zero points (Breeveld et al. 2011). The fluxes were

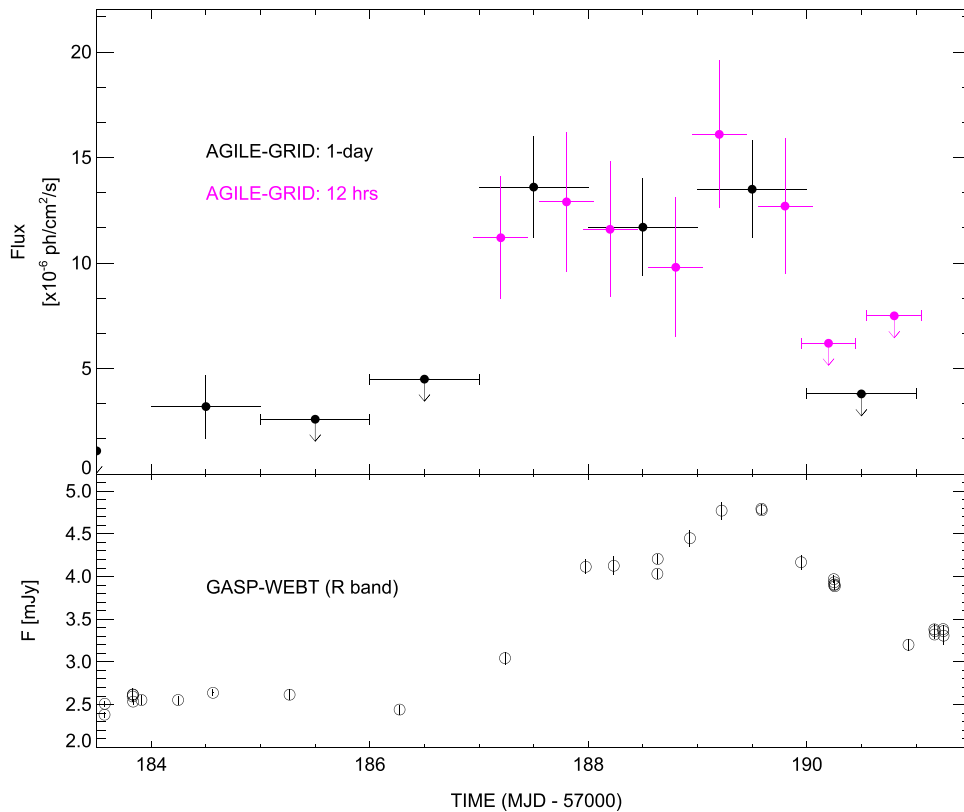


**Figure 1.** Top panel: *AGILE*-GRID 3C 279  $\gamma$ -ray light curve ( $E \geq 100$  MeV) during the 2015 June flare. Bottom panel: simultaneous GASP-WEBT optical data (R-band, de-absorbed flux densities), showing a well-defined maximum peaking around MJD = 57189.

finally dereddened using the appropriate value  $E(B-V) = 0.0245$ , taken from Schlegel et al. (1998) and Schlafly & Finkbeiner (2011), with  $A_{\lambda}/E(B-V)$  ratios calculated for UVOT filters using the mean Galactic interstellar extinction curve from Fitzpatrick (1999). These fluxes were then included in the multiwavelength SED (see Section 3.2).

#### 2.4. Fermi-LAT Observations

We compared *AGILE*  $\gamma$ -ray observations with published *Fermi*-LAT data from Ackermann et al. (2016), and with public *Fermi* data obtained from the online data analysis tool at SSCC.<sup>38</sup> As described in Ackermann et al. (2016), events in the energy range 100 MeV–300 GeV were extracted within a  $15^{\circ}$  acceptance cone of the Region of Interest (ROI) centered on the location of the source. Gamma-ray fluxes and spectra were determined by an unbinned maximum likelihood fit with `gtlike`. The background model included all known  $\gamma$ -ray sources within the ROI from the third *Fermi*-LAT catalog (Acero et al. 2015). Additionally, the model included the isotropic and Galactic diffuse emission components. Flux normalization for the diffuse and background sources were left free in the fitting procedure.

### 3. RESULTS

#### 3.1. Light Curves

In Figure 1, we present the simultaneous (and as yet unpublished) *AGILE*  $\gamma$ -ray and GASP-WEBT optical light

curves during the 3C 279 flare in 2015 June. In order to produce the *AGILE* light curve, we divided the data collected in the period from 2015 June 11 to 18 (MJD: 57184–57191) in 24 and 12 hr timebins. To derive the estimated flux of the source, we ran the *AGILE* Multi-Source Maximum Likelihood Analysis (ALIKE) task with an analysis radius of  $10^{\circ}$ . The ALIKE was carried out by fixing the position of the source to its nominal radio position (Johnston et al. 1995),  $(l, b) = (305.104, 57.062)$  (deg) and using Galactic and isotropic diffuse emission parameters (GAL-ISO) fixed at the values estimated during the two weeks preceding the analyzed *AGILE* data set.

The extended GASP-WEBT optical light curve (R-band magnitude) of 3C 279 since the end of 2014, including the  $\gamma$ -ray flaring period (MJD: 57010–57220), is shown in Figure 2. It includes the polarization percentage  $P$  and electric vector polarization angle (EVPA) variations. The total brightness variation in this period is  $\sim 1.5$  magnitude, from  $R = 16.07$  at MJD = 57142.1 to  $R = 14.58$  at MJD = 57189.6.

The multiwavelength behavior of the source during the flare is then summarized in Figure 3, which includes  $\gamma$ -ray light curves, as observed by *AGILE*-GRID and *Fermi*-LAT, the prompt *Swift*-XRT X-ray followup, and the simultaneous GASP-WEBT de-absorbed optical flux densities and polarimetric data.

A well-defined maximum peaking around MJD = 57189 is visible at  $\gamma$ -rays, which is in agreement with the optical observations. The degree of observed polarization  $P$  remains always high, ranging between about 9% and 30%. The maximum observed value occurs at MJD = 57190.2, and the daily sampling allows to identify a 1 day delay of the  $P$

<sup>38</sup> <https://tools.asdc.asi.it/?&searchtype=fermi>

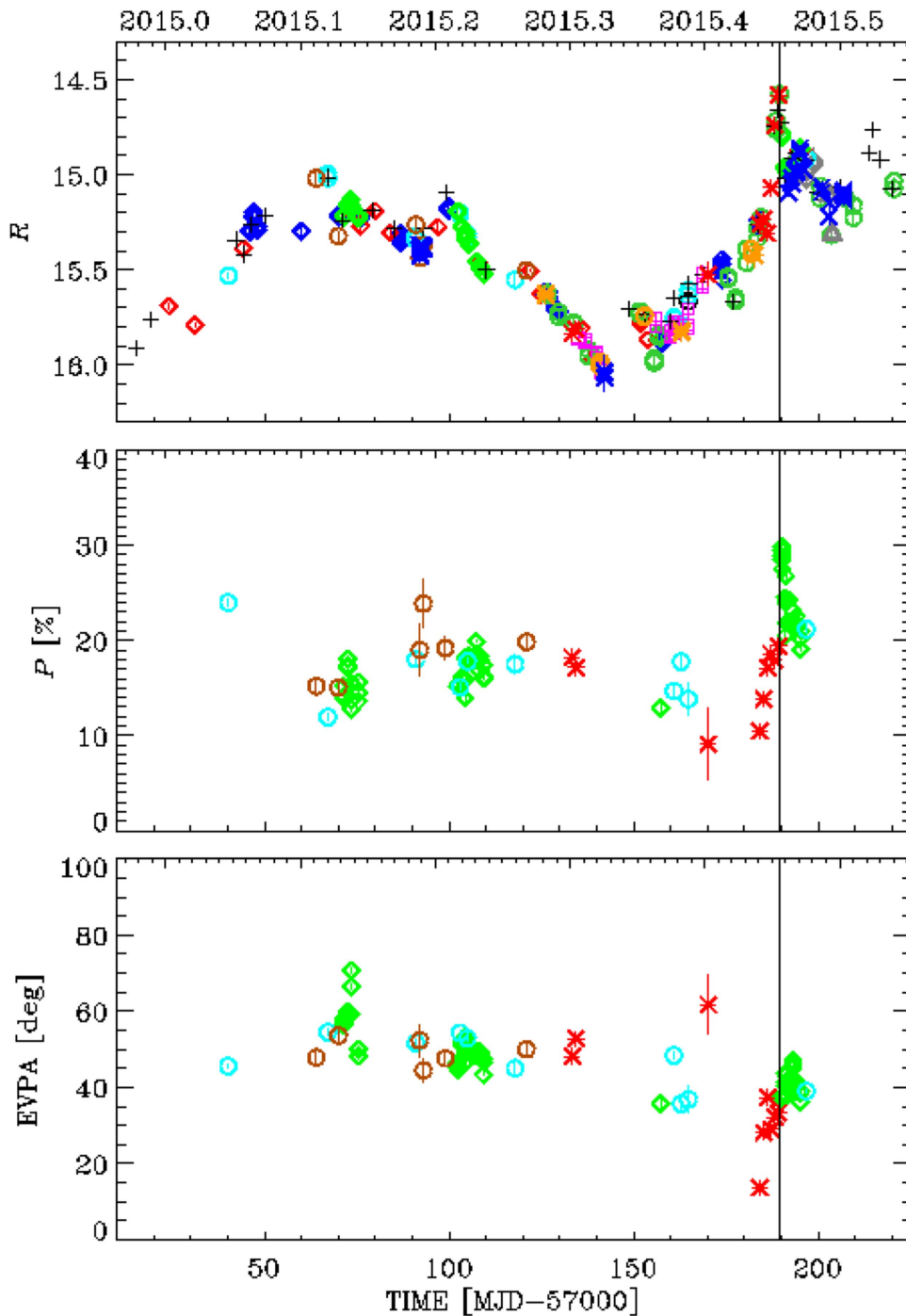


**Figure 2.** Photometric and polarimetric optical data in the  $R$  band acquired by the GASP-WEBT Collaboration from 2014 December 9 (MJD = 57000) to 2015 July 17 (MJD = 57220). The corresponding time in calendar years is shown above the figure. Different colors and symbols highlight data points from different telescopes (see the text for the full list). The vertical line indicates the optical flux measured maximum (MJD = 57189.585).

maximum after the flux peak observed at optical and  $\gamma$ -ray frequencies. The rise and the following decrease of  $P$  and flux is accompanied by a rotation of the electric vector polarization angle of about  $30^\circ$  in 10 days.

As shown in Figure 3's third panel, the X-ray flux variability also appears correlated with the  $\gamma$ -ray and optical ones. The peak X-ray flux value occurs at MJD = 57189.14, and it is about a factor of about four higher than the one observed one day later (see Table 2).

### 3.2. Spectral Energy Distribution

Figure 4 shows the 3C 279 broadband SED obtained with the help of the SSDC SED Builder tool.<sup>39</sup> Simultaneous *AGILE*, GASP-WEBT, *Swift*-XRT, and *Swift*-UVOT data during the 2015 June flare are shown in red. Average  $\gamma$ -ray flux excluding the flaring period and other public non-simultaneous archival data in other wavelengths are shown in gray.

<sup>39</sup> <http://tools.asdc.asi.it/SED>

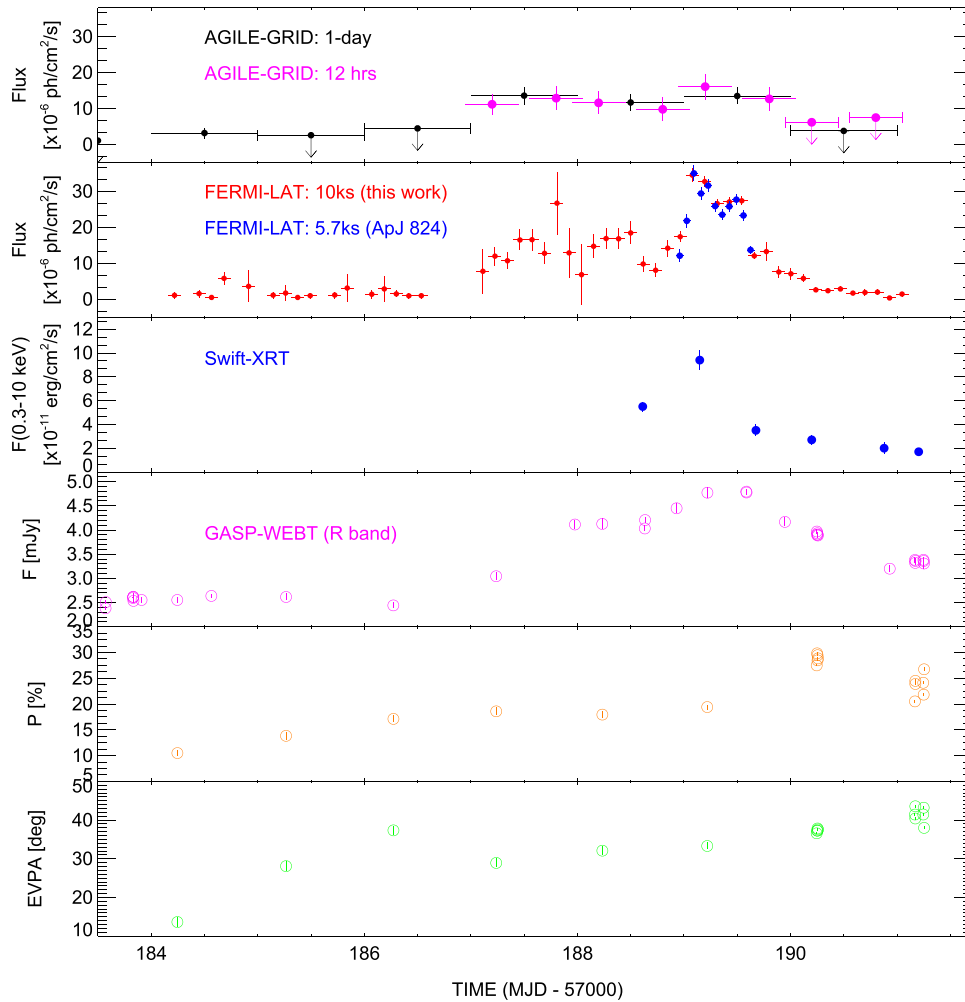


**Figure 3.** Multiwavelength light curves of 3C 279 in 2015 June:  $\gamma$ -rays ( $E \geq 100$  MeV), as observed by *AGILE*-GRID and *Fermi*-LAT, the prompt *Swift*-XRT X-ray followup, and simultaneous GASP-WEBT photometric and polarimetric optical data. Second panel: *Fermi*-LAT blue points are from Ackermann et al. (2016), and the red points are from the public online *Fermi* data analysis tool at SSDC. In the last three panels, we report a selection of the full data set of GASP-WEBT observations already presented in Figure 2, zoomed in around the  $\gamma$ -ray peak.

We have performed the *AGILE* spectral analysis of the peak  $\gamma$ -ray activity, corresponding to the period between 2015 June 14 (MJD = 57187.0) and 2015 June 17 (MJD = 57190.0) over three energy bins: 100–200, 200–400, and 400–1000 MeV. A simple power-law spectral fitting gives a photon index of  $\Gamma_\gamma = (2.14 \pm 0.11)$ , which is consistent within the errors with the values reported by *Fermi* (Paliya et al. 2015; Ackermann et al. 2016). Moreover, we estimated the average  $\gamma$ -ray fluxes obtained by integrating in the whole *AGILE* energy band (100 MeV–50 GeV) during three time periods, defined as a *pre-outburst* (MJD: 57184–57187), a *flare* (MJD: 57187–57190), and a *post-flare* (MJD: 57190–57193). The corresponding *AGILE* integral  $\gamma$ -ray fluxes and spectral indices are summarized in Table 4. Historically, this is the largest  $\gamma$ -ray flare ( $\geq 100$  MeV) of 3C 279 ever observed, including recent activity reported in Bulgarelli et al. (2017).

The SED during the flare (red points in Figure 4) indicates a very high “Compton dominance”: the ratio of the IC peak to the synchrotron 1 is of the order of 100. Specifically, the  $\gamma$ -ray spectrum integrated over 1 day timebins rises by a factor of  $\sim 3$  in a few hours (as shown in Figure 3), yielding a Compton dominance of about 100, and attaining values up to  $\sim 200$  when integrating on even shorter timescales (Ackermann et al. 2016).

#### 4. Simple Flare Modeling and Discussion

In this section, we estimate the parameters of a tentative simple modeling of the multiwavelength 3C 279 data acquired during the 2015 flare. The model parameter values obtained here can be used as reference input for a more detailed further theoretical analysis.

In the framework of the one-zone leptonic model for FSRQs (see e.g., Paggi et al. 2011), the optical and UV data acquired during the 2015 June flare, presented here, would constrain the luminosity of the accretion disk to  $L_D \leq 10^{46}$  erg s $^{-1}$ . We note that this value is larger, by a factor of about 3, than the disk luminosity previously inferred for 3C 279 (Raiteri et al. 2014).

Taking into account also the simultaneous soft X-ray data and the observed variability, we can determine empirical constraints on the model parameters: the size  $l$ , the bulk boost factor  $\Gamma$ , the energetic content in magnetic field  $B$ , and the electron energy distribution  $n_e(\gamma)$  of the emitting region. We assume that the relativistic electrons have a double power-law energy-density distribution:

$$n_e(\gamma) = \frac{K \gamma_b^{-1}}{(\gamma/\gamma_b)^{\zeta_1} + (\gamma/\gamma_b)^{\zeta_2}} \text{ [cm}^{-3}\text{]}, \quad (1)$$

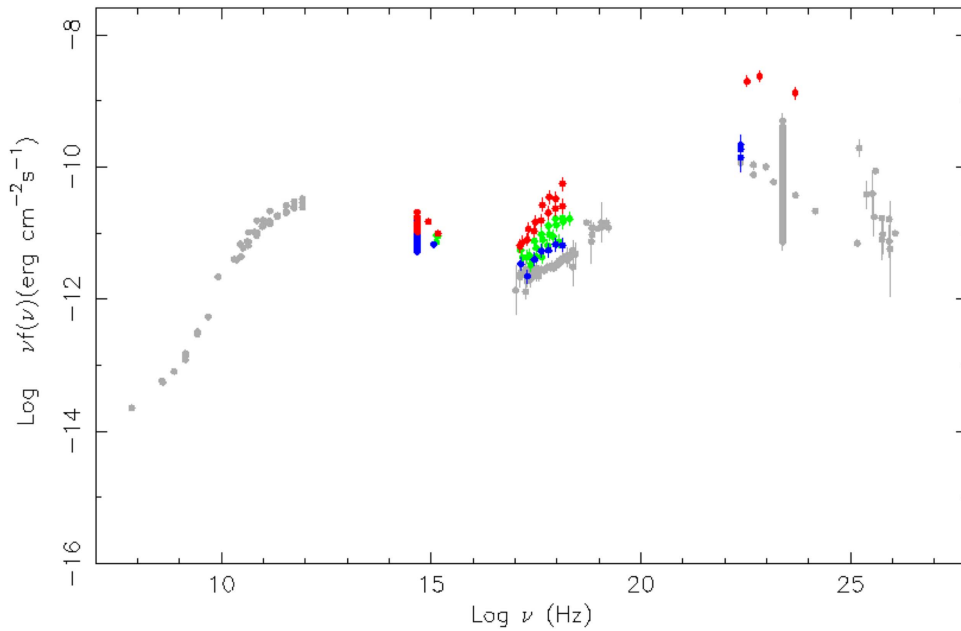


**Figure 4.** 3C 279 broadband SED obtained with the help of the SSDC SED Builder tool (v. 3.2). Red points: *AGILE* data during the 2015 June  $\gamma$ -ray flare (around MJD: 57187–57190), and simultaneous *GASP-WEBT*, *Swift-UVOT*, and *Swift-XRT* ToO data. Green points: *Swift-UVOT* and *Swift-XRT* follow-up data covering approximately 48 hr after the  $\gamma$ -ray peak emission (see Table 1). Blue points: post-flare 2015 data from *GASP-WEBT* (up to MJD = 57220), *Swift-UVOT*, *Swift-XRT* (MJD = 57191), and *AGILE* data (weekly averaged flux above 100 MeV from MJD = 57197.5 to 57218.5). Gray points: public nonsimultaneous archival data from SSDC (CRATES, DIXON, NVSS, PKSCAT90, PMN, VLSS, AT20GCAT, PLANCK, WMAP5, *Swift-BAT*, IBIS/ISGRI, *BeppoSAX*, *AGILE-GRID*, *Fermi-LAT*, and *MAGIC*).

**Table 4**  
*AGILE*  $\gamma$ -ray Fluxes and Spectral Indices

Label	$T_{\text{start}}$ MJD	$T_{\text{stop}}$ MJD	$F(E \geq 100 \text{ MeV})$ ( $10^{-6} \text{ ph cm}^{-2} \text{ s}^{-1}$ )	$\Gamma_{\gamma}$
Pre-outburst	57184.0	57187.0	$(1.7 \pm 0.7)$	$(2.0 \pm 0.4)$
Flare	57187.0	57190.0	$(13.0 \pm 1.3)$	$(2.1 \pm 0.1)$
Post-flare	57190.0	57193.0	$(1.0 \pm 0.5)$	...

**Note.** Over the considered 3 day time periods, the source flux increases of factor of about 7, then rapidly drops more than a factor of 10 in the post-flare, with insufficient statistics for the spectral analysis.

where  $K$  is a normalization factor,  $\gamma_b$  is the break Lorentz factor,  $\zeta_1$  and  $\zeta_2$  are the double power-law spectral indices below and above the break, respectively.

These electrons interact via the IC process with the synchrotron photons internal to the same emitting region, with the external photons coming from the accretion disk and from the BLR. From distances  $R_{\text{BLR}} \simeq 0.1 \text{ pc}$ , the latter reflects a fraction  $\xi \simeq \text{few } \%$  of the disk radiation. In Figure 5, we show our one-zone SED model of the 2015 June flare of 3C 279 for  $\gamma$ -ray fluxes averaged on 1 day timescales. If we assume the emitting region located at a distance  $R < R_{\text{BLR}}$  from the central black hole, then seed photons coming from BLR are good candidates to be scattered into  $\gamma$ -rays of observed energies  $\geq 100 \text{ MeV}$  (see the red line in Figure 5). As shown by the blue lines in the same figure, disk photons entering the emitting region from behind are scattered mainly in the hard X-ray observed band. Instead, the internal scattering of the synchrotron photons are seen mainly in the soft X-ray band, as shown by the green lines.

In this model, we consider the emitting region placed at a distance  $R = 6 \times 10^{16} \text{ cm}$  from the central black hole, while the accretion disk radiates the power  $L_D = 10^{46} \text{ erg s}^{-1}$ ; a

fraction  $\xi = 2\%$  of this is reflected back from the BLR placed at distance  $R_{\text{BLR}} = 0.15 \text{ pc}$ . A summary of the best-fit flare model parameters is shown in Table 5.

When the IC scattering occurs in the Thomson regime, the Compton dominance reads  $q = U'_{\text{ext}}/U'_B$ , i.e., the ratio of the comoving energy density of BLR seed photons  $U'_{\text{ext}} \simeq (1 + \beta_{\Gamma}^2)\Gamma^2\xi L_D / (4\pi c R_{\text{BLR}}^2)$  to the energy density of the magnetic field  $U'_B = B'^2/8\pi$ , thus:

$$q \lesssim 0.2 \Gamma^2 \frac{(\xi/0.02)L_{D,46}}{(B'/\text{G})^2(R_{\text{BLR}}/0.1\text{pc})^2}. \quad (2)$$

For assumed disk luminosities  $L_D \leq 10^{46} \text{ erg s}^{-1}$ , this yields a value of  $q \leq 80$ . Moreover, the one-zone assumption has two other main consequences.

1. First, a strict correlation of optical and  $\gamma$ -ray fluxes: their variations must be of the same entity, so the Compton dominance should not vary.
2. Second, to increase the upper limit for  $q$  up to values above 100, as observed, we should consider faint magnetic fields values  $B \lesssim 0.1 \text{ G}$ , which would in turn imply modest electron accelerations (Mignone et al. 2013). Alternatively, we could assume bulk factors  $\Gamma > 30$  (Ackermann et al. 2016), which considerably exceeds the value  $\Gamma \simeq 20$  inferred from radio observations for this source (Hovatta et al. 2009), that would imply a conspicuous kinetic load in the jet.

Noticeably, the multiwavelength light curves of the flare in Figure 3 show instead that the Compton dominance rises by a factor of three or more in a half day, attaining values up to  $q > 200$  in few minutes when considering the very fast and strong  $\gamma$ -ray variations reported in Ackermann et al. (2016). While the simple one-zone model presented here could account for the SED flaring data integrated on 1 day timescales

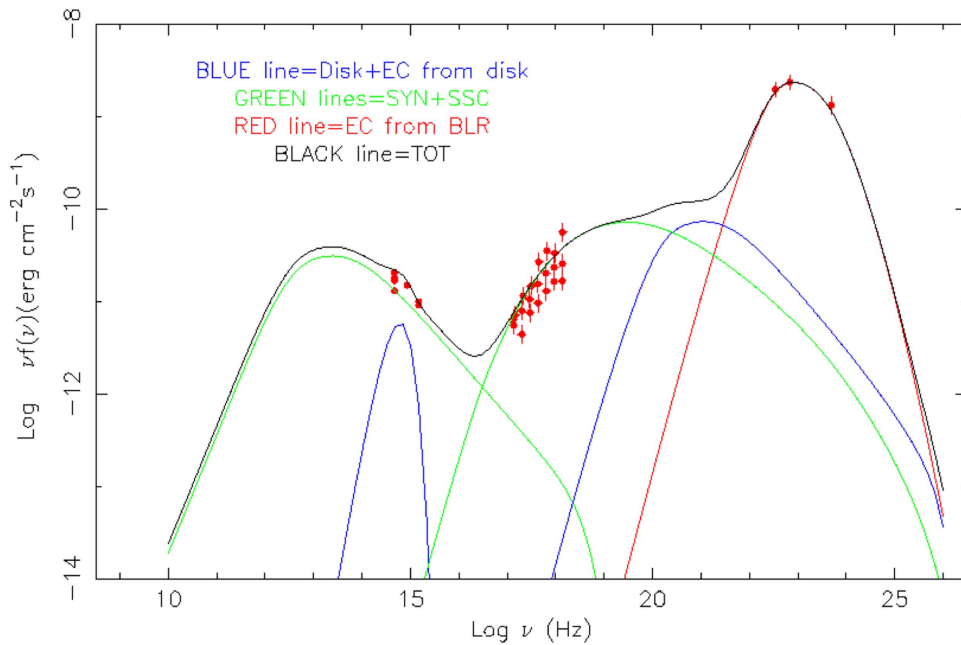


Figure 5. 3C 279: simple one-zone modeling of the 2015 June flare.

**Table 5**  
One-zone Model Parameters for the 2015 Flare of 3C 279,  
as Defined in Section 4

$l$ (cm)	$K$ ( $\text{cm}^{-3}$ )	$\gamma_b$	$\gamma_{\min}$	$\zeta_1$	$\zeta_2$	$\Gamma$	$B$ (G)
$10^{16}$	1100	700	180	2	4.2	20	1

(provided you assume of a very bright underlying disk), it is anyway seriously challenged by the observed strong and fast variation of the Compton dominance.

Furthermore, we notice that a single photon of energy  $E = 52$  GeV was detected on MJD = 57189.62 (Paliya et al. 2015) in correspondence with the peak of optical emission and is consistent with the observed polarization fraction reaching its maximum. The modeling of this specific episode of high-energy emission goes beyond the scope of this paper and provides an additional argument for alternative modes of  $\gamma$ -ray emission.

## 5. Conclusions

In this paper, we present multifrequency optical and X-ray data simultaneous with the 2015  $\gamma$  flaring activity of 3C 279. We use *AGILE*-GRID and *Fermi*-LAT (Paliya et al. 2015; Ackermann et al. 2016)  $\gamma$ -ray data together with the *Swift*-UVOT, the *Swift*-XRT, and as yet unpublished optical GASP-WEBT observations of 3C 279 in 2015 June. We find that from the multiwavelength light curve shown in Figure 3, the high-energy flare is partially correlated with the behavior in other energy bands. Specifically, the  $\gamma$ -ray flux rising by a factor  $\simeq 4$  in half a day shows an optical counterpart rising only by a factor 2 or less on similar timescales. The  $\gamma$ -ray flux during this flare exceeds the largest 3C 279 flares previously detected, although Hayashida et al. (2015) reported an even more extreme multifrequency behavior for this source in the past; e.g., in 2013 December, the  $\gamma$ -ray flux above 100 MeV jumped by a factor  $\simeq 5$  in a few hours without optical or X-ray

counterparts, and the Compton dominance attained values of about 300. Ackermann et al. (2016) discuss the variability of the 2015  $\gamma$ -ray flare with minute timescales.

The observed spectral characteristics and the strong and fast variations of the Compton dominance challenge one-zone models, unless we assume significant variations in the field of seed photons to be IC scattered into  $\gamma$ -rays. We discuss in this paper a one-zone model and provide the model parameters that can be used as a theoretical model of reference. Models alternative to the standard SSC and EC might be considered (e.g., Ackermann et al. 2016). In the moving mirror model (Tavani et al. 2015; Vittorini et al. 2017) localized enhancements of synchrotron photon density may explain the occurrence of gamma-ray flares with faint or no counterpart in other bands. These localized enhancements would persist only for short periods of time, and this would explain the fact that the majority of FSRQ  $\gamma$ -ray flares are not orphan in nature.

We noticed that, as shown in Figure 3, the degree of observed optical polarization  $P$  appears to correlate with the optical flux  $F$  during the flare, with  $P$  peaking about one day after  $F$ . Moreover, the polarization angle rotates by at least  $30^\circ$  in the period encompassing the flare. However, the behavior of the polarization degree of the jet may be very different from the observed one, due to the big blue bump dilution effect. When deriving the intrinsic jet polarization  $P_{\text{jet}}$ , the presence of a very luminous disc, as assumed by the one-zone model used to interpret the observed SEDs, would imply that the correction for the thermal emission contribution becomes noticeable as the flux approaches the observed minimum level. This would lead to much higher  $P_{\text{jet}}$  values than the observed ones, and  $P_{\text{jet}}$  would not maintain the general correlation with flux shown in Figure 2.










Partly based on data taken and assembled by the WEBT Collaboration and stored in the WEBT archive at the Osservatorio Astrofisico di Torino—INAF.<sup>40</sup> For questions about data availability, contact the WEBT President Massimo Villata (villata@oato.inaf.it).

<sup>40</sup> <http://www.oato.inaf.it/blazars/webt/>

We would like to acknowledge the financial support of ASI under contract to INAF: ASI 2014-049-R.0 dedicated to SSDC. Part of this work is based on archival data, software, or online services provided by the ASI SSDC. The research at Boston University was supported by National Science Foundation grant AST-1615796 and NASA Swift Guest Investigator grant 80NSSC17K0309. This research was partially supported by the Bulgarian National Science Fund of the Ministry of Education and Science under grant DN 08-1/2016. The Skinakas Observatory is a collaborative project of the University of Crete, the Foundation for Research and Technology—Hellas, and the Max-Planck-Institut für Extraterrestrische Physik. The St. Petersburg University team acknowledges support from Russian Science Foundation grant 17-12-01029. This article is partly based on observations made with the telescope IAC80 operated by the Instituto de Astrofísica de Canarias in the Spanish Observatorio del Teide on the island of Tenerife. The IAC team acknowledges the support from the group of support astronomers and telescope operators of the Observatorio del Teide. Based (partly) on data obtained with the STELLA robotic telescopes in Tenerife, an AIP facility jointly operated by AIP and IAC. This work is partially based upon observations carried out at the Observatorio Astronómico Nacional on the Sierra San Pedro Mártir (OAN-SPM), Baja California, Mexico. C.P., V.V. and M. T. also thank Professor A. Cavaliere for the insightful discussion.

*Software:* AGILE software Package (AGILE SW 5.0 SourceCode), XRTDAS (v.3.1.0), XSPEC and HEASoft package (v. 6.17).

#### ORCID iDs

C. Pittori  <https://orcid.org/0000-0001-6661-9779>  
 F. Lucarelli  <https://orcid.org/0000-0002-6311-764X>  
 F. Verrecchia  <https://orcid.org/0000-0003-3455-5082>  
 C. M. Raiteri  <https://orcid.org/0000-0003-1784-2784>  
 V. Vittorini  <https://orcid.org/0000-0002-1208-8818>  
 M. Tavani  <https://orcid.org/0000-0003-2893-1459>  
 S. Puccetti  <https://orcid.org/0000-0002-2734-7835>  
 S. Vercellone  <https://orcid.org/0000-0003-1163-1396>  
 A. Morselli  <https://orcid.org/0000-0002-7704-9553>

#### References

Abdo, A. A., Ackermann, M., Ajello, M., et al. 2010, *Natur*, 463, 919  
 Acero, F., Ackermann, M., Ajello, M., et al. 2015, *ApJS*, 218, 23  
 Ackermann, M., Anantua, R., Asano, K., et al. 2016, *ApJL*, 824, L20

Albert, J., Aliu, E., Anderhub, H., et al. 2008, *Sci*, 320, 1752  
 Bottcher, M., Basu, S., Joshi, M., et al. 2007, *ApJ*, 670, 968  
 Breeveld, A. A., Landsman, W., Holland, S. T., et al. 2011, in AIP Conf. Proc., Gamma-Ray Bursts 2010, ed. J. E. McEnery, J. L. Racusin, & N. Gehrels (Melville, NY: AIP), 373  
 Bulgarelli, A., Parmiggiani, N., Pittori, C., et al. 2017, *ATel*, 10563, 1  
 Bulgarelli, A., Trifoglio, M., Gianotti, F., et al. 2014, *ApJ*, 781, 19  
 Burrows, D. N., Hill, J. E., Nousek, J. A., et al. 2004, *Proc SPIE*, 5165, 201  
 Chatterjee, R., Jorstad, S. G., Marscher, A. P., et al. 2008, *ApJ*, 689, 79  
 Fitzpatrick, E. L. 1999, *PASP*, 111, 63  
 Gehrels, N., Chincarini, G., Giommi, P., et al. 2004, *ApJ*, 611, 1005  
 Ghisellini, G., Celotti, A., Fossati, G., Maraschi, L., & Comastri, A. 1998, *MNRAS*, 301, 451  
 Giommi, P., Padovani, P., Polenta, G., et al. 2012, *MNRAS*, 420, 2899  
 Giuliani, A., Chen, A., Mereghetti, S., et al. 2004, *MSAIS*, 5, 135  
 Giuliani, A., D'Ammando, F., Vercellone, S., et al. 2009, *A&A*, 494, 509  
 Gu, M., Cao, X., & Jiang, D. R. 2001, *MNRAS*, 327, 1111  
 Hartman, R. C., Bertsch, D. L., Fichtel, C. E., et al. 1992, *ApJL*, 385, L1  
 Hayashida, M., Madejski, G. M., Nalewajko, K., et al. 2012, *ApJ*, 754, 114  
 Hayashida, M., Nalewajko, K., Madejski, G. M., et al. 2015, *ApJ*, 807, 79  
 Hovatta, T., Valtaoja, E., Tornikoski, M., & Lähteenmäki, A. 2009, *A&A*, 498, 723  
 Johnston, K. J., Fey, A. L., Zacharias, N., et al. 1995, *AJ*, 110, 880  
 Kalberla, P. M. W., Burton, W. B., Hartmann, D., et al. 2005, *A&A*, 440, 775  
 Kniffen, D. A., Bertsch, D. L., Fichtel, C. E., et al. 1993, *ApJ*, 411, 133  
 Larionov, V. M., Jorstad, S. G., Marscher, A. P., et al. 2008, *A&A*, 492, 389  
 Lucarelli, F., Pittori, C., Verrecchia, F., et al. 2015, *ATel*, 7631, 1  
 Lynds, C. R., Stockton, A. N., & Livingston, W. C. 1965, *ApJ*, 142, 1667  
 MacDonald, N. R., Marscher, A. P., Jorstad, S. G., & Joshi, M. 2015, *ApJ*, 804, 111  
 Mignone, A., Striani, E., Tavani, M., & Ferrari, A. 2013, *MNRAS*, 436, 1102  
 Moretti, A., Campana, S., Mineo, T., et al. 2005, *Proc SPIE*, 5898, 360  
 Nilsson, K., Pursimo, T., Villforth, C., Lindfors, E., & Takalo, L. O. 2009, *A&A*, 505, 601  
 Paggi, A., Cavaliere, A., Vittorini, V., D'Ammando, F., & Tavani, M. 2011, *ApJ*, 736, 128  
 Paliya, V. S., Sahayanathan, S., & Stalin, C. S. 2015, *ApJ*, 803, 15  
 Petropoulou, M., Giannios, D., & Sironi, L. 2016, *MNRAS*, 462, 3325  
 Pittori, C. 2013, *NuPhS*, 239, 104  
 Raiteri, C. M., Villata, M., Carnerero, M. I., et al. 2014, *MNRAS*, 442, 629  
 Raiteri, C. M., Villata, M., Lanteri, L., Cavallone, M., & Sobrito, G. 1998, *A&AS*, 130, 495  
 Roming, P. W. A., Kennedy, T. E., Mason, K. O., et al. 2005, *SSRv*, 120, 95  
 Schlafly, E. F., & Finkbeiner, D. P. 2011, *ApJ*, 737, 103  
 Schlegel, D. J., Finkbeiner, D. P., & Davis, M. 1998, *ApJ*, 500, 525  
 Sikora, M., Rutkowski, M., & Begelman, M. C. 2016, *MNRAS*, 457, 1352  
 Tavani, M., Barbiellini, G., Argan, A., et al. 2009, *A&A*, 502, 995  
 Tavani, M., Vittorini, V., & Cavaliere, A. 2015, *ApJ*, 814, 51  
 Tavecchio, F., & Ghisellini, G. 2008, *MNRAS*, 385, L98  
 Urry, C. M., & Padovani, P. 1995, *PASP*, 107, 803  
 Vercellone, S., Chen, A. W., Giuliani, A., et al. 2008, *ApJL*, 676, L13  
 Villata, M., Raiteri, C. M., Larionov, V. M., et al. 2008, *A&A*, 481, L79  
 Vittorini, V., Tavani, M., & Cavaliere, A. 2017, *ApJL*, 843, L23  
 Woo, J.-H., & Urry, C. M. 2002, *ApJ*, 579, 530



# The sdB pulsating star V391 Peg and its putative giant planet revisited after 13 years of time-series photometric data<sup>★,★★</sup>

R. Silvotti<sup>1</sup>, S. Schuh<sup>2</sup>, S.-L. Kim<sup>3</sup>, R. Lutz<sup>4</sup>, M. Reed<sup>5</sup>, S. Benatti<sup>6</sup>, R. Janulis<sup>7</sup>, L. Lanteri<sup>1</sup>, R. Østensen<sup>5</sup>,  
T. R. Marsh<sup>8</sup>, V. S. Dhillon<sup>9,10</sup>, M. Paparo<sup>11</sup>, and L. Molnar<sup>11</sup>

<sup>1</sup> INAF – Osservatorio Astrofisico di Torino, strada dell’Osservatorio 20, 10025 Pino Torinese, Italy  
e-mail: silvotti@oato.inaf.it

<sup>2</sup> Max Planck Institute for Solar System Research, Justus-von-Liebig-Weg 3, 37077 Göttingen, Germany

<sup>3</sup> Korea Astronomy and Space Science Institute, Daejeon 34055, South Korea

<sup>4</sup> German Aerospace Center (DLR), Remote Sensing Technology Institute, Münchener Str. 20, 82234 Weßling, Germany

<sup>5</sup> Department of Physics, Astronomy and Materials Science, Missouri State University, Springfield, MO 65897, USA

<sup>6</sup> INAF – Osservatorio Astronomico di Padova, Vicolo dell’Osservatorio 5, 35122 Padova, Italy

<sup>7</sup> Institute of Theoretical Physics and Astronomy, Vilnius University, Gostauto 12, Vilnius 01108, Lithuania

<sup>8</sup> Department of Physics, University of Warwick, Coventry CV4 7AL, UK

<sup>9</sup> Department of Physics and Astronomy, University of Sheffield, Sheffield S3 7RH, UK

<sup>10</sup> Instituto de Astrofísica de Canarias, Via Lactea s/n, La Laguna, 38205 Tenerife, Spain

<sup>11</sup> Konkoly Observatory of the Hungarian Academy of Sciences, Konkoly-Thege M. u 15-17, 1121 Budapest, Hungary

Received 29 June 2017 / Accepted 3 November 2017

## ABSTRACT

V391 Peg (alias HS 2201+2610) is a subdwarf B (sdB) pulsating star that shows both  $p$ - and  $g$ -modes. By studying the arrival times of the  $p$ -mode maxima and minima through the O–C method, in a previous article the presence of a planet was inferred with an orbital period of 3.2 years and a minimum mass of  $3.2 M_{\text{Jup}}$ . Here we present an updated O–C analysis using a larger data set of 1066 h of photometric time series ( $\sim 2.5\times$  larger in terms of the number of data points), which covers the period between 1999 and 2012 (compared with 1999–2006 of the previous analysis). Up to the end of 2008, the new O–C diagram of the main pulsation frequency ( $f_1$ ) is compatible with (and improves) the previous two-component solution representing the long-term variation of the pulsation period (parabolic component) and the giant planet (sine wave component). Since 2009, the O–C trend of  $f_1$  changes, and the time derivative of the pulsation period ( $\dot{p}$ ) passes from positive to negative; the reason of this change of regime is not clear and could be related to nonlinear interactions between different pulsation modes. With the new data, the O–C diagram of the secondary pulsation frequency ( $f_2$ ) continues to show two components (parabola and sine wave), like in the previous analysis. Various solutions are proposed to fit the O–C diagrams of  $f_1$  and  $f_2$ , but in all of them, the sinusoidal components of  $f_1$  and  $f_2$  differ or at least agree less well than before. The nice agreement found previously was a coincidence due to various small effects that are carefully analyzed. Now, with a larger dataset, the presence of a planet is more uncertain and would require confirmation with an independent method. The new data allow us to improve the measurement of  $\dot{p}$  for  $f_1$  and  $f_2$ : using only the data up to the end of 2008, we obtain  $\dot{p}_1 = (1.34 \pm 0.04) \times 10^{-12}$  and  $\dot{p}_2 = (1.62 \pm 0.22) \times 10^{-12}$ . The long-term variation of the two main pulsation periods (and the change of sign of  $\dot{p}_1$ ) is visible also in direct measurements made over several years. The absence of peaks near  $f_1$  in the Fourier transform and the secondary peak close to  $f_2$  confirm a previous identification as  $l=0$  and  $l=1$ , respectively, and suggest a stellar rotation period of about 40 days. The new data allow constraining the main  $g$ -mode pulsation periods of the star.

**Key words.** stars: horizontal-branch – stars: oscillations – asteroseismology – stars: individual: V391 Peg – planets and satellites: detection – planets and satellites: individual: V391 Peg b

## 1. Introduction

V391 Peg was the first case of a post-red giant branch star showing evidence of the presence of a planet (Silvotti et al. 2007 (hereafter SJS07); Silvotti 2008), indicating that giant planets may survive the first giant expansion of a star, provided that the orbital distance is large enough. For V391 Peg b, a minimum

mass of  $3.2 M_{\text{Jup}}$  was found, with an orbital period of 3.2 years, corresponding to an orbital distance of about 1.7 AU. The presence of the planet was inferred by measuring the arrival times of the maxima and minima of the stellar light, given that V391 Peg is a pulsating subdwarf B (sdB) star with at least four  $p$ -mode pulsation periods between 344 and 354 s (Silvotti et al. 2002, 2010), and a few longer-period  $g$ -modes (Lutz et al. 2009). A recent review on hot subdwarfs of spectral type O and B is given by Heber (2016).

V391 Peg b is not the first case in which the light travel-time delay is used to detect secondary low-mass bodies. In principle, the timing technique may be used on any star or stellar system that has a sufficiently stable clock, which may be given by the oscillations of the stellar flux in pulsating stars (like in this case),

\* The complete set of data shown in Fig. 1 is only available at the CDS via anonymous ftp to [cdsarc.u-strasbg.fr](http://cdsarc.u-strasbg.fr) (130.79.128.5) or via <http://cdsarc.u-strasbg.fr/viz-bin/qcat?J/A+A/611/A85>

\*\* Based on observations obtained at the following observatories: WHT 4.2m, TNG 3.6m, Calar Alto 2.2m, NOT 2.5m, Loiano 1.5m, LOAO 1.0m, MDM 1.3m, Moletai 1.6m, MONET-North 1.2m, Pizskéstető 1.0m, Mercator 1.2m, Wise 1.0m, Lulin 1.0m, Baker 0.6m.

but also radio signals in pulsars or eclipse timing in eclipsing binaries. Radio timing was used to detect the first planetary system around the pulsar PSR 1257+12 (Wolszczan & Frail 1992). The extremely high precision of the radio pulse made it possible to detect PSR 1257+12 b, the Moon-mass innermost planet of the system (Konacki & Wolszczan 2003). Of the planets detected through eclipse timing, the most convincing case is given by two circumbinary planets orbiting the pre-cataclysmic binary NN Ser. Eight years after the discovery paper (Qian et al. 2009; see also Beuermann et al. 2010) and 26 years after the first data, their existence remains the best explanation for the observed eclipse time variations (Bours et al. 2016). Many other detached close binaries show eclipse time variations: for some of them, the presence of planets is excluded by dynamic stability computations and the periodic O–C trends may be caused by other effects, such as Applegate-like mechanisms (Applegate 1992; Lanza 2006). However, for some others, the energy required to produce the quasi-periodic changes in the quadrupole moment of the secondary star referred to as the Applegate mechanism, is too high; and the presence of Jovian planets remains the most plausible explanation (Völschow et al. 2016).

The idea of using stellar pulsation to measure the reflex motion that is due to a companion is not new (e.g., Barnes & Moffett 1975). Recently, the high photometric accuracy achievable from space, in particular with the *Kepler* mission, has led to a renewed interest in this technique (Silvotti et al. 2011), and two systematic approaches based on frequency modulation (FM) and phase modulation (PM, equivalent to the O–C method) were proposed (Shibahashi & Kurtz 2012; Telting et al. 2012; Shibahashi et al. 2015; Murphy et al. 2014, 2016b).

However, to detect low-mass (substellar) companions, we need very stable pulsators. When we exclude all the solar-like oscillators, good candidates are the delta Scuti stars (Compton et al. 2016; see also recent discovery by Murphy et al. 2016a) and compact stars like white dwarfs or sdB stars. As for white dwarfs, many articles in the literature have addressed this issue (e.g., Kepler et al. 1991), but it has become increasingly evident that other effects are present that can mimic light travel time effects in the O–C diagrams of these stars (e.g., Dalessio et al. 2015). For sdB stars the situation looks more promising, perhaps because these stars have a fully radiative envelope, and there is at least one case in which the presence of a low-mass stellar companion detected from pulsation timing was confirmed by radial velocity measurements (Barlow et al. 2011b). Another recent case of a pulsation-timing detection of an F5V companion to an sdB pulsator is reported by Otani et al. (2017).

After the detection of V391 Peg b, some other planet or brown dwarf (BD) candidates orbiting sdB stars were proposed using different detection methods. From eclipse timing, about one-third of the known detached sdB/sdO + dM (dM = M-dwarf) post-common-envelope binaries (PCEB) are suspected to host planets/BDs: HW Vir (Beuermann et al. 2012 and references therein), HS 0705+6700 (alias V470 Cam, Qian et al. 2013 and references therein), HS 2231+2441 (Qian et al. 2010 and references therein; but see also Lohr et al. 2014), NSVS 14256825 (Almeida et al. 2013; Hinse et al. 2014 and references therein), NY Vir (Lee et al. 2014 and references therein), and 2M 1938+4603 (Baran et al. 2015). Interesting explorations on the origin of PCEB (and specifically sdB+MS/BD) circumbinary planets can be found in Zorotovic & Schreiber (2013), Schleicher & Dreizler (2014), Bear & Soker (2014), and Völschow et al. (2016). Very different planets or planetary remnants with terrestrial radii have been proposed from tiny reflection effects detected by the *Kepler* spacecraft

**Table 1.** Stellar parameters.

$U$	$13.35 \pm 0.03^1$
$B$	$14.35 \pm 0.02^1$
$V$	$14.57 \pm 0.02^1$
$J$ (2MASS)	$15.17 \pm 0.05$
$H$ (2MASS)	$15.16 \pm 0.10$
$K$ (2MASS)	$15.38 \pm 0.20$
$T_{\text{eff}}$	$29\,300 \pm 500 \text{ K}^2$
$\log g$	$5.4 \pm 0.1 \text{ (cgs)}^2$
$\log(N(\text{He})/N(\text{H}))$	$-3.0 \pm 0.3^2$
$M$	$0.47^3 M_{\odot}$
$R = R(M, g)$	$0.23 R_{\odot}$
$L = L(T_{\text{eff}}, R)$	$34 L_{\odot}$
$M_V = M_V(L, \text{BC})$	$3.88^4$
$d = d(V, M_V)$	$1\,400 \text{ pc}$

**Notes.** <sup>(1)</sup> Our calibration at TNG. <sup>(2)</sup> From Østensen et al. (2001). <sup>(3)</sup> SdB canonical mass (assumed), see e.g., Heber (2016). <sup>(4)</sup> Absolute  $V$  mag assuming a bolometric correction  $\text{BC} = -2.95$ .

in KIC 05807616 (Charpinet et al. 2011) and KIC 10001893 (Silvotti et al. 2014). However, none of these sdB planet/BD candidates has been confirmed with at least two independent detection methods. More robust detections of a few brown dwarfs (BDs) in eclipsing sdB binaries (also called HW Vir systems from the sdB+dM prototype) were obtained by combining stellar radial velocities (RVs) with photometric measurements: J08205+0008, J1622+4730 and V2008-1753 have companion masses of about 71, 67, and 69  $M_{\text{Jup}}$ , respectively (Geier et al. 2011; Schafftenroth et al. 2014a, 2015). At least two more sdB+BD eclipsing systems were recently found from the OGLE survey (Schafftenroth, in prep., priv. comm.). Finally, two more BD candidates in sdB binaries were found by combining radial velocities (RVs) with photometric reflection effects: CPD-64° 6481 and PHL 457, with minimum masses of 50 and 28  $M_{\text{Jup}}$ , respectively (Schafftenroth et al. 2014b).

In this paper we reconsider the case of V391 Peg, for which we have collected 6 years of new photometric time-series data, increasing the number of data points by a factor of about 2.5. The main stellar parameters of V391 Peg are summarized in Table 1. We note that the JHK magnitudes are compatible with a single sdB star and do not indicate any near-IR excess.

In Sect. 2 a short summary of the data acquisition and reduction is given, including the extraction of the pulsation frequencies. The analysis of the amplitude spectrum of the  $p$ -modes at different frequency resolutions is presented in Sect. 3. Section 4 is dedicated to the O–C analysis of the two main  $p$ -modes. In Sect. 5 we discuss the presence of the planet in the light of the new O–C results, including a perspective on future developments. In Sect. 6 we present an analysis of the  $g$ -mode amplitude spectrum. Finally, a summary of our results is given in Sect. 7.

## 2. Time-series photometric data: extraction of the pulsation frequencies

The new time-series photometric data were obtained using different telescopes and instruments (see Table 2) with at least one and often two or more comparison stars close to the target in order to remove spurious photometric modulations that are due to atmospheric transparency variations. The distribution of the

**Table 2.** Time-series photometry.

Telescope/instrument	Observers	# runs	# hours
Previous data (1999–2006) <sup>1</sup>		168	421.3
Loiano 1.5m/BFOSC	RS	20	75.4
Pizskéstető 1.0m/CCD	MP/LM	14	67.5
Moletai 1.6m/CCD	RJ	26	79.4
Wise 1.0m/CCD	EL	6	35.7
Lulin 1.0m/CCD	WSH	7	24.2
MDM 1.3m/CCD	MR	7	33.4
LOAO 1.0m/CCD	SLK	47	134.1
Monet-N 1.2m/CCD	SS/RL	20	55.0
Baker 0.6m??/CCD	MR	4	11.5
Mercator 1.2m/CCD	RØ+students	24	69.8
WHT 4.2m/ULTRACAM	TRM/VSD	7	36.7
NOT 2.6m/ALFOSC	RØ	3	11.2
TNG 3.6m/DOLORES	RS	8	18.7
Calar Alto 2.2m/CAFOS	SS/RL	10	25.9
Total new data (2007–2012)		203	644.9 <sup>2</sup>
All data (1999–2012)		371	1066.2

**Notes.** <sup>(1)</sup> See SSI07 Supplementary Information for more details (a Monet-N run of November 2006 was added to that list). <sup>(2)</sup> This number is smaller than the sum of Col. 4 given that sometimes overlapping data from different telescopes were averaged using a weighted mean.

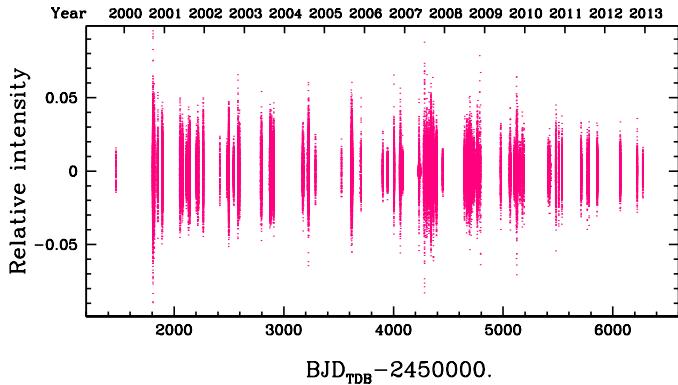


**Fig. 1.** Distribution of the 217 232 data points over 13 years. The overall duty cycle is 0.92%, and the best coverage is obtained in 2007 with a duty cycle of 5.55%. The varying relative intensity is caused by the beating between the main frequencies and also depends on the varying quality of the data.

data during the 13 years of observation is shown in Fig. 1. Most of the data were taken using a standard Johnson *B* filter. Only at NOT and MERCATOR did we use a Bessell *B* and a Geneva *B* filter, respectively. Moreover, a SLOAN *g* filter was used in the WHT-MDM run of October 2007<sup>1</sup>. The data obtained in October 2007 at the Pizskéstető, Loiano, and Lulin Observatories were collected without any filter in order to maximize the signal-to-noise ratio (S/N) of that run. The differences introduced by the different filters in terms of amplitudes or phases of the pulsation modes were considered and found to be negligible

<sup>1</sup> The WHT data were simultaneously obtained with ULTRACAM in three photometric bands (*u*, *g*, and *r*) but only the *g*-band data are used in this article, while multi-band data were previously used to identify the main pulsation modes of V391 Peg (Silvotti et al. 2010).

because of the much larger volume of standard *B* measurements. From nonadiabatic models, these differences (in particular the phase differences) are expected to be very small for  $l=0$  and  $l=1$  modes (Randall et al. 2005; see in particular their Figs. 13 and 14). The data were reduced mainly by the observers using standard procedures for aperture differential photometry. The times of all the data (new and old) were converted into Barycentric Dynamical Times ( $\text{BJD}_{\text{TDB}}$ ) following Eastman et al. (2010).

From the reduced data we extracted accurate pulsation frequencies using a classical prewhitening technique: an iterative Fourier transform (FT) process was applied subtracting the main frequency from the data residuals at each iteration, until no frequencies with amplitudes larger than four times the FT mean noise level were present. At the end of this iterative process, the pulsation frequencies, amplitudes, and phases were optimized through a multi-sinusoidal fit, whose results are given in Table 3. Appropriate statistical weights were set and considered in the sinusoidal fits of the  $p$ -modes (Silvotti et al. 2006) in order to take the varying quality of the data into account that is due to different telescope apertures, instrument efficiencies, and weather conditions.

### 3. $p$ -modes

The first problem in analyzing a data set of several years is that the pulsation frequencies are no longer constant. This was already known for V391 Peg, and a quantitative measurement of  $\dot{p}$  had been obtained from previous data giving  $\dot{p} = 1.46 \pm 0.07 \times 10^{-12}$  and  $2.05 \pm 0.26 \times 10^{-12}$  for  $f_1$  and  $f_2$ , respectively (SSI07). In general, the time variation of a pulsation frequency gradually broadens the width of the peak in the Fourier transform and may split it into different close peaks if the data set is long enough. For a linear frequency variation, the time needed to split a pulsation frequency into different close peaks is given by

$$T \approx P \left( \frac{1.5}{\dot{P}} \right)^{1/2}, \quad (1)$$

where  $P$  is the pulsation period, and the value 1.5 comes from the actual frequency resolution, given by  $\sim 1.5/T$  (Loumos & Deeming 1977). For V391 Peg we obtain  $T \approx 10$  years. However, after a few years, this effect already becomes important and makes the standard prewhitening technique (which assumes fixed frequencies and amplitudes) less efficient in returning precise frequencies. For this reason, after several tests we decided to split our analysis of the amplitude spectrum into three steps with data sets of different length and different frequency resolution.

It is useful to recall here that the two main pulsation modes of V391 Peg were identified as  $l=0$  and  $l=1$  from high-precision multi-color photometry obtained with ULTRACAM at the WHT (Silvotti et al. 2010). We show below that this identification is well supported by the current analysis.

#### 3.1. Low-frequency resolution: main pulsation frequencies

As a first step, we consider our best-quality run of October 2007, with a length of 7.9 days and a duty cycle of 35%. At this level of frequency resolution,  $\delta f \approx 2.2 \mu\text{Hz}$ , the amplitude spectrum is very clean and shows only four pulsation modes without any trace of multiplets of close frequencies (Fig. 2).

**Table 3.** Pulsation frequencies.

		$\bar{F}$ [ $\mu\text{Hz}$ ]	$\bar{P}$ [s]	$\bar{A}$ [ppt] <sup>1</sup>	Phase <sup>2</sup>
<i>p</i> -modes <sup>3</sup>	$f_1$	2860.938272(06)	349.5356784(07)	7.56	0.7327(06)
	$f_2$	2824.096225(10)	354.0955832(13)	4.06	0.7492(11)
	$f_3$	2881.123233(62)	347.0868544(74)	0.77	0.3285(58)
	$f_4$	2909.995332(63)	343.6431630(75)	0.65	0.2560(58)
	$f_2^-$	2823.932963(57)	354.1160549(72)	0.93	0.1015(54)
<i>g</i> -modes <sup>4</sup>	$F_1$	201.96312(16)	4951.3991(40)	1.01	0.116(09)
	$F_2$	295.11065(23)	3388.5596(26)	0.78	0.475(12)
	$F_3$	320.19726(23)	3123.0748(22)	0.71	0.918(13)

**Notes.** <sup>(1)</sup> ppt = parts per thousand = 0.1%. <sup>(2)</sup> Normalized phases corresponding to  $\text{BJD}_{\text{TDB}} 24\,514\,70.476568$  (1st datum). <sup>(3)</sup> For the *p*-modes, frequencies and periods are the mean values in the period 1999–2012, corresponding to  $\text{BJD}_{\text{TDB}} \sim 24\,54\,090$  (or year  $\approx 2007.0$ ), which is the weighted mean time. We note that in 10 years of observation, the secular variations of the pulsation frequencies and periods are larger than the  $1\sigma$  errors reported here, obtained from a Monte Carlo simulation assuming constant frequencies. <sup>(4)</sup> Because of the noise in the Fourier transform at low frequencies (Fig. 11), the multi-sinusoidal fits for the *g*-modes are less stable than those for the *p*-modes, and therefore the  $1\sigma$  frequency/period errors for the *g*-modes reported here are underestimated.

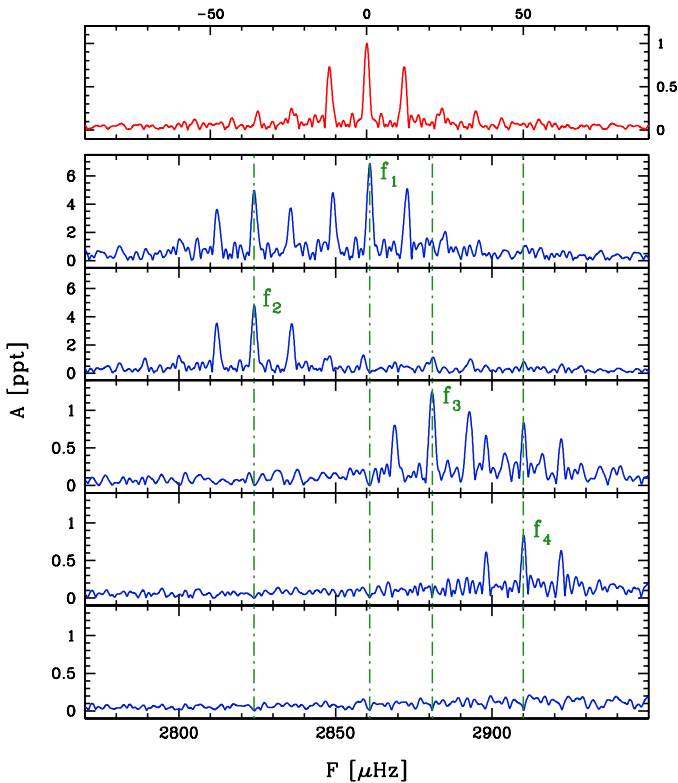


**Fig. 2.** *p*-mode amplitude spectrum of our best-quality run of 7.9 days, with a duty cycle of 35%, obtained in October 2007 with a SLOAN *g* filter using two telescopes at different longitudes: the WHT 4.2m in La Palma, equipped with ULTRACAM, and the MDM 1.3m at Kitt Peak. The upper panel shows the spectral window (red), while the other panels from top to bottom show the amplitude spectra of the data and of the residuals after one, two, three, and four prewhitening steps. A plot showing the high quality of the ULTRACAM data is presented in Silvotti et al. (2010).

### 3.2. Medium-frequency resolution: rotational splitting of $f_2$ ?

As a second step, we consider a larger data set of about 220 days, collected in 2007. This data set is a compromise between best duty cycle, best data quality, and relatively long duration in order

to detect possible rotational splitting of the pulsation modes with  $l > 0$ . At the same time, with 220 days, the effects of the long-term variations of the pulsation frequencies are still small, which keeps the amplitude spectrum relatively clean (Fig. 3). When we removed the four main pulsation frequencies through prewhitening, two low-amplitude peaks emerged from the noise, close to  $f_2$  and  $f_3$ , while nothing appeared close to  $f_1$ , which confirms that this must be an  $l=0$  mode. The peak close to  $f_3$  ( $f_3^+$ ) is only  $\sim 3.4\sigma$  above the noise, which is below our detection threshold of  $4\sigma$ . Secondary peaks close to  $f_3$  are also visible when we use the whole data set (1999–2012), but with a very low S/N. The peak close to  $f_2$  ( $f_2^-$ ), at about  $4.3\sigma$  above the noise, differs by  $-0.181\ \mu\text{Hz}$  from  $f_2$  and is also detected in the whole data set, but at a lower S/N and smaller separation of  $-0.163\ \mu\text{Hz}$  (Fig. 4 lower right panel). Using the latter separation, which is more precise, and assuming that  $f_2^-$  is part of an  $l=1$  triplet split by stellar rotation in which  $f_2$  is the central component, we obtain a stellar rotation period of about 40 days. This value is obtained in the slow rotation approximation ( $\Omega_{\text{ROT}} \ll f$ , see Ledoux 1951),

$$f_{k,l,m} = f_{k,l,0} + m\Omega_{\text{ROT}}(1 - C_{k,l}), \quad (2)$$

in which we have used a value of 0.43 for the Coriolis term  $C_{k,l}$  according to the adiabatic evolutionary models by Charpinet et al. (2002) (the model that fits best  $T_{\text{eff}}$ ,  $\log g$  and  $P$  of V391 Peg is model 19 of sequence 4). The low amplitude of the secondary peak suggests a low inclination. This interpretation is consistent with the previous identification of  $f_2$  as an  $l=1$  mode by Silvotti et al. (2010). A rotation period of  $\sim 40$  days would be compatible with the distribution of rotation periods as recently measured by the *Kepler* spacecraft in a sample of 18 dB *g*-mode pulsators (see Zong 2017 and references therein). Thirteen of them show periods between 6 and 88 days, with a mean value of about 33 days. The other five do not show any rotational splitting of the frequencies, indicating that they may have very low inclinations and/or extremely long rotation periods.

### 3.3. High-frequency resolution: frequency and amplitude variations

When we further increase the length of the data set and consider the whole light curve in the period 1999–2012, the amplitude spectrum is much more complex because of the effects of the

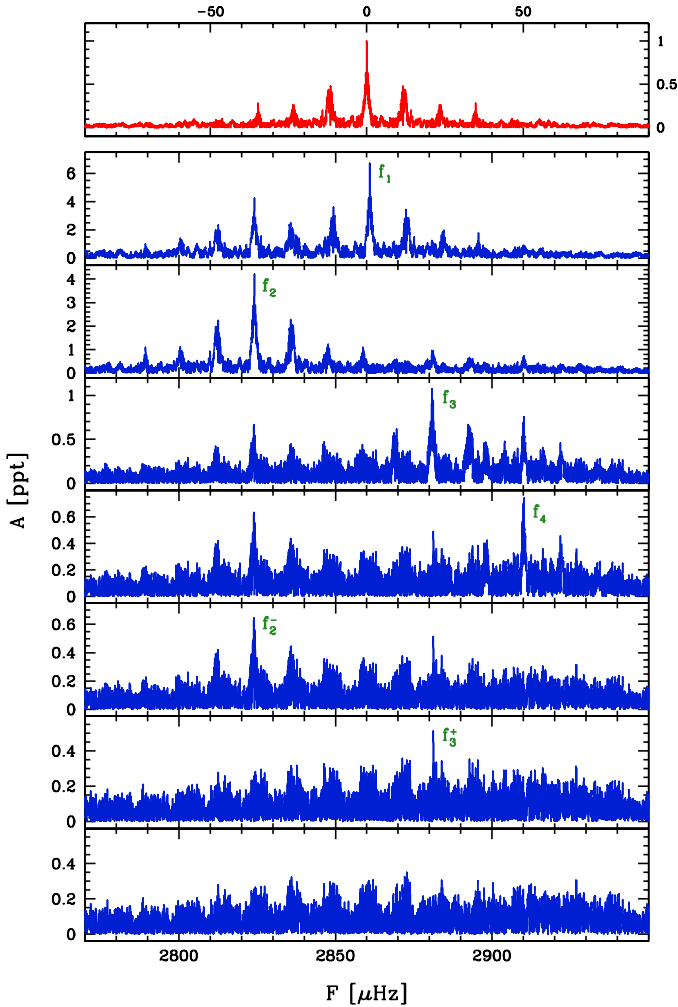


**Fig. 3.** Same as Fig. 2, but using all the data of 2007, the year with the best coverage. Thanks to the increased frequency resolution, we see that after four prewhitening steps, there is still significant power, with secondary peaks near  $f_2$  and  $f_3$  that may be due to the rotational splitting of these modes.

frequency variations, which become important (Fig. 4). When we subtract the main pulsation frequencies from the light curve through prewhitening, secondary peaks emerge very close to the main pulsation frequencies. The reason is that prewhitening subtracts from the data at each step a sine wave with constant frequency and amplitude, while on timescales of many years, pulsation frequencies and amplitudes are no longer constant. This effect, which is well visible for  $f_1$  (Fig. 4 lower left panels), adds noise to the amplitude spectrum of the residuals and may lead to incorrect determinations of the low-amplitude frequencies. In this respect, the average values of  $f_3$  and  $f_4$  might be slightly different from those reported in Table 3, with differences even larger than the errors reported there.

In order to decipher the information contained in the peaks close to  $f_1$ , we conducted a small experiment with a synthetic light curve. Since the behavior of  $f_1$  is fairly regular and relatively easy to model in the period up to 2009.0, while it becomes more irregular later on (see Figs. 7–9), we considered only the period up to 2009.0. The synthetic light curve contains a single sine wave without noise with the same time distribution as the data, a frequency and amplitude equal to  $f_1$ , and similar frequency and amplitude variations. In practice, we imposed a linear variation of the period with  $\dot{p} = 1.34 \times 10^{-12}$  (the value

found from the O–C analysis described in Sect. 4) and a sinusoidal variation of the amplitude corresponding to the sinusoidal fit shown in Fig. 7 (top right panel). The amplitude spectrum of this synthetic light curve near  $f_1$  is shown in Fig. 5 (right panels) and can be compared with the real data in the left panels. Up to the secondary peak on the right side of  $f_1$ , the agreement between real and synthetic data is very good both in terms of frequency and amplitude: we obtain  $2860.9418 \mu\text{Hz}$  and 2.74 ppt vs.  $2860.9414 \mu\text{Hz}$  and 2.61 ppt, respectively (the main peak being at  $2860.9382 \mu\text{Hz}$  with an amplitude of 8.84 ppt). Thus we verified that a linear time variation of a pulsation period splits the frequency into three close peaks almost equally spaced in frequency. If the amplitude is constant, the two secondary peaks have the same amplitude. If the amplitude is variable as in this case, the two secondary peaks have different amplitudes.

Before proceeding with our analysis on frequency and amplitude variations, it is important to verify that the uncertainties associated with frequencies and amplitudes such as those reported in Table 3 are correctly estimated. These uncertainties are the  $1\sigma$  errors obtained from a Monte Carlo (MC) simulation on 1000 synthetic light curves in which random Gaussian noise (at the same level as the data) was added to the five  $p$ -modes listed in Table 3. In Fig. 6 the distribution of frequencies and amplitudes obtained from the MC simulations is shown for the two main pulsation modes of V391 Peg ( $f_1$  and  $f_2$ ).

After we verified that the error bars of our measurements were reliable, we measured the pulsation periods and amplitudes for  $f_1$  and  $f_2$  in each observing season (Fig. 7), where observing season means the period from May to December of the same year in which V391 Peg is observable. The frequencies and amplitudes shown in Fig. 7 were obtained from multi-sinusoidal fits considering only four frequencies ( $f_1$  to  $f_4$ ), while  $f_2^-$  was excluded because it is not detected in most of these one-season runs. The same exercise was repeated using all five frequencies, but the results were less reliable.

When we consider only the data up to 2009.0, corresponding to the green part of Fig. 7, the variation of  $p_1$  can be fit with a straight line whose slope corresponds to  $\dot{p}_1 = (1.60 \pm 0.20) \times 10^{-12}$ . In the same period, the amplitude  $a_1$  shows a fairly regular sinusoidal pattern with a period of about 3400 days (9.3 years) and an amplitude of 29%. After 2009.0, the trend of the period and amplitude variations of  $p_1$  changes and  $p_1$  starts to decrease. The reason for this behavior, which is also confirmed by the O–C analysis in Figs. 8 and 9, is not known. Although we normally attribute period and amplitude variations to nonlinear interactions between different pulsation modes, in this case, with an  $l=0$  mode, we cannot invoke the resonant mode coupling between the components of a multiplet of modes split by the stellar rotation, nor even the three-mode resonance, which would require that  $f_1$  corresponds to a linear combination of the other two pulsation modes that we do not see. These two mechanisms were recently invoked as a possible explanation for the frequency and amplitude variations observed in the sdB  $g$ - and  $p$ -mode pulsator KIC 10139564 (Zong et al. 2016). The lower left panel of Fig. 7 shows that when we use all the available data, the variation in  $p_2$  can be fit with a straight line whose slope corresponds to  $\dot{p}_2 = (1.47 \pm 0.41) \times 10^{-12}$ . In the lower right panel we see quite irregular variations of  $a_2$ , but these apparent variations can be at least partially attributed to the interaction (beating) between  $f_2$  and  $f_2^-$ . When we also consider  $f_2^-$  in the fit, the individual measurements of  $a_2$  may vary by several tenths of ppt, indicating that the  $1\sigma$  error bars of  $a_2$  are underestimated. At shorter timescales, we did not find any periodicity in the amplitude variations of  $a_2$  that could confirm

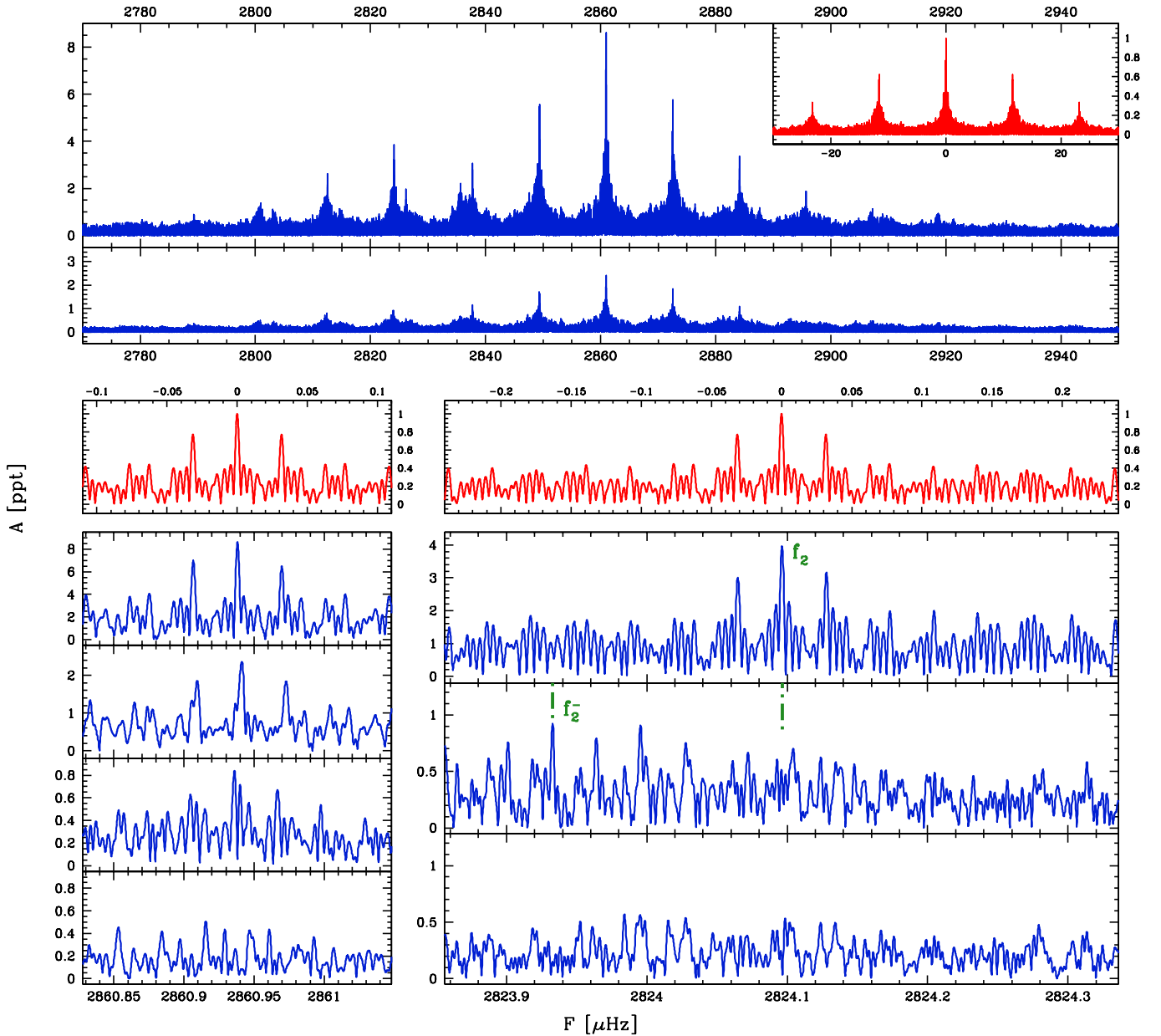


**Fig. 4.** Same as Figs. 2 and 3, but using the whole data set (1999–2012). *Upper panels:* amplitude spectrum of the data and of the residuals (on the same vertical scale) after subtracting the four main pulsation frequencies ( $f_1$  to  $f_4$ ). We note that the residual power is significantly higher than in Fig. 3. The small box shows the normalized spectral window (red) with the one-day aliases at  $\pm 11.57 \mu\text{Hz}$ . *Lower panels (from top to bottom):* normalized spectral window (red) with the 1-year aliases at  $\pm 31.7 \text{ nHz}$ , and details of the amplitude spectrum of data and residuals near  $f_1$  (left) and  $f_2$  (right). The horizontal scale in the left and right panels is the same. Two vertical dashed lines (green) highlight two components of a possible rotational splitting. See text for more details.

the beating effect and thus the rotation period of the star around 40 days. The mean quality of the data is not sufficient for detecting this effect. Based on our best-quality run of October 2007 at the WHT-MDM, we can only exclude short timescale variations (from night to night) for both  $a_1$  and  $a_2$ .

We also attempted to fit the data from 1999 to the end of 2008 with two sine waves corresponding to  $f_1$  and  $f_2$ , leaving as free parameters not only the frequencies, amplitudes, and phases, but also  $\dot{p}_1$  and  $\dot{p}_2$ . The fit converged only when we fixed  $\dot{p}_2$ , but the value that we obtained for  $\dot{p}_1$  is about ten times higher than the value obtained from the direct measurements. This method is less reliable than the direct method or the O–C method described in the next section because it makes use of

constant amplitudes, but we know that the amplitudes are not constant, and in particular,  $a_1$  varies significantly (Fig. 7).

While amplitude variations in sdB  $p$ -mode pulsators have been known for a long time, with time scales ranging from days to years, the results reported in this section show that even the frequencies are less stable than previously believed and may suffer significant variations that are not simply due to the long-term modifications of the stellar structure. Amplitude and frequency variations have recently been detected in most of the sdB pulsators observed by the *Kepler* spacecraft, with complex patterns that sometimes are stochastic (Østensen et al. 2014) and sometimes more regular and periodic (e.g., Zong et al. 2016).

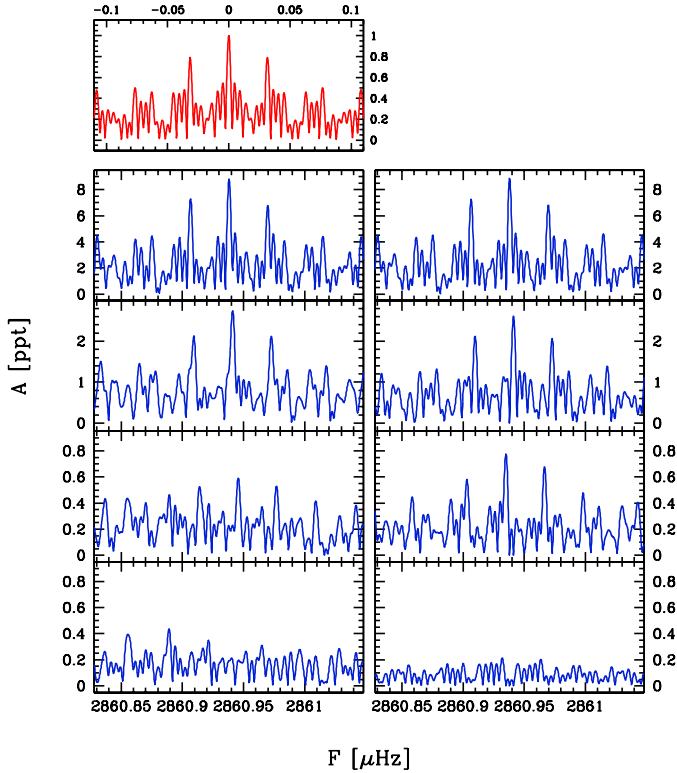


**Fig. 5.** Comparison between the amplitude spectrum near  $f_1$  of the data (*left*) and the amplitude spectrum near  $f_1$  of a simulated data set (*right*) with the same time distribution. In this test we used only the data up to 2009.0 because in this period it is easier to simulate the behavior of  $f_1$ . For the simulated data we used a single pure sine wave (no noise) with the same frequency and amplitude of  $f_1$  and also with similar long-term frequency and amplitude variations (linear variation of the period with  $\dot{p} = 1.34 \times 10^{-12}$ , as derived by the O–C analysis, and sinusoidal variation of the amplitude like in Fig. 7 upper right panel, green section). Like in the previous figures, the upper left panel is the normalized spectral window (red), while the other panels are the amplitude spectra of data and residuals after one, two, and three prewhitening steps. This simple test shows that up to the secondary peak on the right side of  $f_1$ , the data are well reproduced by the simulation, both in terms of frequency and amplitude. See text for more details.

#### 4. O–C analysis

The O–C analysis (Sterken 2005; and subsequent articles in the same volume) is a powerful method for detecting tiny variations of the pulsation periods on long timescales that cannot be seen or clearly seen from direct independent measurements (like in Fig. 7). The O–C method is more sensitive than the direct method because instead of directly measuring the period change, it measures the phase variations induced by the period change. When we consider a period that changes linearly in time (a good approximation on timescales of a few years, extremely short with respect to the evolutionary timescales), the phase variations have the great advantage of being proportional to  $T^2$ , where  $T$  is the duration of the observation.

In order to reduce the phase errors, the data for the O–C analysis were considered in monthly subsets. A four-sinusoid fit was applied to each subset using the best (fixed) frequencies from Table 3 ( $f_1$  to  $f_4$ ) and leaving amplitudes and phases as free parameters.  $f_2^-$  was not used because it is not detected in the monthly subsets.

The difference between these monthly phases and those obtained from the whole data set are the O–C differences shown

in Fig. 8, in which the phase differences have been converted into time differences. In Fig. 8 we see the same effect as was already seen in Fig. 7: since 2009, the curvature in the O–C diagram of  $f_1$  changes. We do not know the reasons for this change, it might be related to nonlinear interactions between different pulsation modes. In any case, it is clear from Fig. 8 (upper panels) that a two-component fit with a parabola plus a sinusoid (like in SSJ07) can give satisfactory results only up to  $\sim 2009$ . When considering only the data up to 2009.0, the long-term parabolic variation of the main pulsation period corresponds to  $\dot{p}_1 = (1.36 \pm 0.06) \times 10^{-12}$ . In order to also fit the more recent data, we tried a different approach using two sinusoids (lower panels of Fig. 8). Even in this way, we did not obtain a reasonable fit of the whole data set, and moreover, the quality of the fit up to 2009 is lower, indicating that a sinusoidal  $\dot{p}$  is not the solution.

As a second step, the O–C analysis was repeated using larger data subsets covering a whole observing season (that is, from May to December for V391 Peg) and using the same pulsation frequencies as before. Again,  $f_2^-$  was not used because it is not detected in almost all runs. These larger subsets are particularly useful for  $f_2$  (the secondary pulsation frequency), in order to reduce the phase errors that are very large when we use the monthly subsets. The results are shown in Fig. 9. In the upper panels (from 1A to 2B), we see the O–C diagram of  $f_1$  and  $f_2$  when using only the data from 1999 to 2007.0, basically the same data as in SSJ07 (only three short runs were added), but with the new updated frequencies. These plots show that when we use better values for  $f_3$  and  $f_4$ , the sinusoidal components of  $f_1$  and  $f_2$  (panels 1B and 2B) differ: even if the amplitudes and the initial phases are still in agreement (like in SSJ07), the periods are now different. In the central panels (from 3A to 4B), we see the new fits when we use the data from 1999 to 2009.0, before the change of sign of  $\dot{p}_1$ : the sinusoidal components of  $f_1$  and  $f_2$  (panels 3B and 4B) are similar to the previous ones (panels 1B and 2B), except for a larger amplitude for  $f_2$ , which increases the differences between  $f_1$  and  $f_2$ . The parabolic components (panels 3A and 4A) correspond to  $\dot{p}_1 = (1.34 \pm 0.04) \times 10^{-12}$  and  $\dot{p}_2 = (1.62 \pm 0.22) \times 10^{-12}$ , in good agreement with the previous measurements of SSJ07. These numbers also agree with adiabatic theoretical expectations for the secular variation of the pulsation periods (Charpinet et al. 2002). However, the fact that  $\dot{p}_1$  changed sign near 2009 indicates that in real stars, these processes may be more complicated. Finally, in the lower panels of Fig. 9 (from 5A to 6B), we show the best two-component fits of the whole data set using two sinusoids with different periods for  $f_1$ , and a parabola plus a sinusoid for  $f_2$ . Except for the last points, these fits can reproduce the general trend of the O–C data (panels 5A and 6A), but show a large dispersion, particularly for  $f_1$ : the sinusoidal fits in panels 5B and 6B (chi-squared equal to 894 and 276, respectively) are only slightly better than a simple straight line ( $\chi^2 = 1075$  and 322). At the same time, the two sinusoidal components have similar periods, amplitudes, and phases within 4%, 8%, and 7% respectively.

In order to explore this in more detail, we made a weighted average of the O–C data in panels 5B and 6B (which means a weighted average of the O–C data of  $f_1$  and  $f_2$  after subtracting their long-term component). The result is illustrated in Fig. 10 and shows that when we sum the information from  $f_1$  and  $f_2$ , the fit of the sinusoidal component improves, and at the end, we have 9 points out of 13 that are consistent with a sine wave with a period of  $1127 \pm 45$  days (or  $3.09 \pm 0.12$  years) and an amplitude of  $3.02 \pm 0.85$  light seconds. Assuming that the sine wave is caused by the planet and that the mass of the sdB star is  $0.47 M_\odot$ ,

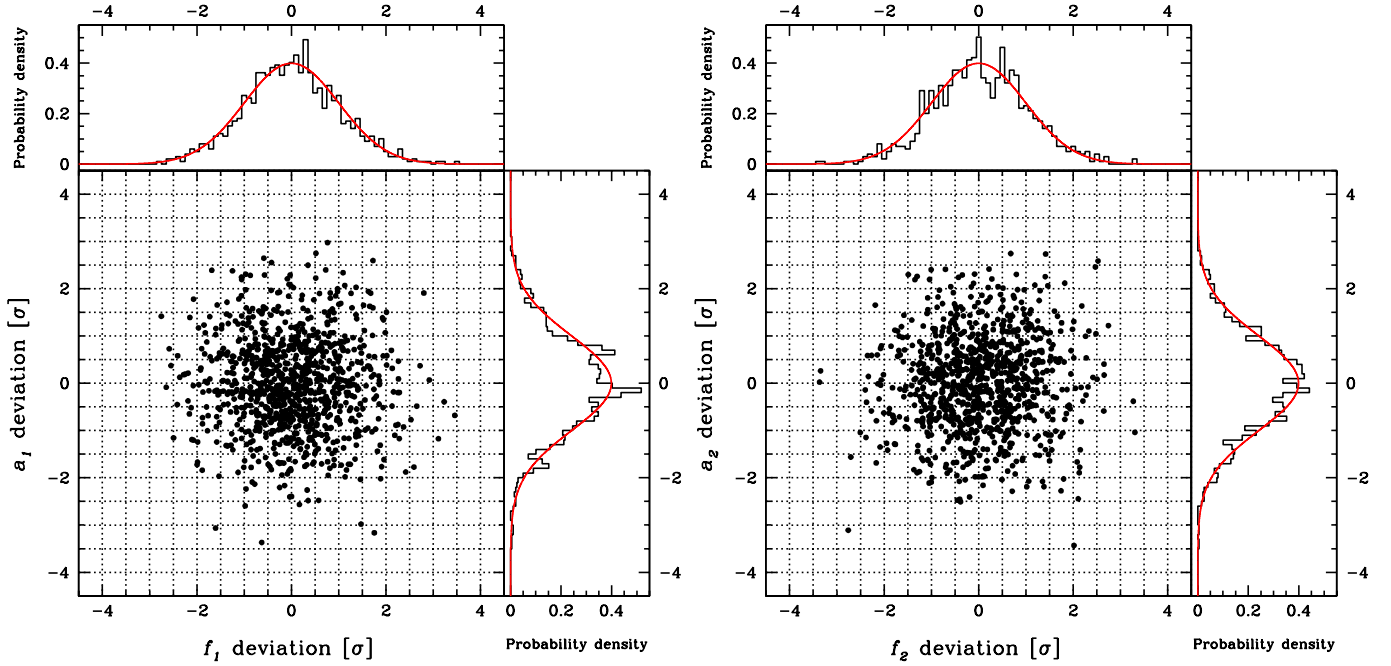


**Fig. 6.** Distribution of the frequency and amplitude deviations for the two main pulsation modes of V391 Peg. The deviations, in units of  $1\sigma$  errors, are the differences between the values obtained from the original light curve and those obtained from 1000 artificial light curves created by the MC simulator of Period04 (Lenz & Breger 2005). The synthetic light curves are built using the five  $p$ -modes of Table 3 and adding Gaussian noise at the same level as the original data. The 2D distributions are also projected into 1D histograms and compared with a normal distribution (red).

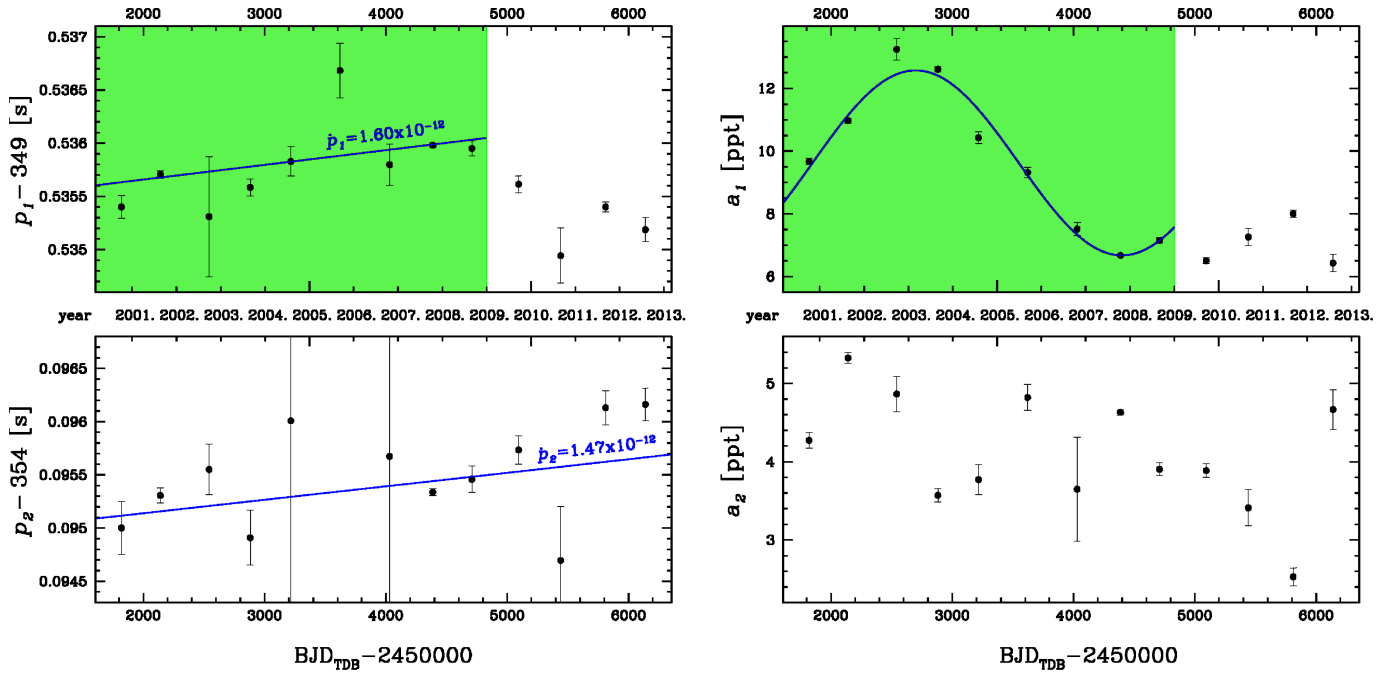


**Fig. 7.** Period and amplitude variations of the two main pulsation modes of V391 Peg. The variation of  $p_1$  is compatible with a linear increase up to 2009.0, when a change of regime appears. The same change is also visible for the amplitude: up to 2009.0,  $a_1$  shows a fairly regular sinusoidal shape with a period of about 3400 days or 9.3 years. A linear increase of the pulsation period is visible also for  $p_2$  when considering the whole data set, while the irregular variations of  $a_2$  can be at least partially attributed to the beating between  $f_2$  and  $f_2^-$ . More details are given in the text.

these numbers correspond to an orbital distance of 1.6 AU and a minimum mass of  $1.8 M_{\text{Jup}}$ .

Although not shown in Fig. 9, we also tried to fit the O-C plots of  $f_1$  and  $f_2$  with a parabola plus two sinusoids (corresponding to two potential planets), but we were unable to find any solution for which the six parameters of the two sinusoids were in reasonable agreement between  $f_1$  and  $f_2$ .

Several checks were made in order to ensure that the new O-C results reported in this section are correct and robust and to understand why in SSJ07 periods, amplitudes, and phases of the sinusoidal components of the O-C diagrams of  $f_1$  and  $f_2$  agreed so well. As stated previously, the current O-C results were obtained using four frequencies ( $f_1$  to  $f_4$ ), also including the data taken with filters different from Johnson  $B$ , and



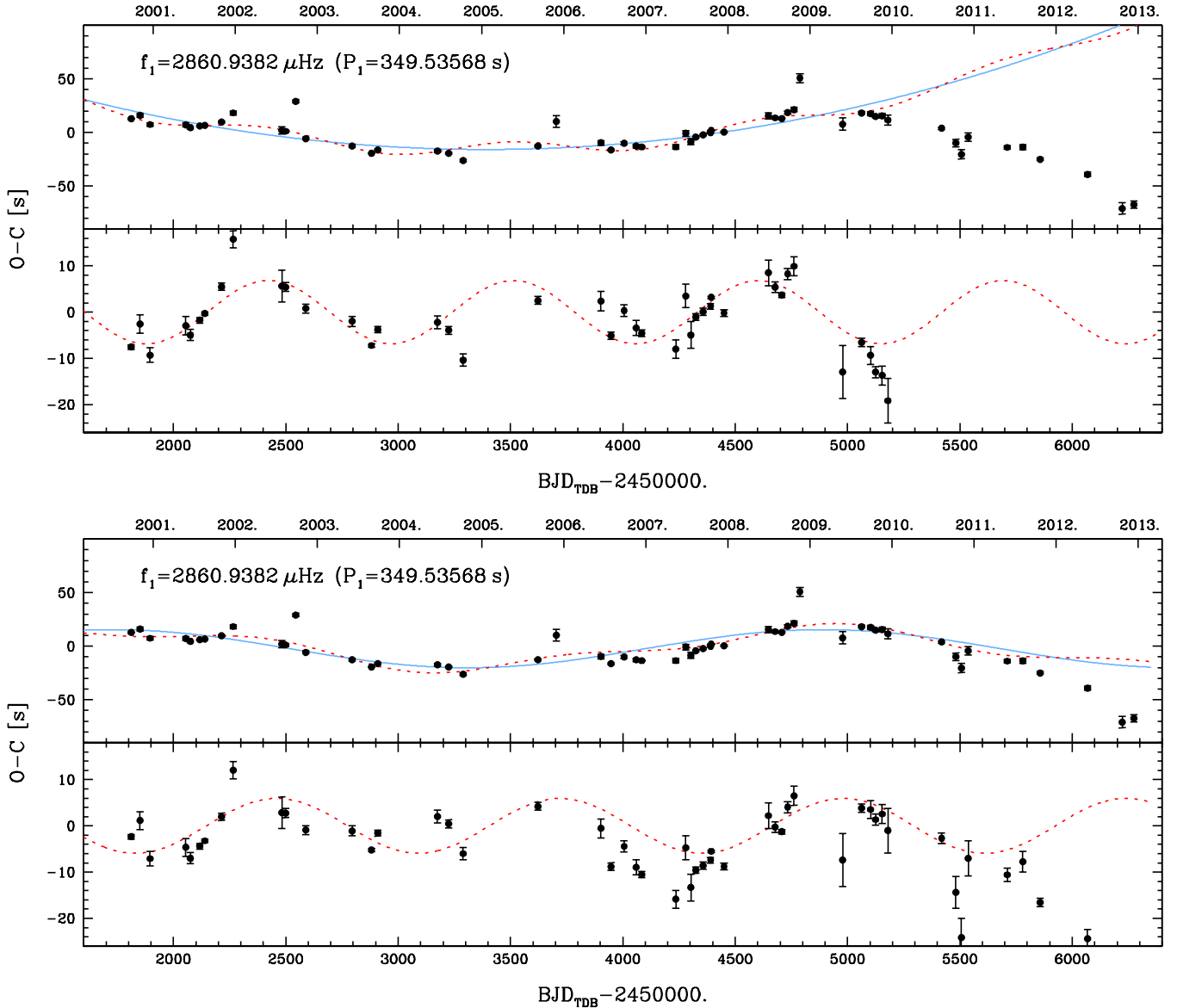


**Fig. 8.** O–C diagram of the main pulsation mode of V391 Peg when using monthly runs (each point represents the data collected within one month). Upper panels: fit of the O–C data with a parabola (long-term variation, blue continuous line) plus a sine wave (“planetary component”, red dashed line) and planetary component alone after subtracting the long-term component. This solution gives satisfactory results only up to the end of 2008, and the fit was made considering only the data up to 2009.0. Lower panels: same as upper panels, but using two sinusoids. In this case, the fit was made using all the data, but a reasonable fit is obtained only up to  $\sim 2010$ , indicating that two components are simply not enough to obtain a reasonable fit of all the data. When we compare the planetary component alone in the period 2000–2009.0, the fit is better when we use parabola + sine wave ( $\chi^2 = 762$ ) with respect to the double sine wave ( $\chi^2 = 1267$ ); for comparison, a straight line would give  $\chi^2 = 1376$ .

making use of statistical weights. However, we also tested different combinations without statistical weights, excluding all the data taken in filters different from Johnson *B* (see Sect. 2), and considering only the two main frequencies  $f_1$  and  $f_2$ . In all these tests, the results varied little<sup>2</sup>. Thus it is not easy to understand the differences between our current results and those obtained in SSJ07 (even in that analysis, similar tests with different combinations were made). We conclude that the good

<sup>2</sup> When we consider only  $f_1$  and  $f_2$  in the multi-sinusoidal fits instead of four frequencies, the results are almost identical to those reported in panels 3A to 4B of Fig. 9. When we use only Johnson-*B*-filter data, the main difference is that the period of the sinusoidal component of  $f_1$  increases by 7%. When we do not use statistical weights, we obtain the largest difference, with the amplitude of the sinusoidal component of  $f_2$  reduced from 9.4 to 5.4 s, while all other parameters remain about the same.

agreement found in SSJ07 was a coincidence due to a few small differences between the two analyses: slightly different pulsation frequencies, two NOT observing runs that were excluded in SSJ07 because they were taken with a Bessell *B* filter and that are now included (after careful tests of the effects on phase and amplitude), and one new standard-*B*-filter Monet-N observing run that was not yet available in SSJ07. Of these factors, the greatest is probably given by the different frequencies that were used. In SSJ07 we used  $f_1 = 2860.9387$ ,  $f_2 = 2824.0965$ ,  $f_3 = 2880.6842$ ,  $f_4 = 2921.8463$ , and  $f_5 = 2882.0039 \mu\text{Hz}$ . Comparing these values with those in Table 3, we see very small differences for  $f_1$  and  $f_2$ , compatible with real period variations; the new value of  $f_3$  is higher by  $0.4390 \mu\text{Hz}$ ;  $f_5$  is not confirmed and used not at all in the new analysis, but its influence must be small because of the very low amplitude. Finally and mostly important, the updated value of  $f_4$  is lower by  $11.8510 \mu\text{Hz}$  with

respect to the old value, which means that in SSJ07, because of the poorer spectral window, we used an incorrect value corresponding to the one-day alias on the right side of the correct peak. This is probably the mean reason of the different results. An incorrect value of  $f_4$  can modify the multi-sinusoidal fits and thus slightly modify the phases of  $f_1$  and  $f_2$  as well.

## 5. V391 Peg b: real planet or false detection?

Whether V391 Peg b is a real planet or a false detection is an open question. The O–C diagrams of  $f_1$  and  $f_2$  provide arguments in favor and against the presence of V391 Peg b.

- (1)  $f_1$ : considering the period up to 2009.0, the O–C diagram of  $f_1$  still has a sinusoidal component that can be explained by the presence of a giant planet with a minimum mass of  $3.5 M_{\text{Jup}}$ , orbiting V391 Peg in 3.1 years at a distance of 1.7 AU. However, the behavior of  $f_1$  after 2009.0 shows that this is more complex, and we see from Figs. 8 and 9 that a simple two-component fit of the O–C data is not enough to interpret the whole data set up to 2012. Using two sinusoids with different periods allows us to fit the O–C data up to 2010 or 2011, but the quality of the fit is much poorer. When we use two sinusoids, the period of the sine wave corresponding to the planet (Fig. 9/5B) is longer than the period obtained with a parabola plus a sine wave (Fig. 9/3B);
- (2)  $f_2$ : up to 2009.0, the O–C diagram of  $f_2$  also shows a sinusoidal component, but now, unlike SSJ07, the period and the amplitude differ from  $f_1$  by  $\sim 20\%$  and  $\sim 36\%$ , respectively. The new data support the previous identification of  $f_2$  as an  $l=1$  mode, and this implies that frequency splitting due to stellar rotation must be at work. Regardless of whether our detection of  $f_2^-$  is real, these modes split by stellar rotation must be there, close to  $f_2$ , and this is a source of noise for the O–C computations of  $f_2$ . This argument makes the O–C results from  $f_1$  (which is an  $l=0$  mode) more reliable, and this is one of the reasons why the presence of the planet cannot be excluded. At the same time, this argument can partially explain the discrepancies between the O–C diagrams of  $f_1$  and  $f_2$ ;
- (3)  $f_1+f_2$ : when we try to fit the whole set of O–C data using a sine wave plus a longer-period sinusoid for  $f_1$  and a parabola for  $f_2$  (panels 5 and 6 of Fig. 9), we see that the sine wave corresponding to the planet is very similar for  $f_1$  and  $f_2$  in terms of period, amplitude, and phase (panels 5B and 6B of Fig. 9). Although these fits are of poor quality, it is possible to obtain a substantial improvement when we use both pulsation frequencies together (Fig. 10). If we interpret this effect with the presence of the planet, we obtain a minimum mass of  $1.8 M_{\text{Jup}}$ , while the orbital period and distance, 3.1 years and 1.65 AU, do not change much with respect to the values obtained previously.

In conclusion, while in SSJ07 the presence of a planet orbiting V391 Peg was robustly and independently suggested by the two main pulsation modes of the star, these two modes now give contradictory indications. A sinusoidal component is still visible in the O–C diagrams of both  $f_1$  and  $f_2$ , but the parameters of the two sinusoids are different in general. The presence of a planet orbiting V391 Peg is clearly much less robust than before, although it cannot be entirely excluded.

The peculiar behavior of  $f_1$  with a quite sudden change of sign of its time derivative after 2008 suggests that pulsation

timing is a delicate method, with aspects that are still unclear and are likely related to nonlinear pulsation effects. As a consequence, the reliability of the O–C method to find low-mass companions should be questioned, without forgetting, however, that for sdB stars we have at least two cases in which the presence of a stellar companion was detected through pulsation timing (Barlow et al. 2011a; Otani et al. 2017), and in one case, for CS 1246, this detection was confirmed by radial velocity (RV) measurements (Barlow et al. 2011b). With respect to V391 Peg, the O–C detection was easier in both cases because of the much higher companion mass, and for CS 1246, also because of the much shorter orbital period of  $\sim 14$  days, which meant no problems with the long-term variation of the pulsation period. Unlike CS 1246, which exhibits a single large-amplitude radial mode, and EC 20117-4014, which shows three low-amplitude pulsation modes with frequency separations of  $\sim 250$  and  $\sim 680 \mu\text{Hz}$  (Otani et al. 2017), with V391 Peg we have the additional difficulty that all four pulsation modes are concentrated within  $86 \mu\text{Hz}$ , which makes it more difficult to measure the phases accurately.

In order to confirm or definitively reject the presence of V391 Peg b, an independent confirmation with another method is needed. Given that *Gaia* astrometry is not accurate enough at a distance of about 1400 pc, spectroscopic RVs seem the most natural way to proceed. However, the RV “noise” produced by the pulsations is a serious concern and can easily reach several hundred m/s, while the expected planetary signal is no more than 100 m/s. Given the very different time scales, it is in principle possible to remove or reduce the noise due to the pulsations, provided that we know the Fourier spectrum and the main pulsation modes in detail. This is true for the high-frequency part of the spectrum (the  $p$ -modes), which is relatively simple, with only two dominant modes that have similar periods. The noise due to the  $p$ -modes can be reduced by choosing an exposure time close to an integer multiple of  $\sim 350$  s. For the  $g$ -modes, the situation is more complicated as the low-frequency part of the Fourier spectrum is not well known (see next section). The noise can be reduced by averaging the results obtained from different spectra taken in the same epoch at different pulsation phases. A great help for a precise determination of the  $g$ -modes may come from the Transiting Exoplanet Survey Satellite (TESS; Ricker et al. 2016), which can observe V391 Peg continuously for 54 days in some years from now, with a sampling time of 20 or 120 s.

## 6. $g$ -modes

$g$ -modes were detected in V391 Peg by Lutz et al. (2009). Our new larger data set has been used to confirm this detection. Given that the  $g$ -modes are particularly disturbed by the atmospheric variations that act at similar frequencies, we selected a subset of high-quality data with a length of each single run of at least a few hours. This subset, which has a total duration of 192.8 h spread over 5.8 years (between 2002 and 2008), was corrected for differential atmospheric extinction (the comparison stars are always much redder than the sdB) and analyzed. The amplitude spectrum in Fig. 11 shows two regions with an excess of power near 180 and  $310 \mu\text{Hz}$  and three peaks that emerge from the noise at more than  $5\sigma$ . The corresponding frequencies, amplitudes, and phases are listed in Table 3. The noise threshold, which was  $4\sigma$  for the  $p$ -modes, was increased to  $5\sigma$  because the spectrum is much more noisy in this region. After these three peaks were subtracted from the data, the lower panel of Fig. 11 shows that some residual power is still there, suggesting that further low-amplitude frequencies are likely present below

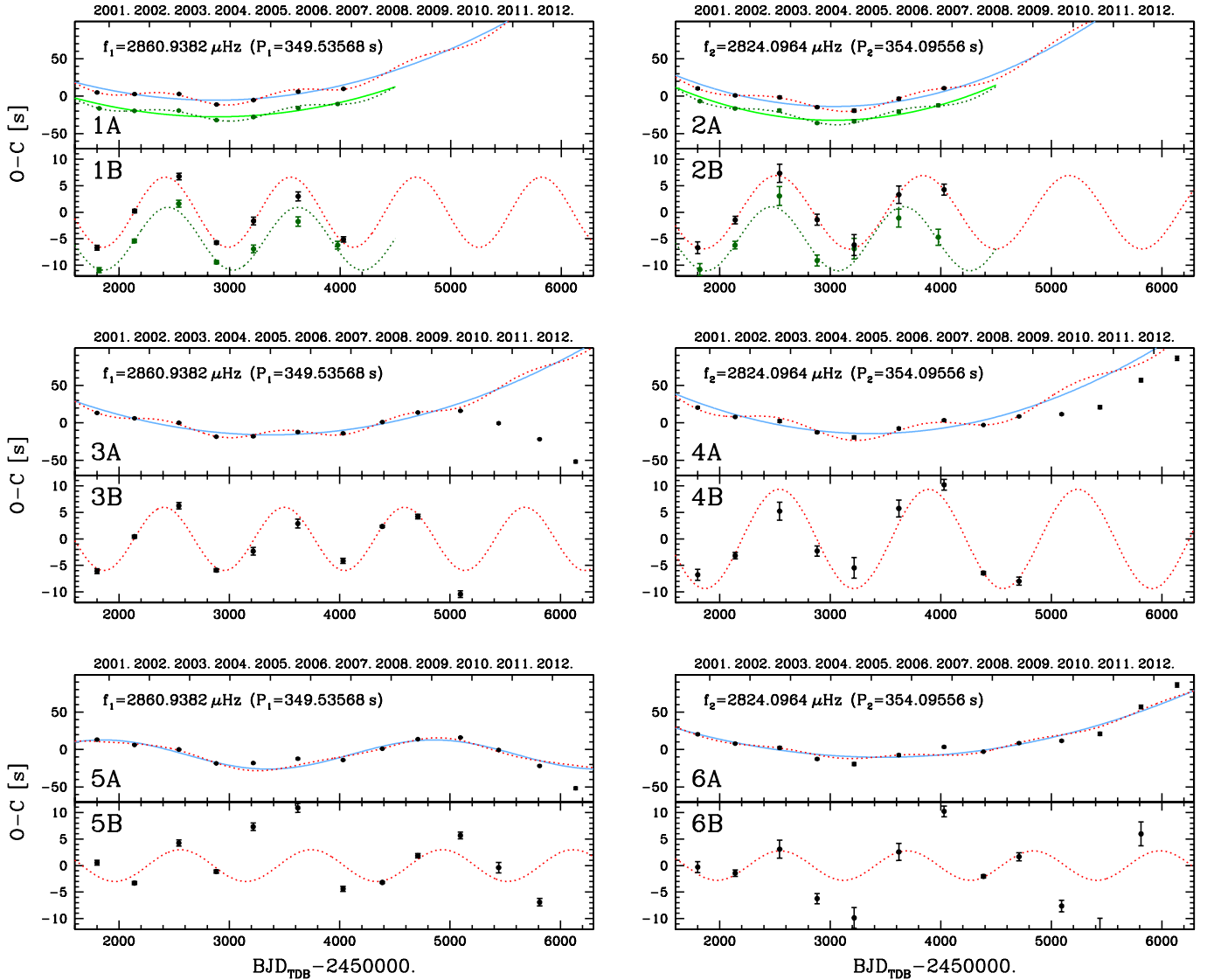


**Fig. 9.** Same as Fig. 8 for  $f_1$  (left) and  $f_2$  (right) for one-season runs. Panels 1A, 1B, 2A, and 2B are obtained using only the data up to 2007.0, so that we can directly compare the current results (blue and red lines) with those obtained by SSJ07 (green lines shifted by  $-20$  and  $-5$  s in panels 1A and 2A and 1B and 2B, respectively). The small horizontal shifts of the first and last points are due to the addition of three observing runs that were not present in SSJ07. Panels 1B and 2B show that in the current results, the period of the sinusoid is slightly shorter for  $f_1$  but longer for  $f_2$ , so that at the end the agreement between  $f_1$  and  $f_2$  is worse with respect to SSJ07. The reasons of these differences are discussed in the text. When we add the new data, the longer period of the sinusoidal component of  $f_2$  with respect to  $f_1$  is confirmed (panels 3B and 4B), and moreover, we note a further difference in amplitude. Panel 3A confirms the change of regime of  $f_1$  near 2009 that was already visible in Figs. 7 and 8. This change also tends to worsen the fit of  $f_2$  (4A), and for this reason, the fits shown in panels 3A to 4B are obtained considering only the data up to 2009.0. Panels 5A and 5B show an alternative solution obtained using a low-frequency sine wave for the long-term component of  $f_1$ , as in the lower panels of Fig. 8. The fits shown in panels 5A to 6B were obtained using all the available data. More comments are given in the text.

the noise threshold. As anticipated in the previous section, in 2 years from now, TESS will be able to shed light on this part of the Fourier spectrum and likely measure the rotation period of the star, confirming or refuting the tentative rotation period of  $\sim 40$  days suggested by the  $p$ -mode analysis in Sect. 3.2.

## 7. Summary

Interpreting the new O-C results shown in Figs. 8 and 9 is more complicated than it was 10 years ago. At that time, the very good agreement between the sine-wave component of  $f_1$  and  $f_2$  strongly supported the presence of a giant planet (SSJ07). Now, with many more data, this agreement is much more uncertain and the presence of V391 Peg b is weaker and requires confirmation

with an independent method. Like in SSJ07, a two-component fit (parabola + sine wave) still gives satisfactory results for both  $f_1$  and  $f_2$ , at least up to 2009. The sinusoidal components of  $f_1$  and  $f_2$ , however, now differ in period and amplitude by  $\sim 20\%$  and  $\sim 36\%$ , respectively. Starting in phase, after two cycles the O-C sine wave of  $f_2$  is antiphased with respect to  $f_1$ . When we consider all the O-C data from 1999 to 2012, a two-component fit is in general not satisfactory. For  $f_1$ , we tried to fit the O-C data with a double sine wave, corresponding to a sinusoidal behavior of  $\dot{p}_1$ . The result is a very poor fit. However, this solution produces a certain agreement between the sinusoidal components of  $f_1$  and  $f_2$ .

The change in sign of the time derivative of the main pulsation period near 2009 is an intriguing phenomenon that is difficult to explain. Nonlinear interactions between pulsation

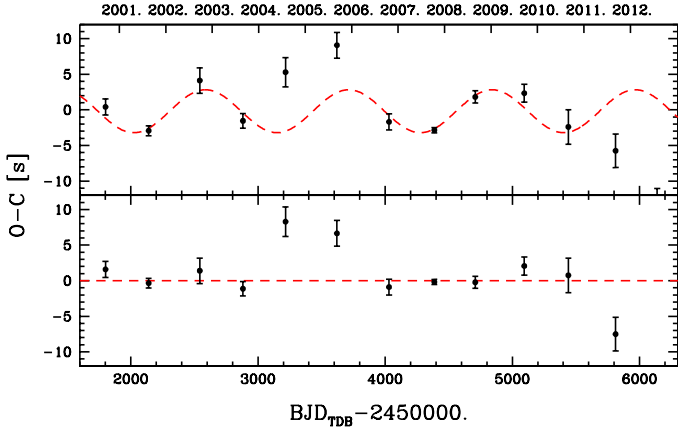


**Fig. 10.** O–C diagram obtained by combining the information from  $f_1$  and  $f_2$ . In practice, we have computed the weighted average of the points in panels 5B and 6B of Fig. 9 and recomputed the best fit with a sine wave. Compared with these panels, the fit is significantly improved and the residuals of 9 points out of 13 (including all those with smaller error bars) are close to zero.

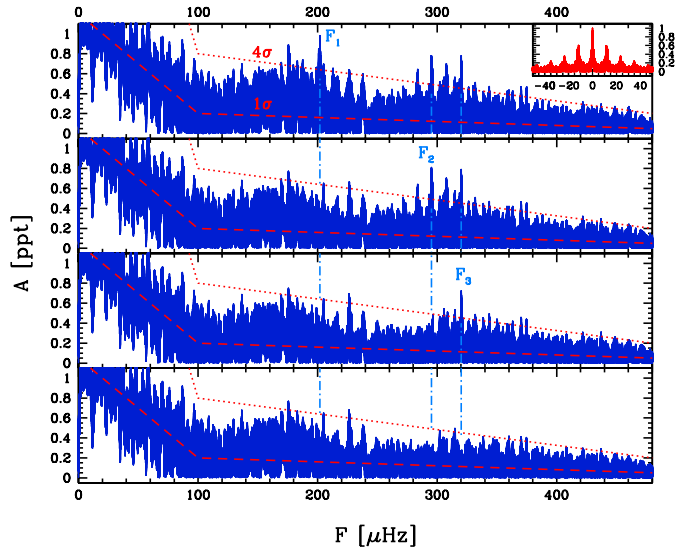


**Fig. 11.**  $g$ -mode amplitude spectrum using our best-quality runs between 2002 and 2008 (192.8 h of observations in total). The upper right panel shows the spectral window (red), while the other panels from top to bottom show amplitude spectrum and residuals after one, two, and three prewhitening steps. We note an excess of power in two main regions near 180 and 310  $\mu\text{Hz}$ . After prewhitening, this excess of power is not completely removed near 180  $\mu\text{Hz}$ , suggesting that further low-amplitude frequencies are present in that region.

modes seem the most natural explanation, but the  $l=0$  identification (Silvotti et al. 2010), which is confirmed by the new data, does not help as we cannot invoke resonant mode coupling between the components of a multiplet nor resonance between modes linked by linear combinations that we do not see. The irregular behavior of  $f_1$  agrees to a certain extent with recent *Kepler* results, which showed that sdB pulsation frequencies are in general less stable than previously believed. The *Kepler* results are mostly focused on  $g$ -modes, but a similar behavior seems also relatively common for the  $p$ -modes. At least this is suggested by our results.

The  $l=1$  identification for  $f_2$  (Silvotti et al. 2010) is also confirmed by the new data (or at least  $l$  must be  $>0$ ). A retrograde

mode is detected, although at the limit of our detection threshold, and this suggests a stellar rotation period of about 40 days.

Using only the data up to 2009.0, we can improve our previous measurements of  $\dot{p}$  for  $f_1$  and  $f_2$  and obtain  $\dot{p}_1 = (1.34 \pm 0.04) \times 10^{-12}$  and  $\dot{p}_2 = (1.62 \pm 0.22) \times 10^{-12}$ . The order of magnitude of these numbers is in agreement with theoretical expectations for evolved models of extreme horizontal branch stars (Charpinet et al. 2002), and their positive sign would normally be interpreted as an indicator of a stellar expansion. At least for  $f_1$ , however, the change in curvature near 2009 implies that these numbers are not simply or directly related to the evolutionary timescales expected from theory, and the situation is more complicated.

Finally, the new data confirm that V391 Peg is a hybrid pulsator, showing both  $p$ - and  $g$ -modes. The next opportunity for a more detailed study of this star, and in particular for the study of the low-frequency part of its Fourier spectrum, is given by the TESS mission, which may observe V391 Peg continuously for 54 days in about 2 years from now. With a better knowledge of the Fourier spectrum at low frequencies as well, it should be easier to confirm or reject the presence of a planet orbiting V391 Peg by measuring the spectroscopic radial velocities of the star.

*Acknowledgements.* We thank Elia Leibowitz, who made the data collected at the Wise Observatory available to us, Christopher D. J. Savoury for helping us with the ULTRACAM observations and data reduction, and Wen-Shan Hsiao for contributing the Lulin data. We also thank Patrick Lenz for providing us with a modified version of period04, which facilitated the error estimation from the MC simulations. V. S. D. and ULTRACAM are supported by STFC grant ST/J001589/1. L. M. was supported by the Hungarian National Research, Development and Innovation Office (NKFIH) grant PD-116175 and the János Bolyai Research Scholarship of the Hungarian Academy of Sciences.

## References

- Almeida, L., Jablonski, F., & Rodrigues, C. 2013, *ApJ*, 766, 11
- Applegate, J. H. 1992, *ApJ*, 385, 621
- Baran, A. S., Zola, S., Blokesz, A., Østensen, R. H., & Silvotti, R. 2015, *A&A*, 577, A146
- Barlow, B. N., Dunlap, B. H., & Clemens, J. C. 2011a, *MNRAS*, 414, 3434
- Barlow, B. N., Dunlap, B. H., & Clemens, J. C. 2011b, *ApJ*, 737, L2
- Barnes, T. G. III, & Moffett, T. J. 1975, *AJ*, 80, 48
- Bear, E., & Soker N. 2014, *MNRAS*, 444, 1698
- Beuermann, K., Hessman, F. V., Dreizler, S., et al. 2010, *A&A*, 521, L60
- Beuermann, K., Dreizler, S., Hessman, F. V., & Deller, J. 2012, *A&A*, 543, A138
- Bours, M. C. P., Marsh, T. R., Parsons, S. G., et al. 2016, *MNRAS*, 460, 3873
- Charpinet, S., Fontaine, G., Brassard, P., & Dorman, B. 2002, *ApJS*, 140, 469
- Charpinet, S., Fontaine, G., Brassard, P., et al. 2011, *Nature*, 480, 496
- Compton, D. L., Bedding, T. R., Murphy, S. J., & Stello, D. 2016, *MNRAS*, 461, 1943
- Dalessio, J., Provencal, J. L., & Shipman, H. L. 2015, *ASP Conf. Ser.*, 493, 157
- Eastman, J., Siverd, R., & Gaudi, S. 2010, *PASP*, 122, 935
- Geier, S., Schaffenroth, V., Drechsel, H., et al. 2011, *ApJ*, 731, L22
- Heber, U. 2016, *PASP*, 128, 966
- Hinse, T., Lee, J.-W., Goździewski, K., Horner, J., & Wittenmyer, R. A. 2014, *MNRAS*, 438, 307
- Hutchens, Z. L., Barlow, B. N., Vasquez Soto, A. et al. 2017, *Open Astron.*, 26, 252
- Kepler, S. O., Winget, D. E., Nather, R. E., et al. 1991, *ApJ*, 378, L45
- Konacki, M., & Wolszczan, A. 2003, *ApJ*, 591, L147
- Lanza, A. F. 2006, *MNRAS*, 369, 1773
- Ledoux, P. 1951, *ApJ*, 114, 373
- Lee, J.-W., Hinse, T. C., Youn, J.-H., & Han, W. 2014, *MNRAS*, 445, 2331
- Lenz, P., & Breger, M. 2005, *Commun. Asteroseismol.*, 146, 53
- Lohr, M. E., Norton, A. J., Anderson, D. R., et al. 2014, *A&A*, 566, A128
- Loumos, G. L., & Deeming, T. J. 1977, *Ap&SS*, 56, 285
- Lutz, R., Schuh, S., & Silvotti, R. 2009, *A&A*, 496, 469
- Murphy, S. J., Bedding, T. R., Shibahashi, H., Kurtz, D. W., & Kjeldsen, H. 2014, *MNRAS*, 441, 2515

- Murphy, S. J., Bedding, T. R., & Shibahashi, H. 2016a, *ApJ*, 827, L17
- Murphy, S. J., Shibahashi, H., & Bedding, T. R. 2016b, *MNRAS*, 461, 4215
- Østensen, R., Solheim, J.-E., Heber, U., et al. 2001, *A&A*, 368, 175
- Østensen, R. H., Reed, M. D., Baran, A. S., & Telting, J. H., 2014, *A&A*, 564, L14
- Otani, T., Oswalt, T. D., Lynas-Gray, A. E., et al. 2017, *ApJ*, submitted, [[arXiv:1708.06029](https://arxiv.org/abs/1708.06029)]
- Qian, S.-B., Zhu, L.-Y., Zola, S., et al. 2009, *ApJ*, 695, L163
- Qian, S.-B., Zhu, L.-Y., Liu, L., et al. 2010, *Ap&SS*, 329, 113
- Qian, S.-B., Shi, G., Zola, S., et al. 2013, *MNRAS*, 436, 1408
- Randall, S. K., Fontaine, G., Brassard, P., & Bergeron, P. 2005, *ApJS*, 161, 456
- Ricker, G. R., Vanderspek, R., Winn, J., et al. 2016, *Proc. SPIE*, 9904, 99042B
- Schaffenroth, V., Geier, S., Heber, U., et al. 2014a, *A&A*, 564, A98
- Schaffenroth, V., Classen, L., Nagel, K., et al. 2014b, *A&A*, 570, A70
- Schaffenroth, V., Barlow, B. N., Drechsel, H., & Dunlap, B. H. 2015, *A&A*, 576, A123
- Schleicher, D. R. G., & Dreizler, S. 2014, *A&A* 563, A61
- Shibahashi, H., & Kurtz, D. W. 2012, *MNRAS*, 422, 738
- Shibahashi, H., Kurtz, D. W., & Murphy, S. J. 2015, *MNRAS*, 450, 3999
- Silvotti, R. 2008, *ASP Conf. Ser.*, 392, 215
- Silvotti, R., Janulis, R., Schuh, S., et al. 2002, *A&A*, 389, 180
- Silvotti, R., Bonanno, A., Bernabei, S., et al. 2006, *A&A*, 459, 557
- Silvotti, R., Schuh, S., Janulis, R., et al. 2007, *Nature*, 449, 189
- Silvotti, R., Randall, S. K., Dhillon, V. S., et al. 2010, *Astron. Nachr.*, 331, 1034
- Silvotti, R., Szabó, R., Degroote, P., Østensen, R. H., & Schuh, S. 2011, *AIP Conf. Ser.*, 1331, 133
- Silvotti, R., Charpinet, S., Green, E., et al. 2014, *A&A*, 570, A130
- Sterken, C. 2005, *ASP Conf. Ser.*, 335, 3
- Telting, J. H., Østensen, R. H., Baran, A. S., et al. 2012, *A&A*, 544, A1
- Völschow, M., Schleicher, D. R. G., Perdelwitz, V., & Banerjee, R. 2016, *A&A*, 587, A34
- Wolszczan, A., & Frail, D. A. 1992, *Nature*, 355, 145
- Zong, W. 2017, *PhD Thesis, Univ. of Toulouse*, <https://tel.archives-ouvertes.fr/tel-01434986/document>
- Zong, W., Charpinet, S., & Vauclair, G. 2016, *A&A*, 594, A46
- Zorotovic, M., & Schreiber, M. R. 2013, *A&A*, 549, A95



## SN 2017ens: The Metamorphosis of a Luminous Broadlined Type Ic Supernova into an SN II<sub>n</sub>

T.-W. Chen<sup>1</sup> , C. Inserra<sup>2</sup> , M. Fraser<sup>3</sup> , T. J. Moriya<sup>4</sup> , P. Schady<sup>1</sup>, T. Schweyer<sup>1</sup>, A. V. Filippenko<sup>5,6</sup> , D. A. Perley<sup>7</sup> , A. J. Ruiter<sup>8,9</sup> , I. Seitenzahl<sup>8,9</sup> , J. Sollerman<sup>10</sup> , F. Taddia<sup>10</sup>, J. P. Anderson<sup>11</sup> , R. J. Foley<sup>12</sup>, A. Jerkstrand<sup>13</sup> , C.-C. Ngeow<sup>14</sup> , Y.-C. Pan<sup>12</sup>, A. Pastorello<sup>15</sup>, S. Points<sup>16</sup>, S. J. Smartt<sup>17</sup> , K. W. Smith<sup>17</sup>, S. Taubenberger<sup>13,18</sup> , P. Wiseman<sup>2</sup>, D. R. Young<sup>17</sup>, S. Benetti<sup>15</sup>, M. Berton<sup>19,20</sup> , F. Bufano<sup>21</sup>, P. Clark<sup>17</sup>, M. Della Valle<sup>22,23,24</sup> , L. Galbany<sup>25</sup> , A. Gal-Yam<sup>26</sup> , M. Gromadzki<sup>27</sup>, C. P. Gutiérrez<sup>2</sup>, A. Heinze<sup>28</sup> , E. Kankare<sup>17</sup>, C. D. Kilpatrick<sup>12</sup>, H. Kuncarayakti<sup>19,29</sup> , G. Leloudas<sup>30</sup> , Z.-Y. Lin<sup>14</sup>, K. Maguire<sup>17</sup>, P. Mazzali<sup>7</sup> , O. McBrien<sup>17</sup>, S. J. Prentice<sup>17</sup>, A. Rau<sup>1</sup> , A. Rest<sup>31,32</sup>, M. R. Siebert<sup>12</sup>, B. Stalder<sup>33</sup> , J. L. Tonry<sup>28</sup>, and P.-C. Yu<sup>14</sup>

<sup>1</sup> Max-Planck-Institut für Extraterrestrische Physik, Giessenbachstraße 1, D-85748, Garching, Germany; [jchen@mpe.mpg.de](mailto:jchen@mpe.mpg.de)

<sup>2</sup> Department of Physics and Astronomy, University of Southampton, Southampton SO17 1BJ, UK

<sup>3</sup> School of Physics, O'Brien Centre for Science North, University College Dublin, Belfield, Dublin 4, Ireland

<sup>4</sup> Division of Theoretical Astronomy, National Astronomical Observatory of Japan, National Institutes for Natural Sciences, 2-21-1 Osawa, Mitaka, Tokyo 181-8588, Japan

<sup>5</sup> Department of Astronomy, University of California, Berkeley, CA 94720-3411, USA

<sup>6</sup> Miller Senior Fellow, Miller Institute for Basic Research in Science, University of California, Berkeley, CA 94720, USA

<sup>7</sup> Astrophysics Research Institute, Liverpool John Moores University, IC2, Liverpool Science Park, 146 Brownlow Hill, Liverpool L3 5RF, UK

<sup>8</sup> School of Physical, Environmental and Mathematical Sciences, University of New South Wales, Australian Defence Force Academy, Canberra, ACT 2600, Australia

<sup>9</sup> Research School of Astronomy and Astrophysics, Australian National University, Canberra, ACT 0200, Australia

<sup>10</sup> The Oskar Klein Centre, Department of Astronomy, AlbaNova, Stockholm University, SE-106 91 Stockholm, Sweden

<sup>11</sup> European Southern Observatory, Alonso de Córdova 3107, Casilla 19, Santiago, Chile

<sup>12</sup> Department of Astronomy and Astrophysics, University of California, Santa Cruz, CA 95064, USA

<sup>13</sup> Max-Planck Institut für Astrophysik, Karl-Schwarzschild Str. 1, D-85748 Garching, Germany

<sup>14</sup> Graduate Institute of Astronomy, National Central University, No. 300, Zhongda Road, Zhongli District, Taoyuan City 32001, Taiwan

<sup>15</sup> INAF - Osservatorio Astronomico di Padova, Vicolo dell'Osservatorio 5, I-35122 Padova, Italy

<sup>16</sup> CTIO/NOAO, Casilla 603, La Serena, Chile

<sup>17</sup> Astrophysics Research Centre, School of Mathematics and Physics, Queen's University Belfast, Belfast BT7 1NN, UK

<sup>18</sup> European Southern Observatory, Karl-Schwarzschild-Str. 2, D-85748 Garching, Germany

<sup>19</sup> Finnish Centre for Astronomy with ESO (FINCA), FI-20014 University of Turku, Finland

<sup>20</sup> Aalto University Metsähovi Radio Observatory, Metsähovintie 114, FI-02540 Kylmälä, Finland

<sup>21</sup> INAF—Osservatorio Astrofisico di Catania Via Santa Sofia, 78, I-95123, Catania, Italy

<sup>22</sup> INAF—Osservatorio Astronomico di Napoli, Salita Moiariello, 16, I-80131, Napoli, Italy

<sup>23</sup> Instituto de Astrofísica de Andalucía (IAA-CSIC), Glorieta de la Astronomía s/n, E-18008 Granada, Spain

<sup>24</sup> International Center for Relativistic Astrophysics, Piazza della Repubblica 10, I-65122 Pescara, Italy

<sup>25</sup> PITT PACC, Department of Physics and Astronomy, University of Pittsburgh, Pittsburgh, PA 15260, USA

<sup>26</sup> Department of Particle Physics and Astrophysics, Weizmann Institute of Science, Rehovot 76100, Israel

<sup>27</sup> Warsaw University Astronomical Observatory, Al. Ujazdowskie 4, 00-478 Warszawa, Poland

<sup>28</sup> Institute for Astronomy, University of Hawaii, 2680 Woodlawn Drive, Honolulu, HI 96822, USA

<sup>29</sup> Tuorla Observatory, Department of Physics and Astronomy, FI-20014 University of Turku, Finland

<sup>30</sup> DTU Space, National Space Institute, Technical University of Denmark, Elektrovej 327, DK-2800 Kgs. Lyngby, Denmark

<sup>31</sup> Space Telescope Science Institute, 3700 San Martin Drive, Baltimore, MD 21218, USA

<sup>32</sup> Department of Physics and Astronomy, Johns Hopkins University, Baltimore, MD 21218, USA

<sup>33</sup> LSST, 950 North Cherry Avenue, Tucson, AZ 85719, USA

Received 2018 August 12; revised 2018 October 10; accepted 2018 October 20; published 2018 November 9

### Abstract

We present observations of supernova (SN) 2017ens, discovered by the ATLAS survey and identified as a hot blue object through the GREAT program. The redshift  $z = 0.1086$  implies a peak brightness of  $M_g = -21.1$  mag, placing the object within the regime of superluminous supernovae. We observe a dramatic spectral evolution, from initially being blue and featureless, to later developing features similar to those of the broadlined Type Ic SN 1998bw, and finally showing  $\sim 2000$  km s<sup>-1</sup> wide H $\alpha$  and H $\beta$  emission. Relatively narrow Balmer emission (reminiscent of a SN II<sub>n</sub>) is present at all times. We also detect coronal lines, indicative of a dense circumstellar medium. We constrain the progenitor wind velocity to  $\sim 50$ – $60$  km s<sup>-1</sup> based on P-Cygni profiles, which is far slower than those present in Wolf–Rayet stars. This may suggest that the progenitor passed through a luminous blue variable phase, or that the wind is instead from a binary companion red supergiant star. At late times we see the  $\sim 2000$  km s<sup>-1</sup> wide H $\alpha$  emission persisting at high luminosity ( $\sim 3 \times 10^{40}$  erg s<sup>-1</sup>) for at least 100 day, perhaps indicative of additional mass loss at high velocities that could have been ejected by a pulsational pair instability.

**Key words:** supernovae: general – supernovae: individual (SN 2017ens)

**Supporting material:** data behind figure

## 1. Introduction

Type Ic supernovae (SNe) arise from the core collapse of a massive star that has lost its hydrogen and helium layers prior to exploding, through either strong stellar winds or interaction with a binary companion (e.g., Filippenko 1997; Gal-Yam 2017). Their light curves are powered by the radioactive decay of  $^{56}\text{Ni}$  that is produced in the SN explosion. Related to these events, but with luminosities up to 100 times higher, are the Type I superluminous SNe (SLSNe I; see Gal-Yam 2012; Inserra et al. 2018a; Moriya et al. 2018b for reviews of observations and models). SLSNe exhibit spectral similarities to SNe Ic (Pastorello et al. 2010), but their luminosities are such that they cannot be powered solely by radioactive decay (Quimby et al. 2011). The nature of the additional energy source remains unknown, with suggestions ranging from a central engine (Kasen & Bildsten 2010; Woosley 2010) to interaction with a massive H and He-free circumstellar medium (CSM; Chevalier & Irwin 2011).

Some SNe Ib/Ic have been observed to develop relatively narrow ( $\sim 500\text{--}1000\text{ km s}^{-1}$ ) emission lines of hydrogen in their spectra; examples include SNe Ib 2014C and 2004dk (Milisavljevic et al. 2015; Mauerhan et al. 2018), and SNe Ic 2001em and 2017dio (Gal-Yam 2017; Kunzarayakti et al. 2018). This has been interpreted as evidence that for at least some H-poor SNe, the fast ejecta are colliding with H-rich material relatively far from the star. This late-time interaction has also been observed in some SLSNe Ic which show  $\text{H}\alpha$  emission at +70 to +250 day after their peak brightness (Yan et al. 2015, 2017).

In this Letter we report on the discovery of an unusual SN with our Gamma-Ray Burst Optical/Near-Infrared Detector (GROND)/extended-Public ESO Spectroscopic Survey for Transient Objects (ePESSTO)/Asteroid Terrestrial-impact Last Alert System (ATLAS) (GREAT; Greiner et al. 2008; Smartt et al. 2015; Tonry et al. 2018) survey. We introduce this program here, which is designed to rapidly identify hot blue transients, with the specific goal of finding very young SLSNe in faint galaxies (Chen et al. 2017c). SN 2017ens (ATLAS17-gqa) was discovered by the ATLAS survey on 2017 June 5 (UT dates are used herein), located at (J2000)  $\alpha = 12^{\text{h}}04^{\text{m}}09^{\text{s}}.37$ ,  $\delta = -01^{\circ}55'52''.2$ . Prompted by the high blackbody temperature of  $21,000 \pm 3000\text{ K}$  that we measured with our GREAT data on 2017 June 8 (Chen et al. 2017a), we began an intensive spectroscopic and photometric follow-up campaign (Section 2).

The adopted redshift of SN 2017ens,  $z = 0.1086$  (Section 3.3), implies an absolute magnitude of  $M_g = -21.1$  at peak, and thus a luminosity consistent with a SLSNe (Gal-Yam 2012). In Section 3 we present the spectral evolution of SN 2017ens, which began to show  $\sim 2000\text{ km s}^{-1}$  wide  $\text{H}\alpha$  and  $\text{H}\beta$  emission after +163 day (phases are corrected for time dilation and are relative to the GROND  $r$ -band maximum on MJD = 57,924.011). We compare the spectral properties of SN 2017ens to those of other SLSNe and broadlined SNe Ic (SNe Ic-BL), and also present the detections of rarely seen coronal lines. The bolometric light curve and modeling results are described in Section 4. Finally, in Section 5 we discuss plausible scenarios that may explain the spectral evolution and luminosity of SN 2017ens. We adopt a cosmology of  $H_0 = 72\text{ km s}^{-1}\text{ Mpc}^{-1}$ ,  $\Omega_\Lambda = 0.73$ , and  $\Omega_m = 0.27$ . The foreground reddening toward SN 2017ens is  $A_V = 0.058\text{ mag}$  (Schlafly & Finkbeiner 2011), and we assume that host-galaxy extinction is

negligible because no Na I D absorption is visible in the SN spectrum.

## 2. Observations

Our photometric coverage of SN 2017ens spans the ultraviolet (UV) with the Ultraviolet and Optical Telescope (UVOT) on the Neil Gehrels *Swift* Observatory, optical wavelengths with GROND, ATLAS, LCO 1 m,<sup>34</sup> and Lulin-SLT,<sup>35</sup> and near-infrared (NIR) bands with GROND. We use standard procedures to reduce the data (Poole et al. 2008 for UVOT; Krühler et al. 2008 for GROND). Ground-based optical photometry is calibrated against the Sloan Digital Sky Survey (SDSS). For ATLAS magnitudes we apply passband corrections using spectra (prescription from Inserra et al. 2018b); for Super Light Telescope (SLT) data we use the conversion of R. Lupton.<sup>36</sup> The NIR magnitudes are calibrated against Two Micron All Sky Survey (2MASS) field stars. All data are reported in the AB system, and errors include the statistical and systematic uncertainties. We do not have host-galaxy templates, but we estimate a  $<15\%$  contribution from host light ( $r > 23\text{ mag}$  measured in pre-explosion Panoramic Survey Telescope and Rapid Response System (PanSTARRS) images) to our SN photometry after +150 day. Our photometric results are given in a machine-readable table and shown in Figure 1 (top panel).

We obtained a series of spectra of SN 2017ens, following the SN evolution from +4 day to +265 day (log of observations in Table 1). Spectra are reduced in the standard fashion (ALFOSCGUI pipeline<sup>37</sup> for ALFOSC) or using custom-built pipelines PyWiFeS (Childress et al. 2014) for WiFeS, LPipe<sup>38</sup> for LRIS, Krühler et al. (2015) for X-Shooter, and Smartt et al. (2015) for EFOSC2. Finally, we correct the spectral-flux calibration against  $r$ -band photometry. The resulting calibration error estimated by comparing to  $g$ -band photometry is generally  $<0.10\text{ mag}$ , with the exception of the WiFeS (0.15 mag) and Keck (0.25 mag) spectra. (Those data were taken at very high airmass, making flux calibration difficult.) All spectra will be available through WISeREP (Yaron & Gal-Yam 2012).

## 3. Analysis and Results

### 3.1. Light Curves and Comparison

The discovery epoch of SN 2017ens with  $M_r \approx -19.8\text{ mag}$  is at MJD = 57,909.3. ATLAS monitored the field daily for 23 day before discovery. From a deep image taken 3 day before discovery ( $M_r \approx -18.7\text{ mag}$ ), we constrain the explosion date of SN 2017ens to MJD =  $57,907.8 \pm 1.5$ ; thus, the rest-frame rise time is  $\sim 15\text{ day}$ .

Figure 1 (middle panel) shows the absolute  $g$ -band light curve, which we compare to SLSNe, SNe IIn, and SNe Ic-BL selected based on the photometric properties and spectral evolution (see Section 3.2) of SN 2017ens. At peak, SN 2017ens is  $\sim 10$  times more luminous than the SNe Ic-BL 1998bw (Patat et al. 2001), 2003jd (Valenti et al. 2008), and SN Ic 2017dio (Kunzarayakti et al. 2018), which shows narrow H and He emission in its spectra. The early-phase light-curve evolution of SN 2017ens is

<sup>34</sup> <https://lco.global/observatory/sites/>

<sup>35</sup> [http://www.lulin.ncu.edu.tw/slt76cm/slt\\_introduction.htm](http://www.lulin.ncu.edu.tw/slt76cm/slt_introduction.htm)

<sup>36</sup> <http://classic.sdss.org/dr4/algorithms/sdssUBVRITransform.html>

<sup>37</sup> <http://sngroup.oapd.inaf.it/foscgui.html>

<sup>38</sup> <http://www.astro.caltech.edu/~dperley/programs/lpipe.html>

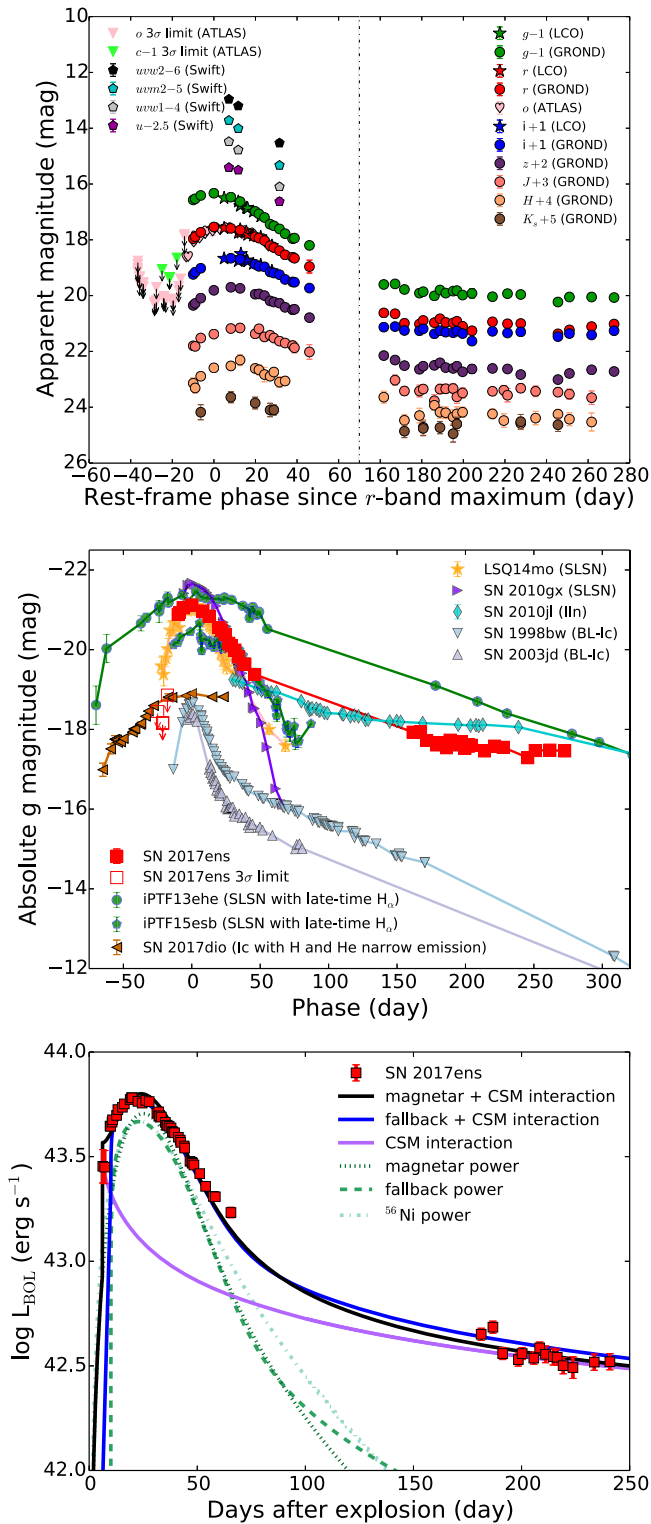


**Figure 1.** Top panel: multiband light curves of SN 2017ens. Note the discontinuous abscissa. Middle panel: light-curve comparison in absolute  $g$ -band with the SNe chosen for spectroscopic comparison. Bottom panel: bolometric light curve of SN 2017ens and model fitting. The pseudobolometric luminosity and photometry of SN 2017ens (UV through NIR) is available as data behind the figure. The data used to create this figure are available.

similar to that of rapidly evolving SLSNe such as LSQ14mo (Leloudas et al. 2015; Chen et al. 2017b) and SN 2010gx (Pastorello et al. 2010). SN 2017ens shows no sign of

undulations in its light curves, as are often observed in slowly evolving SLSNe as well as SLSNe that exhibit late-time  $H\alpha$  such as iPTF13ehe (Yan et al. 2015) and iPTF15esb (Yan et al. 2017). At late times, the light curves of SN 2017ens remain approximately constant, indicating that strong interaction dominates, as in SN IIn 2010jl before +300 day (Fransson et al. 2014).

### 3.2. Spectroscopic Evolution and Comparison

We show the spectral evolution of SN 2017ens in Figure 2. Around maximum light the spectra are blue and featureless. In the first spectrum taken at +4 day after peak, we detect narrow  $H\alpha$  and  $H\beta$  emission lines (barely resolved width of  $\sim 100 \text{ km s}^{-1}$ ). Fitting the dereddened spectra with a blackbody gives a temperature of  $T_{\text{BB}} \geq 10,300 \text{ K}$ , consistent with our estimate from the GROND analysis ( $\geq 11,500 \text{ K}$ ). At  $\sim 1$  month after peak, some broad features emerge, similar to those seen in SNe Ic-BL after peak brightness (e.g., Patat et al. 2001). Apart from narrow  $H\alpha$  and  $H\beta$ , we detect a narrow He I  $\lambda 5876$  emission line. The commonly observed [O II], [O III], and [N II] host-galaxy emission lines are absent, suggesting that the observed Balmer lines originate from the transient itself, not the underlying host (Perley et al. 2017). We also check the WiFeS datacubes and see no [O III] emission at the SN position.

At late times ( $>160$  day) after the SN emerged from solar conjunction, our data reveal dramatic evolution, with the spectra more resembling those of SNe IIn. The spectra are still blue, but now dominated by prominent,  $\sim 2000 \text{ km s}^{-1}$  wide Balmer emission lines, indicative of a much stronger interaction with H-rich CSM. The luminosity and the velocity of the  $\sim 2000 \text{ km s}^{-1}$   $H\alpha$  line does not vary significantly between +163 and +264 day, staying at  $\sim 3 \times 10^{40} \text{ erg s}^{-1}$ .

The spectral evolution of SN 2017ens is unique, sharing features with several distinct SN subclasses (Figure 3, top panel). In the earliest phases, the blue and featureless spectra share a similarity with young core-collapse SN spectra. We do not see the O II absorption features commonly associated with SLSNe. However, we may have missed them in SN 2017ens. For example, SLSN 2010gx (Pastorello et al. 2010) displayed O II absorption before it peaked and then became blue and featureless.

As the spectra evolve, SN 2017ens is not well matched to other SLSNe such as LSQ14mo (Chen et al. 2017b) and iPTF15esb (Yan et al. 2017). Rather, it appears to be more similar to SNe Ic-BL. The classification tool GELATO (Harutyunyan et al. 2008) applied to the SN 2017ens +27 day spectrum returns the closest similarity with SN 1998bw at +22 day (Patat et al. 2001) and SN 2003jd at  $-0.3$  day (Modjaz et al. 2014). These two SNe Ic-BL still provide a good match to SN 2017ens when we remove the continua assuming a blackbody (Figure 3, middle panel). SN 2017ens has a somewhat bluer continuum, perhaps due to CSM interaction, as was the case for SN 2017dio at +6 day (Kuncarayakti et al. 2018). The origin of the broad feature around  $6530 \text{ \AA}$  is uncertain; it could be attributed to a blend of Si and Fe/Co lines,  $H\alpha$  associated with interaction, or the C II  $\lambda 6580$  line sometimes seen in SLSNe (e.g., SN 2018bsz; Anderson et al. 2018).

During the late-time strongly interacting phase, the overall spectral features of SN 2017ens are well matched with those of SN 2017dio at +83 day. Both SNe exhibit a blue pseudocontinuum (below  $\sim 5000 \text{ \AA}$ ) that is more significant than in



**Table 1**  
Log of Spectroscopic Observations of SN 2017ens and Its Host Galaxy

UT Date	MJD	Phase (day)	Telescope	Instrument	Grating/Grism /Arm	Exp. Time (s)	Slit (")	Resolution (Å)	Range (Å)
2017 Jun 24	57928.392	3.95	ANU 2.3 m	WiFeS <sup>a</sup>	B3000/R3000	1200/1200	IFU	1.6/2.5	3500–5700/5400–9500
2017 Jun 26	57930.356	5.72	NOT	ALFOSC	Gr#4	1800	1.0	16	3300–9700
2017 Jul 20	57954.264	27.29	Keck I	LRIS	B600/R400	1125	0.7	5/6	3200–10,000
2017 Jul 26	57960.356	32.78	ANU 2.3 m	WiFeS <sup>a</sup>	B3000/R3000	1200/1200	IFU	1.6/2.5	3500–5700/5400–9500
2017 Dec 17	58104.325	162.65	NTT	EFOSC2	Gr#13	2700	1.0	18.2	3700–9200
2017 Dec 27	58114.301	171.65	NTT	EFOSC2	Gr#11/Gr#16	2700/2700	1.0/1.0	13.8/13.4	3400–7400/6000–9900
2018 Jan 14	58132.275	187.86	VLT	X-Shooter	UVB/VIS/NIR	3600/3400/3680	0.9/0.9/1.0	1/1.1/3.3	3000–5560/5450–10,200/10,000–20,600
2018 Jan 14	58132.312	187.90	NTT	EFOSC2	Gr#11	3600	1.0	13.8	3400–7400
2018 Jan 15	58133.263	188.75	VLT	X-Shooter	UVB/VIS/NIR	7200/6800/7360	0.9/0.9/1.0	1/1.1/3.3	3000–5560/5450–10,200/10,000–20,600
2018 Jan 15	58133.273	188.76	NTT	EFOSC2	Gr#16	2700	1.0	13.4	6000–9900
2018 Jan 16	58134.268	189.66	VLT	X-Shooter	UVB/VIS/NIR	3600/3400/3680	0.9/0.9/1.0	1/1.1/3.3	3000–5560/5450–10,200/10,000–20,600
2018 Jan 19	58137.305	192.40	VLT	X-Shooter	UVB/VIS/NIR	3600/3400/3680	0.9/0.9/1.0	1/1.1/3.3	3000–5560/5450–10,200/10,000–20,600
2018 Feb 14	58163.277	215.83	NTT	EFOSC2	Gr#11	8100	1.0	13.8	3400–7400
2018 Feb 18	58167.245	219.41	NTT	EFOSC2	Gr#16	5400	1.0	13.4	6000–9900
2018 Apr 9	58217.065	264.35	NTT	EFOSC2	Gr#13	2700	1.0	18.2	3650–9200

**Note.**

<sup>a</sup> WiFeS is an integral field unit (IFU) with 25 slitlets that are 1" wide and 38" long. Resolution is measured from the night-sky lines.

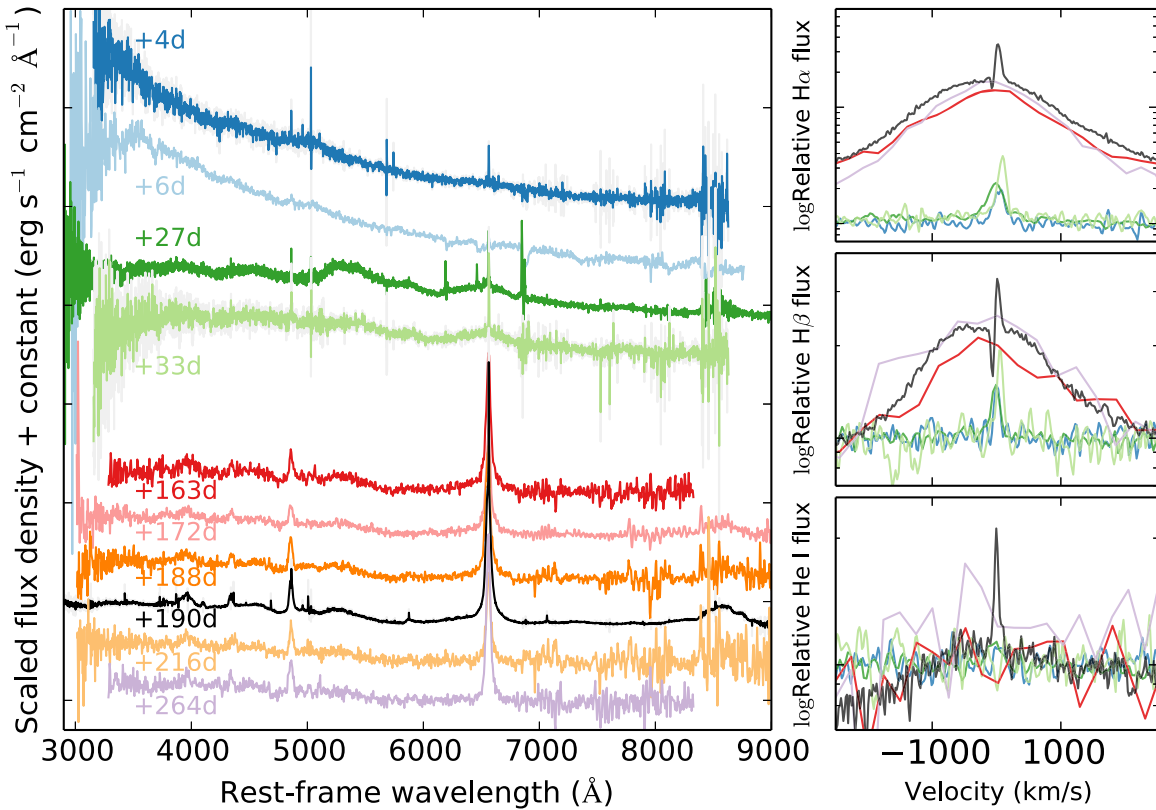


**Figure 2.** Spectroscopic evolution of SN 2017ens. The right panels show the velocity of the H $\alpha$ , H $\beta$ , and He I  $\lambda$ 5876 lines at selected epochs. Each phase is shown with the same color as in the main panel.

iPTF13ehe at +251 day (Yan et al. 2015); it is likely produced by Fe II lines (Smith et al. 2009).

### 3.3. Nebular and Coronal Lines

The VLT/X-Shooter spectra around +190 day (Figure 4) provide higher resolution and wider wavelength coverage than our other spectra, enabling us to detect many narrow emission lines. Interestingly, we find that the flux ratio of the nebular [O III]  $\lambda\lambda$ 4959, 5007 and auroral [O III]  $\lambda$ 4363 lines is 0.45, consistent with coronal lines that may arise from X-ray photoionization (Fransson et al. 2002) of dense gas (see Filippenko & Halpern 1984, their Figure 11). Therefore, we conclude that the [O III]  $\lambda$ 4363 line comes from the SN, and we use it to constrain the redshift of SN 2017ens to  $z = 0.1086$ , consistent with the average of the [O II]  $\lambda$ 3727 and [O III]  $\lambda\lambda$ 4959, 5007 lines.

These narrow coronal lines have been seen in only a handful of SNe IIn and the transitional object SN 2011hw (Pastorello et al. 2015). The ratio [O III] $\lambda$ 4363/[O III] $\lambda\lambda$ 4959, 5007 for SN 2017ens is similar to that seen in SN 2005ip at +173 day (Smith et al. 2009), SN 2006jd at +1542d (Stritzinger et al. 2012), and SN 2010jl at +461 day and +573 day (Fransson et al. 2014). Other coronal lines detected in SN 2017ens are similar to those seen in SN 2010jl (Figure 3, bottom panel): [Fe X]  $\lambda$ 6374.5 is strong, as are [Fe XI]  $\lambda$ 7891.8, [Ne V]  $\lambda\lambda$ 3345.8, 3425.9, [Ca V]  $\lambda$ 6086.8, and [Ar X]  $\lambda$ 5533.2. The presence of these lines is indicative of a highly ionized and dense CSM, although we do not

detect the highest-ionization coronal lines such as [Fe XIV]  $\lambda$ 5302.9 and [Ar XIV]  $\lambda$ 4412.3, which were seen in SN 2005ip.

The flux ratio of the [O III]  $\lambda$ 4363 to  $\lambda$ 5007 lines is a function of the CSM density and temperature. Following Fransson et al. (2014, their Figure 26), we use our measured flux ratio,  $\log(\lambda$ 4363/ $\lambda$ 5007) =  $-0.22$ , to constrain the CSM electron density to lie between  $10^6$  and  $10^8$  cm $^{-3}$  for  $T_e = 50,000$  to  $10,000$  K. This density range is consistent with that observed for SN 2010jl.

From our mid-resolution X-Shooter data, we resolve narrow P-Cygni profiles on top of the  $\sim 2000$  km s $^{-1}$  wide Balmer and Paschen lines. We measure the blueshifted wavelength from the absorption component of the H $\gamma$ , H $\beta$ , and H $\alpha$  P-Cygni profiles, which suggests that the unshocked CSM has a low velocity of  $\sim 50$  km s $^{-1}$ . A similar velocity of  $\sim 60$  km s $^{-1}$  is obtained from the P-Cygni profile of the He I  $\lambda$ 10,830 line. Moreover, we measure the FWHM intensity of the wide components, such as H $\alpha$  ( $2500 \pm 700$  km s $^{-1}$ ), H $\beta$  ( $2300 \pm 400$  km s $^{-1}$ ), Pa $\gamma$  ( $2000 \pm 200$  km s $^{-1}$ ), and He I  $\lambda$ 10,830 ( $2200 \pm 200$  km s $^{-1}$ ). We also detect narrow absorption lines from the Balmer series (no clear emission), spanning H $\epsilon$  to H33 (3659 Å).

In addition, we see emission from the H II region close to the host-galaxy center (see Figure 4, marked B1), as part of a faint galaxy (SDSS J120409.47–015552.4) with  $g = 21.92 \pm 0.24$  mag ( $M_g \approx -16.5$  mag). These lines have a slightly different redshift ( $z = 0.1084$ ) than SN 2017ens. In particular, the (noisy) detection of the weak auroral [O III]  $\lambda$ 4363 line indicates a low host-galaxy metallicity of  $\sim 0.04$ – $0.4 Z_\odot$  using the direct  $T_e$ -based method. If

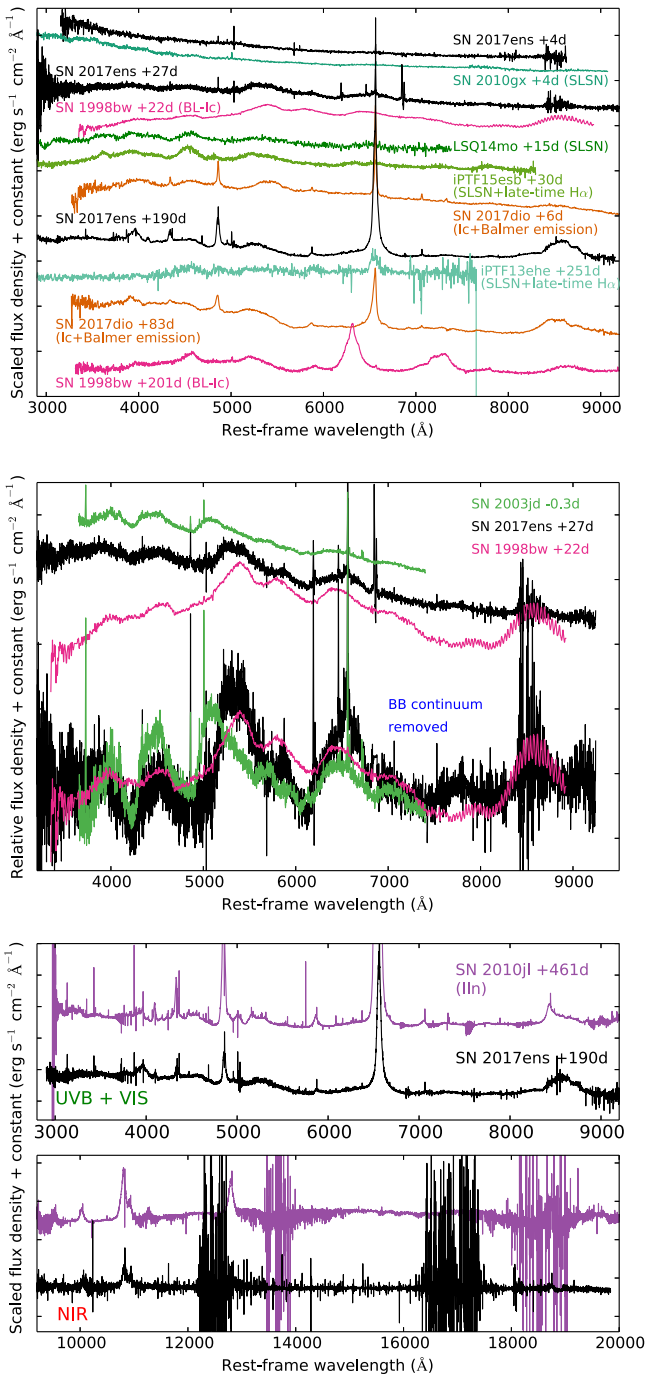


**Figure 3.** Top panel: comparison between SN 2017ens and other SNe at three selected epochs. Middle panel: comparison between SN 2017ens and the Type Ic-BL SNe 1998bw and 2003jd. The lower spectra have their continuum removed assuming a blackbody. Bottom panel: comparison between SN 2017ens and the Type IIc SN 2010jl at optical and NIR wavelengths.

we instead use the empirical N2 metallicity diagnostic (Pettini & Pagel 2004), we measure  $Z = 0.3 \pm 0.2 Z_{\odot}$ .

#### 4. Bolometric Light Curve and Model Fitting

Using all of our available UV-through-NIR photometry, we built a pseudobolometric light curve for SN 2017ens using the prescription from Inserra et al. (2018b). The results are very similar to those derived when using a blackbody fit, as expected as our photometry covers a large wavelength range.

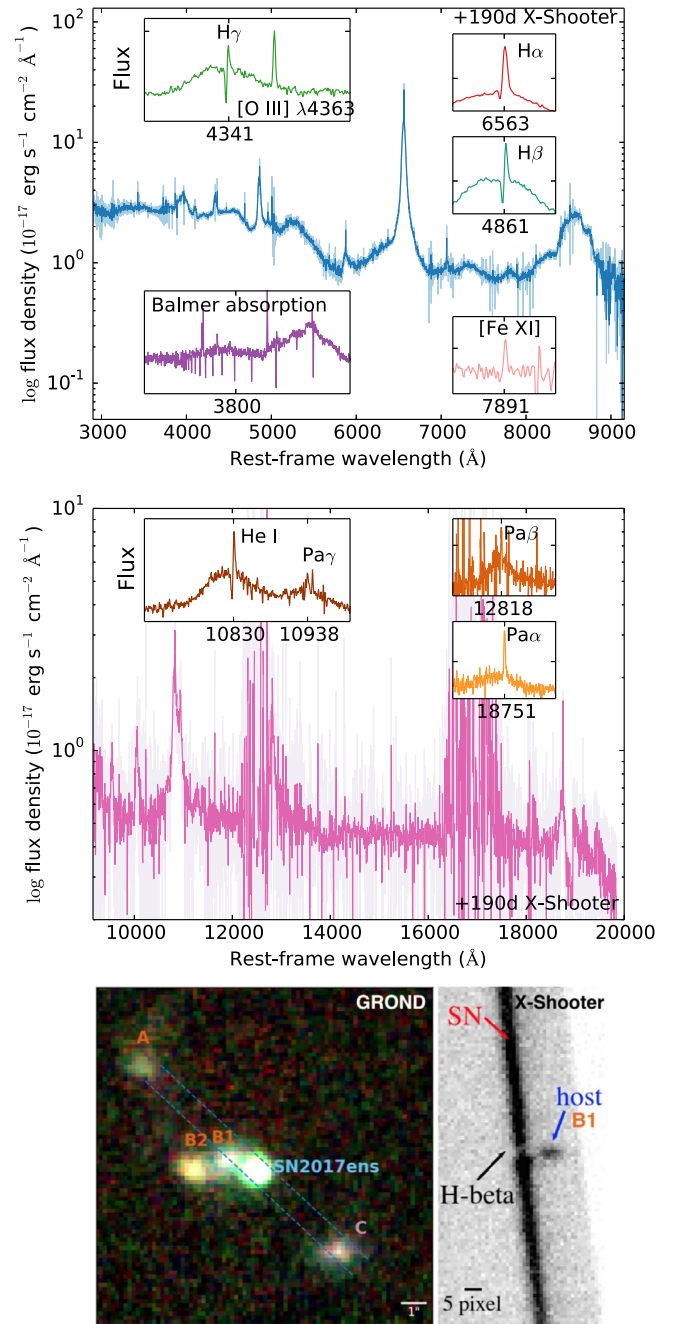


**Figure 4.** VLT/X-Shooter spectra of SN 2017ens at +190 day. Top panel: UVB and optical (VIS) parts. Middle panel: NIR part. The main panels use a log scale in order to present details in the continuum (rebinned to  $2 \text{ \AA pixel}^{-1}$  (UVB+VIS) and  $5 \text{ \AA pixel}^{-1}$  (NIR)); inset panels use a linear scale without binning. Bottom panel, left: color-combined image from GROND  $r'i'z'$  bands. SN 2017ens is associated with host-galaxy B1+B2, and there is a possible tidal tail connecting to the nearby object A (redshift unknown). Source C is a background galaxy at  $z = 0.30$ . The X-Shooter slit position is indicated with two dashed lines. Bottom panel, right: the  $H\beta$  position in the two-dimensional raw image.

From a polynomial fit to the bolometric data we obtain  $L_{\text{bol}} = (5.86 \pm 0.20) \times 10^{43} \text{ erg s}^{-1}$  at peak and an integrated energy of  $(3.53 \pm 1.42) \times 10^{50} \text{ erg}$ .

To fit our bolometric light curve, we used a two-component model consisting of a central heating and an interaction component. First, the centrally heated component uses the standard Arnett method (Arnett 1982; Inserra et al. 2013). We tested three

possible central power sources: the nuclear decay of  $^{56}\text{Ni}$ , the spindown of a magnetar (Kasen & Bildsten 2010), and fallback accretion (Dexter & Kasen 2013; Moriya et al. 2018a). The  $^{56}\text{Ni}$  decay and the magnetar spindown light curves are obtained as by Inserra et al. (2013), but the magnetar model takes the gamma-ray opacity from the magnetar into account as by Chen et al. (2015). The fallback accretion power is obtained by assuming a central energy input of  $L_{\text{fallback},1}(t/1\text{ s})^{-5/3}$ , where  $L_{\text{fallback},1}$  is a constant (Dexter & Kasen 2013). Second, for the interaction component, we adopted a steady-wind CSM, and the input luminosity from this component goes as  $L_{\text{int},1}(t/1\text{ s})^{-3/5}$ , where the outer SN density structure is proportional to  $r^{-7}$  (Moriya et al. 2013). The inner SN density structure is assumed to be constant.

We first used the interaction component to fit the bolometric light curve 150 day after explosion, assuming that interaction is the dominant light source at this time. We then derived the contribution required from a central power source at early times to provide a good light-curve match. Given that the spectra of SN 2017ens and SN 1998bw are similar (Figure 3), we used the relation  $(E_{\text{ej}}/10^{51}\text{ erg})/(M_{\text{ej}}/M_{\odot}) \approx 3$  found for SN 1998bw (Nakamura et al. 2001) to break the degeneracy between  $E_{\text{ej}}$  and  $M_{\text{ej}}$ .

Figure 1 (bottom panel) shows the results of our fits. In all cases, the CSM interaction model that we used has  $L_{\text{int},1} = 7.7 \times 10^{46}\text{ erg s}^{-1}$ . The inner edge of the CSM is set at  $1.2 \times 10^{15}\text{ cm}$  to match the early light-curve rise in the model, but this constraint is not strong. We find that all three centrally heated models provide reasonable fits to the bolometric light curve. They all have  $E_{\text{ej}} = 1.5 \times 10^{52}\text{ erg}$  and an ejecta mass of  $5 M_{\odot}$ . However, the  $^{56}\text{Ni}$ -powered light curve requires a very high  $^{56}\text{Ni}$  mass of  $3.5 M_{\odot}$ . This is close to the ejecta mass, and we therefore find the  $^{56}\text{Ni}$ -powered model to be unlikely. Alternatively, a magnetar central engine with an initial spin of 3.8 ms and a magnetic field of  $8 \times 10^{13}\text{ G}$ , and fallback accretion with  $L_{\text{fallback},1} = 6 \times 10^{53}\text{ erg s}^{-1}$ , provide good qualitative fits to the light curve. It is of course possible that the entire light curve is driven by different degrees of interaction. The contribution of the interaction component at early times (0–70 day after explosion) is  $\sim 20\%$ , while it is  $\gtrsim 90\%$  at late times (200 day).

Assuming the above best-fit results and a kinetic energy to radiation conversion efficiency at the shock of 0.1 (Moriya et al. 2013), we estimate the mass-loss rate of the progenitor to be  $5 \times 10^{-4} M_{\odot}\text{ yr}^{-1}$ , with a constant wind velocity of  $50\text{ km s}^{-1}$ . The CSM density estimate is similar to those of SNe IIn showing similar coronal lines (Taddia et al. 2013).

## 5. Discussion

One important clue to interpreting the possible powering mechanisms behind SN 2017ens is that we measured the H-rich material to have a velocity of  $\sim 50\text{--}60\text{ km s}^{-1}$  from the blueshifted absorption of the narrow P-Cygni profiles. This wind velocity is far slower than those present in Wolf–Rayet star winds. If this wind is from the progenitor, it could come from a massive H-rich progenitor (such as a luminous blue variable) that explosively ejected its H envelope shortly before the SN explosion. Alternatively, this wind could come from a pulsational pair-instability SN with a slow and long-term stable wind (Woosley 2017).

It is also possible that SN 2017ens exploded as a SN Ic-BL inside a patchy, H-rich CSM from a binary companion; the expanding ejecta interact with the bulk of the CSM at later times, as has been suggested for SN 2017dio (Kuncarayakti et al. 2018). Alternatively, as proposed for ASASSN-15no

(Benetti et al. 2018), a dense inner CSM may have hidden the SN features at early times, before they become briefly visible as the CSM was swept up by the ejecta. At late times they could have again been masked by an increasingly strong interaction component. A special CSM geometry (e.g., doughnut shape) is also probable, and we see the SN Ic-BL along a certain viewing angle.

In the case of a binary companion, the wind of  $\sim 50\text{--}60\text{ km s}^{-1}$  and mass-loss rate of  $5 \times 10^{-4} M_{\odot}\text{ yr}^{-1}$  are consistent with a red supergiant (Goldman et al. 2017), albeit at the more extreme end, which can be explained by the companion having gained mass from the SN progenitor during an earlier accretion phase. If so, this may suggest that the progenitor of SN 2017ens lost its H and He layers through interaction with a binary companion.

We must also consider the apparent  $\sim 2000\text{ km s}^{-1}$  material, given its high luminosity. If this is associated with mass loss from the progenitor, and the line width is not from electron scattering as seen in many SNe IIn, then the material is moving much faster than the winds of H-rich stars (or the CSM of SNe IIn). It is difficult to imagine how this could be produced by anything other than a sudden ejection of the H envelope, shortly before the SN explosion. In fact, the luminosity of the  $\sim 2000\text{ km s}^{-1}$  wide component of H $\alpha$  is comparable to that seen in SN 1995N (Fransson et al. 2002) ( $\sim 2.3 \times 10^{40}\text{ erg s}^{-1}$ ), and it may be too large to be coming solely from swept-up material. A pulsational pair-instability explosion is at least qualitatively consistent with an outburst that can unbind the H envelope shortly before an SN explosion. This scenario is also consistent with the measured low-metallicity environment.





The unique spectroscopic evolution of SN 2017ens together with its high luminosity poses challenges to all currently known SN scenarios. While detailed modeling can help elucidate the nature of this transient, ongoing surveys for SLSNe such as GREAT will find more such peculiar transients. With a larger sample and high-cadence follow-up spectroscopy, we will be able to further understand the nature of SN 2017ens-like objects and the role of interaction in SLSNe.

T.W.C. acknowledges Thomas Krühler for the X-Shooter data reduction, Lin Yan and Claes Fransson for providing comparison spectra, Jason Spyromilio for useful discussions, Chien-Hsiu Lee and You-Hua Chu for coordinating observational resources, and funding from the Alexander von Humboldt Foundation. M.F. acknowledges the support of a Royal Society—Science Foundation Ireland University Research Fellowship. P.S. acknowledges support through the Sofia Kovalevskaja Award (Alexander von Humboldt Foundation). A.V.F. is grateful for the support of the TABASGO Foundation, the Christopher R. Redlich fund, and the Miller Institute for Basic Research in Science (U.C. Berkeley). A.J.R. and I.R.S. are supported by the Australian Research Council through grants FT170100243 and FT160100028, respectively. F.T. and J.S. acknowledge support from the KAW Foundation. S.J.S. acknowledges funding from the European Research Council Grant agreement #291222 and STFC grant ST/P000312/1. M.G. is supported by Polish National Science Centre grant OPUS 2015/17/B/ST9/03167. K.M. acknowledges support from the UK STFC through an Ernest Rutherford Fellowship and from a Horizon 2020 ERC Starting Grant (#758638). L.G. was supported in part by US NSF grant AST-1311862. C.P.G. acknowledges support from EU/FP7-ERC

grant #615929. Z.Y.L., C.C.N., and P.C.Y. are grateful for funding from MoST (Taiwan) under grants 105-2112-M-008-002-MY3, 104-2923-M-008-004-MY5, and 106-2112-M-008-007. A.P. and S.B. are partially supported by PRIN-INAF 2017 “Toward the SKA and CTA era: discovery, localization, and physics of transient sources” (P.I.: Giroletti). A.G.-Y. is supported by the EU via ERC grant No. 725161, the Quantum Universe I-Core program, the ISF, the BSF Transformative program, and a Kimmel award.

Part of the funding for GROND was generously granted from the Leibniz Prize to Prof. G. Hasinger (DFG grant HA 1850/28-1). Some observations were made with the Nordic Optical Telescope using ALFOSC. This publication has made use of data collected at Lulin Observatory, partly supported by MoST grant 105-2112-M-008-024-MY3. Some of the data presented herein were obtained at the W. M. Keck Observatory, which is operated as a scientific partnership among the California Institute of Technology, the University of California, and NASA; the observatory was made possible by the generous financial support of the W. M. Keck Foundation.

### ORCID iDs

T.-W. Chen  <https://orcid.org/0000-0003-1532-0149>  
 C. Inserra  <https://orcid.org/0000-0002-3968-4409>  
 M. Fraser  <https://orcid.org/0000-0003-2191-1674>  
 T. J. Moriya  <https://orcid.org/0000-0003-1169-1954>  
 A. V. Filippenko  <https://orcid.org/0000-0003-3460-0103>  
 D. A. Perley  <https://orcid.org/0000-0001-8472-1996>  
 A. J. Ruiter  <https://orcid.org/0000-0002-4794-6835>  
 I. Seitenzahl  <https://orcid.org/0000-0002-5044-2988>  
 J. Sollerman  <https://orcid.org/0000-0003-1546-6615>  
 J. P. Anderson  <https://orcid.org/0000-0003-0227-3451>  
 A. Jerkstrand  <https://orcid.org/0000-0001-8005-4030>  
 C.-C. Ngeow  <https://orcid.org/0000-0001-8771-7554>  
 S. J. Smartt  <https://orcid.org/0000-0002-8229-1731>  
 S. Taubenberger  <https://orcid.org/0000-0002-4265-1958>  
 M. Berton  <https://orcid.org/0000-0002-1058-9109>  
 M. Della Valle  <https://orcid.org/0000-0003-3142-5020>  
 L. Galbany  <https://orcid.org/0000-0002-1296-6887>  
 A. Gal-Yam  <https://orcid.org/0000-0002-3653-5598>  
 A. Heinze  <https://orcid.org/0000-0003-3313-4921>  
 H. Kuncarayakti  <https://orcid.org/0000-0002-1132-1366>  
 G. Leloudas  <https://orcid.org/0000-0002-8597-0756>  
 P. Mazzali  <https://orcid.org/0000-0001-6876-8284>  
 A. Rau  <https://orcid.org/0000-0001-5990-6243>  
 B. Stalder  <https://orcid.org/0000-0003-0973-4900>  
 P.-C. Yu  <https://orcid.org/0000-0001-8894-0854>

### References

- Anderson, J. P., Pessi, P. J., Dessart, L., et al. 2018, arXiv:1806.10609  
 Arnett, W. D. 1982, *ApJ*, **253**, 785  
 Benetti, S., Zampieri, L., Pastorello, A., et al. 2018, *MNRAS*, **476**, 261  
 Chen, T.-W., Inserra, C., Smartt, S. J., et al. 2017a, *ATel*, **10478**, 1  
 Chen, T.-W., Nicholl, M., Smartt, S. J., et al. 2017b, *A&A*, **602**, A9  
 Chen, T.-W., Schady, P., Kruehler, T., et al. 2017c, *ATel*, **10510**, 1  
 Chen, T.-W., Smartt, S. J., Jerkstrand, A., et al. 2015, *MNRAS*, **452**, 1567  
 Chevalier, R. A., & Irwin, C. M. 2011, *ApJL*, **729**, L6  
 Childress, M. J., Vogt, F. P. A., Nielsen, J., & Sharp, R. G. 2014, *Ap&SS*, **349**, 617  
 Dexter, J., & Kasen, D. 2013, *ApJ*, **772**, 30  
 Filippenko, A. V. 1997, *ARA&A*, **35**, 309  
 Filippenko, A. V., & Halpern, J. P. 1984, *ApJ*, **285**, 458  
 Fransson, C., Chevalier, R. A., Filippenko, A. V., et al. 2002, *ApJ*, **572**, 350  
 Fransson, C., Ergon, M., Challis, P. J., et al. 2014, *ApJ*, **797**, 118  
 Gal-Yam, A. 2012, *Sci*, **337**, 927  
 Gal-Yam, A. 2017, in *Observational and Physical Classification of Supernovae*, ed. A. W. Alsabti & P. Murdin (Dordrecht: Springer), 195  
 Goldman, S. R., van Loon, J. T., Zijlstra, A. A., et al. 2017, *MNRAS*, **465**, 403  
 Greiner, J., Bornemann, W., Clemens, C., et al. 2008, *PASP*, **120**, 405  
 Harutyunyan, A. H., Pfahler, P., Pastorello, A., et al. 2008, *A&A*, **488**, 383  
 Inserra, C., Prajs, S., Gutierrez, C. P., et al. 2018a, *ApJ*, **854**, 175  
 Inserra, C., Smartt, S. J., Gall, E. E. E., et al. 2018b, *MNRAS*, **475**, 1046  
 Inserra, C., Smartt, S. J., Jerkstrand, A., et al. 2013, *ApJ*, **770**, 128  
 Kasen, D., & Bildsten, L. 2010, *ApJ*, **717**, 245  
 Krühler, T., Küpcü Yoldaş, A., Greiner, J., et al. 2008, *ApJ*, **685**, 376  
 Krühler, T., Malesani, D., Fynbo, J. P. U., et al. 2015, *A&A*, **581**, A125  
 Kuncarayakti, H., Maeda, K., Ashall, C. J., et al. 2018, *ApJL*, **854**, L14  
 Leloudas, G., Patat, F., Maund, J. R., et al. 2015, *ApJL*, **815**, L10  
 Mauerhan, J. C., Filippenko, A. V., Zheng, W., et al. 2018, arXiv:1803.07051  
 Milisavljevic, D., Margutti, R., Kamble, A., et al. 2015, *ApJ*, **815**, 120  
 Modjaz, M., Blondin, S., Kirshner, R. P., et al. 2014, *AJ*, **147**, 99  
 Moriya, T. J., Maeda, K., Taddia, F., et al. 2013, *MNRAS*, **435**, 1520  
 Moriya, T. J., Nicholl, M., & Guillochon, J. 2018a, arXiv:1806.00090  
 Moriya, T. J., Sorokina, E. I., & Chevalier, R. A. 2018b, *SSRv*, **214**, 59  
 Nakamura, T., Mazzali, P. A., Nomoto, K., & Iwamoto, K. 2001, *ApJ*, **550**, 991  
 Pastorello, A., Benetti, S., Brown, P. J., et al. 2015, *MNRAS*, **449**, 1921  
 Pastorello, A., Smartt, S. J., Botticella, M. T., et al. 2010, *ApJL*, **724**, L16  
 Patat, F., Cappellaro, E., Danziger, J., et al. 2001, *ApJ*, **555**, 900  
 Perley, D. A., Chen, T.-W., Filippenko, A. V., Brink, T. G., & Zheng, W. 2017, *ATel*, **10587**, 1  
 Pettini, M., & Pagel, B. E. J. 2004, *MNRAS*, **348**, L59  
 Poole, T. S., Breeveld, A. A., Page, M. J., et al. 2008, *MNRAS*, **383**, 627  
 Quimby, R. M., Kulkarni, S. R., Kasliwal, M. M., et al. 2011, *Natur*, **474**, 487  
 Schlafly, E. F., & Finkbeiner, D. P. 2011, *ApJ*, **737**, 103  
 Smartt, S. J., Valenti, S., Fraser, M., et al. 2015, *A&A*, **579**, A40  
 Smith, N., Silverman, J. M., Chornock, R., et al. 2009, *ApJ*, **695**, 1334  
 Stritzinger, M., Taddia, F., Fransson, C., et al. 2012, *ApJ*, **756**, 173  
 Taddia, F., Stritzinger, M. D., Sollerman, J., et al. 2013, *A&A*, **555**, A10  
 Tonry, J. L., Denneau, L., Heinze, A. N., et al. 2018, *PASP*, **130**, 064505  
 Valenti, S., Benetti, S., Cappellaro, E., et al. 2008, *MNRAS*, **383**, 1485  
 Woosley, S. E. 2010, *ApJL*, **719**, L204  
 Woosley, S. E. 2017, *ApJ*, **836**, 244  
 Yan, L., Lunnan, R., Perley, D. A., et al. 2017, *ApJ*, **848**, 6  
 Yan, L., Quimby, R., Ofek, E., et al. 2015, *ApJ*, **814**, 108  
 Yaron, O., & Gal-Yam, A. 2012, *PASP*, **124**, 668

# 工作報告

# 鹿林天文台觀測時數統計(2003-2018)

林宏欽、蕭翔耀、林啟生

鹿林天文台自 2002 年 9 月開始人員常駐，2003 年鹿林一米望遠鏡(LOT)上線，開始有正式觀測時數紀錄，可供瞭解鹿林長期的天氣狀況。依 2003-2018 共 16 年的統計結果，鹿林天文台年平均觀測時數為 1141 小時。一年可分為四個觀測季，

- 最佳觀測季：10-12 月。
- 次佳觀測季：1-3 月。
- 最差觀測季：4-6 月。4 月開始進入雨季，5-6 月受梅雨影響，天氣最差。
- 次差觀測季：7-9 月。主要受颱風及西南氣流影響，天氣變化大。此外夏季晝長夜短，每晚可觀測時間比冬季為短。

詳細統計資料及統計圖如下，

表 1 每月觀測時數統計 (2003-2018)

Month	2003	2004	2005	2006	2007	2008	2009	2010	2011	2012	2013	2014	2015	2016	2017	2018	Average
1	78.75	125	163.25	129	127.32	179	234.52	206.9	90.8	113.42	153.58	269.62	188.55	75.4	160.85	110.4	150.40
2	142.5	145.98	94.75	149	128.55	118.25	165.7	100.6	123.8	64.88	183.63	109.8	131.65	60.25	105.3	66.7	118.21
3	147.5	163	143	126.05	116.4	138.5	146.75	181.3	75.9	168.23	134.26	78.7	111.1	72.8	96.4	173.7	129.60
4	126.5	110.5	144.75	86.8	53.75	85.25	71.8	75.8	151.45	32.75	55.83	135.95	124	82.9	86.9	125.7	96.91
5	129.75	106.25	136.25	59.5	106.6	98.25	167.4	86.05	56.6	74.3	41.02	32.4	64.2	86.05	84.55	190.7	94.99
6	24	133	45	39.3	54	37	81.75	26.5	61.5	35.15	80.14	33.7	146.9	114.05	76.1	70.35	66.15
7	222.5	48	167.75	91.57	128.88	88.4	76.6	99.85	81.75	106.4	88.05	114.65	87.45	123.95	105.25	80.65	106.98
8	137.75	142	76	111.65	56.6	118.95	6.8	98.3	97.9	35.7	72.2	110.9	45.1	61	139.9	50.35	85.07
9	142	116	129.25	60.05	69.55	59.8	0	109.95	90.1	117.35	107.84	134.39	93.25	42.85	128.2	93.45	93.38
10	149.25	219.75	210.25	150.6	172.63	191.38	175.6	139.8	136.95	214.51	200.57	232.33	145.4	142.2	187.8	142.05	175.69
11	166.5	214.5	216.25	71.75	160.55	152.55	175.8	163.65	87.2	93.81	136.1	166.15	197.05	171.85	134.55	148.15	153.53
12	271.5	232.45	129	132	261.09	211.17	169.8	169.65	115.25	132.21	86	137.3	161.2	193.27	156.7	170.05	170.54
Total	1738.5	1756.43	1655.5	1207.27	1435.92	1478.5	1472.52	1458.35	1169.2	1188.71	1339.22	1555.89	1495.85	1226.57	1462.5	1422.25	1141.45

\* 2009 年因受莫拉克颱風八八風災影響，自八月八日起至十月初約 2 個月期間道路中斷並停電，無法觀測。所以 2009 年之八、九月觀測時數很少，甚至為 0。

\*\*Average 值為扣除最高及最低值後取平均。

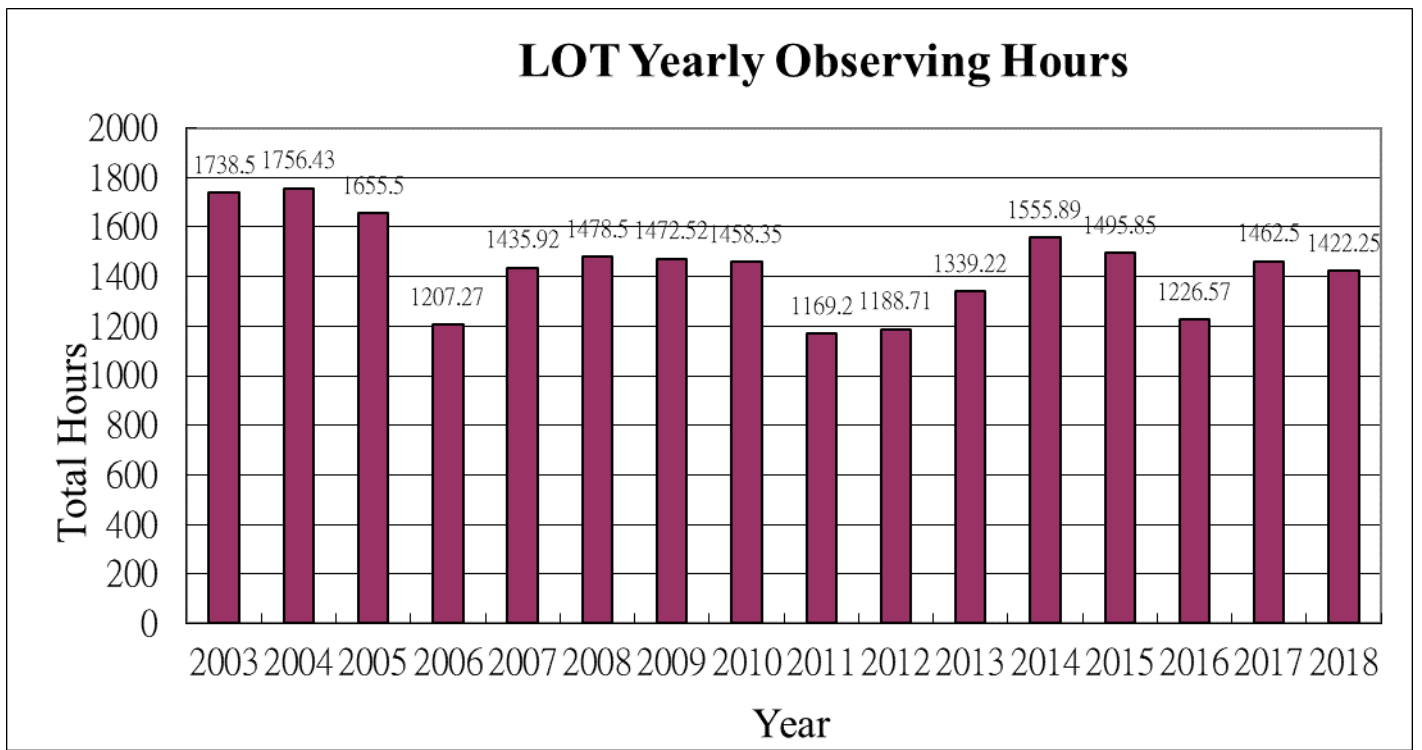


圖 1 鹿林天文台年平均觀測時數統計圖(2003-2018)

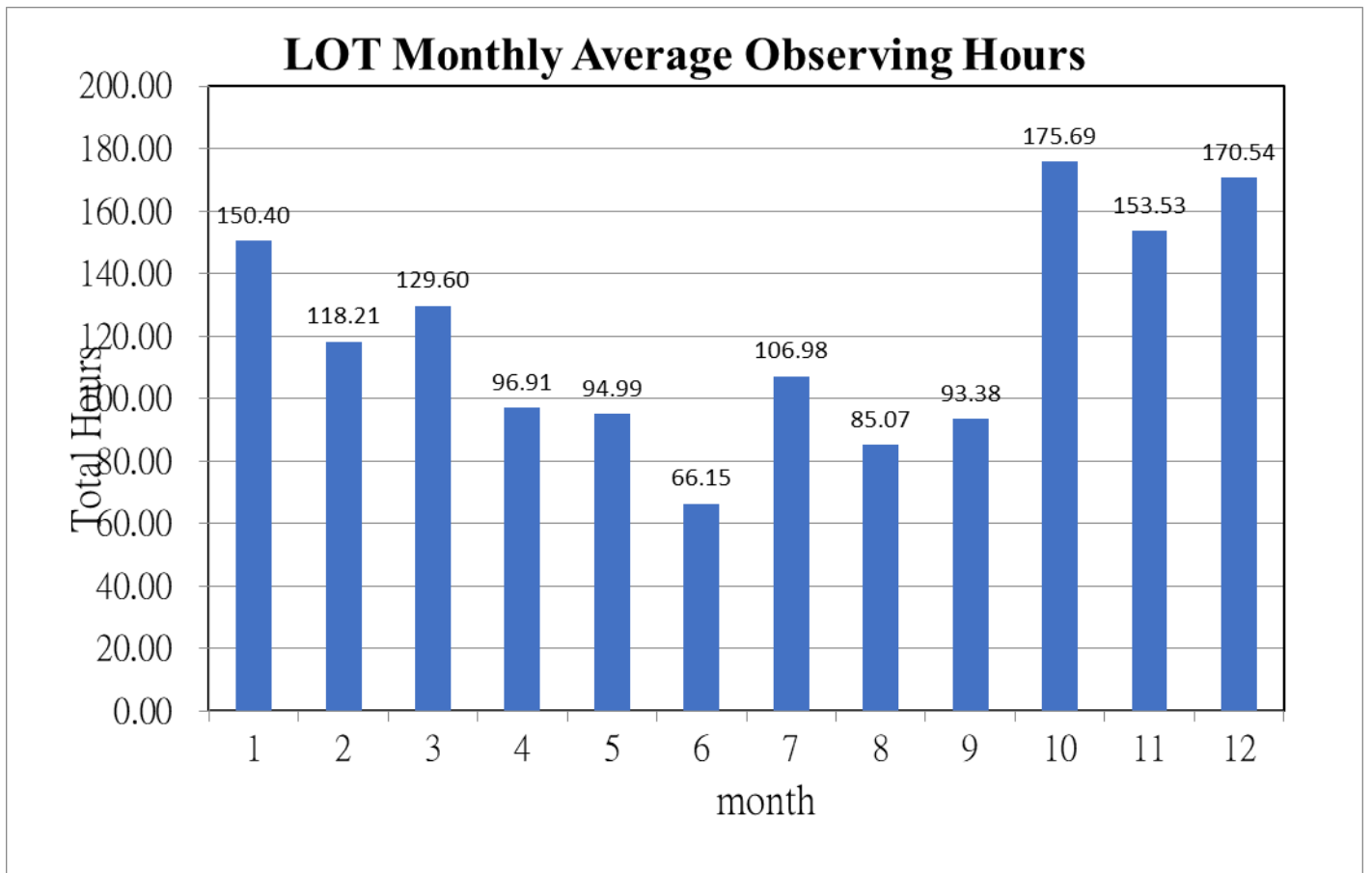


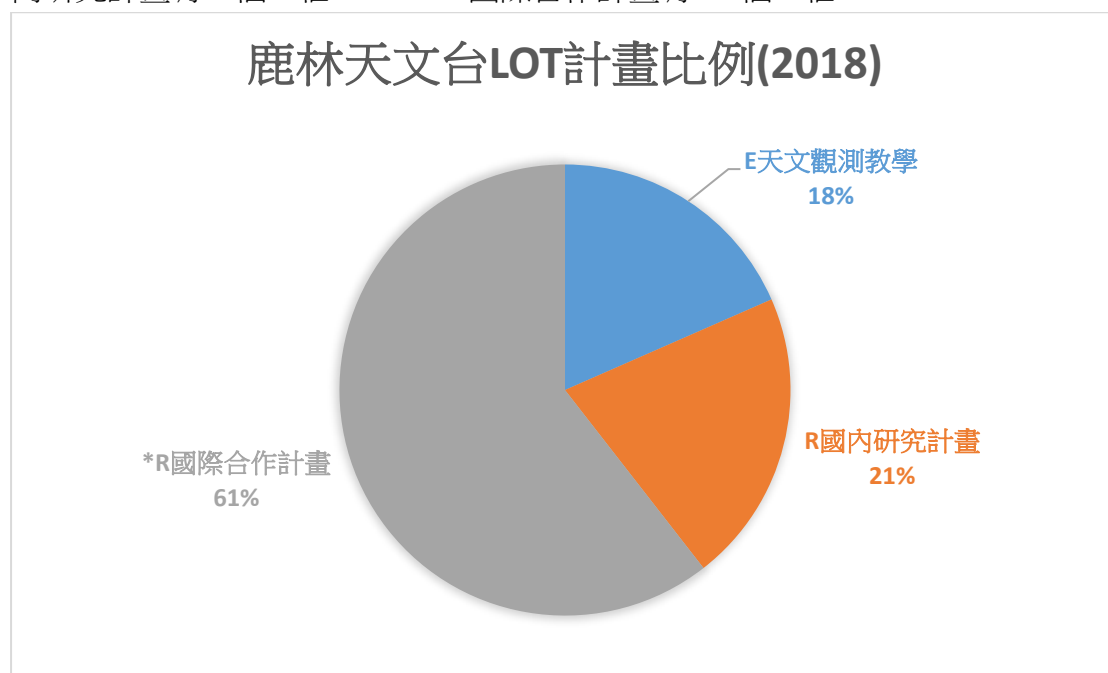
圖 2 鹿林天文台月平均觀測時數統計圖 (2003-2018)



## 鹿林天文台 LOT 觀測研究計畫統計 (2018)

鹿林天文台一米望遠鏡(LOT)觀測研究計畫時間安排以 4 個月為一個觀測期，一年分為三期 (A=1-4 月、B=5-8 月、C=9-12 月)，其中字母 E、R 和 \*R 分別為天文觀測教學、國內研究計畫與國際合作計畫。

2018 年的觀測計畫如下，統計結果：E 天文觀測教學有 7 個，佔 18%。R 國內研究計畫有 8 個，佔 21%。\*R 國際合作計畫有 23 個，佔 61%。



### LOT 2018A (01 Jan – 30 Apr, 2018)

#### Education Program:

E01 – Observing Training for “Advanced Observational Astronomy” Course

PI: Chow-Choong Ngeow (cngeow@astro.ncu.edu.tw)

E02 – Observation Training for Taipei CHENGGONG High School Students

PI: Hao-Yuan Duan (hyduan@gapp.nthu.edu.tw)

E03 – Practical Class of "Fundamentals of Observational Astronomy"

PI: Albert Kong (akong@phys.nthu.edu.tw)

E04 – Observation Training for National Hsinchu Girl' Senior Hig

PI: You-Ting Yeh (ray42082003@yahoo.com.tw)

**Research Program:**

\*R01 – ToO Follow-Up Observations of GROWTH Targets: NEA and Transients

PI: Chow-Choong Ngeow (cngeow@astro.ncu.edu.tw)

\*R02 – Narrow-band Imaging of New Planetary Nebulae from LAMOST DR4 Database (I)

PI: Chih-Hao Hsia (chhsia@must.edu.mo)

R03 – The Rotation Period Confirmations for Large Super-Fast Rotating Asteroids PI: Chan-Kao Chang ([rex@astro.ncu.edu.tw](mailto:rex@astro.ncu.edu.tw))

\*R04 – Systematic Study of Rotational Spectral Variations of Large Asteroids (I) Chih-Hao Hsia (chhsia@must.edu.mo)

\*R05 – Late-time observations for the most nearby superluminous supernova SN 2017egm

PI: Ting-Wan Chen (jchen@mpe.mpg.de)

\*R06 – The Nature of Unidentified Fermi Objects

PI: Albert Kong (akong@phys.nthu.edu.tw)

\*R07 – YETI Campaign for the chi Per and h Per Open Cluster

PI: Pawel Zielinski (pawel@physics.muni.cz) [MU/Czech Republic]

\*R08 – Rotationally Resolved Spectra on Large Asteroids with  $D > 200$  km

PI: Kang-Shian Pan (m989005@astro.ncu.edu.tw)

\*R09 – Taxonomical Survey on Near-Earth Asteroids

PI: Chih-Hao Hsia (chhsia@must.edu.mo)

\*R10 – A Polarization Phase Curve Study of (16) Psyche and (246) Asporina

PI: Hao Zhang (zhanghao@cug.edu.cn)

R11 – Rotationally Resolved Polarization Observations of Main Belt Asteroids

PI: Kang-Shian Pan ([m989005@astro.ncu.edu.tw](mailto:m989005@astro.ncu.edu.tw))

## LOT2018B (08 May – 31 Aug, 2018)

### Research Program:

\*R01 – The Follow-Up Observations for the Transit Exoplanet Candidates in Open Clusters

PI: Po-Chieh Huang ([pochiehuang1@gmail.com](mailto:pochiehuang1@gmail.com))

\*R02 – ToO Follow-Up Observations of GROWTH Targets: NEA and Transients

PI: Chow-Choong Ngeow ([cngeow@astro.ncu.edu.tw](mailto:cngeow@astro.ncu.edu.tw))

R03 – BV RI Monitoring of Classical Cepheids in M31 For Distance Scale Applications

PI: Chow-Choong Ngeow ([cngeow@astro.ncu.edu.tw](mailto:cngeow@astro.ncu.edu.tw))

\*R04 – Comet Observing Campaign of Comets 21P, 46P and C/2017 S3 PanSTARRS

PI: Zhong-Yi Lin ([zylin@astro.ncu.edu.tw](mailto:zylin@astro.ncu.edu.tw))

R05 – Capturing Superflares in G, K, and M Dwarfs with Time-Domain Spectroscopy

PI: Zhen-Kai Gao ([izkgao@astro.ncu.edu.tw](mailto:izkgao@astro.ncu.edu.tw))

\*R06 – Transients within Hours of Explosion

PI: Yen-Chen Pan ([ypan6@ucsc.edu](mailto:ypan6@ucsc.edu))

\*R07 – Taxonomical Study for Unclassified Near-Earth Asteroids

PI: Chih-Hao Hsia ([chhsia@must.edu.mo](mailto:chhsia@must.edu.mo))

R08 – The Long Period Variable Stars in Kepler Field Distinguish with Spectra

PI: Jia-Yu Ou ([m1039004@gm.astro.ncu.edu.tw](mailto:m1039004@gm.astro.ncu.edu.tw))

## LOT2018C (01 September – 31 December, 2018)

### Education Program:

E01 - Student Training for NTHUs Fundamentals of Observational Astronomy Course

PI: Shih-Ping Lai ([slai@phys.nthu.edu.tw](mailto:slai@phys.nthu.edu.tw))

E03 – Observation Training for Lin-kou Senior High School and Taoyuan Senior High School Students

PI: Hao-Yuan Duan (hyduan@gapp.nthu.edu.tw)

E04 – Practical Class of "Fundamentals of Observational Astronomy"

PI: Albert Kong (akong@phys.nthu.edu.tw)

**Research Program:**

R01 – The Rotation Period Confirmations for Large Super-Fast Rotating Asteroids

PI: Chan-Kao Chang (rex@astro.ncu.edu.tw)

R02 - BVRI Monitoring of Classical Cepheids in M31 For Distance Scale Applications

PI: Chow-Choong Ngeow (cngeow@astro.ncu.edu.tw)

R03 - Photopolarimetric Observations of Known UXor and Potential Candidates

PI: Po-Chieh Huang (pochiehuang1@gmail.com)

\*R04 - The Follow-Up Observations for the Transit Exoplanet Candidates in Open Clusters

PI: Po-Chieh Huang (pochiehuang1@gmail.com)

\*R05 - Taxonomical Study for Unclassified Near-Earth Asteroids (II)

PI: Chih-Hao Hsia (chhsia@must.edu.mo)

\*R06 – Transients within Hours of Explosion

PI: Yen-Chen Pan (ypan6@ucsc.edu)

\*R07 – The Nature of Unidentified Fermi Objects

PI: Albert Kong (akong@phys.nthu.edu.tw)

\*R08 – ToO and Follow-Up Observations of GROWTH and ZTF Targets

PI: Chow-Choong Ngeow (cngeow@astro.ncu.edu.tw)

\*R09 – Narrow-Band Imaging of Extended Planetary Nebulae (I) - M 2-55 and Abell 2

PI: Chih-Hao Hsia (chhsia@must.edu.mo)

\*R10 – A Worldwide Campaign of Comet 46P/Wirtanen

PI: Zhong-Yi Lin (zylin@astro.ncu.edu.tw)

\*R11 – A Study of Asteroid 2005 UD, A Target of DESTINY+ (A Space Mission by JAXA)

PI: Zhong-Yi Lin (zylin@astro.ncu.edu.tw)

\*R12 – An EDEN Campaign to Search for Habitable Exo-Earths around M Dwarfs

PI: Wen-Ping Chen ( wchen @astro.ncu.edu.tw)

# 鹿林天文台工作報告 2018

林宏欽

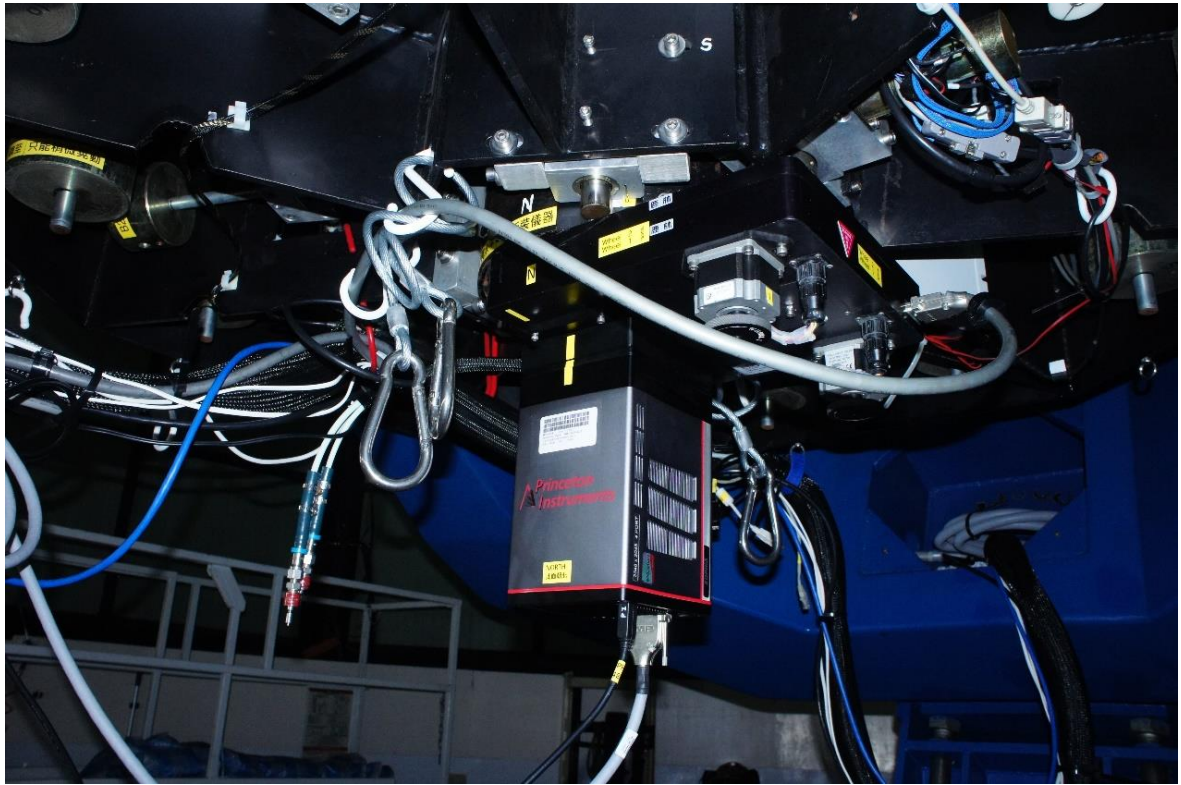
鹿林天文台一米望遠鏡 (LOT) 自 2002 年 9 月開始運作以來已歷 15 年，2017 年將 LOT 望遠鏡軟硬體系統升級、次鏡重鍍、採購 CCD 相機。2018 年新 CCD 相機上線、科學濾鏡更新、光學系統加像場修正鏡優化，更換網路為 4G 系統，大幅提升觀測效率及科學產出。

## 1. 具體工作

### 1.1 LOT CCD 相機更新

一米望遠鏡(LOT)之主力 CCD 相機 Princeton Instruments PI-1300B 於 2014 年故障淘汰，備用機 Apogee U42 CCD 相機也已經使用 10 多年，運作開始不穩定，此外 CCD 原廠也已終止維修。為維持 LOT 正常運作，有效執行研究計畫，更新 CCD 相機勢在必行。新一代的 Princeton Instruments SOPHIA 2048B CCD 相機相較舊 CCD 性能提升許多，更有以下獨特優點，

1. 可冷卻 CCD 感測器到 $-90^{\circ}\text{C}$  以下，不需要額外的冷卻裝置和制冷機。
2. 全金屬真空密封，永久的真空保證，不需常抽真空。
3. 2048 x 2048 背照式 CCD， $15\mu\text{m} \times 15\mu\text{m}$  像元，峰值量子效率高達 $> 95\%$ 。
4. 獨有的 eXcelon 專利技術，具備更寬的波長範圍，增強靈敏度，抑制近紅外紋影效應
5. 高達 16MHz 讀出速率，4 通道同時讀出
6. 全新的超低雜訊讀出電子電路與極平穩的背景雜訊
7. USB 3.0 資料傳輸介面



## 1.2 LOT 像場修正鏡

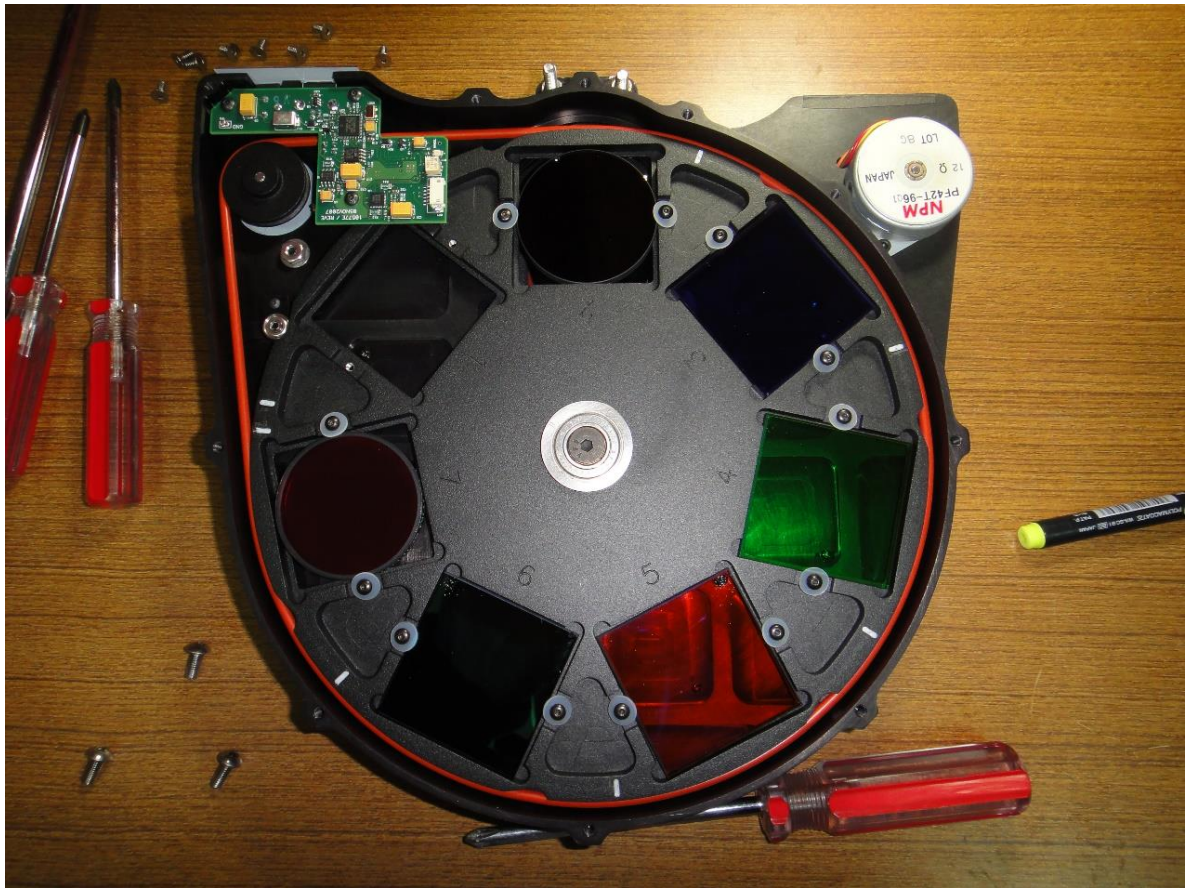
新 Princeton Instruments SOPHIA 2048B CCD 相機晶片較大，為改善周邊成像，特為一米望遠鏡 LOT 訂製專用像場修正鏡。已於 2018 年 5 月到，將於 2018 下半年安裝測試。





## 1.3 科學濾鏡更新

目前 LOT 使用的天文標準濾鏡系統 UBVRI 與 SDSS 也已經使用超過 10 年，有老化現象，將與 CCD 相機一起同步更新。



## 2. 科學成果(2018)

標題、作者、年份、期刊名稱、卷期、起(迄)頁數

( Title, authors, year, journal, volume, first page )

1. Star-disk Interaction in Multi-band Photometric Monitoring of the Classical T Tauri Star GI Tau, Guo, Zhen, Herczeg, Gregory, Jose, Jessy, et al. (including Chiang, P. S. and Chen, W. P. from NCU), 2018, *Astroph. J.*, 852, 56
2. Photometric survey and taxonomic identifications of 92 near-Earth asteroids, Lin, Chien-Hsien; Ip, Wing-Huen; Lin, Zhong-Yi; Cheng, Yu-Chi; Lin, Hsing-Wen; Chang, Chan-Kao, 2018, *Planetary and Space Science*, 152, 116-135.
3. The Bright Gamma-ray Flare of 3C 279 in June 2015: AGILE Detection and Multifrequency Follow-up Observations, Pittori, C., Lucarelli, F., Verrecchia, F. et al. (AGILE and GLAST collaborations, including Chen, W. P., Hsiao, H. Y., and Samal, M. from NCU), 2018, *Astroph. J.*, 856, 99
4. The sdB pulsating star V391 Peg and its putative giant planet revisited after 13 years of time-series photometric data, Silvotti, R.; Schuh, S.; Kim, S.-L., et al., 2018, *Astronomy & Astrophysics*, 611, A85; doi.org/10.1051/0004-6361/201731473
5. SN 2017ens: The Metamorphosis of a Luminous Broadlined Type Ic Supernova into an SN IIn, Chen, T.-W.; Inserra, C.; Fraser, M.; et al., 2018, *Astroph. J.*, 867, L31

## 3. 其他成果

### 3.1 目前參與之國際合作計畫

1. 泛星計畫 (Pan-STARRS; the Panoramic Survey Telescope And Rapid Response System)
2. 全球望遠鏡聯合觀測計畫 (The Whole Earth Telescope, WET)
3. 全球蠍虎 BL 類星體聯合觀測計畫 (The Whole Earth Blazar Telescope, WEBT)
4. 年輕系外行星掩星計畫 (Young Exoplanet Transit Initiative, YETI)
5. 帕洛馬瞬變工廠計畫 (Palomar Transient Factory, PTF)
6. 史維基瞬變探測器計畫 (Zwicky Transient Facility, ZTF)

# 天文台參觀及觀測教學 2018

時間	單位	參觀人數
20180113	中和高中	31
20180116	海大天文社	19
20180118	台清交大天文社	70
20180124	逢甲天文社	26
20180201	新豐高中天文社	46
20480209	中山女高	60
20180212	興大天文社	17
20180304	南瀛天文館	27
20180312	國庫署	23
20180412	東汴國小	18
20180526	嘉中天文社	39
20180701	錚駿公司	9
20180705	彰化鹿東國小	18
20180727	內政部建研所	15
20180929	香林國小	16
20180804	明華國中	40
20180807	中科實中	19
20180813	南十字	39
20180813	麗山高中	33
20180908	成功大學天文社	18
20180908	嘉義羽球愛好	10
20180929	中大心悅讀書會	40
20181006	台南天文學會	41
20181013	台灣親子觀星會	
20181101	南投地方法院	16
20181108	玉管處	20
20181117	祥暉關懷協會	35
20181201	中正大學通識中心	35
20181208	嘉義高中	35
20181208	苗栗社區大學	19
20181208	師大附中	5
20181214	陳文屏等	13

20181215	新竹高中	33
20181215	興大附中	22



南十字參訪



中正大學通識中心參訪

# Analysis of Lunar Impact Flashes Recorded during the Geminids meteor shower in 2017

Zong-Yi Lin<sup>1</sup>, Chih-Cheng Liu<sup>2</sup>, Bo-Hao Wang<sup>2</sup>, Yan-Syun Jhang<sup>2</sup>, Bingsyun Wu<sup>3</sup>, Jim Lee<sup>4</sup>, Zhong-Yi Lin<sup>5</sup>, Hung-Chin Lin<sup>5</sup>, Hsin-Chang Chi<sup>1</sup>

<sup>1</sup>Department of Physics, National Dong Hwa University, Hualien, Taiwan

<sup>2</sup>Department of Applied Mathematics, National Dong Hwa University, Hualien, Taiwan

<sup>3</sup>Taichung municipal Hui-Wen high school, Taichung, Taiwan

<sup>4</sup>Taipei Astronomical Museum, Taipei, Taiwan

<sup>5</sup>Graduate Institute of Astronomy, National Central University, Taoyuan, Taiwan



## **Abstract**

We attended the worldwide campaign of asteroid 3200 Phaethon which is the target of Japan's space mission called DESTINY. One of the campaign's propose is to realize the size distribution of the dust particle within the trail of 3200 Phaethon. Radar observation and meteor optical detector systems from ground-based can provide information about the size ranges in micro- and meter-meteorite but there is no clear size-strength correlation over the size range of centimeter to tens of meters. Fortunately, the issue can be solved and estimated directly from a study of Lunar impact flash. In the end of 2017, we started to monitor the lunar surface with small telescopes to detect light flashes resulting from the hypervelocity collisions of meteoroids. In this work, we report our primarily results from 1.5 hours of our Lulin lunar impact flashes monitoring system.

## **1. Introduction**

Light flashes produced by meteoroids impacting the night side of the Moon have been identified mostly during the peak activity of several major meteor showers (see e.g. Dunham et al. 2000, Ortiz et al. 2000, Yanagisawa and Kisaichi 2002, Cudnik et al. 2002, Ortiz et al. 2002, Yanagisawa et al. 2006, Cooke et al. 2006, Yanagisawa et al. 2008, Madiedo et al. 2015b). Routine impact monitoring has been carried out with an automatic system at NASA Marshall Space Flight Center (MSFC) since 2006 (Cooke et al. 2007; Oberst et al. 2012). During the first five years they found a total of 240 impacts; on average one flash for every two hours of observation, with dramatically higher rates during meteor showers. In addition, they also noted an asymmetry between the impact rate on the western hemisphere of the Moon ( the leading edge, observed during evening crescent moon) and the eastern hemisphere (trailing edge, morning crescent moon) of about 1.5:1 (Kim et al. 2015)

In December 2017, we participated for the first time in the monitoring campaign of lunar impact flashes by using two small telescopes at Lulin observatory during the Geminid meteor storms. In this work, we will describe our monitoring system, report our first plausible detection of lunar impact flash in detail, and estimate some physical properties of our candidate.

## **2. Observations**

Our 2017 lunar impact flashes monitoring campaign was conducted at Lulin Observatory (latitude: 23.4686 °N, longitude: 120.8736 °E, height: 2862 m above the sea level), where two identical 0.40m and 0.20m Schmidt-Cassegrain telescopes manufactured by Celestron (Table 1) were employed to monitor the same part of the night side of the Moon. Two telescopes

0.40m and 0.20m Schmidt-Cassegrain telescopes manufactured by Celestron (Table 1) were employed to monitor the same part of the night side of the Moon. Two telescopes were used in order to have duplicity of impact flash detections to distinguish true impact flashes from noise or cosmic ray hits in the detectors. This is the usual procedure that we follow to detect impact flashes unambiguously.

During the Geminid meteor shower last December, we fortunately found a plausible candidate lunar impact flash (Figure 1) in one telescope (SLT) on Dec. 15.89 UT, 2017 at selenographic longitude 44.50 degrees and latitude 2.09 degrees. The flash lasted for 0.033 s and the brightness is 5.77 mag. using the field star (Figure 2) for comparison.

**Table 1** : Lunar impact flash system at Lulin observatory

	C16(SLT)	C8(TAOs)
Camera type	Watec 902H2U	ASI 174MM
Diameter	400mm	200mm
Initial focal length	3910mm	2000mm
Focal reducer system	0.63x+0.5x	0.5x
Time recording system	GPS-time inserters	GPS-time inserters

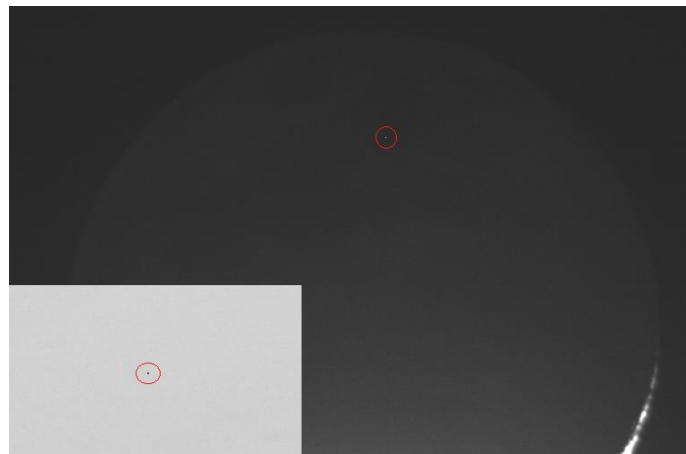


**Fig. 1** A plausible candidate lunar impact flash

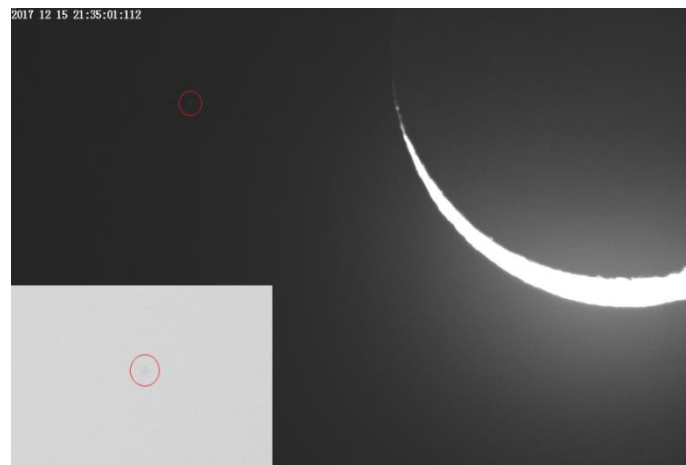


**Fig. 2** Field star used for estimating the mag of detected event.

### 3. Impact Dynamics Analysis

According the equation of bolometric energy and translate to kinetic energy (R.M. Suggs, et al. (2014)) :

$$E_{lum} = f_{\lambda} \Delta \lambda f \pi d^2 t \quad \text{where } f_{\lambda} \text{ is } 10^{-7} \times 10^{-(R+21.1+zp_R)/2.5} \dots (1),$$

$$E_k = \frac{E_{lum}}{\eta} \quad \dots (2)$$

Then we can learn the diameter of crater by Gault's (1974) crater-scaling equation (in CGS-system) for the Moon : (Assuming the angle  $\theta$  between  $v$  and ground is  $90^\circ$ )

$$D(cm) = 1.5 \times 10^{-3} \rho_p^{\frac{1}{6}} \rho_t^{-\frac{1}{2}} E_k^{0.37} (\sin\theta)^{2/3} \dots (3), \quad D(m) = D(cm)/100$$

The inferred energy parameters of flash is given in Table 2. The kinetic energy of meteoroids is directly obtained by converting visible light energy on the Moon.

Table2 : The information parameters of bolometric and energy translate equations.

$\Delta \lambda(\text{\AA}) : 3600$ $d(cm) : 3.884 \times 10^{10}$ $\eta : 1.5 \times 10^{-3}$ $f : 2$	$t(s) : 0.033$ $R(\text{mag}) : 5.77$ $zp_R : 0.555$ $v : 16 \text{ km/s}$
---	---

<p><math>d</math>: The distance to the Moon.  <math>f</math> : in free space <math>f</math> is 4 ; For a flash close to the lunar surface <math>f</math> is 2.  <math>v</math> : a typical impact speed of a sporadic impactor on the Moon.  <math>R</math>: The zero point magnitude.  <math>t</math>: The exposure time.  <math>\eta</math>: Luminous efficiency factor.  <math>zp_R</math>: The zero point magnitude for the R filter.  <math>\Delta \lambda(\text{\AA})</math>: The width of effective detecting passband.  <math>f_{\lambda}</math> : The equation about magnitude.</p>
--



#### 4. Results

We can calculate the bolometric energy with magnitude and translate bolometric energy to kinetic energy with luminous efficiency factor, we learn  $E_{lum}$  is  $1.2 \times 10^6$  (J) and  $E_k$  is  $7.9 \times 10^8$  J ( $7.9 \times 10^{15}$  g · cm<sup>2</sup>/s<sup>2</sup>.)

The diameter of the impact crater can be estimated using the simplified Gault's formula (Gault et al. 1974) that only requires kinetic energy as the input parameter. Table 3 shows the sizes found for different densities of meteoroids ( $\rho_p = 1.5, 3.1$  and  $4.2$  g/cm<sup>3</sup>) and lunar crust ( $\rho_t = 2.2, 2.7$  and  $3.1$  g/cm<sup>3</sup>) (Huang and Wieczorek 2012).

Table 3 : the crater diameter of different densities (g/cm<sup>3</sup>) of Moon and projectile (Htm Halley-type meteoroids, Jfs Jupiter-family sporadics, As asteroidal meteoroids).

Moon density, $\rho_t$	2.2			2.7			3.1		
Meteoroid density, $\rho_p$	1.5(Htm)	3.1(Jfs)	4.2(As)	1.5(Htm)	3.1(Jfs)	4.2(As)	1.5(Htm)	3.1(Jfs)	4.2(As)
D(m)	5.50	6.21	6.53	4.97	5.61	5.90	4.63	5.23	5.50

#### 5. Conclusions

- 1) A plausible candidate lunar impact flash was fortunately found on Dec. 15.89 UT, 2017 at eastern hemisphere of selenographic longitude 44.50 degrees and latitude 2.09 degrees.
- 2) The diameter of the crater produced by this impact would range from 4.63-5.50 m (for a bulk density  $1.5$  g/cm<sup>3</sup>) to 5.50-6.53m (for  $\rho_p = 4.2$  g/cm<sup>3</sup>) depending on which Moon density is used for estimation.

#### References

1. Mamoun Ait Moulay Larbi et al, 2015, First Lunar Flashes Observed from Morocco (ILIAD Network): Implications for Lunar Seismology. Earth Moon Planets **115** 1-21(2015). Doi: 10.1007/s11038-015-9462-1
2. D.E. Gault, R. Greeley, P.H. Schultz, A primer in lunar geology. Moffett Field: NASA Ames Research Center (1974), pp. 137–175
3. L.R. B. Rubio, J.L. Ortiz, P.V. Sada, Luminous efficiency in hypervelocity impacts from the 1999 lunar Leonids. Astrophys. J. 542, L65–L68 (2000a). doi:10.1086/312914
4. Dunham et al. 2000
5. Ortiz et al. 2000
6. Yanagisawa and Kisaichi 2002
7. Cudnik et al. 2002
8. Ortiz et al. 2002
9. Yanagisawa et al. 2006
10. Cooke et al. 2006
11. Yanagisawa et al. 2008
12. Madiedo et al. 2015b
13. Cooke et al. 2007
14. Oberst et al. 2012
15. Kim et al. 2015
16. Huang and Wieczorek 2012

#### Acknowledgements

The Ministry of Science and Technology of Taiwan supported this work. The work of Zhong-Yi Lin was supported by Grant No. MOST 105-2112-M-008-002-MY3.

# Meteor investigations using the TMDS

Bo-Hao Wang<sup>1</sup>, Zong-Yi Lin<sup>2</sup>, Chih-Cheng Liu<sup>1</sup>, Yan-Syun Jhang<sup>1</sup>, Bingsyun Wu<sup>3</sup>, Jim Lee<sup>4</sup>, Zhong-Yi Lin<sup>5</sup>, Hsin-Chang Chi<sup>1</sup>

<sup>1</sup>Department of Applied Mathematics, National Dong Hwa University, Hualien, Taiwan,

<sup>2</sup>Department of Physics, National Dong Hwa University, Hualien, Taiwan,

<sup>3</sup>Taichung municipal Hui-Wen high school, Taichung, Taiwan,

<sup>4</sup>Taipei Astronomical Museum, Taipei, Taiwan,

<sup>5</sup>Graduate Institute of Astronomy, National Central University, Taoyuan, Taiwan,



## Abstract

Taiwan Meteor Detection System (TMDS) is a joint platform under a collaborative development among National Dong-Hwa University (NDHU), National Central University (NCU) and Taipei Astronomical Museum (TAM). The TMDS aims to scope meteor events in the sky surrounding Taiwan and performs successive analyses of recorded events. Currently, four observing stations including Lulin, Kenting, Yang Ming Shan National park and Fushoushan, were constructed. From July 2016 to April 2018, the TMDS has detected about eight thousand events. But only 106 multi-station orbits are precisely determined and some of them are associated with the parent body of 109P (Swift–Tuttle) and (3200) Phaethon by using Southworth-Hawkins criterion ( $D_{SH}$ ). In addition, 45 meteor spectra have been recorded and these spectra can be used to identify the chemical compositions of meteors.

## 1. Introduction

A meteor occurs when a meteoroid (comet debris or asteroid fragment) strikes Earth's atmosphere at high speed. Intense heat is created by the compression of the air ahead of the meteoroid, which usually causes the object to burn up in the atmosphere, creating the white "shooting star" that we are all familiar with. Taiwan Meteor Detection System (TMDS), which is an interdisciplinary project dedicated to study these meteoroids streams and the interaction of these particles of interplanetary matter with Earth's atmosphere. TMDS located in different places in Taiwan employ a high-sensitivity CCD video cameras to monitor the night sky. The first two of these stations were setup at Hutain elementary school located in Yang-Ming-Shan National Park, and Lulin observatory in 2016, and two more stations were setup at Kenting observatory in 2017 and Fushoushan Farm in 2018 (Figure 1). Over 7847 meteor trails have been registered from 2016 to 2018 but only 1% (Figure 2) can be used to determine the orbits due to the bad weather in Northern (Hutain) and Southern (Kenting) Taiwan. In this work, we focus on the detected orbits and use  $D_{SH}$  criterion to find out which parent body is related to especially in known meteor showers (i.e. Perseids-August, and Geminids-December)

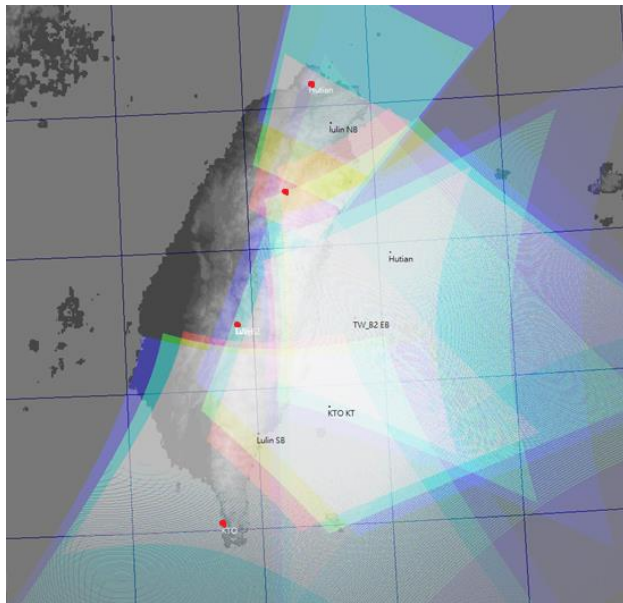


Fig. 1 The locations for Taiwan Meteor Detection System (TMDS).



Fig. 2 Two Meteor Cameras being operated 200 km apart captured the same meteor.

## 2. Observations and Analyses

### 2.1 Observations

The TMDS started operation in August 2015 after Hutain site setup. So far, over 7847 meteor trails have been detected (Table 1) and about one hundred events can be used to determine the orbits (Table 2).

Three cameras are also endowed with holographic diffraction gratings (600 grooves per millimeter) for obtaining meteor spectra. Because the calibration to the spectra is still undergoing, we therefore focus on the results of the orbits analysis.

### 2.2 Meteor Orbit

The triangulation method was applied to calculate the positions and velocities of simultaneously detected meteors. With the position and velocity components of individual meteors, the meteor orbits can be determined. Part of them are shown in Table 3 and Table 4.

Table 1. The total detections in Taiwan Meteor Detection System (TMDS) from July 2016 to April 2018

No. of detections \ Stations (Direction)	Lulin (E.N.S)	Hutain (E)	KTO (E)	Fushoushan (E. S)
Events	6732	779	297	39

Table 2. The orbits in Taiwan Meteor Detection System (TMDS) from August 2017 to April 2018

Orbits \ Stations (Direction)	Lulin & Hutain	Hutain & KTO	KTO & Lulin
Orbits	69	3	37

Table 3. Physical characteristics and orbital elements of the detected meteors

Local Time (Date_hms)	Meteor Streams	Mag	duration (sec)	high of start point (km)	high of end point (km)	a semi-major axis (au)	q perihelion (au)	e eccentricity	p period (year)	$\omega$ argument of perihelion (deg)	$\Omega$ longitude of ascending node (deg)	i inclination (deg)
20180405_040646	spo	-1.3	1.1	92.6	81.5	2.8	0.7	0.764	4.7	257.0	14.8	1.1
20171222_185014	J5Urs	1.5	1.6	99.4	87.1	6.9	0.9	0.866	18.3	207.3	270.5	54.2
20171127_230742	J5sTa	-0.4	0.9	85.5	62.0	2.6	0.4	0.863	4.1	113.1	65.3	7.0
20170917_223409	J5sPe	-2.6	0.7	113.3	89.3	-8.9	0.5	1.058	$\infty$	267.1	174.7	139.7
20170815_044057	J5Per	-0.5	0.3	106.7	93.6	-71.7	0.9	1.013	$\infty$	147.7	142.0	113.5
20171026_045011	J5Ori	-0.8	0.2	106.5	96.0	4.3	0.5	0.892	8.9	97.8	32.4	164.6
20180422_223146	J5Lyr	-1.6	1.7	109.5	82.9	-5.0	0.9	1.186	$\infty$	210.4	32.2	82.3
20171118_043411	J5Leo	-2.1	0.4	113.7	85.9	-4.9	1.0	1.200	$\infty$	173.1	235.4	162.9
20171215_000428	J5Gem	-0.4	0.3	79.5	68.9	1.4	0.1	0.904	1.7	324.6	262.6	22.2
20180101_051333	J5Com	-1.2	0.2	106.2	91.4	-2.9	0.6	1.209	$\infty$	253.6	280.1	138.6

Table 4 .The known meteor stream detected in TMDS from August 2017 to April 2018.

Meteor streams	Quantity
spo	54
J5Urs	1
J5sTa	1
J5sPe	1
J5Per	10
J5Ori	1
J5nuE	1
J5Lyr	1
J5Leo	2
J5Gem	17
J5eVi	1
J5Com	4

### 2.3 Southworth-Hawkins criterion ( $D_{SH}$ )

The widely used  $D_{SH}$  criterion of Southworth-Hawkins criterion is a quantitative measure of the similarity of two orbits. The smaller  $D_{SH}$ , the more similar orbits.

$$[D_{SH}]^2 = (e_2 - e_1)^2 + (q_2 - q_1)^2 + (2 \sin \frac{I_{21}}{2})^2 + \frac{1}{4} (e_2 + e_1)^2 (2 \sin \frac{II_{21}}{2})^2$$

$$I_{21} = \arccos[ \cos i_1 \cos i_2 + \sin i_1 \sin i_2 \cos(\Omega_2 - \Omega_1) ]$$

$$II_{21} = \omega_2 - \omega_1 + 2 \Gamma \arcsin ( \cos \frac{i_2 + i_1}{2} \sin \frac{\Omega_2 - \Omega_1}{2} \sec \frac{I_{21}}{2} )$$

$$\Gamma = \begin{cases} +1, & |\Omega_2 - \Omega_1| \leq 180^\circ \\ -1, & |\Omega_2 - \Omega_1| > 180^\circ \end{cases}$$

Where the e is eccentricity, q is perihelion, i is inclination,  $\omega$  is argument of perihelion, and  $\Omega$  is longitude of ascending node. The subscripts 1 and 2 are referred to meteor- and parent-orbit (NEAs or comets), respectively. We present here results for selected cases in Table 5 and Figure 3.

Table 5. Associated orbit of known parent body and detected meteors by using Southworth-Hawkins criterion ( $D_{SH}$ ).

	No. of orbit	Parent body	Maximum $D_{SH}$	Minimum $D_{SH}$	Mean $D_{SH}$	Standard deviation
Geminid	17	3200 (Phaethon)	0.1109	0.0005	0.0215	0.0299
Perseids	10	109P (Swift-Tuttle)	0.0806	0.0005	0.0194	0.0227

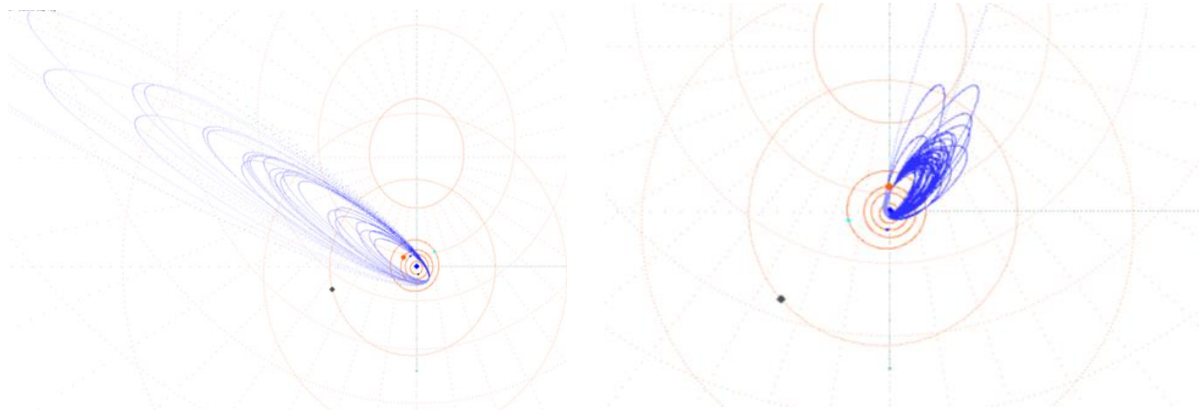


Fig. 3. The detected orbits of the Perseids (3a) and Geminid (3b) meteor shower in 2017

### 3. Conclusions

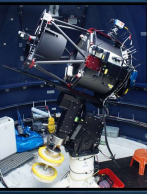
1. The TMDS contained precise 106 multi-station orbits captured during 2016-2018. The orbits data can be applied to acquire the activity information of the meteor parent bodies (i.e. Near-Earth Asteroids or Comets).
2. With  $D_{SH}$  parameter, we successfully found out the associated parent body (i.e. (3200) Phaethon is the parent body of the Geminid meteor shower ) from the multi-station orbits.
3. A new comparable station, Fushoushan, to the Lulin observatory was established in March 2018. In the future, we hope to get more meteor detections and multi-stations orbits to improve our estimation of the orbital characteristics of meteor showers.

### References

1. Jakub Koukal *et al*, 2016, WGN, The Journal of the IMO 44:1
2. NASA JPL Small Bodies Database Browser (<http://ssd.jpl.nasa.gov/sbdb.cgi#top>)
3. William Stewart *et al*, 2013, "NEMETODE: The Network for Meteor Triangulation and Orbit Determination. System Overview and Initial Results from a UK Video Meteor Network ", Journal of the IMO ,41, 84-91
4. R. B. Southworth and G.S. Hawkins, Statistics of Meteor Streams 1963

### Acknowledgements

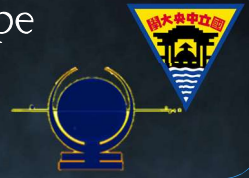
The Ministry of Science and Technology of Taiwan supported this work. The work of Zhong-Yi Lin was supported by Grant No. MOST 105-2112-M-008-002-MY3.



# Lulin Widefield Telescope (LWT): a Robotic Telescope for the Near-Earth Objects Follow-up Observation

Jian-Fong Huang<sup>1\*</sup>, Chow-Choong Ngeow<sup>1</sup>, Ting-Jhang Yang<sup>1</sup>, Hung-Chin Lin<sup>1</sup>

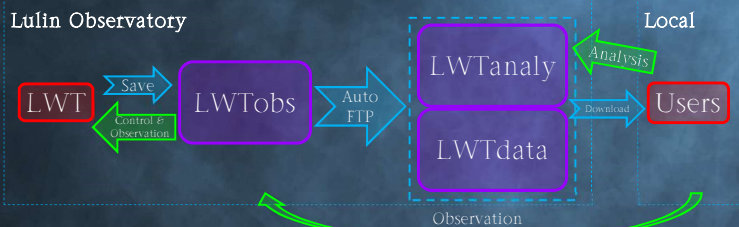
<sup>1</sup>Graduate Institute of Astronomy, National Central University, Taoyuan, Taiwan



## ABSTRACT

The Lulin Widefield Telescope (LWT), which is an Officina Stellare's 0.4m RiFast 400 telescope, was installed at the Lulin Observatory on October 17<sup>th</sup>, 2017. The telescope was equipped with a FLI ProLine PL16803 monochrome CCD camera to reach a field of view up to about 2 square degrees and the limiting magnitude approaches to 19mag. We are working on making the follow-ups of Near-Earth Objects (NEOs) with the LWT a daily routine, as well as the complete procedures from observation, image calibration and reduction to analysis be **totally automatic**. We show some successful observations, and cases were a crucial step for the LWT to track the NEOs. At the last part, we describe the prospect of the LWT.

## SYSTEM

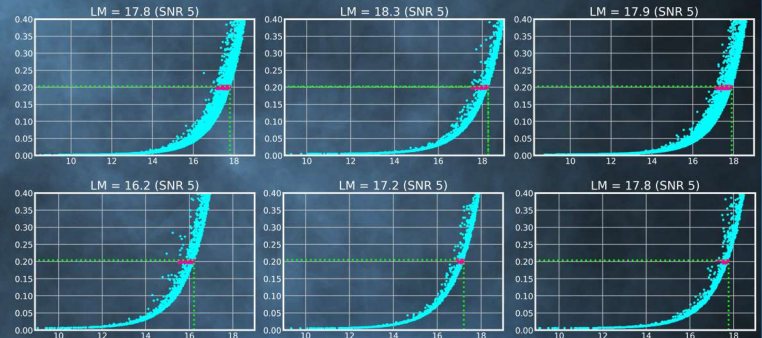


➡ : Data Flow    ➡ : User Access

- LWTobs: a computer has all the required programs installed and is responsible for the automatic observation.
- LWTanaly: a computer provides a high performance computing for the automatic analysis.
- LWTdata: a NAS system stores and backups all the data automatically.

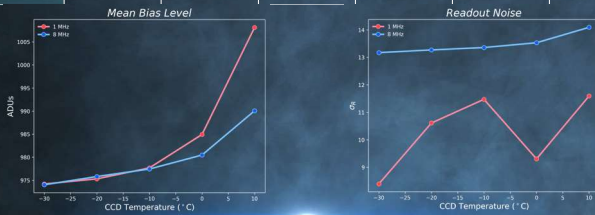
## LIMITING MAGNITUDE

The limiting magnitudes of V-band 300s exposures during **new** (the three above) and **full** (the three below) moon for **signal-to-noise ratio (SNR) 5** at different altitudes (40°, 50° and 60° from left to right).



## READOUT NOISE

e <sup>-</sup>	-30°C	-20°C	-10°C	0°C	10°C	Manufacturer
1MHz	8.2	11.8	8.6	9.2	13.1	10
8MHz	14.3	14.5	14.7	14.9	15.6	14



## TRANSFER CURVE

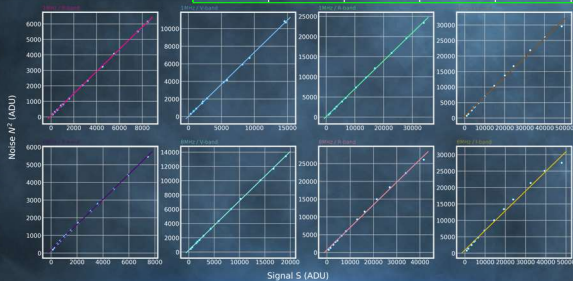
$$N^2 = \frac{1}{g} \times S + \frac{1}{g^2} \times \sigma_R^2$$

☞: [www.narrowbandimaging.com](http://www.narrowbandimaging.com)

e <sup>-</sup> / ADU	B	V	R	I	☞
1MHz	1.4	1.4	1.7	1.4	1.4
8MHz	1.4	1.3	1.5	1.4	

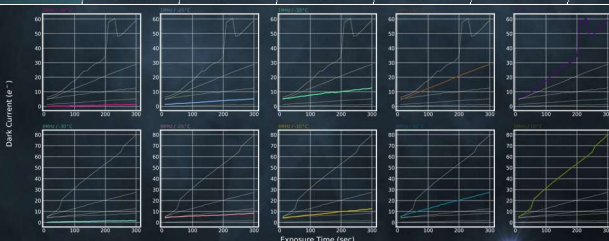
  

ADU	B	V	R	I	Manufacturer
1MHz	14.3	10.7	54.1	13.1	7.1
8MHz	21.9	16.4	27.2	20.5	10

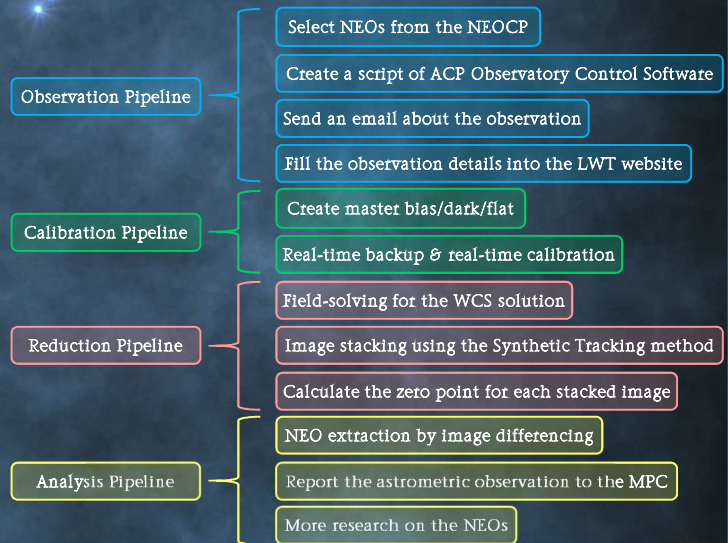


## DARK CURRENT

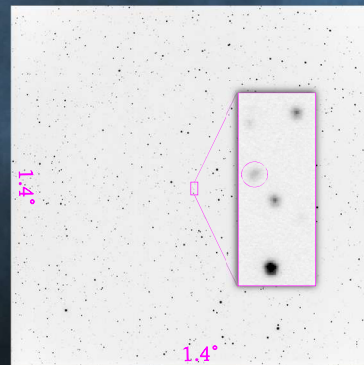
e <sup>-</sup> / s	-30°C	-20°C	-10°C	0°C	10°C	Manufacturer
1MHz	0.004	0.01	0.03	0.08	0.21	-35°C
8MHz	0.004	0.01	0.03	0.07	0.25	< 0.005



## PROCESSING FLOWCHART



## ASTEROID



A stacked image of asteroid (769) Tatjana with 15mag at V-band and 60s exposure on Mar. 10, 2018. We can see that the pointing is good enough to track NEOs in the future work.

The whole system of the LWT is not complete yet. Because the NEOs are **too faint to capture** (many of them > 19mag), we are finding ways to make them appear in our images. Our ultimate goal is to make the LWT become a **robotic telescope** dedicated to the **NEO follow-ups**.

## REFERENCE

1. Near-Earth Objects Confirmation Page (NEOCP): [www.minorplanetcenter.net/iau/NEO/toconfirm\\_tabular.html](http://www.minorplanetcenter.net/iau/NEO/toconfirm_tabular.html)

Contact Information: Jian-Fong Huang (smoBEE@astro.ncu.edu.tw)

# 新聞報導

# 面對 AI、全球暖化威脅 葉永烜帶領眺望五十年後的今天

中大新聞

2018/10/31 HiNet 新聞

由中央大學與余紀忠文教基金會共同成立的「余紀忠講座」，今年邁入第十個年頭，特別邀請葉永烜院士擔任主講人，並以「眺望 50 年後的今天」為題，從歷史、人文、天文等面向，引導師生和社會大眾如何安身立命，面對全球暖化、人工智慧的威脅，如何善盡台灣身為世界公民之社會責任。

葉永烜為國際知名天文學家，研究專長為彗星物理和太陽系及行星起源等。1982 年他提出了著名的跨國土星探測計畫卡西尼－惠更斯號，為國際天文研究寫下輝煌的一頁。2009 年 NASA 授予他特殊公共服務榮譽勳章，表彰在探測土星系統計畫的貢獻。他所發表的期刊論文已超過二百篇，而發表在《Nature》和《Science》之篇數為華人科學家之最。

本講座邀請李羅權院士擔任引言人，並指出在未來的趨勢裏，地球文明毀滅的因素可能有二，分別是核子戰爭和全球暖化，值得大眾關注，也為葉院士的演講揭開了序幕。

葉永烜以歷史背景為主軸，描述二次世界大戰後，美國「自由主義」的黃金時代，乃至冷戰時期美蘇的太空競賽，並以 1968 年為核心，說明當時世界各地均以基礎科學發展為重，強調中央大學當年在台復校，就是順應著「國際地球物理年」，從地球科學研究開始起家，在永續發展上影響甚大。

在氣候變遷，環境改變的環伺下，他說道未來的世界將有很大的不同；在人口結構上，2030-2040 年間可能是現在人類與機器人黃金交叉時，再後便會被超越，相關運用如仿生微型無人飛機與 Space X 太空旅行計畫將可能實現。除此之外，更點出 50 年後的 AI 時代「Life3.0」將會出現巨大變革，並以史蒂芬·霍



金生前預言的「超級人類」為例，說明人類有可能利用科學方式改變 DNA，展開一場未知的 AI 競賽。

葉永烜也以電影「星際迷航」為例，勉勵大家向外去探索未知的世界，尋找宇宙之中外星文明發展的規律與足跡，同時必須要用同情心、使命感與意志力去解決面臨的困難與危機，「不要怕麻煩，我們要把世界變得更好！」

另外，配合本講座的舉辦，圖書館特別安排一場「葉永烜特展」，除了葉院士個人重要的成就外，還有雜誌訪談、教學模型及資料展外；大家可透過影片播放，了解卡西尼任務始末和鹿林天文台，希望燃起學子對天文學及太空科學研究的興趣。另有葉永烜推薦放在圖書館特展的參考書籍，希望透過書本啟發，幫助大家迎接新世代的來臨，眺望 50 年後的未來。

圖書館藝文走廊也展出葉永烜「山外有山」個展。余紀忠文教基金會董事長余範英形容，葉永烜是在複雜年代中沉靜的學者，透過其溫暖的筆觸，開濶的心胸，展現出其對學術的貢獻、對人類的關懷，深具「教育家」精神。

原文轉載自【2018-10-31/HiNet 新聞】

## 媒體報導

<https://times.hinet.net/news/22055124>

[2018/10/31 HiNet 新聞](#)

## 校園新聞

2018-10-31

### 面對 AI、全球暖化威脅 葉永烜帶領眺望五十年後的今天

文／校園實習記者鍾依靜



配合余

紀忠講座之舉辦，中央大學圖書館另舉辦葉永烜院士特展。開幕式貴賓左起圖書館館長李力庸、葉永烜院士、余紀忠基金會董事長余範英、中央大學校長周景揚。劉天祺攝

由中央大學與余紀忠文教基金會共同成立的「余紀忠講座」，今年邁入第十個年頭，特別邀請葉永烜院士擔任主講人，並以「眺望 50 年後的今天」為題，從歷史、人文、天文等面向，引導師生和社會大眾如何安身立命，面對全球暖化、人工智慧的威脅，如何善盡台灣身為世界公民之社會責任。

葉永烜為國際知名天文學家，研究專長為彗星物理和太陽系及行星起源等。1982 年他提出了著名的跨國土星探測計畫卡西尼－惠更斯號，為國際天文研究寫下輝煌的一頁。2009 年 NASA 授予他特殊公共服務榮譽勳章，表彰在探測土星系統計畫的貢獻。他所發表的期刊論文已超過二百篇，而發表在《Nature》和《Science》之篇數為華人科學家之最。

本講座邀請李羅權院士擔任引言人，並指出在未來的趨勢裏，地球文明毀滅的

因素可能有二，分別是核子戰爭和全球暖化，值得大眾關注，也為葉院士的演講揭開了序幕。

葉永烜以歷史背景為主軸，描述二次世界大戰後，美國「自由主義」的黃金時代，乃至冷戰時期美蘇的太空競賽，並以 1968 年為核心，說明當時世界各地均以基礎科學發展為重，強調中央大學當年在台復校，就是順應著「國際地球物理年」，從地球科學研究開始起家，在永續發展上影響甚大。

在氣候變遷，環境改變的環伺下，他說道未來的世界將有很大的不同；在人口結構上，2030-2040 年間可能是現在人類與機器人黃金交叉時，再後便會被超越，相關運用如仿生微型無人飛機與 Space X 太空旅行計畫將可能實現。除此之外，更點出 50 年後的 AI 時代「Life3.0」將會出現巨大變革，並以史蒂芬·霍金生前預言的「超級人類」為例，說明人類有可能利用科學方式改變 DNA，展開一場未知的 AI 競賽。

葉永烜也以電影「星際迷航」為例，勉勵大家向外去探索未知的世界，尋找宇宙之中外星文明發展的規律與足跡，同時必須要用同情心、使命感與意志力去解決面臨的困難與危機，「不要怕麻煩，我們要把世界變得更好！」

另外，配合本講座的舉辦，圖書館特別安排一場「葉永烜院士特展」，除了葉院士個人重要的成就外，還有雜誌訪談、教學模型及資料展外；大家可透過影片播放，了解卡西尼任務始末和鹿林天文台，希望燃起學子對天文學及太空科學研究的興趣。另有葉永烜推薦的一系列好書，希望透過書本啟發，帮助大家迎接新世代的來臨。圖書館藝文走廊也推出葉永烜「山外有山」油畫個展，展期從即日起至 11 月 15 日止。

余紀忠文教基金會董事長余範英形容，葉永烜是在複雜年代中沉靜的學者，透過其溫暖的筆觸，開濶的心胸，展現出其對學術的貢獻、對人類的關懷，深具「教育家」精神。



余紀忠

講座暨葉永烜院士特展開幕，吸引許多校內外貴賓共襄盛舉。劉天祺攝



余紀忠

講座，葉永烜院士（右）以「眺望 50 年後的今天」為題專講，並由李羅權院士（左）引言和對談。余若慈攝

# AI、全球暖化威脅 善盡世界公民社會責任



中央大學圖書館另舉辦葉永烜院士特展。（照片左起）圖書館長李力庸、葉永烜院士、余紀忠基金會董事長余範英、中大校長周景揚。（中央大學提供）

人氣: 33

【字號】 大 中 小

更新: 2018-10-31 4:19 PM 標籤: [AI](#), [全球暖化](#), [世界公民](#), [中央大學](#)

【大紀元 2018 年 10 月 31 日訊】（大紀元記者陳建霖台灣桃園報導）葉永烜院士在中央大學以「眺望 50 年後的今天」為題，從歷史、人文、天文等面向，引導師生和社會大眾如何安身立命，面對[全球暖化](#)、人工智慧的威脅，如何善盡台灣身為[世界公民](#)之社會責任。



葉永烜院士特展開幕，在圖書館有一場「山外有山」油畫個展，葉永烜親自導覽說明。(中央大學提供)

葉永烜為國際知名天文學家，研究專長為彗星物理和太陽系及行星起源等。1982年他提出了著名的跨國土星探測計畫卡西尼－惠更斯號，為國際天文研究寫下輝煌的一頁。2009年NASA授予他特殊公共服務榮譽勳章，表彰在探測土星系統計畫的貢獻。他所發表的期刊論文已超過二百篇，而發表在《Nature》和《Science》之篇數為華人科學家之最。

講座由李羅權院士擔任引言人，並指出在未來的趨勢裏，地球文明毀滅的因素可能有二，分別是核子戰爭和全球暖化，值得大眾關注，也為葉院士的演講揭開了序幕。



葉永烜為國際

知名天文學家，1982 年他所提出的土星探測計畫卡西尼－惠更斯號，為國際天文研究寫下輝煌的一頁！（中央大學提供）

葉永烜以歷史背景為主軸，描述二次世界大戰後，美國「自由主義」的黃金時代，乃至冷戰時期美蘇的太空競賽，並以 1968 年為核心，說明當時世界各地均以基礎科學發展為重，強調中央大學當年在台復校，就是順應著「國際地球物理年」，從地球科學研究開始起家，在永續發展上影響甚大。

在人口結構上，2030-2040 年間可能是現在人類與機器人黃金交叉時，再後便會被超越，相關運用如仿生微型無人飛機與 Space X 太空旅行計畫將可能實現。除此之外，更點出 50 年後的 AI 時代「Life3.0」將會出現巨大變革，並以史蒂芬·霍金生前預言的「超級人類」為例，說明人類有可能利用科學方式改變 DNA，展開一場未知的 AI 競賽。

葉永烜也以電影「星際迷航」勉勵大家向外去探索未知的世界，尋找宇宙之中外星文明發展的規律與足跡，同時必須要用同情心、使命感與意志力去解決面臨的困難與危機，「不要怕麻煩，我們要把世界變得更好！」

配合講座舉辦，中大圖書館安排一場「葉永烜特展」，圖書館藝文走廊也展出葉永烜「山外有山」個展。◇

責任編輯：宇璇

# 面對 AI、全球暖化威脅 葉永烜帶領眺望五十年後的今天

台灣好新聞／記者葉志成／桃園報導 2018.10.31 10:16

記者葉志成／桃園報導





由中央大學與余紀忠文教基金會共同成立的「余紀忠講座」，今年邁入第十個年頭，特別邀請葉永烜院士擔任主講人，並以「眺望 50 年後的今天」為題，從歷史、人文、天文等面向，引導師生和社會大眾如何安身立命，面對全球暖化、人工智慧的威脅，如何善盡台灣身為世界公民之社會責任。

葉永烜為國際知名天文學家，研究專長為彗星物理和太陽系及行星起源等。1982 年他提出了著名的跨國土星探測計畫卡西尼－惠更斯號，為國際天文研究

寫下輝煌的一頁。2009 年 NASA 授予他特殊公共服務榮譽勳章，表彰在探測土星系統計畫的貢獻。他所發表的期刊論文已超過二百篇，而發表在《Nature》和《Science》之篇數為華人科學家之最。

本講座邀請李羅權院士擔任引言人，並指出在未來的趨勢裏，地球文明毀滅的因素可能有二，分別是核子戰爭和全球暖化，值得大眾關注，也為葉院士的演講揭開了序幕。



葉永烜院士特展開幕，在圖書館有一場「山外有山」

油畫個展，葉永烜親自導覽說明。

葉永烜以歷史背景為主軸，描述二次世界大戰後，美國「自由主義」的黃金時代，乃至冷戰時期美蘇的太空競賽，並以 1968 年為核心，說明當時世界各地均

以基礎科學發展為重，強調中央大學當年在台復校，就是順應著「國際地球物理年」，從地球科學研究開始起家，在永續發展上影響甚大。

在氣候變遷，環境改變的環伺下，他說道未來的世界將有很大的不同；在人口結構上，2030-2040 年間可能是現在人類與機器人黃金交叉時，再後便會被超越，相關運用如仿生微型無人飛機與 Space X 太空旅行計畫將可能實現。除此之外，更點出 50 年後的 AI 時代「Life3.0」將會出現巨大變革，並以史蒂芬·霍金生前預言的「超級人類」為例，說明人類有可能利用科學方式改變 DNA，展開一場未知的 AI 競賽。

葉永烜也以電影「星際迷航」為例，勉勵大家向外去探索未知的世界，尋找宇宙之中外星文明發展的規律與足跡，同時必須要用同情心、使命感與意志力去解決面臨的困難與危機，「不要怕麻煩，我們要把世界變得更好！」



葉永烜為國際知名天文學家，1982 年他所提出的土

星探測計畫卡西尼－惠更斯號，為國際天文研究寫下

輝煌的一頁！

另外，配合本講座的舉辦，圖書館特別安排一場「葉永烜特展」，除了葉院士個人重要的成就外，還有雜誌訪談、教學模型及資料展外；大家可透過影片播放，了解卡西尼任務始末和鹿林天文台，希望燃起學子對天文學及太空科學研究的興趣。另有葉永烜推薦放在圖書館特展的參考書籍，希望透過書本啟發，帮助大家迎接新世代的來臨，眺望 50 年後的未來。

圖書館藝文走廊也展出葉永烜「山外有山」個展。余紀忠文教基金會董事長余範英形容，葉永烜是在複雜年代中沉靜的學者，透過其溫柔的筆觸，開濶的心胸，展現出其對學術的貢獻、對人類的關懷，深具「教育家」精神。



余紀忠講座，葉永烜院士（右）以「眺望 50 年後的今天」為題專講，並由李羅權院士（左）作引言和對談。

## 校園新聞

2018-10-22

### 科學與藝術交會在中大 想像力與創新是共同點

文／校園實習記者樂亞妮



當代藝

術家李綱（左二）邀請現場來賓一同創作，共同完成獨一無二的作品，並送給中央大學紀念。劉天祺攝

理性的科學與感性的藝術，看似風馬牛不相及，共同點為何？由中央大學藝文中心與天寶藝術中心一同舉辦的「水舞秩序－科學與藝術交會在中大」論談 10 月 19 日在中央大學黑盒子劇場熱鬧登場。邀請中大太空所劉正彥教授與當代藝術家李綱對談，並由葉永烜院士主持這場「水舞秩序」世紀盛會，在科學與藝術的碰撞下，激發出絢爛的火花。

主講人劉正彥教授，從科學的觀點出發，以不同的思路來探究人文的藝術。而與談人李綱，身為享譽國際的藝術家，善於用中國傳統的紙墨，將水墨藝術重新排序，建立自我的藝術語言。主持人葉院士，理科的權威背景，卻同時醉心於藝術創作與研究，並以科學家與藝術家的雙重身份，引導科學與藝術貫穿理性與感性兩極的核心價值。

這場打破「秩序」的會談，探討了科學和藝術的異同之處，葉永烜院士提出兩

者的共通點都是「想像力」，清楚地分析出人文與科技之間的脈絡；而劉正彥教授以科學的電漿對比李綱的抽象水墨，把藝術的創作，用科學去證明其中依據，將藝術的呈現以理性的分析解構出不同的語言，透析出不約而同之相同點，讓兩者之間的共鳴結合出嶄新的秩序，令人為之驚嘆！

針對科學和藝術之間的聯繫，李綱以耕耘機來作比擬，表示科技是工具，用來創作作品，而藝術則是方向盤，來調整思索傳遞出意義。在現今科技昌盛的時代，藝術給予社會思考的方向，人文藝術和科學文明並不是兩條平行線，兩者共榮共存，相互交疊出存在的價值。

會後主持人邀請觀眾參與提問，李光華副校長分享教導的「無機化學」課所看到的對稱之美；藝術研究所周芳美教授則闡述藝術創作仍需回歸基本功。統計研究所陳玉英教授則期許，無論是科學或藝術創作，都應為人類永續發展而努力。

李綱最後攜來的一幅精心畫作，讓現場來賓親筆簽名，並以杯緣滴取墨水蓋上畫作的獨特方式，共同完成獨一無二的傑作，並贈與中央大學以為紀念，為本場活動畫下圓滿句點。



「水舞

秩序－科學與藝術交會在中大」論談，邀請中大太空所劉正彥教授（左）與當代藝術家李綱（中）對談，並由葉永烜院士（右）主持這場世紀盛會。劉天祺



攝

三

位對談者也一同加入會後的甜點創作，為此活動增添另一美妙插曲。劉天祺攝



# 雙十國慶日 陳樹菊再捐 1600 萬台

## 幣助弱勢就醫



台灣愛心菜販陳樹菊，資料照。(中央社)

人氣: 14172

【字號】 [大](#) [中](#) [小](#)

更新: 2018-10-10 10:19 PM 標籤: [陳樹菊](#), [國慶](#), [雙十國慶](#), [台東](#)

【大紀元 2018 年 10 月 10 日訊】(大紀元記者鍾元台灣綜合報導)時代雜誌百大人物、台灣台東善心賣菜阿嬤陳樹菊，10 月 10 日中華民國的國慶日參加台東縣政府升旗，同時捐出價值約新台幣 1,600 萬元壽險保單給台東兩家醫院，作為幫助弱勢的清寒家庭的救醫費用。

10 日雙十國慶台北總統府前表演內容精采，憲兵快反連重機車隊，帶來高難度的花式操演，今年三軍儀隊，首度融入五月天的歌曲《戀愛 ING》，曾赴美獲獎的海軍儀隊上兵蘇祈麟，也帶來特技表演。幻象 2000 帶來的空軍衝場表演，壓軸登場。

台東縣政府 10 日舉行國慶升旗典禮，典禮中最特別的是愛心菜販陳樹菊捐出兩張目前價值 1,600 萬元的保單，委託台東馬偕、台東基督教醫院成立「陳樹菊醫療貧困暨癌友關懷基金」，希望拋磚引玉助偏鄉醫療。

台灣之光陳樹菊過年前病倒在菜攤上，緊急送醫開刀後在家休養，3 月底由友人接送獨自前往高雄阿蓮區寺廟休養，4 月 9 日返回台東。賣菜近一甲子的她決定退休，將菜攤交給侄子。當時她說退休後財產要信託，用於急難救助，「我賺台東人的錢，所以要回饋台東人。」



台東縣政府 10 日舉行國慶升旗典禮，愛心菜販陳樹菊（右 2）捐出兩張目前價值新台幣 1600 萬元的保單，委託台東馬偕、台東基督教醫院成立「陳樹菊醫療貧困暨癌友關懷基金」，協助偏鄉醫療。（中央社）

台東縣政府 9 日表示，愛心菜販陳樹菊女士，有感台東弱勢鄉親就醫困難，將於 10 日上午 8 時在台東縣政府前廣場辦理國慶升旗典禮後，為台東馬偕紀念醫院及台東基督教醫院捐款，成立醫療貧困基金。



台東善心菜販

陳樹菊，資料照。(中央社)

陳樹菊從小家貧，國小六年級時因拿不出保證金，母親難產而與腹中胎兒同亡。生活儉樸的她，從十幾歲開始吃素，賣菜捐出的善款有近千萬新台幣，用於認養孤兒和興建圖書館。她再度捐出現值 1,600 萬元的儲蓄險給台東馬偕醫院和基督教醫院設立急難醫療基金，作為濟助台東弱勢民眾的就醫費用，這也是她賣菜近一甲子的積蓄。



台東縣政府 10 日舉行國慶升旗典禮，愛心菜販陳樹菊（右 2）捐出兩張目前價值新台幣 1600 萬元的保單，簽署指定受益人為台東馬偕醫院及台東基督教醫院，希望成立「陳樹菊醫療貧困暨癌友關懷基金」，拋磚引玉助偏鄉醫療。（中央社）

69 歲的陳樹菊，13 歲開始在市場賣菜。2010 年獲選為《時代》雜誌的百大人物後，她赴美國領獎接受大紀元採訪，對於辛苦積攢的錢，陳樹菊很淡然地表示，「因為自己用不著，就捐出去啦，做人的態度是積德不積財。」她還表示，幫助人有一種無法形容的快樂，「每次幫助人家，那天會很好睡。」



台灣國立中央大學校長周景揚（左 2）9 月 5 日到台東，將命名為台東和陳樹菊的兩顆小行星證書，頒贈給台東縣長黃健庭（左 1）及陳樹菊（右 2）。（龍芳／大紀元）

今年 9 月陳樹菊還獲得一項榮譽，有小行星以她的名字命名。國立中央大學表示，為表彰台東的絕佳觀星地點及台東善心菜攤陳樹菊女士的善行義舉，該校將鹿林天文台所發現的兩顆小行星，分別命名為台東「Taitung」和陳樹菊「Chenshuchu」，校長周景揚親往台東頒證給台東縣長黃健庭及陳樹菊。陳樹菊笑著說，雖然不知道什麼是行星，但她「很高興」。

台灣之光陳樹菊曾說，自己一天花不到 100 元，希望把錢用在需要的人身上。她退休後堅持繼續行善，如今把最後的儲蓄險也捐出來救助弱勢，僅留下一棟房子終老，陳樹菊的無私大愛令人動容。#

## 校園新聞

2018-10-09

### 全國最高學府名不虛傳 鹿林天文台寫下傳奇與震撼

文／秘書室



在校長

周景揚和副校長李光華的帶隊下，中大同仁參訪鹿林天文台，踏上中央大學所屬的至高之處。林宏欽攝

一張高山門牌價值連城，一次數千顆璀璨的星星映入眼廉，這樣的傳奇與震撼，就在中央大學的至高之處－鹿林天文台！一個沒有鹿與路的地方，跨越了南投與嘉義兩縣，位居全球重要地理觀測位置，這裏是中大與世界接軌最近的地方，也是中大最遠的疆域。

鹿林天文台位於海拔 2,862 公尺處，為全國最高的天文台，擁有全國最大口徑的一米望遠鏡。10 月 5 日在周景揚校長和李光華副校長的帶領下，中大同仁造訪鹿林天文台。一直宣傳中大是「全國最高學府」的校長周景揚說，鹿林天文台是中大的驕傲，希望能樹立一個模式，鼓勵各單位辦活動時有機會去參訪，探索星空之美，引發更多對人類宇宙永續關懷。

1999 年成立的鹿林天文台，轉眼明年將邁入 20 週年，當年韋路藍縷，在沒水、沒電和沒路的情況下，一路走來格外艱辛，最後總算克服種種困難，率先在嘉

義阿里山鄉設立觀測站，樹立第一塊門牌，也促使台電投入大筆經費完成供電，因此讓天文台觀測人員笑稱「這塊門牌價值不菲！」

中大近年來透過小行星的發現與命名，與各地縣市政府有所互動，也紀念一些對國家社會有貢獻者，感念他們的作為。小行星的發現，源自鹿林巡天計畫，該計畫自 2006 年 3 月啟動以來，已發現 800 多顆小行星、1 顆近地小行星 和 1 顆鹿林彗星。根據國際天文聯合會小行星中心資料統計，鹿林天文台為亞洲發現小行星最活躍處之一，充份展現了台灣人「以小搏大」之精神。

參訪鹿林天文台，不像一般旅遊，對天氣、路況的掌握特別重要。尤其夜晚最好是晴天，天空透明度高，才有機會看到滿天星斗。而曲折蜿蜒的新中橫公路，在信義鄉台 21 線 133K 處容易坍塌，在出發前，務必掌握路況。住宿建議以臨近為優先，避免舟車勞頓。可喜的是，學校去年新採購的 20 人座中巴正好派上用場，行政會議通過在合於「公務車輛管理辦法」規範內，各單位可多多使用。

## 校園新聞

2018-09-06

### 「最美星空」與「最美人心」 台東、陳樹菊小行星躍上宇宙

文／秘書室、天文所



學將鹿林天文台發現小行星命名為臺東和陳樹菊，並頒贈銘板以為紀念。照片左起台東縣長黃健庭、中央大學校長周景揚、陳樹菊女士、台東縣議長饒慶鈴。陳如枝攝

為表彰臺東的絕佳觀星地點，以及陳樹菊女士的善行義舉，中央大學特將鹿林天文台所發現的第 281561 號小行星命名為臺東「Taitung」，第 278986 號小行星命名為陳樹菊「Chenshuchu」，並經國際天文學聯合會（IAU/CSBN）通過。「最美星空」與「最美人心」相交輝映，傳遞出台灣美善的人文價值。

臺東，臺灣後山美景，以高山、縱谷、平原、海岸勾勒出海天一色的山海風情。綠島、蘭嶼美麗的海島風光、各原住民族多元的文化底蘊，呈現出兼容並蓄的多元文化風貌。台東因地理環境優勢、自然景觀遼闊、人為光害非常低，是絕佳的觀星環境，天氣好的夜晚滿天星斗震撼人心。台東縣政府今年特別舉辦「台東最美星空選拔」活動，希望藉由活動的進行，讓大家感受到星空的魅力，找回在燈光下失去的美好。



台東最美星空下最美的人心－陳樹菊女士，她的世界雖然只有一個小菜攤，但她捐款助人的善行義舉，全世界都知道；她的精神，更與中央大學校訓「誠樸」不謀而合。她做生意最講求商譽和信用，以誠相待，即使 2010 年獲選美國《時代》雜誌最具影響力百大人物、2010 年獲《富比世》雜誌亞洲慈善英雄、《讀者文摘》亞洲英雄，未曾改變陳樹菊女士質樸的性格。她最大的財富，就是心靈的富有，將捐款助人當作一生志業。

中央大學校長周景揚表示，中大擁有全國海拔最高的鹿林天文台，以及全國最大的天文望遠鏡，為國內天文觀測的重鎮。而台灣是亞洲發現小行星最活躍的地方之一，中央大學目前已發現 800 多顆小行星，其中有 90 多顆通過正式命名。

要在宇宙蒼穹間發現新星體，一如大海撈針般，誠屬不易，須有專業的判斷和堅忍的毅力，再經長時間的軌道確認，才能確認是新天體。尤其在海拔 2,862 公尺的高山觀測相當克難，工作型態更是日夜顛倒，需要恆久的堅持，才能讓「臺東」和「陳樹菊」小行星躍上宇宙、揚名國際！

中央大學天文所表示，臺東和陳樹菊小行星同為鹿林天文台蕭翔耀及加州理工學院葉泉志博士所發現，發現時間在 2008 年 10 月，大小約在 1-3 公里之間。臺東小行星發現時是在鯨魚座，陳樹菊小行星則在白羊座，目前兩者已一起運行到金牛座。

臺東小行星繞行太陽一圈 4.8 年（軌道週期），離太陽最近時（近日點）為 3.87 億公里，最遠時（遠日點）為 4.66 億公里。陳樹菊小行星繞行太陽一圈 4.91 年，離太陽最近時為 4 億公里，最遠時為 4.6 億公里。2018 年 9 月兩者一同在台東最美星空中閃耀光芒，照亮世人。



陳樹菊

女士（右）與發現者中央大學鹿林天文台觀測員蕭翔耀（中）擁抱合影，場面溫馨，左為台東縣長黃健庭。陳如枝攝



中央大

學以台東和陳樹菊小行星，表彰台灣「最美星空」與「最美人心」美善價值。陳如枝攝

# 小行星命名沈君山 學界緬懷一代人文科學家



[中央社](#)

6.1k 人追蹤

The Central News Agency 中央通訊社

2018 年 9 月 12 日 下午 3:50

（中央社記者陳至中台北 12 日電）知名物理學家、前清華大學校長沈君山今天辭世，他是具有人文素養的科學家，甚至太空裡有一顆小行星被命名為「沈君山」，表彰他對天文學的貢獻，他的逝去，令學界緬懷不已。

清華大學前校長、物理學家沈君山今天上午 10 時病逝於新竹馬偕醫院，享壽 87 歲。

沈君山的父親（沈宗瀚）是農業專家，曾任農村復興聯合委員會（今農委會）主委。沈君山和父母來台後，在台灣大學取得物理學士學位，後赴美深造，於馬里蘭大學取得物理博士學位，任教於普度大學。回台任教後，於民國 83 年上任清大學長，致力發展通識教育，並讓理工為主的清大，兼具人文學風和藝術氣息。

中央大學前副校長、天文所教授葉永烜表示，沈君山本來在美國可以有很好的發展，但他卻選擇回到台灣，帶動台灣的研究和教育，影響了一個世代的學者。

葉永烜表示，沈君山在學界一路走來，都非常有魄力，出版、翻譯了許多重要書籍，也寫了很多文章，將天文學知識介紹到台灣，可以說台灣的天文學研究，最先是沈君山一手促成的。

沈君山致力於科普推廣，好文筆也讓人津津樂道，曾著有「浮生三記」、「浮生後記」、「浮生再記」等。葉永烜回憶自己在念大學時，讀過沈君山一本介紹反物質的書，看完非常興奮，激起他找尋更多相關的書籍來看，沈君山寫過很多科普文章，啟迪許多台灣學生，對天文產生興趣。

中央大學鹿林天文台曾將一顆新發現的小行星（編號 202605），於民國 98 年命名為沈君山（Shenchunshan），如今地球上的沈君山已消逝，但太空裡的「沈君山」仍持續存在星海中。

沈君山除了是物理學家，也是橋藝、圍棋高手，引領清大發展人文學風，教育部長葉俊榮表示，沈君山不只是科學家，也關心社會和人文議題，是學生們效法的對象。

葉俊榮在台灣大學任教時，曾在一些機會與沈君山針對國家核能政策有些討論。他回憶沈君山雖然是物理學家，但關注的層面卻不只侷限於物理現象、科學上的詮釋，而是包含社會、人文等議題，對他非常敬佩。

葉俊榮表示，沈君山是一個傑出的物理學家、教育家，在清大校長任內，充分展現愛大學、愛學校、愛學生的情懷，更重要的是他心胸非常開闊、興趣非常廣泛，時常成為學生和社會討論與模仿的對象。

葉俊榮也提到，最近除了沈君山，包括胡佛、胡勝正、楊國樞等「老師輩」的自由主義學者接連去世，在台灣發展過程中帶領後輩做思考、做實踐，都非常值得景仰。他們都在 80 歲左右高齡去世，是台灣社會的損失，教育部門也希望把他們的想法和典範延續下去。（編輯：陳清芳）1070912

# 最美星空、最美人心 相輝映

2018 年 09 月 11 日 00:58 [中國時報](#)

黃健庭

全台首創「最美星空選拔」歷經 2 個月、由專業評審及破萬民眾網路票選，結果出爐。關山親水公園、台東加路蘭遊憩區、池上大坡池及成功三仙台獲得絕美一星等認證，其餘 10 個觀星點也各有特色。天文專家擔任的評審老師們告訴我，這大概是史上最難評選比賽，因為台東空氣好、光害低、天際線開闊，到處都很適合觀星。

會有台東「最美星空選拔」，緣自去年我到日本長野縣招商及促銷農產時，見識到「日本第一星空」阿智村，當下便決定也要把台東星空推廣出去，回國後立刻找同仁研商，整個籌劃過程歷時一年，不僅融合美、日認證，也加入實地勘察與歷年氣象均值等數據，力求比賽的公平與嚴謹。

藉台東最美星空公布，另有一項極具意義的命名證書致贈儀式。國立中央大學將鹿林天文台所發現的編號第 281561 號及第 278986 號小行星，分別命名為台東「Taitung」及陳樹菊「Chenshuchu」，並經國際天文學聯合會（IAU/CSBN）通過，讓台東「最美星空」及「最美人心」兩相輝映。

搭配辦理的最美星空攝影大賽中，台北來的陳勇明藉著到台東參加熱氣球嘉年華，拍下浩瀚無垠、滿天星斗的美景，奪得首獎。後續我們還會辦理探討星空行銷的觀光產業工作坊、最美星空音樂會等活動，誠如中大周景揚校長所言，台東這幾年蛻變為品牌及幸福城市，和陳樹菊令人感動的善心，都值得肯定和表彰。對於台東和陳樹菊 2 顆星能雙雙常存在永恆宇宙中，我們何等榮幸、與有榮焉。

(中國時報)

# 鹿林天文台以「陳樹菊」命名小行星 表彰台東「最美人心」

國立中央大學校長周景揚，5日將到台東舉行命名儀式，並將小行星命名證書頒贈給台東善心菜販陳樹菊女士

By [宇妍](#), 台灣英文新聞－編輯  
2018/09/03 20:37



陳樹菊今年 6 月 16 日曾獲國立清華大學頒授榮譽校友，並發表演說。（中央社檔案照片）

（台灣英文新聞／生活組 綜合報導）今年 6 月 16 日才獲得國立清華大學頒授榮譽校友的台東善心菜販陳樹菊，又將增添一樁喜事。

中央社報導，隸屬國立中央大學的鹿林天文台，將以陳樹菊這位台灣之光，為新發現的小行星命名，讓台東成為名副其實、最美的星空。

台東縣政府 3 日表示，為表彰台東的絕佳觀星地點，以及善心菜販陳樹菊女士

的善行義舉，由國立中央大學設立的鹿林天文台，特將所發現的編號第 281561 號小行星命名為 Taitung，意即台東。

另一編號第 278986 號小行星，則命名為 Chenshuchu，即陳樹菊名字的英譯。

國立中央大學校長周景揚，5 日將到台東舉行命名儀式，並將前述兩顆小行星的命名證書，頒贈予台東縣長黃健庭及陳樹菊女士，充分展現台東擁有「最美星空」及「最美人心」的意涵。



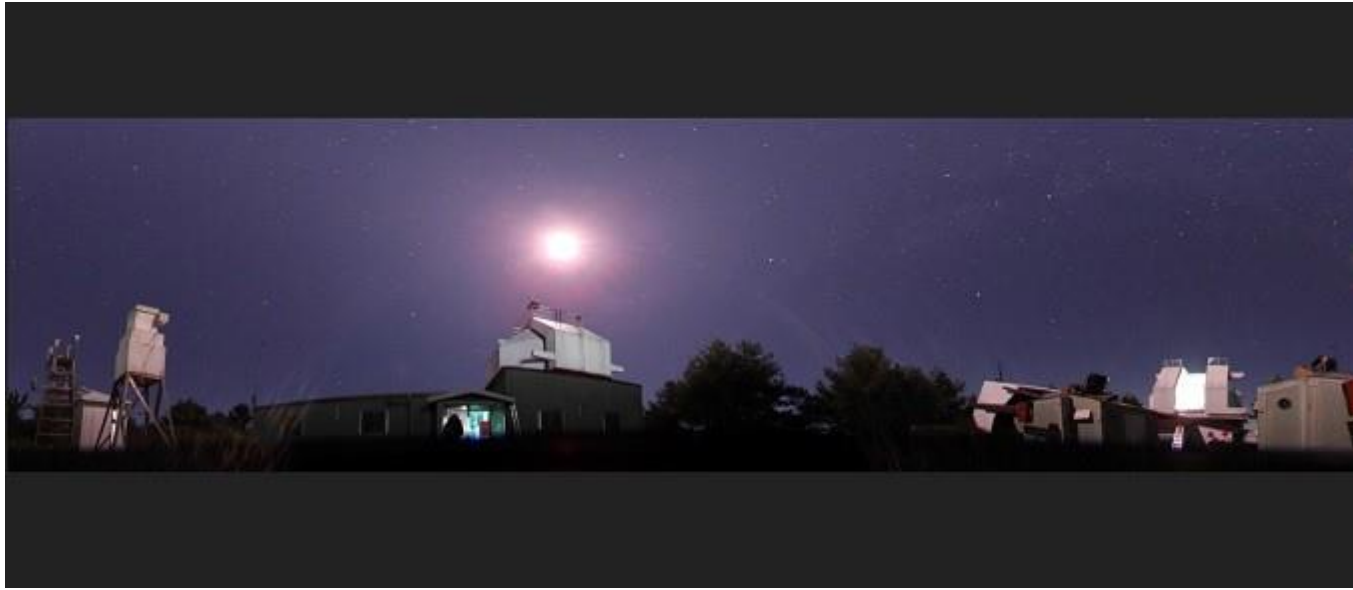


中央社檔案照片

今年 6 月陳樹菊在清大獲頒榮譽校友時，曾致詞鼓勵學子及時行善，一天捐 10 元也能做善事，不必等到賺大錢。

68 歲的陳樹菊，從 13 歲開始賣菜，20 歲論及婚嫁時，因父親一句話「妳嫁了，兄弟姐妹怎麼辦」，而錯過婚期，後又因母親早逝兼任母職，幫忙賣菜與照顧弟妹，至今孑然一身。陳樹菊為感激外界早年對自己母親與弟弟的幫忙，於是將辛苦賣菜的錢捐給需要幫助的人。

陳樹菊的善行，讓她從市井小民，成為美國時代雜誌 2010 年百大人物之一。如今她雖已因病退休，不再賣菜。但有小行星以她命名，將讓她的善行繼續流傳，台東的星空也更加美善與閃耀。



圖片來源:鹿林天文台臉書

## 最美星空 新發現小行星命名陳樹菊



陳樹菊的菜攤經營時間長，清晨賣到晚上幾乎沒休息。（圖／本報資料照片，黃力勉攝）

### [友善列印](#)

- [小字型](#)
- [中字型](#)
- [大字型](#)
  
- Facebook
- Google+
- Twitter
- Weibo
- 

2018年09月03日 22:48 [中時電子報](#)

## 丁世傑

鹿林天文台新發現的小行星，將以台灣之光、善心賣菜阿嬤陳樹菊命名，展現最美的星空。

根據中央社獨家報導，台東縣政府為表彰善心菜攤陳樹菊女士的善行義舉以及台東的絕佳觀星地點，鹿林天文台特將所發現的編號第 278986 號小行星命名為 Chenshuchu，即陳樹菊名字的英譯。另外，編號第 281561 號小行星命名為 Taitung，就是台東。

報導說，國立中央大學校長周景揚 5 日將到台東舉行命名儀式，並將前述兩顆小行星的命名證書頒贈予台東縣長黃健庭及陳樹菊女士，充分展現台東「最美星空」及「最美人心」的意涵。

68 歲的陳樹菊，13 歲開始賣菜，20 歲論及婚嫁時，因父親一句話「妳嫁了，兄弟姐妹怎麼辦」，而錯過婚期，再因母親早逝兼母職，幫忙賣菜與照顧弟妹，至今孑然一身，想起早年困苦且生病的母親、弟弟受到外界幫忙，於是她將辛苦賣菜的錢捐給需要幫助的人。

阿嬤的善行讓她從菜市場走上美國紐約林肯中心的紅地毯，從市井小民成為時代雜誌的百大人物，被譽為台灣之光、台東之光，如今有小行星以她命名，將讓星空更美善。

鹿林天文台設於嘉義縣阿里山鄉及南投縣信義鄉交界處鹿林前山的天文台，在玉山國家公園之內，海拔 2862 公尺，目前由國立中央大學天文研究所管理。

(中時電子報)

## 最美人心 陳樹菊登小行星名

記者郭曉蓓／綜合報導





鹿林天文台 10 年前發現 2 顆小行星，經過一連串國際認證，1 顆命名臺東「Taitung」，另 1 顆則選擇以賣菜善舉聞名國際的「陳樹菊 Chenshuchu」命名。陳樹菊特別現身，大呼自己實在好幸運。這 2 顆富有意義的星，也將永遠被世界上的人所紀念。

#### 最美星空 命名臺東

「臺東縣最美星空選拔」昨日進行頒獎典禮，除了一星等點位結果出爐外，最受矚目的是鹿林天文台所觀測員蕭翔耀發現的小行星，第 281561 號小行星，命名為臺東「Taitung」；編號第 278986 號小行星，命名為陳樹菊「Chenshuchu」，並經國際天文學聯合會（IAU/CSBN）通過，充分展現了臺東「最美星空」及「最美人心」的意涵。

為了感謝陳樹菊的善行，特別用她的名字來命名。陳樹菊說：「從來都沒有想過，這麼好康的事情怎麼發生在我身上！」本來在高雄調養身體的她，這回專程回到臺東接受表揚。陳樹菊接下小行星證書後非常高興，她也客氣說「不敢當」。

行星發現人、中央大學天文觀測員蕭翔耀說：「陳樹菊真的很厲害，我滿佩服她的。其實我當時知道可以用樹菊阿姨的名字，對我來講是一個榮幸。」

#### 臺東最美星空 4 鄉鎮出線

另外，「臺東縣最美星空選拔」評選結果，一星等點位從 14 個鄉鎮中脫穎而出，共有 4 個，包括關山鎮的關山親水公園、臺東市的加路蘭遊憩區、池上鄉的大坡池，以及成功鎮的三仙台。



# 中大新發現小行星命名「陳樹菊」

## 中大新聞

2018/09/06 新浪新聞

中央大學鹿林天文台發現的太陽系兩顆小行星，以台東和愛心菜販陳樹菊命名，特別到台東頒發證書給。

台東縣政府首創全國舉辦最美星空選拔，包括東海岸三仙台和伽路蘭風景區等，一共十四個地點被選為最佳觀星地點。同時也公布星空攝影前三名的作品，提昇台東的夜間觀光知名度。

但是台東最美的一顆星，是不斷捐款扶助弱勢的愛心菜販陳樹菊。中央大學鹿林天文台十年前發現太陽系兩顆小行星，並確定是穩定繞行太陽的行星後，一顆用台東命名，另一顆就決定用愛心菜販陳樹菊的名字來命名，5號中央大學特別到台東頒發命名證書給陳樹菊。

陳樹菊說，「很高興啊，我也不知道星星是什麼，專程回來，結果是說，我們台東是有兩顆星，有縣長就有我嘛。」

中央大學校長周景揚表示，「不是隨便命名、它有一定的規則，譬如說人名，他一定要對各行各業都有貢獻的。」

愛心菜販陳樹菊已經退休不再賣菜，專心在高雄養病，這次回台東出席這場領證典禮，她的臉上堆滿笑容，也謙虛的對外界的關心表達感謝。

原文轉載自【2018-09-06/新浪新聞】

## 媒體報導

<https://news.sina.com.tw/article/20180905/280935>

[70.html](#)

[2018/09/06 新浪新聞](#)

# 愛心善行被讚揚 小行星命名陳樹菊



華視

2018年9月5日 下午 7:59



台東縣 / 陳君毅 報導

最近中央大學發現新的小行星取的名字很特別，叫陳樹菊小行星，為了要感謝台灣之光陳樹菊女士賣菜做愛心的善舉，還有一顆小行星命名為台東小行星，兩顆小行星的命名，分別突顯了台灣最美的人心，以及台東最美的星空。

從國立中央大學校長周景揚手中接過陳樹菊小行星的獎牌，台灣之光陳樹菊女士笑得好開心，畢竟能由國際天文學聯合會通過，直接把鹿林天文台發現的第278986號小行星命名為陳樹菊小行星，絕對是全球性的無上榮耀。

退休後不賣菜，終於能夠休養的陳樹菊胖了五公斤，也不用拐杖了，這次，中央大學鹿林天文台，恰巧在陳樹菊生日發現一顆未命名的小行星，加上之後發現的另一顆小行星，就決定以陳樹菊還有台東來分別命名。

陳樹菊還有台東這兩顆小行星永遠在宇宙中運行，為了慶祝，台東縣還舉辦最美星空活動，讓全民都能分享這兩顆小行星，替台灣帶來的榮耀。

# 小行星命名陳樹菊 中央大學校長頒 證



發現小行星的鹿林天文台研究員蕭祥耀（中）和陳樹菊（右）喜相逢，兩人都很開心。（龍芳／大紀元）

人氣: 52

【字號】 大 中 小

更新: 2018-09-05 10:37 PM 標籤: [陳樹菊](#), [小行星](#), [命名](#), [台東](#), [中央大學](#)

【大紀元 2018 年 09 月 05 日訊】（大紀元記者龍芳台灣台東報導）為表彰台東的絕佳觀星地點及台東善心菜攤陳樹菊女士的善行義舉，國立中央大學將鹿林天文台所發現的兩顆小行星，分別命名為台東「Taitung」和陳樹菊「Chenshuchu」，校長周景揚表示，這是最美星空與最美人心相互輝映。

周景揚 5 日到台東頒贈小行星證書給台東縣長黃健庭及陳樹菊。目前已正式退休的陳樹菊笑著說，雖然不知道什麼是行星，但她「很高興」。黃健庭則說，

台東是沾陳樹菊的光，兩顆命名為台東和陳樹菊的小行星，在宇宙中運行，代表有愛、有希望。議長饒慶鈴稱讚說：「照亮宇宙，生生不息」。

兩顆小行星是由鹿林天文台研究員蕭祥耀及另一位同仁 10 年前發現。周景揚強調，浩瀚的宇宙中，要發現小行星相當不易，要有最尖端的儀器，還要經年徹夜守候，發現後還要報請國際認證，確認其存在。

這兩顆小行星與太陽的距離，是地球與太陽距離的 3 倍，而繞太陽一圈需要約 5 年時間，肉眼看不見。

蕭祥耀在現場擁著陳樹菊說，10 年前發現小行星時，並不認識陳阿姨，見面很高興，覺得這次命名很有意義。命名為台東的小行星編號為第 281561 號，命名為陳樹菊的是編號第 278986 號小行星，並已經國際天文學聯合會（IAU/CSBN）通過。◇



國立中央大學校長周景揚(左 2) 5 日到台東，將命名為台東和陳樹菊的兩顆小行星證書，頒贈給台東縣長黃健庭(左 1)及陳樹菊(右 2)。(龍芳／大紀元)

責任編輯：陳玟綺

# 台東最美星空出爐！關山親水公園 等 4 處評定一星等點位

- [【抽籤】2019 豬年運勢籤 求媽祖指點迷津！](#)



▲台東最美星空一星等點位出爐，宣布記者會中央大學周景揚校長（左二）特別到場主持將鹿林天文台所發現的 2 顆小行星命名台東「Taitung」及陳樹菊「Chenshuchu」的頒贈儀式。（圖／台東縣政府提供，下同）

記者王兆麟／台東報導

台東縣政府今年首創「台東縣最美星空選拔」，歷經的激烈評選後，台東最美星空一星等點位終於自 14 個鄉鎮中脫穎而出、在眾所期待中出爐，其中關山親水公園等 4 處評定一星等點位，會中國立中央大學周景揚校長特別到場將鹿林天文台所發現的 2 顆小行星命名台東「Taitung」及陳樹菊「Chenshuchu」的頒贈儀式，同時，也公布了「最美星空攝影大賽」前三名得獎者。



台東縣府 5 日上午 10 點 30 分在大禮堂舉行台東最美星空公佈記者會，縣長黃健庭表示，台東縣因自身地理環境優勢，自然景觀遼闊，人為光害非常低，到了夜晚可說是抬頭就能看見滿天星斗、處處皆適合觀星，都是最美的星空，也因此大幅加高了本次「最美星空選拔」評選難度及門檻，參與選拔的 14 個鄉鎮的星空更是各個美不勝收，難以分出高下。此次評選綜合專業評審 60%、民眾票選 20%、媒體評審 10% 及書面審查 10%，從專業的角度、旅遊的角度、民眾的角度共同選出台東最美的星空。

十名專業評審由中研院天文所，現為國家地理雜誌專欄作家的天文學博士李昫岱，及台北市天文協會常務理事、台灣星空守護聯盟創辦人劉志安兩位專家擔任顧問，更號召另外八位天文專家共同不辭辛勞地親自實地走訪 14 個鄉鎮點位，並邀請媒體與部落客進行評選，讓整體賽事更具公正性與權威性。





台東最美星空評選結果：一星等點位一共有四個包括關山鎮的關山親水公園、台東市的加路蘭遊憩區、池上鄉的大坡池及成功鎮的三仙台；二星等點位一共有五個包括綠島鄉的帆船鼻草原、東河鄉的都蘭觀海公園、鹿野鄉的鹿野高台眺望亭、長濱鄉的金剛大道及太麻里鄉的金針山湛藍若洗觀景平台；三星等點位一共有五個包括卑南鄉的富源觀景平台、大武鄉的大武濱海公園、金峰鄉的嘉蘭溫泉公園、海端鄉的霧鹿砲台及達仁鄉的南田觀景台。

此次記者會上除了正式公布星等點位外，更安排了一個極具意義的頒贈儀式，為表彰台東的絕佳觀星地點及台東善心菜攤陳樹菊女士的善行義舉，國立中央大學特將鹿林天文台所觀測員蕭翔耀 2 人發現的第 281561 號小行星，命名為台東「Taitung」；編號第 278986 號小行星，命名為陳樹菊「Chenshuchu」，並經國際天文學聯合會（IAU/CSBN）通過，充分展現了台東「最美星空」及「最美人心」的意涵。

國立中央大學周景揚校長也特別到場，將此兩顆小行星頒贈予台東縣長黃健庭及陳樹菊女士，傳遞台灣美善的人文價值。陳樹菊女士接下小行星證書後非常高興，她也客氣說「不敢當」，黃健庭則說，台東是沾陳樹菊女士的光，也讓台東再度打響世界知名度。



▲獲得最美星空攝影大賽第一名的陳勇明先生

此外，記者會上也公布了「最美星空攝影大賽」前三名得獎者，分別為第一名陳勇明、第二名黃以新及第三名吳信智，可獲得由 festaria Tokyo 獨家贊助的超美鑽石，在這幾位得獎者精彩的鏡頭下，也讓大家看到台東星空璀璨的美麗。

「最美星空選拔」系列活動也將在 10 月 13 日晚上七點，於剛選出來熱騰騰的一星等點位池上鄉大坡池舉辦【台東最美星空音樂會】，屆時將邀請到知名世界級管弦樂團-樂興之時，以及曾獲兩屆鐵花村樂團比賽第一名、來自台東卑南族建和部落的安懂 x SAVAKAN 樂團現場演出；當天來參與的民眾不僅可參加抽獎活動，有機會抽中由 festaria Tokyo 獨家贊助總價值超過兩萬元的超美鑽石項鍊，前 500 名抵達現場的民眾更可免費獲得活動特製的最美星空野餐墊！

詳情歡迎至「台東最美星空」官方網站 <https://www.台東最美星空.tw/>及 Facebook 粉絲專頁查詢。

原文網址: [台東最美星空出爐！關山親水公園等 4 處評定一星等點位 | ETtoday 地方 | ETtoday 新聞雲](https://www.ettoday.net/news/20180905/1252046.htm#ixzz5ap0B3yas)

<https://www.ettoday.net/news/20180905/1252046.htm#ixzz5ap0B3yas>

Follow us: [@ETtodaynet on Twitter](#) | [ETtoday on Facebook](#)

# 陳樹菊獲頒小行星證書 (圖)



[中央社](#)

6.1k 人追蹤

The Central News Agency 中央通訊社

2018 年 9 月 5 日 下午 3:54

為表彰台東的絕佳觀星地點及台東善心菜攤陳樹菊的善行義舉，中央大學特別將鹿林天文台所發現的第 281561 號小行星，命名為台東「Taitung」，編號第 278986 號小行星，命名為陳樹菊「Chenshuchu」。中央大學校長周景揚（左）將小行星證書牌頒贈予陳樹菊（右）。（台東縣政府提供）

中央社記者李先鳳傳真 107 年 9 月 5 日

# 台東最美星空選拔結果出爐 台 東、陳樹菊都成小行星之名

中大新聞

2018/09/07 Hinet

台東縣首辦【最美星空選拔】活動，從 14 個鄉鎮中歷經的激烈評選，脫穎而出，結果出爐揭曉，台東最美星空一星等，也就是台東最美的星空地點，包括成功鎮的三仙台、池上鄉的大坡池、台東市的加路蘭遊憩區以及關山鎮的關山親水公園等。另外，會中國立中央大學周景揚校長特別到場將鹿林天文台所發現的 2 顆小行星命名台東「Taitung」及陳樹菊「Chenshuchu」的頒贈儀式，同時，也公布了亦同時公布了【最美星空攝影大賽】前三名得獎者。

黃健庭縣長表示，台東縣因自身地理環境優勢，自然景觀遼闊，人為光害非常低，到了夜晚可說是抬頭就能看見滿天星斗、處處皆適合觀星，都是最美的星空，也因此大幅加高了本次【最美星空選拔】評選難度及門檻，參與選拔的 14 個鄉鎮的星空更是各個美不勝收，難以分出高下。

原文轉載自【2018-09-07/Hinet】

媒體報導

<https://times.hinet.net/news/21947119>

[2018/09/07 Hinet](https://times.hinet.net/news/21947119)

# 東縣推觀光無光害環境 首創最美

## 星空選拔

中大新聞

2018/09/07 原民台

經過兩個多月的激烈評選，台東縣最美星空選拔，終於在 5 號結果出爐，包括關山親水公園、加路蘭遊憩區、以及大坡池跟三仙台，都列入台東最佳一星等觀星點位，另外包含大武、太麻里、金峰以及達仁等南迴四鄉，也都分別列入二星以及三星等。

(台東縣金峰鄉長 宋賢一 排灣族：列入三星等，我也覺得很高興，因為這個地方地處偏遠，他們評選的規則是交通方便，但是我們這個地方有它的獨到之處，列入三星等，也讓大家知道有這個嘉蘭溫泉公園。)除了最美星空選拔，縣府也藉由攝影比賽，讓全國各地的攝影愛好者，透過鏡頭，展現台東璀璨的夜晚，而這張位在加路蘭遊憩區所拍攝的星空照，完美的構圖跟高超攝影技術，最獲評審與民眾青睞，拿下第一名，而攝影師也現場分享當天拍攝心得。

(台北市天文協會常務理事 劉志安：他那張畫質的話比較豐富一點，地景取得比較多，銀河的話也是有比較明亮的銀河，可以展現出台東這邊海岸的一個狀況這樣。)(台東最美星空攝影冠軍 陳勇明：那邊路燈有先關閉，所以我們就去到那邊去看，然後現場一看，就是滿天星，那天拍攝是用大概 ISO1600，然後光圈 3.5，然後再去曝 25 秒這樣。)

另外除了表揚最美星空，國立中央大學鹿林天文台，也將新發現的 2 個小行星，命為名為「台東」，以及因為善心賣菜爆紅的女士「陳樹菊」，希望透過這 2 顆行星的命名，使台東「最美星空」與「最美人心」相互輝映。(台東善心菜商 陳樹菊：很開心餒，都想不到好的都在我這裡。)(國立中央大學鹿林山天文台觀測助理 蕭翔耀：樹菊阿姨她其實真的很厲害，我還滿佩服她的，其實我當時知道可以用樹菊阿姨的名字，我覺得對我來講是一個榮幸。)

台東人為光害少，許多部落都是絕佳的觀星地點，透過舉辦最美星空選拔，縣

府期待利用漫天星斗，轉化成可用的觀光資源，帶動地方收益，也更顯自然環境的珍貴。

原文轉載自【2018-09-07/原民台】

## 媒體報導

<http://titv.ipcf.g.tw/news-42010>

[2018/09/07 原民台](#)

# 台東最美！獲小行星命名 陳樹

## 菊：很高興成為一顆星

[#地方](#) [#星空](#) [#陳樹菊](#)

聯合報 記者尤聰光／台東縣報導

台東縣政府舉辦「台東縣最美星空選拔」昨天頒獎，鹿林天文台 10 年前發現 2 顆小行星，將 1 顆命名為「台東」，另 1 顆以「台灣之光」愛心女菜販陳樹菊命名，中央大學校長周景揚昨天將小行星的命名證書頒贈給台東縣長黃健庭及陳樹菊，充分展現台東「最美星空」及「最美人心」的意涵。

陳樹菊輕裝來到活動現場，走上主辦單位安排的星光大道接受媒體拍照，陳樹菊不好意思的笑說「謝謝、謝謝，我不是明星啦」，她說，「自己不知道天空有什麼星星，但很高興能和縣長成為天上的一顆星」。

[好房網 TV／房產專家直播交戰 預售屋是個食人島？](#)

[價格殺戮戰不遠了...顏炳立給自住客 4 個建議](#)

[放寬陸資解救餘屋賣壓？名嘴砲轟「蠢蛋市長」](#)

鹿林天文台 10 年前發現 1 顆編號第 278986 號小行星，正式命名為「Chenshuchu（陳樹菊英譯）」，昨天由國立中央大學校長周景揚（左）頒贈證書給陳樹菊

(右)。 記者尤聰光／攝影



台東縣長黃健庭表示，台東最美星空由專家評選，讓整體賽事更具公正性與權威性。

台東最美星空評選結果，一星等點位共有 4 個，包括關山親水公園、台東市的加路蘭遊憩區、池上鄉的大坡池及成功鎮三仙台；二星等點位共有 5 個，包括綠島鄉的帆船鼻草原、東河鄉都蘭觀海公園、鹿野鄉的鹿野高台眺望亭、長濱鄉金剛大道及太麻里鄉金針山湛藍若洗觀景平台；三星等點位共 5 個，包括卑南鄉的富源觀景平台、大武鄉大武濱海公園、金峰鄉嘉蘭溫泉公園、海端鄉霧鹿砲台及達仁鄉南田觀景台。



# 全大運揭序幕 聖火母火源自鄒族

## Mayasvi

觀看次數 / 385 次

2018-04-29 【Ciwasi Yamai 蔣淮薇/Calaw Opic 丁至軒/許家榮 桃園中壢】

小 中 大

全大運聖火在選手的傳遞下，正式點燃，也象徵著揭開 2018 全國大專校院運動會序幕。

而本屆聖火，是首次從鄒族特富野社的 Mayasvi 戰祭中，取得母火，作為聖火之源，而特富野社長老也為此趕來參加盛會，見證榮耀的時刻。

(特富野社長老 Avayi(高德生) 鄒族:

我希望透過這樣的一個原住民聖火發源的傳遞，帶到校園裡，因為在台灣裡面很多的運動選手，原住民佔多數，所以我們希望透過這樣的機會，再展現原住民體育的能力，讓原住民在這個土地上面再發光。)

延續著 2017 年世界大學運動會的熱潮，吸引了一萬六千位選手參加，是歷年來規模最大，然而運動員的栽培，不是，副總統陳建仁提到，政府預計要投注百億經費，讓選手無後顧之憂。

(副總統 陳建仁:

去年我們通過的國民體育法，就是我們體育改革的開端，使得各體育協會陸續改選，有年輕新血的加入，讓協會組織的運作更加透明，更重要的，相關的部會，運動發展基金，還有前瞻計畫，四年內會投入，超過百億的經費。)

本屆全國大專校院運動會，也首次將電競納入正式運動競賽項目中，替競賽種類增添了多元性。

而全大運也將從 4 月 28 號到 5 月 2 號，一連 5 天在中央大學盛大登場。

# 107 全大運聖火引燃 4/28 中大開 戰

更新：2018年03月30日



全大運聖火。(記者陳柏州／攝影)

字 字

【記者喬奕／綜合報導】107年全國大專校院運動會將於4月28日在中央大學點燃戰火，30日聖火率先引燃，此次聖火沿用台北世大運的聖火火把，期盼能延續台北世大運的熱血風潮。

中央大學睽違 30 年後再度承辦全大運，30 日舉行聖火引燃典禮，請來鄒族頭目、族長等人替活動祈福，並從鄒族戰祭中取得母火，祈求征戰勝利，喚起運動員秉持運動家精神。

聖火將傳遞經過中央警察大學等校，以及 108 年全大運承辦校中正大學，預計 4 月 14 日抵達中央大學。今年全大運共有 19 個運動項目，首次納入電子競技運動和滑輪溜冰，承辦種類及選辦項目都是歷年來最多。◇

# 全大運》延用去年台北世大運火把

## 4/14 抵達中央大學



[麗台運動報](#)

2018 年 3 月 31 日 上午 12:45



檢視相片

今年全大運延用去年台北世大運火把。李天助攝



檢視相片

中央大學校長周景揚(右)王水文。李天助攝

107年全國大專校院運動會(以下簡稱107年全大運)，由教育部統籌規劃，國立中央大學承辦，今(30)日於中央聯合辦公大樓南棟1樓舉行聖火引燃典禮。聖火引燃後，將繞行傳遞，預計4月14日抵達國立中央大學，完成107年全大運聖火傳遞。

107年全大運聖火於3月30日由教育部及國立中央大學共同引燃，延用2017臺北世大運的聖火火把，期能延續2017臺北世大運熱血風潮，期許107年全大運圓滿順利，選手參賽成績亮眼，觀眾觀賽熱潮再現！聖火引燃與傳遞，象徵揭開107年全大運序幕，聖火預計從4月9日至14日傳遞6天，行經四中五校（中央警察大學、中原大學、國防大學中正理工學院和中華大學）、臺灣聯合大學系統學校（交通大學、清華大學和陽明大學）、107年全大運各協辦學校

（國立體育大學、元智大學、健行科技大學和萬能科技大學），及 108 年全大運承辦學校（中正大學），最後來到海拔 2,862 公尺的中央大學鹿林天文臺，於 4 月 14 日抵達國立中央大學。



檢視相片

全大運吉祥物表演。李天助攝

火，代表著生命的開始，文化的延續。107 年全大運聖火從鄒族戰祭 Mayasvi 中取得母火，鄒族男子會所「庫巴」Kuba 之火象徵祈求征戰勝利，喚起運動員秉持「相互尊重、了解、奮鬥、團結、公平競爭」的運動家精神，在本次賽會展現實力、旺盛企圖心與運動家精神，向自我征戰，創造佳績。國立中央大學周景揚校長從鄒族頭目取得 107 年全大運聖火母火，高聲呼喊「yokeoasu」（有「祝你健康生生不息」之意），用鄒族的祝福語，期望全國的運動選手、主辦單位和來賓觀眾，都能平安圓滿的享受這一場力與美的運動饗宴。



檢視相片

全大運聖火隊。李天助攝

本屆全大運邀請行政院長賴清德、教育部長潘文忠、體育署署長林德福、桃園市長鄭文燦、中華民國大專校院體育總會會長江漢聲及 2017 臺北世大運奪牌選手包括男子標槍鄭兆村、跆拳道莊佳佳、滑輪溜冰楊合貞、撞球許睿安、男子網球李冠毅和女子網球李亞軒等重量級貴賓拍攝宣傳片，共同為 107 年全大運運動員加油，期將國內運動競技水準朝更高、更快、更強目標推進。

本屆全大運延續世大運的感動，共有 19 個運動種類，包括田徑、游泳、體操（競技體操、韻律體操）、桌球、羽球、網球、跆拳道（品勢、對打）、柔道、擊劍、射箭、空手道、舉重、射擊、拳擊、木球、角力、滑輪溜冰、撞球及電子競技運動等種類，預計將有上萬名運動員及隊職員參加本次賽會。

為歡迎全國大專校院運動員來到國立中央大學，本屆全大運搭配主題曲「抬起頭」，知名舞蹈家藍波老師編排 107 年全大運大會舞，由 107 年全大運吉祥物「活力鼠寶」和「松果人」帶領國立中央大學 1,500 位學生一同齊跳大會舞，以舞會友，展現國立中央大學學生活力與團結。